

A Heterostructure Metal Oxide Based Photoanode for Photoelectrocatalytic Degradation of Water Pollutants and Hydrogen Generation.

Submitted to Swansea University in the fulfilment of the requirements for the Degree of

Doctor of Philosophy

By

Katherine Rebecca Davies

Summary

With a growing population the production of medication and cleaning products has increased significantly. This has resulted in these compounds entering freshwater sources as current wastewater treatment technologies are unable to completely remove them. This can cause harm to aquatic and human life while increasing bacteria's resistance to disinfectants. Therefore, this study focused on utilising photoelectrocatalysis (PEC) to determine its feasibility as an alternative process for removing pollutants from water. In this study a $\text{WO}_3/\text{BiVO}_4$ photoanode was successfully synthesised which could produce a high photocurrent of 2.75 mA/cm^2 . Utilising this photoanode with the optimised PEC operating parameters determined in this study a high degradation of ibuprofen (96%), benzyldimethyldodecylammonium chloride (100%) and sodium 2-naphthalenesulfonate (100%) was achieved. This demonstrated how successful the PEC system developed in this study was in degrading pollutants that current water treatment technologies struggle to remove. However, there were some drawbacks identified with utilising PEC. In relation solely to the ibuprofen degradation process, 4-isobutylacetophenone was identified by the mass spectrometer as one of the main by-products. This is an environmental concern as this compound is more hazardous than ibuprofen. Significantly, however it highlighted the importance of utilising a mass spectrometer to identify by-products produced during pollutant degradation and determine the toxicity of the resulting solution. A further drawback identified was that during the degradation of all the pollutants the pH of the treated solution was very acidic (2.59-2.75) which means a post-treatment step is required to help neutralise the solution. However, this study did evidence a significant benefit of utilising PEC in that it can produce considerable amounts of hydrogen with or without pollutant degradation. PEC can be utilised to produce hydrogen in a sustainable way.

Declaration

This work has not previously been accepted in substance for any degree and is not being concurrently submitted in candidature for any degree.

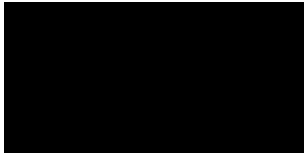
Signed



Date 17th March 2022

This thesis is the result of my own investigations, except where otherwise stated. Other sources are acknowledged by footnotes giving explicit references. A bibliography is appended.

Signed



Date 17th March 2022

I hereby give consent for my thesis, if accepted, to be available for photocopying and for inter-library loan, and for the title and summary to be made available to outside organisations.

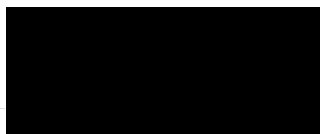
Signed



Date 17th March 2022

The University's ethical procedures have been followed and, where appropriate, that ethical approval has been granted.

Signed



Date 17th March 2022

Table of Contents

<i>Summary</i>	1
<i>Declaration</i>	2
<i>List of Figures</i>	6
<i>List of Tables</i>	10
<i>Acknowledgements</i>	12
<i>Publications</i>	13
Published	13
Under review/Manuscript Preparation	13
<i>Abbreviations and Definitions</i>	14
<i>Chapter 1 : Introduction</i>	15
1.1 Why We Need Water Treatment Processes?	15
1.2. The Effects of Pollutants	16
1.2.1 Pharmaceutical Waste	17
1.2.2 Surfactants	20
1.3. Conventional Wastewater Treatments and their Drawbacks	21
1.4. Advanced Oxidation Processes (AOPs)	24
1.5. How Can Photoelectrocatalysis be Utilised to Degrade the Water Pollutants	27
1.5.1 Fundamentals of PEC	28
1.5.2 PEC System	32
1.5.3 The Advantages of PEC	41
1.5.4 Limitations of PEC	42
1.5.5 Justification of Utilising PEC for Ibuprofen and Surfactant Degradation	42
1.6. Producing Hydrogen Fuel Using Photoelectrocatalysis	45
1.7. Aims of Thesis	48
1.8 Bibliography	49
<i>Chapter 2 : Materials and Methodology</i>	56
2.1 Laboratory Equipment	56
2.2 PEC Set-up	56
2.3 Chemicals	58
2.4 Photoanode Development	58
2.4.1 Chronoamperometry	61
2.4.2 Linear Sweep Voltametry (LSV)	62
2.4.3 Electrochemical Impedance Spectroscopy (EIS) and Intensity-Modulated Photocurrent Spectroscopy (IMPS)	63
2.4.4 Photoanode Characterisation	65
2.5 Pollutant Degradation	68
2.5.1 Liquid Chromatography with UV detector (LC-UV) Methods	68
2.5.2 LC-UV Reproducibility and Calibration	71

2.5.4 Ibuprofen Degradation Experiment Conditions.....	74
2.5.5 BAC-C12 Degradation Experiment Conditions	76
2.5.6 S2NS Degradation Experiment Conditions	77
2.4.7 Analysis of the Pollutant Degradation	77
2.5.8 Reactive Species Identification.....	78
2.5.9 By-Product Identification.....	79
2.6 Hydrogen Production	82
2.6 Bibliography	84
<i>Chapter 3 : Photoanode Development.....</i>	<i>85</i>
3.1 Introduction.....	85
3.2 Results and Discussion	85
3.2.1 Preparing the Primary Semiconductor WO ₃	85
3.2.2 Crystalline Structure Analysis of WO ₃	88
3.2.3 Chemical Environment of WO ₃	89
3.2.4 Optical Property of WO ₃	90
3.2.5 Preparation and Investigation of BiVO ₄ Film.....	93
3.2.6 Creating a Heterostructure Metal Oxide Photoanode	97
3.2.7 Characterization of WO ₃ /BiVO ₄	99
3.2.8 The Photoelectrochemical Activity of WO ₃ /BiVO ₄	104
3.2.9 The Effect of Varying the Semiconductors' Thickness on The Heterostructure Photoanode's Performance	108
3.2.11 How Do the Operating Conditions Effect the Photocurrent Production.....	123
3.3 Conclusion	127
3.4 Bibliography	129
<i>Chapter 4 : Ibuprofen Degradation.....</i>	<i>132</i>
4.1 Introduction.....	132
4.2 Results and Discussion	132
4.2.1 Development of Ibuprofen Analysis.....	132
4.2.2 Ibuprofen Degradation Via Photoelectrocatalysis	139
4.2.3 The Degradation Pathway of Ibuprofen via The Optimised PEC System.....	148
4.2.4 Species Responsible for Ibuprofen Degradation.....	149
4.2.5 Identification of By-Products.....	154
4.2.6 The Feasibility of Utilising PEC for Ibuprofen Degradation.....	162
4.3 Conclusion	165
4.4 Bibliography	167
<i>Chapter 5 : Surfactant Degradation.....</i>	<i>170</i>
5.1 Introduction.....	170
5.2 Results and Discussion	170
5.2.1 Quantification of Surfactant Degradation.....	170
5.2.2 BAC-C12 Degradation.....	175
5.2.3 S2NS Degradation	177
5.2.4 Degradation Pathway Explained.....	179
5.2.5 The Feasibility of Surfactant Degradation Via Photoelectrocatalysis	182

5.3 Conclusion	183
5.4 Bibliography	184
<i>Chapter 6 : Hydrogen Production</i>	<i>186</i>
6.1 Introduction.....	186
6.2 Results and Discussion	186
6.2.1 Hydrogen Production Without Pollutants.....	186
6.2.2 Hydrogen Production During Ibuprofen Degradation	188
6.2.3 Hydrogen Production During Surfactant Degradation	191
6.2.4 Limitations of these Hydrogen Production Studies	193
6.3 Conclusion	195
6.4 Bibliography	197
<i>Chapter 7 : Conclusion and Future Outlook</i>	<i>198</i>
7. 1 Photoanode Development	199
7.2 Ibuprofen Degradation.....	200
7.2.2 Future Work	201
7.3 Surfactant Degradation	201
7.3.2 Future Work	202
7.4 Hydrogen production	203
7.4.2 Future Work	203
7.5 Bibliography	205
<i>Appendix 1.1</i>	<i>206</i>
<i>Appendix 2.1</i>	<i>209</i>
<i>Appendix 2.2</i>	<i>210</i>
<i>Appendix 2.3</i>	<i>211</i>
<i>Appendix 2.4</i>	<i>213</i>
<i>Appendix 2.5</i>	<i>217</i>
<i>Appendix 2.6</i>	<i>219</i>
<i>Appendix 2.7</i>	<i>221</i>
<i>Appendix 2.8</i>	<i>223</i>
<i>Appendix 2.9</i>	<i>229</i>
<i>Appendix 2.10</i>	<i>232</i>
<i>Appendix 2.11</i>	<i>233</i>
<i>Appendix 3.1</i>	<i>236</i>
<i>Appendix 3.3</i>	<i>238</i>
<i>Appendix 3.4</i>	<i>241</i>
<i>Appendix 3.5</i>	<i>246</i>
<i>Appendix 3.6</i>	<i>251</i>

List of Figures

Figure 1.1 - Schematic illustration of pharmaceutical water pollutants pathways from industry to water bodies.	18
Figure 1.2 - Illustration of how surfactants work.	20
Figure 1.3 – A simple illustration explaining how photoelectrocatalysis works in this study.	29
Figure 1.4 - The schematic illustration of energetic structure at electrode/electrolyte interfaces in photoelectrochemical water splitting process with a n-type semiconductor (a) equilibrium condition ($V=V_{fb}$), (b) after immersing the electrode in electrolyte ($V>V_{fb}$) and (c) under light condition ($h\nu = E_g$).	32
Figure 1.5 - A plot displaying the band positions of various n-type semiconductors in regard to their redox potentials and was adapted from a figure created by Jiang et al [55].	33
Figure 1.6 - Schematic illustration of $WO_3/BiVO_4$ electronic structure.	35
Figure 1.7 - Schematic illustration of the PEC cell utilised for pollutant degradation experiments.	40
Figure 2.1 - An image showing the two compartment PEC cell utilised for all PEC experiments.	57
Figure 2.2 - An image showing the PEC cell during a pollutant degradation experiment.	57
Figure 2.3 - The WO_3 paste synthesis method.	59
Figure 2.4 - The equivalent circuit utilised for resistance calculations [3].	64
Figure 3.1 – SEM images for WO_3 film fabricated using (a) Paste 1, (b) Paste 2, EDS analysis of (c) Paste 1 and (d) Paste 2.	86
Figure 3.2 - The chronoamperometry results for Paste 1 and Paste 2, the experiment was run by utilising 2 layer pristine WO_3 as the working electrode, Pt wire as the counter electrode, Ag/AgCl as reference electrode, +1.2 V (vs Ag/AgCl) potential, 0.5 M NaCl electrolyte and a chopped light (30 seconds on/off) with a solar light intensity of 1 Sun.	87
Figure 3.3 - A plot displaying the average photocurrent density produced for each WO_3 paste type.	87
Figure 3.4 - The XRD diffraction pattern of pristine WO_3	88
Figure 3.5 - The XPS core spectra results of pristine WO_3 . The experimental results of W4f core spectra (red colour) are fitted with CasaXPS software.	89
Figure 3.6 – The K-M spectra obtained for pristine WO_3	90
Figure 3.7 – The Tauc plot of WO_3	92
Figure 3.8 - Images obtained for thin film $BiVO_4$ during (a) SEM analysis and (b) EDS analysis.	93
Figure 3.9 – The XRD diffraction pattern of pristine $BiVO_4$	94
Figure 3.10 - The XPS obtained for pristine $BiVO_4$ focused on the Bi4f signals. The experimental results of Bi4f core spectra (red colour) are fitted with CasaXPS software.	95
Figure 3.11 - The XPS obtained for pristine $BiVO_4$ focused on the O1s and V2p signals. The experimental results of O1s and V2p core spectra (red color) are fitted with CasaXPS software.	95
Figure 3.12 – The K-M spectra of pristine $BiVO_4$	96
Figure 3.13 – The Tauc plot of $BiVO_4$	97
Figure 3.14 - The images obtained during the SEM analysis for (a) Pristine WO_3 and (b) $WO_3/BiVO_4$	98

Figure 3.15 - HR-TEM analysis of (a-b) of pristine WO ₃ and (c-d) of WO ₃ /BiVO ₄ photoanodes.	99
Figure 3.16 - The XRD diffraction pattern obtained for the synthesised WO ₃ /BiVO ₄ photoanode.	99
Figure 3.17 - The XPS spectra obtained for pristine WO ₃ focused on W4f peaks. The experimental results of W4f core spectra (red colour) are fitted with CasaXPS software.	100
Figure 3.18 - The XPS spectra obtained for WO ₃ /BiVO ₄ focused on W4f peaks. The experimental results of W4f core spectra (red colour) are fitted with CasaXPS software.	101
Figure 3.19 - The XPS spectra obtained for BiVO ₄ focused on Bi4f peaks. The experimental results of Bi4f core spectra (red colour) are fitted with CasaXPS software.	102
Figure 3.20 - The XPS spectra obtained for WO ₃ /BiVO ₄ focused on Bi4f peaks. The experimental results of Bi4f core spectra (red colour) are fitted with CasaXPS software.	102
Figure 3.21 - The XPS spectra obtained for BiVO ₄ focused on O1s and V2p peaks. The experimental results of O1s and V2p core spectra (red colour) are fitted with CasaXPS software.	103
Figure 3.22 - The XPS spectra obtained for WO ₃ /BiVO ₄ focused on O1s and V2p peaks. The experimental results of O1s and V2p core spectra (red colour) are fitted with CasaXPS software.	103
Figure 3.23 - A graph displaying the production of photocurrent by pristine WO ₃ (2 layers) and WO ₃ /BiVO ₄ (2 layers of WO ₃ and 1 BiVO ₄) with a chopped light (30 secs off/on for 5 minutes), 1.2 V applied potential and 0.5 M NaCl supporting electrolyte.	104
Figure 3.24 - The LSVs for Pristine WO ₃ and WO ₃ /BiVO ₄ the experiment details were that the electrolyte was 0.5M NaCl, 1 sun of solar light (when light was turned on), scan limit from -0.5 V to 1.5 V.	105
Figure 3.25 - The K-M spectra of (blue) WO ₃ , (red) BiVO ₄ and (green) WO ₃ /BiVO ₄	106
Figure 3.26 - The Tauc plot of WO ₃ /BiVO ₄	107
Figure 3.27 - The Nyquist plot obtained from the IMPS analysis of (blue) WO ₃ and (red) WO ₃ /BiVO ₄ . The experimental details summarised in Table 2.6.	108
Figure 3.28 - Transverse SEM analysis of (a) 1 Layer of WO ₃ with BiVO ₄ , (b) 2 Layers of WO ₃ with BiVO ₄ , (c) 3 Layers of WO ₃ with BiVO ₄ and (d) 4 Layers of WO ₃ with BiVO ₄	111
Figure 3.29 - A schematic illustration of how altering the WO ₃ cycles effects the cross-sectional surface morphology	112
Figure 3.30 - The EDS mapping obtained for (a) 1WO ₃ /1BiVO ₄ , (b) 2WO ₃ /1BiVO ₄ , (c) 3WO ₃ /1BiVO ₄ and (d) 4WO ₃ /1BiVO ₄	112
Figure 3.31 - The LSV analysis of (a) 1WO ₃ /1BiVO ₄ , (b) 2WO ₃ /1BiVO ₄ , (c) 3WO ₃ /1BiVO ₄ and (d) 4WO ₃ /1BiVO ₄ . Note that the experiment details were that the electrolyte was 0.5M NaCl, 1 sun of solar light, scan limit from -0.5 V to 1.5 V.	113
Figure 3.32 - A plot displaying the average photocurrent densities for each synthesised WO ₃ /BiVO ₄ photoanode.	114
Figure 3.33 - The EIS Nyquist plots for WO ₃ /BiVO ₄ photoanodes with varying WO ₃ thickness. The experimental details are summarised in Table 2.5.	115
Figure 3.34 - The IMPS Nyquist plot for each WO ₃ /BiVO ₄ photoanode with varying WO ₃ thickness. The experimental details summarised in Table 2.6.	116
Figure 3.35 - The XRD diffraction pattern obtained for each WO ₃ /BiVO ₄ photoanode with different WO ₃ thickness.	118

Figure 3.36 - LSV analysis of (a) $2\text{WO}_3/1\text{BiVO}_4$, (b) $2\text{WO}_3/2\text{BiVO}_4$ and (c) $2\text{WO}_3/4\text{BiVO}_4$. Note that the experiment details were that the electrolyte was 0.5M NaCl, 1 sun of solar light, scan limit from -0.5 V to 1.5 V.....	119
Figure 3.37 - A plot displaying the amount of photocurrent density produced by each $\text{WO}_3/\text{BiVO}_4$ of varying BiVO_4 thickness.	120
Figure 3.38 - The EIS Nyquist plot for each $\text{WO}_3/\text{BiVO}_4$ with varying BiVO_4 thickness. The experimental details are summarised in Table 2.5.....	121
Figure 3.39 - The XRD diffraction pattern obtained for each $\text{WO}_3/\text{BiVO}_4$ photoanode with varying BiVO_4 thickness.....	122
Figure 3.40 - The chronoamperometry obtained for the optimised photoanode with (blue) pure water, (red) 0.5 M Na_2SO_4 and (green) 0.5 M NaCl. Note that all the experiments had an applied potential + 0.6 V with a chopped light (30 secs off/on for 5 minutes)..	123
Figure 3.41 - The J-V plots when utilising 0.5 M Na_2SO_4 electrolyte (blue) and 0.5 M NaCl (red). Note that the experiment details were that 1 sun of solar light was utilised with a scan limit from -0.5 V to 1.5 V at a rate of 50 mV/s.	124
Figure 3.42 - The chronoamperometry obtained for the optimised photoanode with (blue) 0.1 M NaCl, (red) 0.5 M NaCl and (green) 1 M NaCl supporting electrolyte. Note that the constant experimental details were that an applied potential of 0.6 V was utilised with a chopped 1 Sun of solar light (on/off, 30 s each) for 5 minutes.....	125
Figure 3.43 - The chronoamperometry obtained for the optimised photoanode with (blue) 0.6 V, (red) 0.9 V, (green) 1.2 V and (yellow) 1.5 V. Note that the constant experimental details were that an 0.5 M NaCl supporting electrolyte was utilised with a chopped 1 Sun of solar light (on/off, 30 s each) for 5 minutes.	126
Figure 4.1 - Chromatogram of the ibuprofen standard when utilising LC-UV method 1.	133
Figure 4.2 - A graph showing the ibuprofen concentration achieved for each filter.	137
Figure 4.3 - A graph showing the ibuprofen degradation during the dark and light (1 Sun of solar light) PEC process with the following conditions 0.5 M NaCl as supporting electrolyte, 0.6 V (vs Ag/AgCl) as an applied potential and 2 hours of run time.....	140
Figure 4.4 - Chromatogram obtained from the LC-UV analysis of 0-minute dark sample...	141
Figure 4.5 - Chromatogram obtained from the LC-UV analysis of 120-minute dark sample.	141
Figure 4.6 - Chromatogram obtained from the LC-UV analysis of 30-minute light sample.	142
Figure 4.7 - A graph demonstrating the ibuprofen degradation achieved for each PEC experiment with the following conditions 0.5 M NaCl, 30 minutes in dark then 2 hours with 1 Sun of Simulated Solar Light (blue) 0.6 V vs Ag/AgCl, (red) 0.9 V vs Ag/AgCl, (green) 1.2 V vs Ag/AgCl and (yellow) 1.5 V vs Ag/AgCl.	143
Figure 4.8 - The photocurrent produced by the photoanode during the ibuprofen degradation experiments in Figure 4.7.	144
Figure 4.9 - PEC ibuprofen degradation vs time plot for different concentrations of the NaCl electrolyte. Note that the PEC experiment was conducted at applied potential 1.2 V Vs Ag/AgCl). The simulated solar light irradiation (1 Sun) was used for PEC experiments.	146
Figure 4.10 - The photocurrent produced by the photoanode during the ibuprofen degradation experiments in Figure 4.9.	147
Figure 4.11 - The chromatogram obtained from the final sample of the optimised PEC ibuprofen degradation experiment.	149
Figure 4.12 - A graph displaying the coumarin degradation achieved by the utilisation of the optimised PEC system. Note that the experiment was run with $2\text{WO}_3/1\text{BiVO}_4$ as the photoanode, Pt wire as the counter electrode, Ag/AgCl as the reference electrode, 1 M	

NaCl as the supporting electrolyte, 1.2 V applied potential and 1.5 hr of 1 Sun solar light irradiation.	150
Figure 4.13 - The PL spectra obtained during the coumarin degradation experiment.	151
Figure 4.14 - A graph of the ibuprofen degradation achieved during each run of the optimised PEC system while utilising the same 2WO ₃ /1BiVO ₄ photoanode.	164
Figure 5.1 - The chromatogram obtained for a pure BAC-C12 standard utilising the best method developed.	171
Figure 5.2 - The chromatogram obtained for a pure S2NS standard utilising the best method developed.	171
Figure 5.3 - A plot comparing the degradation of high concentration (100 µg/mL) vs low concentration (50 µg/mL) of BAC-C12 during the PEC experiment. The experiment details are the supporting electrolyte was 1 M NaCl, with 1.2 V (vs Ag/AgCl) and 2 hours of 1 Sun solar light irradiation with an initial 30 minutes in the dark.	176
Figure 5.4 - The chromatogram obtained for the analysis of 150-minute sample from the PEC degradation of 100 µg/mL BAC-C12.	176
Figure 5.5 - A plot showing the photocurrent produced during the BAC-C12 degradation experiments.	177
Figure 5.6 - A plot comparing the degradation of (red)50 µg/mL BAC-C12 vs (blue) µg/mL S2NS during the PEC process. The experiment details are the supporting electrolyte was 1 M NaCl, with 1.2 V (vs Ag/AgCl) and 2 hours of 1 Sun solar light irradiation with an initial 30 minutes in the dark.	178
Figure 5.7 - The photocurrent produced by the photoanode during the two surfactant degradation experiments.	179
Figure 6.1 - Hydrogen production for the developed PEC system. Note that The PEC system utilised for hydrogen production used 2WO ₃ /1BiVO ₄ (photoanode), Pt mesh (counter electrode), Ag/AgCl (reference electrode), 1.2 V applied potential, 0.5 M sodium chloride as the supporting electrolyte and 1 Sun of Solar Light irradiation (2 hours) after 30 minutes in the dark.	187
Figure 6.2 - Hydrogen production for the developed PEC system during ibuprofen degradation (red) and no ibuprofen degradation (blue). Note that The PEC system utilised for hydrogen production used 2WO ₃ /1BiVO ₄ (photoanode), Pt mesh (counter electrode), Ag/AgCl (reference electrode), 1.2 V applied potential, 0.5 M sodium chloride as the supporting electrolyte and 1 Sun of Solar Light irradiation (2 hours) after 30 minutes in the dark.	189
Figure 6.3 - Hydrogen production for the developed PEC system in complete dark conditions (blue) and during 1 Sun of Solar Light irradiation (2 hours) after 30 minutes in the dark (red). Note that The PEC system utilised for hydrogen production used 2WO ₃ /1BiVO ₄ (photoanode), Pt mesh (counter electrode), Ag/AgCl (reference electrode), 1.2 V applied potential and 0.5 M sodium chloride as the supporting electrolyte.	190
Figure 6.4 - Hydrogen production for the developed PEC system in ibuprofen degradation in 0.5 M NaCl (blue) and ibuprofen degradation in 1 M NaCl (red). Note that The PEC system utilised for hydrogen production used 2WO ₃ /1BiVO ₄ (photoanode), Pt mesh (counter electrode), Ag/AgCl (reference electrode), 1.2 V applied potential and 1 Sun of Solar Light irradiation (2 hours) after 30 minutes in the dark.	191
Figure 6.5 - Hydrogen production for the developed PEC system during S2NS degradation (blue), BAC-C12 degradation (red) and ibuprofen degradation. Note that The PEC system utilised for hydrogen production used 2WO ₃ /1BiVO ₄ (photoanode), Pt mesh (counter electrode), Ag/AgCl (reference electrode), 1.2 V applied potential, 1 M sodium chloride as the supporting electrolyte and 1 Sun of Solar Light irradiation (2 hours) after 30 minutes in the dark.	192

List of Tables

Table 1.1 - A table displaying the different type of pollutants detected in the environment and drinking water.	16
Table 1.2 - A table displaying all the different pharmaceutical pollutants and their effects. ..	19
Table 1.3 - A table summarising the different types of conventional wastewater technologies and their removal efficiencies for different pollutants.	24
Table 1.4 - A table summarising the different types of AOPs wastewater technologies and their removal efficiencies for different pollutants.	26
Table 1.5 - A table presenting the ibuprofen concentration in different environmental water sources around the world [90, 94].	43
Table 2.1 - The method utilised for determining the best supporting electrolyte for the PEC system.	61
Table 2.2 - The method utilised for determining the best supporting electrolyte concentration for the PEC system.	62
Table 2.3 - The method utilised for determining the best applied potential for the PEC system.	62
Table 2.4 - The method utilised for the LSV experiments.	63
Table 2.5 - The method utilised for the EIS experiments.	63
Table 2.6 - The method utilised for the IMPS experiments.	65
Table 2.7 - The UV method for photoanode analysis.	66
Table 2.8 - The chosen method developed for ibuprofen analysis.	69
Table 2.9 - The chosen method developed for BAC-C12 analysis.	70
Table 2.10 - The chosen method developed for S2NS analysis.	70
Table 2.11 - A table showing the concentrations of the calibration standards for each pollutant.	73
Table 2.12 - A table showing the concentrations of the QC standards for each pollutant.	73
Table 2.13 - The PEC experiment method for ibuprofen degradation in the dark.	75
Table 2.14 - The PEC experiment method for ibuprofen degradation in the light.	75
Table 2.15 - The PEC experiment method for optimising the applied potential.	75
Table 2.16 - The PEC experiment method for optimising the supporting electrolyte concentration.	76
Table 2.17 - The PEC experiment method for the higher concentration of BAC-C12 degradation.	76
Table 2.18 - The PEC experiment method for the lower concentration of BAC-C12 degradation.	76
Table 2.19 - The PEC experiment method for the of S2NS degradation.	77
Table 2.20 - The method utilised for the LC part of the LCMS.	81
Table 2.21 - The method utilised for the MS part of the LCMS.	81
Table 2.22 - The collision energies chosen for the fragmentation of the by-product compounds.	82
Table 2.23 - The PEC experiments ran for hydrogen production.	83
Table 4.1 - The first method developed for detection of ibuprofen via LC-UV.	133
Table 4.2 - The calculated CV% and F-test value obtained for the retention time reproducibility.	134
Table 4.3 - The calculated CV% and F-test value for the injection repeatability of ibuprofen.	134
Table 4.4 - A table displaying the values obtained from the regression statistics analysis. ...	135

Table 4.5 - A table displaying the calculated mean concentrations, accuracy % and precision % of the QCs.	135
Table 4.6 - A table displaying the difference in ibuprofen concentration between the filtered samples and the non-filtered standards.	138
Table 4.7 - A table displaying the calculated percentage yields and loss (%).	139
Table 4.8 - The optimised photoelectrocatalysis method.	148
Table 4.9 - A table displaying rough approximations of the hydrogen peroxide concentration in the solution during the ibuprofen degradation process.	152
Table 4.10 - A table displaying the pH of the solution in the anodic compartment before and after treatment.	153
Table 4.11 - A table displaying the LC-MS method operating parameters.	155
Table 4.12 - A table displaying the m/z values and their retention times obtained from the mass scan.	155
Table 4.13 - A table showing the retention times for each peak associated with the individual m/z ratios.	156
Table 4.14 - A table showing the retention times of each compound obtained by the LC-MS.	157
Table 4.15 - A table showing the optimised collision energy for each compound found.	157
Table 4.16 - A table displaying each compound with their corresponding peaks.	158
Table 4.17 - A table summarising the possible by-products from ibuprofen degradation experiments by PEC and other techniques.	159
Table 4.18 - A table comparing the product ion peaks obtained for the samples and the literature for each compound.	161
Table 4.19 - Display of the COD values obtained before and after treatment.	164
Table 5.1 - Results for retention times repeatable for each surfactant.	172
Table 5.2 - Results for the injection repeatability for each surfactant.	172
Table 5.3 - The values obtained from the regression of the calibration graph.	173
Table 5.4 - The average accuracy and precision calculated for the QCs of BAC-C12 and S2NS.	173
Table 5.5 - The obtained recovery percentages of the surfactants after filtering.	174
Table 5.6 - The H ₂ O ₂ concentration monitored from PEC cell throughout the surfactant degradation process.	180
Table 5.7 - The pH of the solution during the surfactant degradation experiments.	181

Acknowledgements

Firstly, I would like to convey my greatest appreciation to my project supervisor, Dr Sudhagar Pitchaimuthu for giving me the opportunity to complete a Ph.D. Without his trust, support, motivation, and knowledge I would not have been able to complete this Ph.D. I want to thank Prof. Trystan Watson, joint-supervisor of this thesis for his constant support to complete the thesis work in time. Secondly, I would like to say a thank you to my secondary supervisor Dr Moritz Kuehnel and his PhD student Michael Allan who gave me a lot of support and allowed me to utilise their GC and lab.

I want to give a special thank you to two important ladies that without them I would not be the researcher I am today, Dr Ruth Godfrey and Dr Rachel Townsend. Not only did they allowed me to utilise their equipment but with their expert knowledge and trust I was able to get the data needed for this thesis. They also believed in me during times I did not believe in myself which helped improve my confidence and that I am thankful for every day that I meet and worked them.

While I want to thank Dr Matthew Carnie and Dr Adam Pockett as without them I would not have a lab after my lab was involved in a fire and was unusable for 18 months. They also allowed me access to their equipment and with their knowledge helped me understand analysis methods which would further assess my photoanodes. I would also like to thank James Russell, Tom Dunlop and Chalmers University of Technology, Sweden for helping me obtain SEM, XRD, XPS and HR-TEM data.

Finally, I would like to say a massive thank you to my partner Nick that with his continuous love, support and patience helped me to achieve this dream of mine. Also, I would like to thank my family especially my parents who without their support, encouragement and love I would not have been able to submit this thesis.

Publications

Published

1. K.R. Davies, Y. Cherif, G.P. Pazhani, S. Anantharaj, H. Azzi, C. Terashima, A. Fujishima, Sudhagar Pitchaimuthu, The upsurge of photocatalysts in antibiotic micropollutants treatment: Materials design, recovery, toxicity and bioanalysis, *Journal of Photochemistry and Photobiology C: Photochemistry Reviews*, 48 (2021) 100437 – This is a review paper which is not related to the work in this thesis.
2. Ben Jones, Katherine R. Davies, Michael G. Allan, S. Anantharaj, Ian Mabbett, Trystan Watson, James R. Durrant, Moritz F. Kuehnel, Sudhagar Pitchaimuthu*. Photoelectrochemical Concurrent Hydrogen Generation and Heavy Metal Recovery from Polluted Acidic Mine Water. *Sustainable Energy Fuels*, 2021,5, 3084-3091 - Collaboration paper not related to the work in this thesis.

Under review/Manuscript Preparation

1. Katherine Rebecca Davies, Adam Pockett, Sanjay Nagarajan, Tom Dunlop, James D. McGettrick, Matthew J. Carnie, Vijay Asokan, Trystan Watson, Moritz Kuehnel, Sudhagar Pitchaimuthu. Does photoabsorber thickness affect photoelectrochemical water splitting performance? A case study on mesoporous WO₃/BiVO₄ heterostructure photoanode. Manuscript submitted to *Catalysis Communications* (invited article).
2. Katherine Rebecca Davies, Michael G. Allan, Townsend Rachel, Sanjay Nagarajan, Vijay Shankar Asokan, Anantharaj Sengeni, Ruth Godfrey, Trystan Watson, James Durrant, Moritz F. Kuehnel, Sudhagar Pitchaimuthu*. Photoelectrocatalytic in-situ hydrogen peroxide synthesis for pharmaceutical water pollutants treatment and producing green hydrogen gas using WO₃/BiVO₄ photoanode. Under manuscript preparation (to be submitted to *ACS Catalysis*).
3. Katherine Rebecca Davies, Michael G. Allan, Townsend Rachel, Sanjay Nagarajan, Ruth Godfrey, Trystan Watson, Moritz F. Kuehnel, and Sudhagar Pitchaimuthu*. Photoelectrochemical surfactants pollutants degradation and recovering green hydrogen gas. Under manuscript preparation (to be submitted to *Physical Chemistry and Chemical Physics*).

Abbreviations and Definitions

A	Absorption	mg/L	Milligram per litre
ABPE	Applied bias photon-to-current efficiency	mL/min	Millilitre per minute
ACN	Acetonitrile	mL	millilitres
Ag/AgCl	Silver/Silver Chloride	mol/L	Moles per litres
AOPs	Advanced oxidation processes	μM	micromoles
BAC-C12	Benzyltrimethylammonium Chloride	NaCl	Sodium Chloride
Bi	Bismuth	Na_2SO_4	Sodium Sulfate
BiVO_4	Bismuth Vanadate	nm	nanometre
CB	Conduction Band	ng/L	Nanogram per litre
CdS	Cadmium Sulfide	nm	Nanometre
Cl_2	Chlorine Gas	NTAs-Au-	Titanium dioxide Nanotube coupled with Gold and Cadmium Selenide
Cl^-	Chlorine ion	CdSe	
$\text{Cl}\cdot$	Chlorine radical	m/z	Mass-to-charge ratio
ClO^-	Hypochlorite	$\cdot\text{O}_2^-$	Superoxide
CO_2	Carbon dioxide	$\cdot\text{OH}$	Hydroxyl radicals
CV%	Coefficient of Variation	PC	photocatalysis
e^-	electron	PEC	Photoelectrocatalysis
eV		PL	Photoluminescence Spectrometer
FTO	Fluorine-doped Tin Oxide	Pt mesh	Platinum Mesh
GaP	Gallium Phosphide	PVDF	Polyvinylidene Fluoride
GC	Gas Chromatography	QACs	Quaternary Ammonium Compounds
h^+	holes	R	Reflection
H^+	Hydrogen Ion	R_{ct}	Charge Transfer Resistance
H_2	Hydrogen gas	S2NS	Sodium 2-naphthalenesulfonate
H_2O	Water	SC	Semiconductor
HClO	Hypochlorous Acid	SEM	Scanning Electron Microscopy
H^+	Hydrogen Ion	SiC	Silicon Carbide
HPLC-UV	high-performance liquid chromatography with UV detector	τ_D	Transit Time
IPCE	Incident photon-to-current efficiency	Ti	Titanium
ITO	Indium Tin Oxide	TiO_2	Titanium dioxide
K-M	Kulbeka - Munk	$\text{TiO}_2\text{-CdSe}$	Titanium dioxide coupled with Cadmium Selenide
LAS	linear alkylbenzene sulfonates	V	voltage
LC-MS	Liquid chromatography coupled with a mass spectrometer	VB	Valance Band
LSV	Linear Sweep Voltametry	WO_3	Tungsten Trioxide
M	Mole per litre	ω_{max}	Angular Frequency
$\mu\text{g/L}$	Microgram per litre	XRD	X-Ray Powder Diffraction
		XPS	X-ray Photoelectron Spectroscopy
		ZnO	Zinc Oxide

Chapter 1 : Introduction

1.1 Why We Need Water Treatment Processes?

Water is the key for all living things to be able to eat, grow and live. Without water we would be unable to produce a wide range of items from food to life saving medication and even heating for buildings. The World Health Organisation (WHO) found that there are a minimum of 2 billion people without clean drinking water which results in 829,000 deaths per year [1]. These deaths are preventable if better water sanitation is available in the least developed countries. This would allow people to have clean water for drinking, personal hygiene and farming [1].

While there is a large part of the world without access to clean water there is an even larger proportion using excess water. Therefore, it is essential that industries from agricultural to production need to start to capture, clean and reuse their wastewater. It is also important that when water needs to be discharged into the environment it is to a standard which is safe for aquatic life. This is achieved by wastewater plants having 3 - 4 stages of treatment to improve the quality of the water so it can be re-used thus lowering the demand for fresh water [2-4].

The complex nature of the chemical compounds makes them extremely difficult to remove by during current conventional wastewater treatment [5]. The ever-expanding population and rapid industrialization causes an increase of these pollutants to be entering our wastewater, thus resulting in them entering our environment [5]. In recent years the most commonly found and highly concerning pollutants are [2, 4, 6]:

Table 1.1 - A table displaying the different type of pollutants detected in the environment and drinking water.

Category	Examples	Pathway
Pharmaceuticals	Ibuprofen, Paracetamol, Antibiotics,	Domestic wastewater e.g excretion Hospital effluents Incorrect disposal Pharmaceutical manufacturing plants
Hormones	Estrogens,	Domestic wastewater e.g excretion
Cleaning Products	Disinfectants, Antibacterial compounds	Domestic and industrial wastewater e.g washing, cleaning, etc Incorrect disposal Manufacturing plants effluents
Personal Products	Fragrances, Dyes	Incorrect disposal Leaching from landfill
Surfactants	Linear alkylbenzene sulphonic acid (LAS), quaternary ammonium compounds (QACs)	Domestic and industrial wastewater Hospital effluents
Metal Pollutants	Zinc, lead, cadmium	Discharge from underground mines Leaching from spoil heaps Leaching from sludge
Pesticides	Herbicides, fungicides, etc	Drainage from farmland or domestic gardens.

There are many reports that explored the presence of pollutants, in both environmental and drinking water. While these detections are usually in very low concentrations (ng/L) this does not mean that over a long period they may can affect human and animal (including aquatic) health. As WHO stated “*that while there are currently no risk assessments that state trace concentrations of pharmaceutical in drinking water poses risks to human health. There is also no risk assessment associated with the long-term exposure to low concentration of pharmaceuticals and combined effects of the mixture of pharmaceuticals [1]*”. Therefore, it is critical to completely remove the pollutants from water sources to lower the risk to human health. As Table 1.1 has shown there are many pollutants currently affecting our water supplies however pharmaceuticals and cleaning products such as disinfectants are two pollutant categories that stand out and will be the focus of this thesis.

1.2. The Effects of Pollutants

Pharmaceutical and cleaning products have been selected as the primary pollutants to be eradicated using photoelectrocatalysis (PEC). These products are mainly found in our water sources and are used daily by most people.

1.2.1 Pharmaceutical Waste

The pharmaceutical industry is an essential sector in the UK, as the population increases so does the demand for prescription drugs. Of significance between 1999 to 2009, the UK has seen issuing of prescription drugs increase by 65% [7]. While in 2018, it was found that 4000 active pharmaceutical ingredients were issued worldwide [8]. This explains why there is an increased presence of pharmaceutical compounds in our water sources.

Although it is important to produce and issue pharmaceutical drugs, they are considered as one of the most threatening substances due to their bioactive nature and hazardous toxic-metabolites [9]. Thus, having the potential to harm the environment [9]. There are several reasons these compounds end up in our wastewater, these include: human excretion, improper disposal i.e flushing them down the toilet and effluents from pharmaceutical facilities [9]. This results in wastewater treatment plants having to remove large concentrations of a wide variety of pharmaceutical waste [9]. Unfortunately, current water treatment technologies struggle to completely eradicate them from water. This is primarily due to the design of current water treatment technologies which results in them being unable to cope with the variety and higher concentrations. As a result, many of the water treatment technologies are unable to completely remove pharmaceutical compounds or their metabolic forms (when extracted). The primary concern with pharmaceutical compounds entering freshwater sources is that they are designed to cause biological effects in an organism even at low doses [8]. Hence potentially causing huge health complications in aquatic life [10]. Several studies have already exhibited how exposing fish to wastewater effluents has caused changes to their reproductivity, which could result in population levels decreasing [11]. The long term exposure of low concentrations of various pharmaceutical mixtures in our drinking water and freshwater could result in multiple consequences such as acute and chronic damage [12], changes to behaviour [13], a build-up in tissues, damage to reproductive systems [14], and inhibition of cell production [15]. In addition as they are stable they take a considerable time to degrade in the environment thus causing a build-up of the compounds concentration [8].

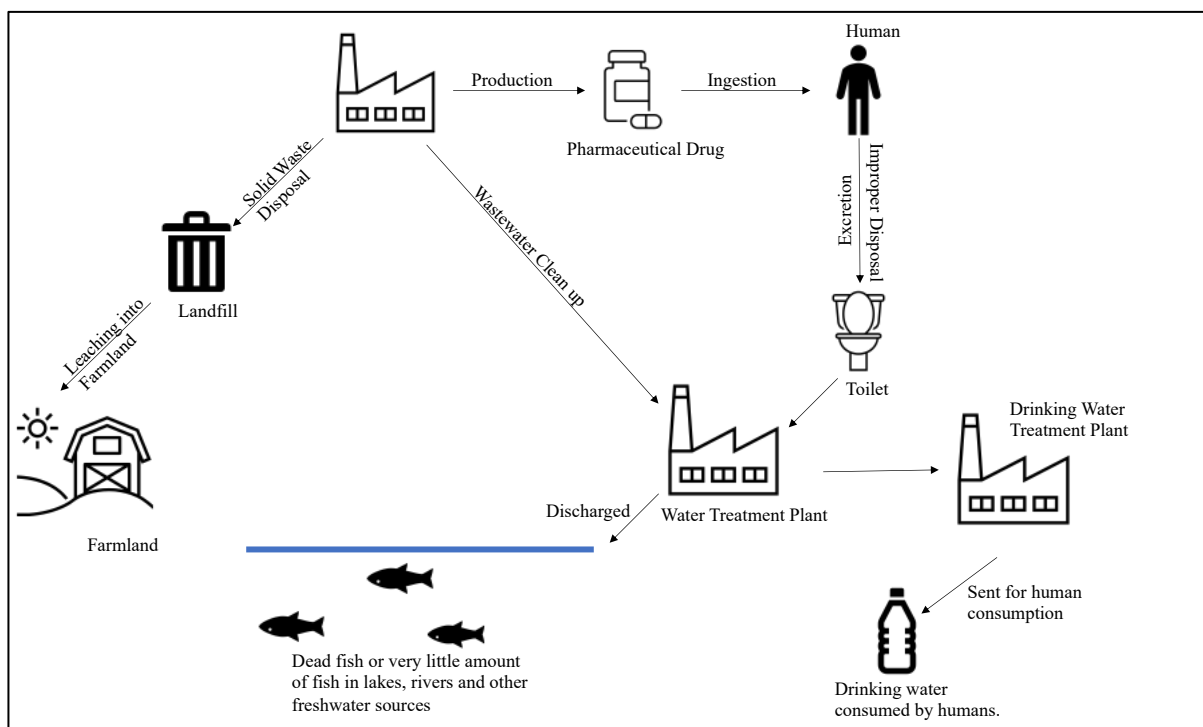


Figure 1.1 - Schematic illustration of pharmaceutical water pollutants pathways from industry to water bodies.

Whilst in the UK the concentration of pharmaceutical compounds in environmental and drinking water does not go above ng/L, in other countries (China, India, Israel, Korea and USA) the pharmaceutical compounds concentration detected has been higher (mg/L) [8]. The effects of the pharmaceutical changes depends on the compound [8] (please see Table 1.2 below) highlighting the importance of completely removing these pollutants from water.

Table 1.2 - A table displaying all the different pharmaceutical pollutants and their effects.

Category	Example	Effect
Analgesics / Painkillers	Aspirin, diclofenac, ibuprofen, paracetamol,	Damages organs, reduces hatching in fish, genotoxicity, neurotoxicity, oxidative stress in mollusks and hormone disturbance in frogs.
Antibiotics		Increasing resistance to antibiotics in bacteria, reduce growth of algae and aquatic plants.
Anti-cancer	Cyclophosphamide1, Mitomycin C, Fluorouracil	Genotoxicity
Antidiabetics	Metformin	Causing disruption to endocrines in fish
Anti- convulsants	Carbamazepine, Phenytoin, valproic acid	Problems with reproduction and delay in growth for fish
Anti-fungals	Ketoconazole, Clotrimazole Triclosan	Diminish growth in algae and fish
Antihistamines	Hydroxyzine, Fexofenadine, Diphenhydramine	Changes in behaviour, growth and feeding rates in fish, changes in behaviour and reproductivity of invertebrates
Antiparasitics	Ivermectin	Reduction in growth and reproduction of invertebrates
Beta blockers	Propranolol	Reproduction toxicity in fish and invertebrates
Endocrine	E2,EE2, Levonorgestrel	Reducing reproduction in fish and frogs due to changing hormones
Psychiatric drugs	Fluoxetine, Sertraline, Oxazepam, Citalopram, Chlorpromazine	Changes in behaviour and hormones for fish and invertebrates.

1.2.2 Surfactants

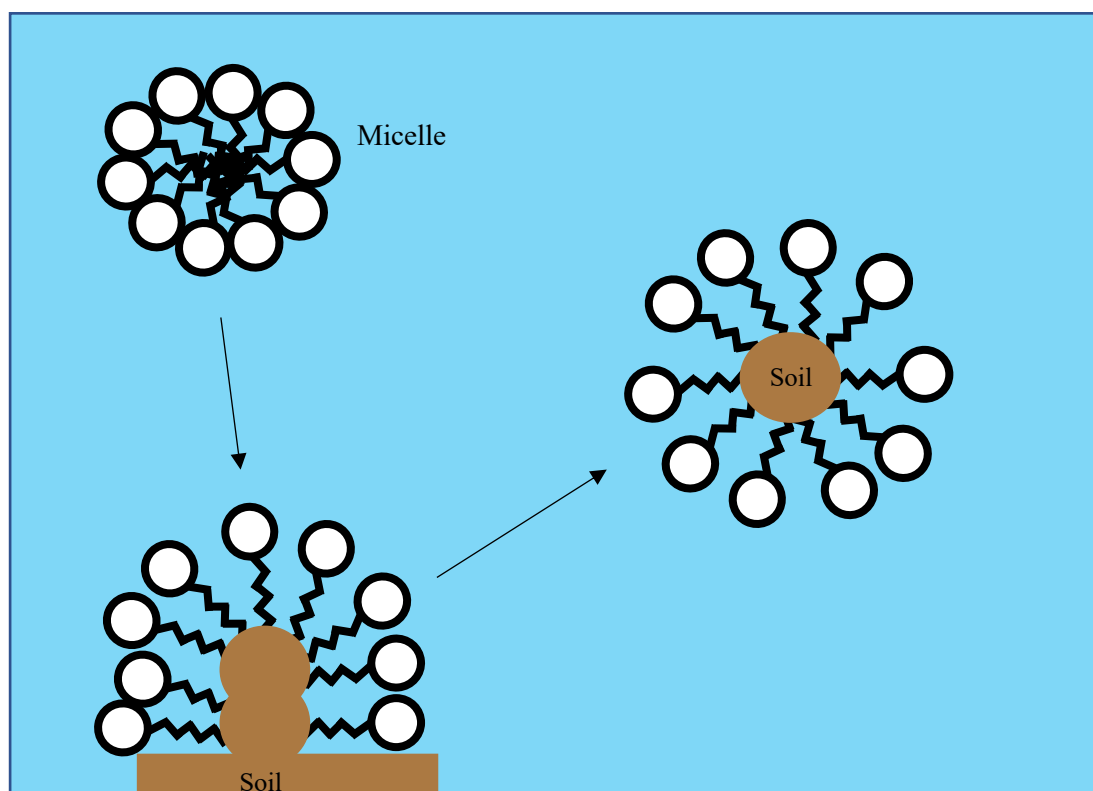


Figure 1.2 - Illustration of how surfactants work.

Surfactants are amphiphilic molecules which have hydrophobic and hydrophilic parts [16]. There are several types of surfactants these are: non-ionic (no charge), anionic (negatively charged head), cationic (positively charged head) or amphoteric (both positively and negatively charged head) [16, 17]. Surfactants have great disinfection properties because their hydrophobic tails can pull the contaminate from the surface while the hydrophobic heads help the micelle to reform and travel with the water that is rising to the surface. The utilisation of the surfactant varies for each type of surfactant. Due to their exceptional disinfection properties, they are widely utilised in households (as soaps, disinfectant sprays, laundry detergents, etc) and industries (such as pharmaceuticals, food, manufacturing etc). This means they are usually used in cleaning products and are constantly being used from morning to night to kill bacteria, virus or dirt from various surfaces. These compounds vary from domestic use such as laundry detergents to hospital or industrial use such as disinfection sprays and due to the COVID pandemic their use has intensified [18]. Consequently, this has resulted in high concentrations of surfactants entering our wastewater treatment plants [17]. Wastewater treatment processes degrade a high number of surfactants from the wastewater however some surfactants are still present in surface waters, soil and sediments. This is a major concern, as due to their toxicity they can change the ecosystem [18]. This toxicity also effects the

microorganisms utilised in wastewater plants thus hindering the degradation efficiencies for other pollutants [18]. Due to these concerns, it is vital to find an alternative water treatment technology that is able to completely remove surfactants. It is also crucial that an alternative water treatment process does not rely on the use of microorganisms which could be affected by the presence of surfactants.

1.3. Conventional Wastewater Treatments and their Drawbacks

Currently wastewater treatment plants are removing pollutants from water by utilising 3 - 4 stages of treatment known as preliminary, primary, secondary and/or tertiary depending on the standard required for the treated water. Each stage utilises a different type of technology to treat the wastewater [19]. The preliminary stage is required for the removal of solids from water and utilises physical and mechanical methods [19]. The primary stage usually utilises physicochemical and chemical methods to remove organic matter, while the secondary utilises a biological and chemical method to further remove any further organic matter [19]. If the water is required to meet a more pure standard for example drinking water than a tertiary stage is required and usually utilises physical and chemical methods [19]. There are various technologies which can be utilised for the wastewater treatment process and are described below.

Biological Treatment: There are several different types of biological treatment technologies such as activated sludge, trickling filter and biofilm reactor. However, they all utilise the same principle which is utilising microorganisms in either aerobic or anaerobic conditions to degrade the organic pollutants in the water [20]. While they are commonly utilised they do have several drawbacks to this technology which are [19, 20]:

- a) High maintenance cost as it requires an optimal environment for the microorganisms and constant management of microorganisms.
- b) Long treatment time.
- c) Low biodegradability of certain pollutants.
- d) Biological sludge is produced with uncontrollable by-products in the sludge.
- e) Complex process thus operators need training especially in enzymatic processes.
- f) Possible foaming.
- g) Toxicity of pollutants can cause the alteration of microorganisms thus hindering the degradation properties.

This technology is not ideal for industries with limited space. In addition, it is not environmentally friendly as it produces greenhouse gases during the process [21].

Adsorption: This technology requires an adsorbent material such as activated carbon (highly porous structure) within a reactor [22]. The contaminated water runs over the adsorbent material which causes liquid-solid intermolecular forces of attraction to occur between the pollutants and the adsorbent material [22]. This results in the pollutants remaining on the adsorbent material while the water exits the reactor [22]. Whilst this technology offers some advantages such as its simple, highly effective process with fast kinetics and excellent quality of treated effluents, there are some limitations such as [19]:

- a) High capital and maintenance cost.
- b) Non-selective.
- c) Performance varies for each type of adsorbent material thus it can require several adsorbents.
- d) Rapid saturation and clogging of the adsorbent material.
- e) High regeneration cost.
- f) Regeneration can cause the loss of adsorbent material.
- g) Not efficient for all pollutants.

Ion-exchange: This involves tanks filled with resin, which are small beads of organic polymer chains containing charged functional groups with either negative or positive charges [23]. Cation resin contains negative functional groups which attract positive charged ions with weak or strong acid [23]. Whilst anion resins are made of positive function groups thus attracting negative charged ions with weak or strong bases [23]. There are also mixed bed resin tanks which contain a mixture of the strong acid cation and strong base anion resin [23]. The tanks are placed in a sequence which enable all the dissolved ions to be removed [23]. The removal occurs by the protons and hydroxide ions attached to the cation or anion resin (respectively) swapping with the negatively or positively charged ions in the wastewater [23]. The hydrogen and hydroxide ions are then able to combine to form pure water while the ions stay on the resin [23]. There are several disadvantages with this technology which are [19]:

- a) High capital, maintenance and regeneration cost.
- b) Time-consuming regeneration.
- c) Large columns for large wastewater volumes thus requiring a huge amount of space.
- d) Fast clogging and saturation of the resin.
- e) Resin degrades with time and certain waste materials.
- f) Sensitive to pH of effluent.

- g) Not selective
- h) Not effective for certain pollutants such as drugs

Membrane Technology: This requires a membrane to help filter the pollutants from water. There are several membrane technologies, these are ultrafiltration, nanofiltration and reverse osmosis. Ultrafiltration and nanofiltration utilise a membrane which contains pores of 10-50 nm and 1-10nm respectively [24, 25]. The water passes through the membrane while ions bigger than these pores are blocked by the membrane. While reverse osmosis utilises a semi-permeable membrane which is hydrophilic thus allowing water to diffuse from the inlet stream (high concentration) into the outlet (low concentration) also known as the permeate line whilst contaminants remain on the outside of the membrane [24]. Due to the membrane being semi-permeable it is able to remove contaminants as small as 0.001 μm [24]. However there are several drawbacks with this technology which are [19]:

- a) High capital, maintenance and operation cost.
- b) High energy demand
- c) Quick membrane clogging.
- d) High membrane waste thus increasing environment impact and cost.
- e) Low flowrates.
- f) Training requirements for operators.

Table 1.3 - A table summarising the different types of conventional wastewater technologies and their removal efficiencies for different pollutants.

Type of Technology	Description of the Technology	Target Pollutant	Removal Efficiencies	Ref
Biological Treatment	Up-flow anaerobic batch reactor	Tylosin	95% - Tylosin 75% - COD	[26]
Biological Treatment	Activated Sludge	QACs: C12TMA C16TMA C12BDMA C16BDMA	13% 88% 67% 89%	[27]
Absorption	Power Activated Carbon	Ibuprofen	95-99.2%	[28]
Membrane Technology	XLE Reverse osmosis	2-Naphthol 4-Phenylphenol Phenacetine Caffeine NAC standard Primidone Bisphenol A Isopropylantipyrine Carbamazepine Sulfamethoxazole 17 β -Estradiol	57-91%	[29]
Ion Exchange	Strong-base Anion Exchange Polymer Resins	Diclofenac	>90%	[30]

1.4. Advanced Oxidation Processes (AOPs)

Even though some of the technologies above have demonstrated sizeable removal they have been unable to eliminate all pharmaceutical or antimicrobial agents from wastewater. These technologies also present other issues namely: high costs, high energy demand, training requirements, space consuming and high waste production. Some of these factors contribute to global warming, thus making them less favourable in the future for industry. Therefore, recently research has focused on alternative technologies that reduce the impact of cleaning

wastewater on the environment [31]. As a result this has drawn researchers to look at advanced oxidation processes (AOPs) [31]. AOPs work by producing hydroxyl radicals which oxidise organic pollutants into less harmful by-products [31]. These technologies include ozonation, Fenton's oxidation, photocatalysis, electrochemical oxidation and photoelectrocatalysis.

Ozonation: This involves utilising the ozone which is a highly oxidative gas which can dissolve in the water [32, 33]. The ozone can either degrade pollutants directly or produce hydroxyl radicals ($\bullet\text{OH}$) which can degrade the pollutants [32-34]. Sometimes ozonation degradation efficiency can be increased by the utilisation of a catalyst, utilising iron or UV light to help increase the production of reactive species such as $\bullet\text{O}_2^-$ or $\bullet\text{OH}$ which improves pollutant degradation [33]. However, there are several limitations to this technology which are [33]:

- a) Incomplete removal of pollutants
- b) Ozone is unstable thus requires to be produced on site, thus increasing cost and space needed.

Fenton's Oxidation Process: The technique utilises an iron catalyst and hydrogen peroxide to produce $\bullet\text{OH}$. The $\bullet\text{OH}$ radicals have highly oxidising properties which enables them to degrade pollutants in the water [33]. However, the main drawback is that it produces iron sludge which is difficult to remove.

Electrochemical oxidation: This technology utilises electrodes to produce reactive species which can degrade pollutants. However, there are some drawbacks which are:

- a) Expensive equipment and maintenance
- b) High energy demand
- c) Deposition formation on the electrodes lowers their performance.

Photocatalysis: A photocatalyst such as TiO_2 is irradiated by a light source such as UV light to excite electrons from the valance to the conduction band of the photocatalyst [35]. This produces holes in the valance band where it can directly degrade pollutants or produce $\bullet\text{OH}$ which degrade pollutants [35]. There are several challenges with photocatalysis:

- a) Low performance due to charge recombination of photogenerated holes and electrons.
- b) Photocatalyst particles leach into the water and can potentially harm aquatic life.

Table 1.4 - A table summarising the different types of AOPs wastewater technologies and their removal efficiencies for different pollutants.

Type of AOP	Description of Study	Pollutant	Removal Efficiency	Ref
Ozonation	Ozone dose = 0.5 mgO ₃ /mgDOC	Sulfadiazine	90%	[36]
Ozonation	Ozone dose = 4.7 mgO ₃ /mgDOC	Diatrizoic acid	90%	[36]
Ozonation	Ozone dose= 1.28 g/hO ₃ with 200 mg/LH ₂ O ₂ and pH = 11 and 30 minutes treatment time	BACs	90%	[37]
Fenton's Oxidation	Utilising FeSO ₄ .7H ₂ O with H ₂ O ₂	Various Pharmaceutical	33-100%	[38]
Fenton's Reagent Treatment	Fe ²⁺ /H ₂ O ₂ = 1:10 with pH = 3 and 1 hour treatment	BAC	80%	[39]
Photocatalysis	ZnO photocatalyst with 120 UVA irradiation	Progesterone Ibuprofen Naproxen	92.3% 94.5% 98.7%	[40]
Photocatalysis	TiO ₂ catalyst which was simulated with UV light for 180 minutes	(70-390mg/L) BAC	100% for all concentrations and 10-15% of TOC.	[41]
Electrochemical Oxidation	TNA photoanode with 1 V (vs Ag/AgCl) applied for 4 hours	ibuprofen	<10%	[42]
Electrochemical Oxidation	Cyclic flow (10 L/h) reactor with 3 g/L sodium chloride and current density of 4 A/dm ²	Gentamicin and dexamethasone	85.56% COD	[43]

Tables 1.3 and 1.4 above show that while current wastewater cleaning technologies achieve high degradation rates, they are unable to completely eliminate these pollutants. This results in low concentrations of pharmaceutical and surfactant compounds reaching our freshwater

sources and drinking water. However, this is not the only problem with current wastewater treatment plants, as there is also the issue of their contribution to greenhouse gas emissions [21]. It has been reported that biological wastewater treatment technologies produce carbon dioxide (CO₂), methane (CH₄) and nitrous oxide (N₂O), while all other technologies produce CO₂ from their high energy demand [21]. There is also the matter that waste is produced by certain wastewater treatment technologies such as biological treatment and membrane technologies. As a result, producing solid waste which requires special disposal that again requires high energy and cost. As current wastewater treatment plants require 3 to 4 (sometimes more) technologies to remove pollutants then there is an opportunity to find a more sustainable and effective technology. This could then replace either the secondary or tertiary stage of current wastewater treatments in order to complete pollutant degradation and reduce greenhouse gases production. Therefore, this thesis investigates if photoelectrocatalysis has potential as an alternative technology which could completely remove pollutants. This could help PEC come one step closer to being an alternative technology for the secondary/tertiary treatment stage.

1.5. How Can Photoelectrocatalysis be Utilised to Degrade the Water Pollutants

Photoelectrocatalysis (PEC) is an advanced oxidation process which combines photocatalytic oxidation and electrochemical oxidation process. Therefore, it requires both light (with energy equal to or more than the bandgap energy of the semiconductor) and electrical energy to achieve degradation of pollutants [44, 45]. The first successful study of this process was conducted by Fujishima and Honda in 1972 which utilised a TiO₂ electrode to split water into H₂ and O₂ [46]. This study sparked interest in photocatalysis (PC) and photoelectrocatalysis (PEC) for treatment of pollutants in water, CO₂ reduction and H₂ generation [47, 48]. Whilst there are a significant number of publications on PC, the PEC process offers some advantages over PC. For instance, photoelectrocatalyst material immobilised on a substrate avoids post-filtration step (lower cost) and applied potential prevents charge recombination thus achieving higher degradation of pollutants [49].

For several reasons PEC was chosen as the technology that would be utilised in this thesis to determine if it could potentially replace current secondary or tertiary water treatment technologies. Firstly it has been identified as being capable of completely removing various

pollutants [44]. Secondly, it only requires a light source and an applied potential to power the process which could be powered by renewable energy. The third reason is that it does not produce any solid waste meaning there is no additional energy or cost required after the treatment process. There is also a significant opportunity for it to not only remove pollutants but also to simultaneously produce hydrogen. As a result, wastewater treatment plants would be able to produce fuel while removing pollutants from water. Whilst there are many reasons why PEC would make a great alternative technology for current wastewater treatment processes there are some barriers. One barrier is that PEC relies heavily on light absorption for effective degradation of pollutants therefore it would not be suited for the primary stage treatment or replacing the whole wastewater treatment process. This is because high concentrations of pollutants can reduce light absorption as it blocks light from reaching the semiconductor [49, 50]. A further concern is that it currently has only been researched on a lab-scale which means its performance for large scale treatment has not been assessed. The final barrier is there is very limited research in utilising photoelectrocatalysis as a continuous process. Therefore, whilst photoelectrocatalysis could be a promising candidate for wastewater treatment there are still some barriers which need to be addressed before it can be utilised in a wastewater treatment plant.

1.5.1 Fundamentals of PEC

The most important component in PEC is the working electrode (photoanode). The working electrode involves a semiconductor on a conductive substrate [45, 49, 51]. Usually when a n-type semiconductor is utilised then the working electrode is referred to as a photoanode as water oxidation occurs on the electrode [49]. This is due to the band-bending being upwards thus driving holes to the surface. While when a p-type semiconductor is employed then it is known as a photocathode as water reduction reactions occurs at the electrode [49]. This is due to the band-bending being downwards thus driving electrons to the surface. It is important that the semiconductor chosen is correct for the selected application, as the type of semiconductor used determines the type of photogenerated majority carriers (electrons or holes) present on the electrode's surface. N-type semiconductors (photoanodes) are the most popular choice of semiconductors for organic pollutant degradation, because they regenerate holes on the surface of the photoanode, which enables the organic material to be oxidised, thus degrading them [49].

PEC usually involves three electrodes (working, reference and counter) which are immersed in a supporting electrolyte and are attached to a potentiostat. The photoanode (working electrode) contains a chosen n-type semiconductor applied onto a conductive substrate (FTO glass, ITO glass, Ti mesh) [45, 49, 51]. This semiconductor has two energy bands known as the higher energy conductive band (CB) and lower energy valence band (VB). The energetic gap between these two bands is known as the bandgap and it is the amount of energy the electron needs in order to jump from VB to CB (electron excitation) [45]. Electron excitation works when the photoanode is simulated by light and photons with energies the same or higher than the bandgap energy is absorbed by the electrons, causing them to move from VB to CB [45, 51]. This causes holes to be left in the VB so that they can oxidise water molecules to form $\bullet\text{OH}$ and H^+ [45, 51]. The $\bullet\text{OH}$ can go on to degrade organic pollutants [45, 49]. Whilst an applied potential drives the electrons in the CB to the counter electrode via an external circuit, so they can react with the H^+ to form hydrogen gas (H_2) [45, 49].

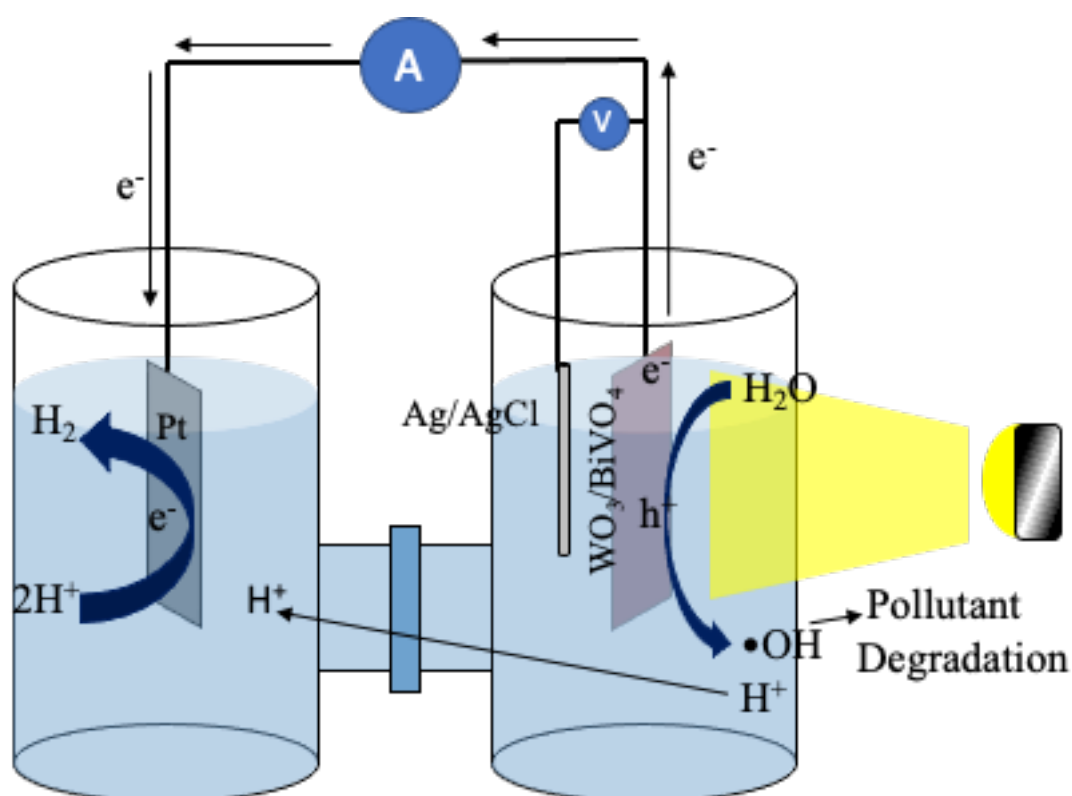
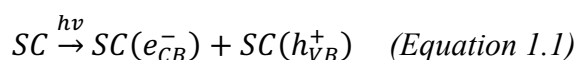
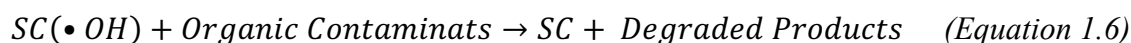
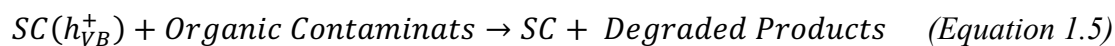
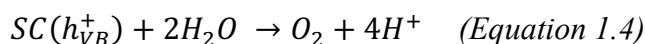
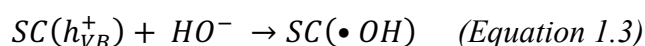
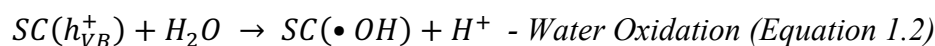


Figure 1.3 – A simple illustration explaining how photoelectrocatalysis works in this study.

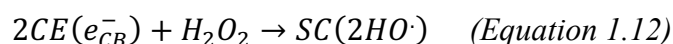
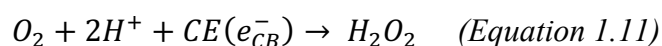
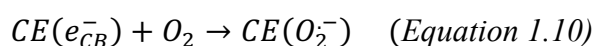
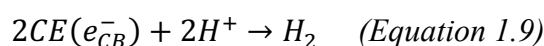
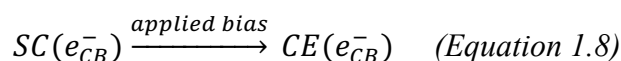
Absorption of Photons:



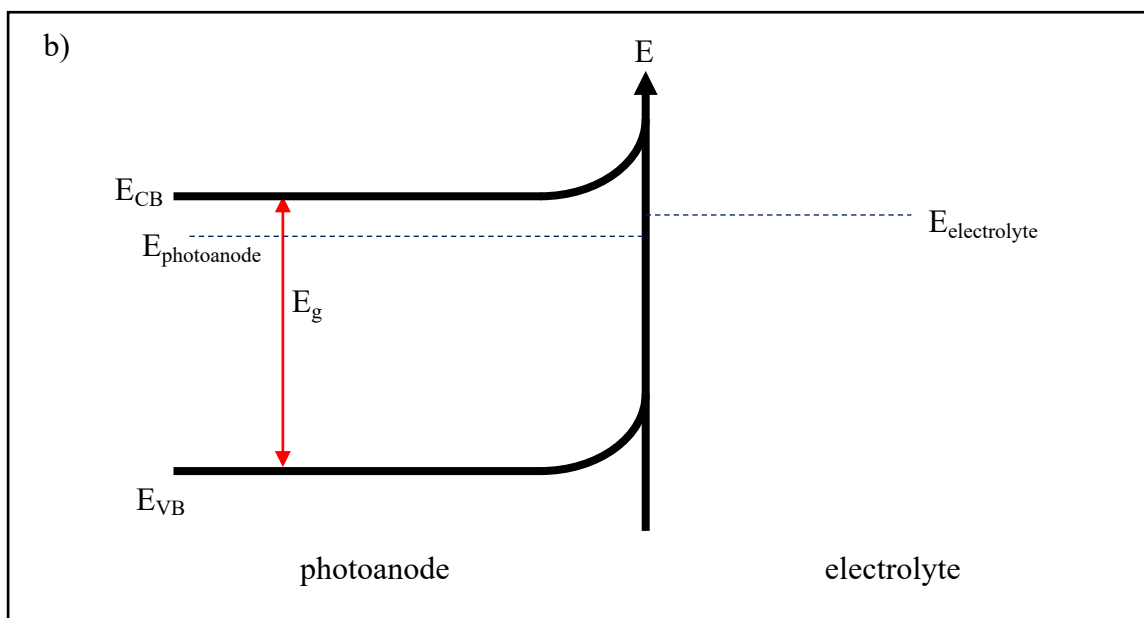
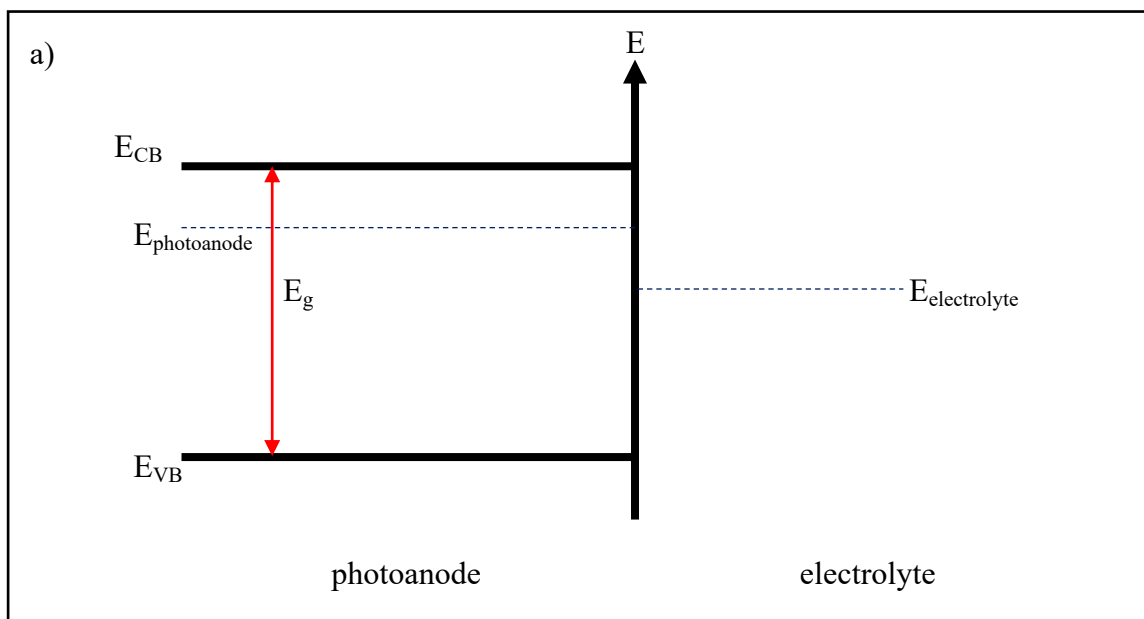
Hydroxyl Radical Production on Photoanode:



Hydrogen and Superoxide Production on Counter Electrode:



The major difference between PEC and PC is that PEC utilises an applied potential to help prevent charge recombination. To fully understand how the applied potential transfers these electrons then researchers have studied the semiconductor/electrolyte interface. A Schottky junction is formed when a semiconductor is in contact with a redox electrolyte due to the difference in electrochemical potentials [49]. To help reach an equilibrium at the interface, the Fermi levels in the semiconductor shift causing a band-bending effect [49]. The region in which band-bending occurs is known as the space charge layer (SCL) or depletion layer as the electrons are transferred from that region [49]. The band-bending helps the separation of the charges and can be controlled by the applied potential [31, 45]. For n-type semiconductors the applied potential needs to be higher than the flat band potential (zero potential) of the semiconductor to help increase the band-bending upwards [49]. This results in a greater gradient thus driving more electrons to the counter electrodes [49]. This extends the holes' lifetimes resulting in higher pollutant degradation. However, if the applied potential is equal to the flat band energy then all charge carriers recombine [49]. This emphasises the importance of applying an applied potential.



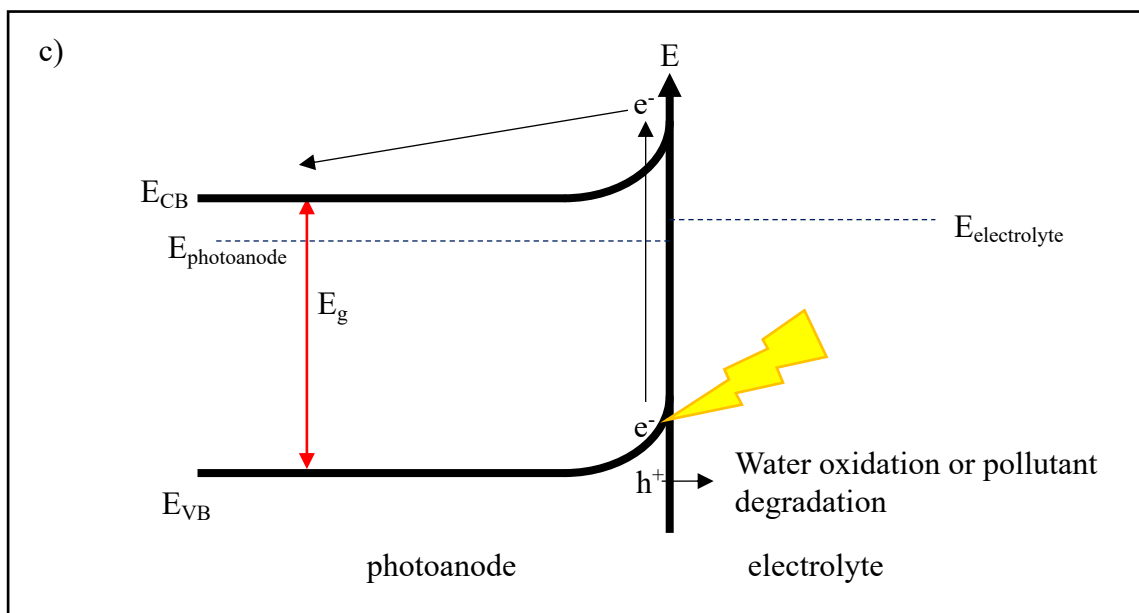


Figure 1.4 - The schematic illustration of energetic structure at electrode/electrolyte interfaces in photoelectrochemical water splitting process with a n-type semiconductor (a) equilibrium condition ($V=V_{fb}$), (b) after immersing the electrode in electrolyte ($V>V_{fb}$) and (c) under light condition ($h\nu = E_g$).

1.5.2 PEC System

There are several ways a PEC system can be set-up in order to remove pollutants, with the most common set-up being a three-electrode configuration in a two-cell compartment electrochemical cell. The three-electrode set up for this thesis involves a photoanode (n-type semiconductor applied to a glass substrate), cathode (Pt mesh) and a reference electrode (Ag/AgCl). All these electrodes are attached to an electrochemical potentiostat which helps apply a bias to the system. This facilitates band-bending, thus allowing for effective charge carrier separation and minimising charge recombination. While the photoanode allows oxidation half reactions and is balanced by the reduction of half reactions that occur on the cathode [52].

1.5.2.1 Photoanode

A photoanode is a key component in PEC to drive the catalytic reactions and requires a n-type semiconductor applied on a conductive substrate (FTO or ITO glass Ti mesh) [45, 51]. The light driven semiconductor in the photoanode controls the number of excited electrons as electrons can only be excited when they absorb a photon with an energy that is the same or higher than the bandgap energy of the semiconductor [45]. The bandgap energy is defined as the gap between the valence band and conduction band and it is the minimum amount of energy needed for the electron to be released from its bond state [45]. Therefore, a semiconductor with

low bandgap energy is recommended. However, as the water splitting process has a thermodynamic potential of 1.23 eV and there would be some energy loss then the bandgap should be above 1.8 eV [53, 54]. There are several semiconductors which are above 1.8 eV shown in Figure 1.5.

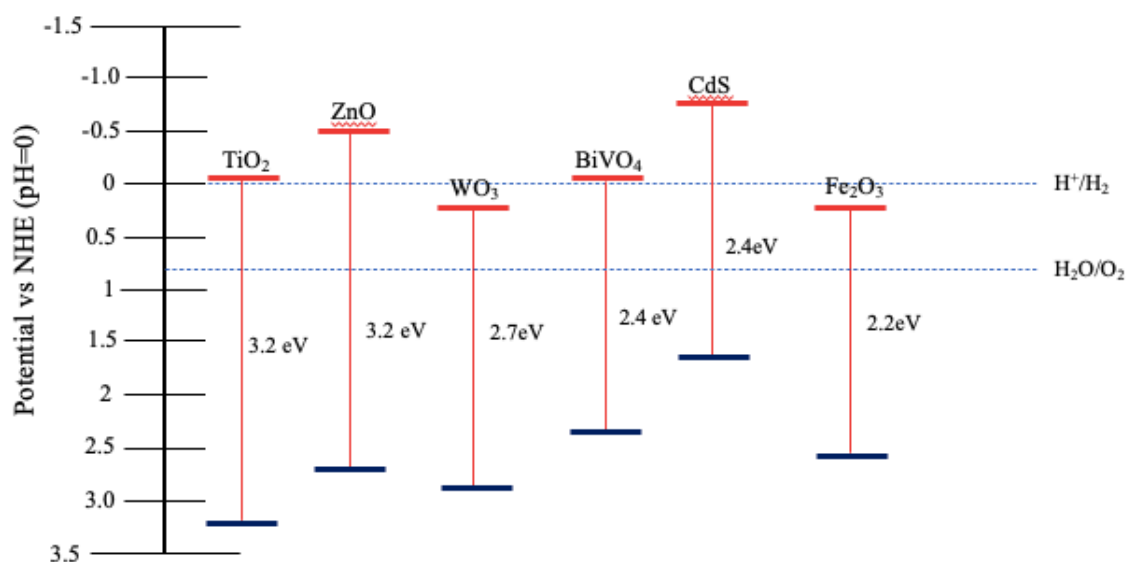


Figure 1.5 - A plot displaying the band positions of various n-type semiconductors in regard to their redox potentials and was adapted from a figure created by Jiang et al [55].

Due to, its success in 1972, wide bandgap energy, good stability, non-toxicity, low cost and ease of manufacture, TiO₂ is a popular choice for PEC [46, 49, 51, 56]. However, there are several drawbacks, such as the photon absorption being limited to the UV light range only (3-5% of solar the spectrum) and it allows rapid charge recombination [56]. This means it has a lower photoactivity when compared to other available semiconductors. Therefore, TiO₂ was not utilised for PEC application in this study as it was vital to select a semiconductor that could utilise a wider range of the solar spectrum.

In this study WO₃ was chosen as one of the semiconductors for the photoanode due to its excellent solar light absorption (12% of solar spectrum) [52, 57]. This is due to its bandgap energy being between 2.5 and 2.8eV, thus allowing wavelengths of up to 500nm to be absorbed [44, 52, 58, 59]. The other significant advantages of utilising WO₃ are: its high stability in low pH, resistance to photocorrosion, good electron mobility (12 cm²V⁻¹s⁻¹) non-toxic, ease of manufacturing, good hole diffusion length, high conductivity [52, 60-62]. However pristine WO₃ can still suffer from weak visible light absorption (< 460 nm) and charge recombination,

thus lowering its PEC performance [63]. One way of overcoming this drawback is to create a heterostructure (by creating a heterojunction) photoanode.

A heterostructure photoanode is recognised as improving the photoactivity of pristine photoanodes [61, 64-68]. This is due to the formation of a heterojunction that drives charge separation [61, 64-68]. A heterojunction is formed when two semiconductors are coupled together [44]. This creates an electric field which depending on the alignment of the two different semiconductors causes the migration of charges [44]. There are several types of alignments namely [44]:

Straddling (Type I) – Semiconductor A has a more negative conduction band and a more positive valence band than semiconductor B.

Staggered (Type II) - Semiconductor A has a more negative conduction and valence band than semiconductor B.

Broken (Type III) – Semiconductor A has a valence band higher than the conduction band of semiconductor B.

Studies have demonstrated that the best alignment for creating an effective heterostructure photoanode is the staggered type as it extends the lifetime of the photogenerated charge carriers. [44]. This is due to the electrons moving from the CB in semiconductor B to the CB in semiconductor A [44]. Whilst the holes move from the VB in semiconductor A to the VB in semiconductor B, thus resulting in the charges being separated [44]. Therefore, doping WO_3 photoanodes with a semiconductor that has CB and VB energies more negative than WO_3 will result in this staggered alignment [44, 65].

One effective semiconductor which has proven to create this staggered alignment with WO_3 is BiVO_4 as the CB and VB in BiVO_4 have energies more negative than the CB and VB of WO_3 [65, 67]. It also has the benefit of a bandgap of 2.5eV which means it is able to absorb a higher proportion of visible light than WO_3 [69]. Therefore, BiVO_4 was the chosen semiconductor to couple with the WO_3 to create a heterostructure photoanode. The benefits of utilising BiVO_4 as a hetero partner to the WO_3 are (a) smaller bandgap which means it utilises more of the solar spectrum, (b) it has good stability against photocorrosion (c) its non-toxic and (d) can achieve good solar-to-hydrogen (STH) efficiency of 9.1% [70]. However, it does have the drawback of poor electron mobility but nevertheless coupling BiVO_4 with WO_3 allows the electrons to

effectively move from the surface to the conductive substrate due to good electron mobility within WO_3 [69].

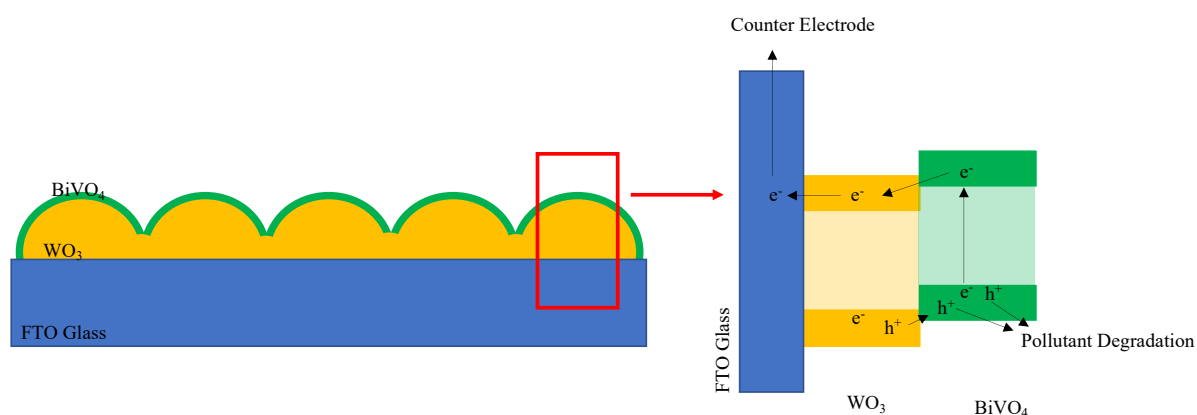


Figure 1.6 - Schematic illustration of $\text{WO}_3/\text{BiVO}_4$ electronic structure.

It is critical to review previous studies of $\text{WO}_3/\text{BiVO}_4$ to help establish its success in PEC and help determine its best structure. There are numerous different structures of WO_3 which can be developed by various methods. Recent studies showed that a 1D nanostructure $\text{WO}_3/\text{BiVO}_4$ exhibits better photocurrent production than pristine WO_3 [63, 71]. The $\text{WO}_3/\text{BiVO}_4$ developed by Xu et al produced a photocurrent 20 times higher than pristine WO_3 due to the BiVO_4 layer enabling charge separation [63]. This was also confirmed by Madhavi et al who created a 1D- $\text{WO}_3/\text{BiVO}_4$ photoanode that generated a photocurrent density (2.24 mA/cm^2) significantly higher than WO_3 and BiVO_4 [71]. During this study it was also established that creating the heterojunction helped improve the stability of the photocurrent production due to the improved charge carrier density, charge separation and decline of recombination losses [71]. The reason why 1D nanostructures are successful is they offer direct electrical pathways for charge transfer and have high interfacial contact area compared with bulk [57]. However, there are other structures that can achieve high photocurrents such as porous nanocrystalline morphology. This was demonstrated by Fujimoto et al who achieved a photocurrent density of 3.43 mA/cm^2 when creating a porous nanocrystalline structure of WO_3 with a layer of BiVO_4 [72]. While Chae et al demonstrated that a smaller sized nanosphere WO_3 layer showed better PEC performance than plate-like or rod-like structure [73]. This structure achieves high photocurrent production due to the improved charge collection efficiency from the shorter transfer lengths improving the holes' transfer to the photoanode/electrolyte interface [57]. This results in higher PEC water oxidation reactions [57]. As Zhou et al found utilising a hierarchical $\text{WO}_3/\text{BiVO}_4$ achieved a higher photocurrent than flat film which improved light harvesting due to the multiple light

scattering caused by the small nanoparticles and sufficient voids [74]. These studies established that the photocurrent density produced by the $\text{WO}_3/\text{BiVO}_4$ photoanode is heavily dependent on the structure as it can facilitate higher charge separation or higher light harvesting. From all these studies it was established that having a porous nanocrystalline structure a very high photocurrent density would be achieved with holes being rapidly transferred to the photoanode surface which is essential for pollutant degradation. Therefore, it was key to create this structure for the $\text{WO}_3/\text{BiVO}_4$ photoanode utilised in this study.

Not only does the structure of the $\text{WO}_3/\text{BiVO}_4$ photoanode affect the photocurrent production, with recent research the thickness of each semiconductor can also affect the photocurrent produced. There has been reports on how the WO_3 thickness plays a role in increasing or decreasing the $\text{WO}_3/\text{BiVO}_4$ photoanode's performance. As recently demonstrated by Grigioni et al increasing the WO_3 thickness decreases the photocurrent produced by the $\text{WO}_3/\text{BiVO}_4$ photoanode as it enables charge recombination to occur in the WO_3 layer [75]. However, another study conducted by Pedroni et al witnessed that increasing the WO_3 layer increased the photocurrent production [76]. They determined that having a high WO_3 thickness helped increase the light absorption capabilities thus more electron excitation [76]. Therefore, it is important that this thesis helps add to this research by looking at the effect of the WO_3 thickness on the $\text{WO}_3/\text{BiVO}_4$ photoanode's performance. Whilst the WO_3 thickness has evidenced its influence on the $\text{WO}_3/\text{BiVO}_4$ photoanode's performance there has also been recent studies focusing on the effect of the BiVO_4 layer's thickness on the photocurrent production. Cao et al found that increasing the BiVO_4 thickness from 3 to 7 cycles (of deposition) increased the photocurrent density demonstrating that a higher amount of BiVO_4 allowed for increased light absorption [77]. However, beyond 7 cycles the photocurrent density decreased as an abundant amount of BiVO_4 can cause charge recombination to occur [77]. This effect was also witnessed by Grigioni et al who found that increasing the BiVO_4 layer thickness from 15 – 75 nm helped improve the photoanode's performance [78]. This is because 75nm gives the best balance between wider light absorption and low charge-carrier recombination during hole transfer to the photoanode surface thus leading to high photocurrents [78]. However, having a thicker layer (115nm beyond) drastically decreases performance as the holes travelling from WO_3 are more likely to combine with the electrons trapped in BiVO_4 [78]. They also found that irradiating the sample front side achieved higher incident photon-to-current efficiency (IPCE) translating to a higher photocurrent production [78]. Whilst these studies show multiple layers of BiVO_4 helps improve the performance of $\text{WO}_3/\text{BiVO}_4$, Hong et al demonstrated that one

single layer of BiVO₄ was sufficient for producing high photocurrent density due to an effective charge separation [68]. They also demonstrated that adding more layers resulted in a decrease in performance due to charge recombination occurring in the BiVO₄ layer as it was identified to be a poor charge transport layer [68]. These studies evidence how vital it is to determine the optimum thickness for each semiconductor utilised in the photoanode, to help produce the highest photogenerated holes for pollutant degradation while exciting the biggest number of electrons for hydrogen production.

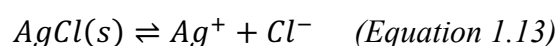
1.5.2.2 Cathode

There is limited choice for a successful cathode to produce hydrogen via the reduction reactions in the cathodic compartment. The best cathode is platinum as it accelerates the hydrogen reduction process [79]. To be able to produce hydrogen and avoid the production of oxygen then the environment in which the Pt cathode is placed must be deoxygenated. This will prevent electrons from reacting with the oxygen and thus allow the production of hydrogen. Therefore, it is important to purge the cathodic compartment before utilising the PEC system for hydrogen production.

1.5.2.3 Reference Electrode

A reference electrode is utilised in a three-electrode set-up, to help gather electrochemical data, as the reference electrode has a known potential which is used as a point of reference for potential control and measurement.

Silver/Silver Chloride (Ag/AgCl) is a common reference electrode as it is simple and robust and therefore it is the reference electrode utilised in this thesis. The Ag/AgCl electrode is made up of a silver wire immersed in a saturated potassium chloride and silver chloride solution all contained in an enclosed glass tube with a porous plug to allow contact between the environment and silver chloride electrolyte. The half reaction occurring in the Ag/AgCl is as follows:



This redox reaction can occur in solutions with pH between 0 and 13.5, thus meaning the electrode can be utilised in varying pH levels.

1.5.2.4 Electrolyte

An electrolyte is a solution which contains ions dissolved in water that enables the system to have conductivity and is essential in PEC [31]. If the conductivity is low, then there is a high

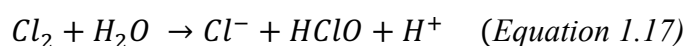
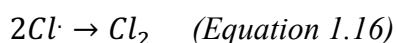
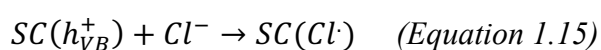
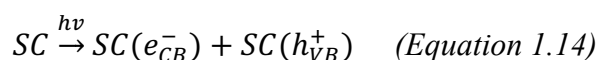
resistance in the solution thus increasing the potential bias requirement [31]. The electrolyte also helps generate band-bending in the semiconductor as a result the holes and electrons come to the surface of the photoanode to facilitate pollutant degradation [49].

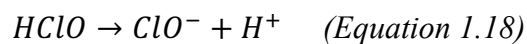
Sodium sulfate (Na_2SO_4) is the most widely utilised electrolyte as it generates excellent photocurrent during the PEC process. It was found that increasing the concentration improves the photocurrent density without affecting the photocurrent potential onset [75]. Concentrations of above 0.05 M Na_2SO_4 allow for higher photocurrent values to be produced with the applied bias having more effect on the photochemical response [75]. However, this is not the only option for the electrolyte there are others such as sodium chloride (NaCl).

Researchers have shown that utilising NaCl as a supporting electrolyte helps improve the degradation of pollutants when compared to Na_2SO_4 [80]. This is due to the NaCl electrolyte shifting the onset potential less positively and producing a higher photocurrent as demonstrated by Shuhu Xiao et al [80]. It was apparent that when utilising the same photocatalysis conditions a 0.05 M NaCl solution produced a photocurrent double the amount of 0.1 M Na_2SO_4 solution [80]. This is due to the preferred absorption of chloride ions onto the surface of an electrode when compared to the sulfate ions [80]. Therefore, a lower potential could be utilised for the oxidation of chloride ions.

There are several reasons why increasing the concentration of NaCl increases the photocurrent production. Firstly, it enables higher conductivity thus improving ion transfer in the solution. Secondly increasing the NaCl concentration results in a higher number of negative chloride ions being absorbed onto the positive photoanode [80]. These chloride ions act as a hole scavenger thus improving the charge separation [80].

The benefit of utilising NaCl as a supporting electrolyte is that it can produce active chlorine species [80, 81]. These active chlorine species have strong disinfection properties thus they can degrade pollutants [80, 81]. The production of active species is as following [80, 81]:





Therefore, NaCl will be the main electrolyte for the PEC system utilised in this thesis.

1.5.2.5 Applied Bias

For PEC to be successful then an applied potential is required to provide a driving force for electrons to move to the cathode (charge separation) [45, 49, 51]. This is achieved by attaching all three electrodes to an electrochemical potentiostat. The user interface on the computer allows the desired potential to be set and applied to the system. The applied bias must be more positive than the flat band potential of the PEC system in order to help transfer the electrons to the cathode from the photoanode [49]. This will be dependent on each PEC system, as the photoanode and the electrolyte type and concentration all affect the flat band potential which needs to be overcome to prevent the recombination of charges.

1.5.2.6 Light Source

For PEC to be successful then it is essential to have a light source which can allow for electron excitation from the absorption of photons (with energies the same or more than the semiconductor's bandgap energy) provided by the light [45, 51]. In this thesis the PEC system utilises an ASAHI HAL-320 solar simulator to provide the semiconductor with light due to the availability of this equipment and the benefit of it being able to provide the PEC system a wide range of wavelengths for photon absorption. However, there is an alternative option to utilising a solar simulator which is utilising LED light sources. LEDs are beneficial as they are compact, lower cost, energy efficient and mercury free [82]. LED light sources can also provide different wavelengths depending on their composition thus allowing the user to select the appropriate light source for the semiconductor being used [82].

1.5.2.7 Two Compartment PEC Cell

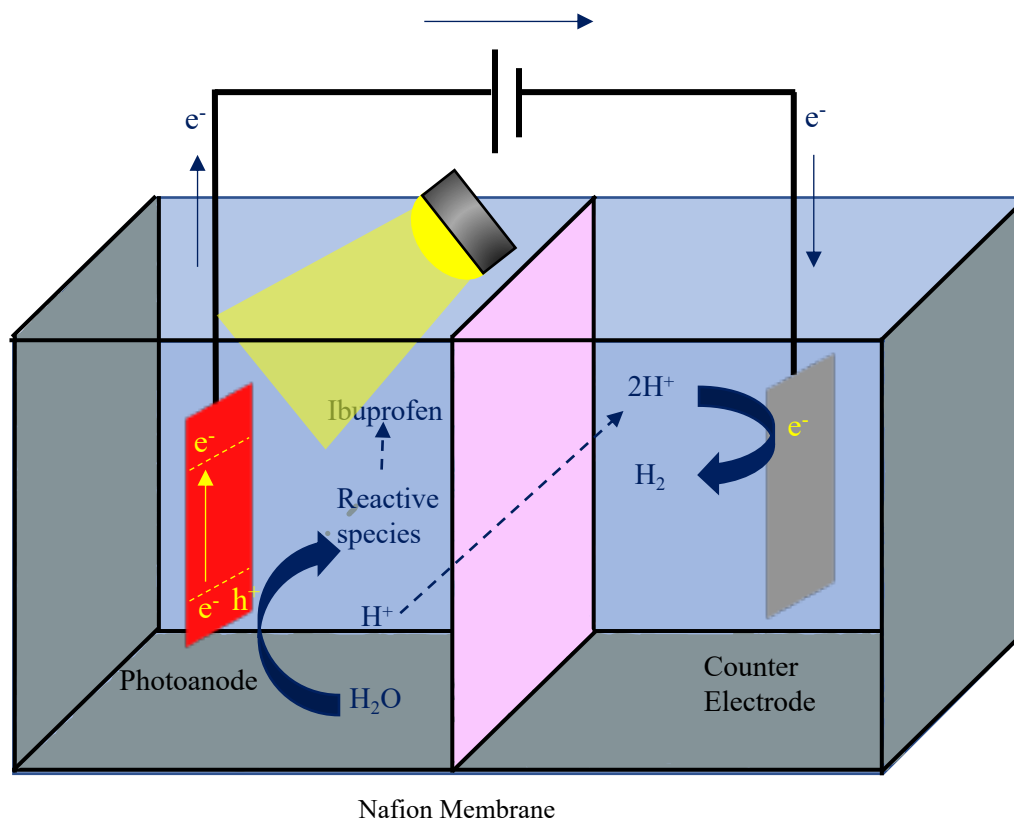


Figure 1.7 - Schematic illustration of the PEC cell utilised for pollutant degradation experiments

The PEC cell utilised in this thesis is a two compartment PEC cell (Figure 1.2) with a Nafion membrane. The anodic side of the compartment consists of the photoanode and reference electrode with a quartz window for the light to pass through so it can be absorbed by the photoanode. While the cathodic side of the compartment consists of just the cathode. The Nafion membrane is utilised to ensure that the anodic oxidation of pollutants remain in one compartment while the cathodic reduction of hydrogen takes place in the other compartment (Figure 1.7). This is due to its selectivity of hydrogen protons, meaning they are the only species allowed to pass through [83]. This prevents any undesirable reactions with the ibuprofen or surfactants, as the success of PEC for degrading pollutants is based on the production of holes (h^+) as it generates hydroxyl radicals ($\bullet OH$) and active chlorine. These reactive oxidising species have been reported to cause the degradation of these pollutants [42, 84, 85]. The Nafion membrane keeps the electrons in the cathodic compartment, so they do not react with any of the reactive oxidising species or pollutant degradation products produced in the anodic compartment but combine with the hydrogen protons to produce hydrogen gas. Therefore, it was important to utilise this membrane in the two compartment PEC cell to allow

for simultaneous pollutant degradation and hydrogen production without pollutant degradation significantly affecting hydrogen production.

In the PEC process there are four steps which are (a) mass transfer to the photoanode, (b) adsorption of pollutants onto the surface of the photoanode, (c) degradation of pollutants, (d) desorption of the by-products from the photoanode surface and then (d) mass transfer of the by-products from the electrode surface [86]. One or more of these steps would be a rate limiting step which means a step which has the slowest kinetics. The mass transfer of the pollutants towards and away from the photoanode are not the rate determining step during this study as experiments are under continuous magnetic stirring. This means there is good circulation of pollutants in the electrolyte meaning that the photoanode is exposed to fresh electrolyte constantly. When there is constant stirring it would imply that the mass transfer cannot be the rate limiting [86]. However, a study by Liu et al found that for photoelectrocatalytic reactions the rate limiting step is the charge transfer or the adsorption of the pollutants onto the photoanode surface [86]. This can make pollutant degradation and hydrogen production slow. Another reason for slow hydrogen production could be utilising a membrane with a low proton conductivity. Therefore, it is important that the membrane utilised has excellent proton transport properties to allow this step and avoid hydrogen production becoming a rate limiting step. This is the reason why the Nafion membrane was chosen as Nafion is known to have excellent proton transport conductivity.

1.5.3 The Advantages of PEC

Through various studies it has been established that PEC is the preferred advanced oxidation process (AOPs) for water treatment as compared to other AOPs because it effectively reduces the toxicity by removing organic pollutants in the shortest amount of time [42, 85, 87]. Many researchers refer to the semiconductors used in PC and PEC as photocatalysts as they accelerate the redox reactions when stimulated with light. This makes it a superior process to electrochemical which only utilises applied potential to degrade pollutants.

Another benefit of PEC is due to the cathode, hydrogen can be generated in a more sustainable way than its current process. Currently most of the hydrogen produced happens through the steam reforming process, which involves methane and steam to produce hydrogen and CO₂ [88]. However due to climate change, this process is not ideal as it produces CO₂ whilst requiring high energy demand [88]. This produces hydrogen contaminated with carbon

monoxide [88]. In comparison producing hydrogen via the photoelectrocatalysis process is a very attractive option as not only is it sustainable, but it also produces clean and uncontaminated hydrogen. This helps make hydrogen an appealing alternative fuel to fossil fuels.

PEC can also provide a renewable and environmentally friendly method to remove pollutants through the utilisation of solar power (as a light source) and bias potential which can be powered by renewable energy. Therefore, it is essential to find a photocatalyst which has a low bandgap energy in order to absorb photons in the visible light. Thus, utilising a higher proportion of solar light which could result in natural sunlight being utilised.

1.5.4 Limitations of PEC

PEC has many advantages over other AOPs and conventional wastewater treatment processes, such as complete mineralisation, having lower energy demand and lower waste production, however there are still some limitations to this process. These limitations involve:

- a) The adsorption of light is dependent on the bandgap of the semiconductor, eg TiO_2 can only absorb UV light (5% solar spectrum).
- b) An applied bias above the flat band potential is needed, otherwise charge recombination can still occur in pristine photocatalysts, therefore requiring minimum energy input.
- c) High pollutants can hinder the PEC process due to less light penetrating the photocatalyst. While the volume of pollutants able to be degraded is limited to the number of active sites on the photocatalyst.

1.5.5 Justification of Utilising PEC for Ibuprofen and Surfactant Degradation

1.5.5.a Ibuprofen

Marchlewicz et al identified ibuprofen as the third most consumed drug due to doctor's high prescription rate and it's easy availability over the counter [89]. This increasing demand causes the concentration of ibuprofen in our wastewater to increase daily. Therefore, ibuprofen was chosen as a model pharmaceutical pollutant to investigate in this thesis.

There are several issues with the presence of ibuprofen in our environmental waters, these are: its endocrine disruption in *Mytilus galloprovincialis* [90], oxidative stress, membrane damage within the digestive gland and an increase of the lipid peroxidation level in mussels [91]. Han

et al found that ibuprofen can cause an increase in 17- β estradiol production and aromatase activity while decreasing testosterone production in *Oryzias latipes*, *Moina macrocopa* and *Daphnia magna* [92]. Also Lange et al found that concentrations between 1-100 ng/L caused a decrease in the activity of amphipod crustacean in *Gammarus pulex* [93]. This emphasises the necessity of fully eliminating ibuprofen from water streams before its released into the environment.

A review conducted by Sunil Chopra et al and Sarah Letsinger et al helped summarise the various ibuprofen concentrations found in environmental waters around the world, please see Table 1.5 below [90, 94].

Table 1.5 - A table presenting the ibuprofen concentration in different environmental water sources around the world [90, 94].

Environmental Water Type	Location	Ibuprofen Concentration ($\mu\text{g/L}$)
River	Mississippi, USA	0.03
Lake	North Ohio, USA	1.2
River	KwaZulu-Natal, South Africa	19.2
River	South China	1.417
Surface Water	Canada	0.98
Surface Water	Greece	1-67
Surface Water	Korea	<15-414
Surface Water	Taiwan	5-280
Surface Water	France	8
Wastewater	Canada	45
Wastewater	Pakistan	703-1673
Wastewater	South Africa	1.38
Wastewater	Belgium	5.78
Estuary	UK	0.67

Table 1.5 shows ibuprofen present in the environment and wastewater effluents at $\mu\text{g/L}$ scale. Thus, highlighting that current wastewater technologies have failed to completely remove ibuprofen from their wastewater effluents. This evidence shows that water technologies are currently not up to the standard we require today.

There are also currently several reports on utilising PEC for ibuprofen degradation [42, 84, 85]. Whilst the reports show 80-100% degradation percentages they do not explain how alternating the operating parameters could vary the ibuprofen degradation whilst only one report identified the by-products produced during the ibuprofen degradation. Therefore, it is necessary for this

research to help determine what by-products are formed in order to establish if this technology is environmentally friendly and has the potential for replacing tertiary wastewater treatment technologies.

1.5.5.b Surfactants

This thesis will focus on two different types of surfactants which are the anionic and cationic surfactants. The reason why it will focus on removing anionic surfactants is that it is one of the most commonly utilised surfactants which affect microorganisms [18]. Popular types of anionic surfactants are linear alkylbenzene sulfonates (LAS). It has been evidenced that LAS are biodegradable in wastewater treatment plants with aerobic conditions [18, 95]. However, these compounds still occur in surface waters as current wastewater treatment technologies cannot eliminate LAS from water. The other drawback of biodegrading LAS is that it can alter the microorganisms thus hindering their performance for other pollutants [18]. The problem with LAS entering surface water is that it is toxic to a range of aquatic organisms such as invertebrates which has shown that at even very low concentrations (0.02 – 1.0 mg/L) they can cause damage to fish gills, excels mucus secretion, respiration problems in goby, decrease in settling rate and the swimming patterns changing in blue mussel larvae amongst other issues [18, 96]. Hence, it's important that anionic surfactants are completely removed from wastewater to ensure fish and other organisms are not negatively impacted. There are several alternative methods reported on the degradation of LAS compounds. However, none of these methods (except for utilising special bacteria) were able to degrade LAS fully. Therefore, more research is required to achieve complete degradation [97]. Due to inadequate charge separation at the semiconductor photocatalyst/electrolyte interface then the degradation of LAS lowers. However, in the case of PEC, the applied potential to the circuit encourages charge separation at the semiconductor/electrolyte interface which should enhance LAS degradation compared to photocatalysis. For testifying the feasibility of PEC for anionic surfactant degradation then sodium 2-naphthalenesulfonate (S2NS) was selected in this thesis due to its availability.

The other type of surfactant which this thesis will focus on are cationic. This is due to cationic (such as quaternary ammonium compounds (QACs)) being one of the most toxic surfactants [18]. Cationic surfactants such as QACs have antibacterial properties which means they are utilised in disinfectants, detergents, etc, resulting in high concentrations (500 µg/L) entering wastewater [18, 98]. Due to their antibacterial properties they are highly toxic to aquatic life

and cause organisms to build up a resistance to disinfectants [99, 100]. Wastewater treatment plants do not completely eliminate these types of compounds from water, resulting in treated effluents and surface waters having an average QACs concentration of 50 µg/L and 40 µg/L, respectively [98]. This is highly concerning as excessive exposure of QACs to bacteria could give a rise in bacterial resistance to these compounds [18]. Hence, indicating the importance for these compounds to be completely eradicated from water.

Benzylalkyl dimethyl ammonium compounds (BACs) are the most frequently detected QACs in wastewater effluents with the most common BACs being C12, C14 and C16 [98, 101]. It has been established that BACs is stable in direct photodegradation [98]. However, there is limited research on the degradation of BAC, with there being only one study. This suggests more research is required to find a technology that could completely degrade BACs. Hence, BAC-C12 was the model pollutant for cationic surfactants in this thesis.

PEC has been proven to degrade many pollutants due to the production of strong reactive species such as hydroxyl radicals, holes and active chlorine. It does not rely on microorganisms to degrade surfactants, therefore, there should be no issues with surfactants affecting the removal efficiency due to inhabitation of the activated sludge. However, currently there is no evidence of using this effective technology to degrade surfactants. Therefore, it would be beneficial to see if PEC technology can completely degrade surfactants, as currently there is no technology that can.

1.6. Producing Hydrogen Fuel Using Photoelectrocatalysis

While the world's population is ever-growing so is the need for clean fuels. The use of fossil fuels causes the production of CO₂ which forms a heat insulating layer in our atmosphere, thus causing a greenhouse effect and slowly warming the earth [102]. Many researchers are in a race to identify a more renewable source of energy to prevent escalating the problem and simultaneously hopefully reverse some of the damage already caused.

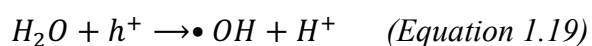
Hydrogen is attracting considerable attention as an alternative fuel to fossil fuels. This is mainly due to its high yield of energy (122 kJ/mol), which produces energy when utilised in a fuel cell [103]. However, the major issue with hydrogen as a fuel relates to the current manufacturing process, "steam reforming" as it emits high amounts of CO₂ (due to energy demand), which impacts on the environment [88]. Steam reforming utilises high temperature steam in order to

break methane into hydrogen, carbon monoxide and carbon dioxide [88]. It is therefore vital for research to focus on a more sustainable and environmentally friendly method of hydrogen production to ensure it is a viable option for the future.

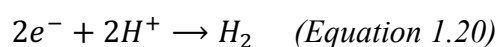
PEC is an advanced oxidation process (AOP) that has recently received considerable attention for green hydrogen gas generation [83, 104-106]. This is achieved by water splitting reactions when a photoanode is simulated with light and an applied potential is used to help charge separation by transferring photogenerated electrons to the counter electrode [105]. These electrons react with the hydrogen ions produced from the water splitting process to produce hydrogen (please see Figure 1.2) [105].

The benefit of PEC over photocatalysis relates to the use of an applied potential that drives the electrons away from the photoanode surface and towards the counter electrode, thus allowing charge separation [31, 107]. This charge separation enables effective hydrogen production as the holes' lifetimes are extended [31]. This enhances the amount of water oxidation reactions thus improving the production of hydroxyl and hydrogen ions. In addition the excited electrons lifetime are enhanced, thus allowing more electrons to react with the protons to form hydrogen gas at the cathode [31]. The overall PEC water splitting process by photoelectrons and holes can be explained as the following [108]:

Anodic Water Oxidation Reaction:



Cathodic Water Reduction Reaction:



The significant advantage of PEC is that it can be driven by solar light and an external electrical power supply (which can be driven by renewable energy sources). This makes PEC a sustainable route compared to the conventional steam reforming process. A fresh water based electrolyte would be favourable as any possible waste by-products from contaminant degradation would be eliminated. However, on a larger scale, utilising freshwater for the electrolyte would be more expensive and would have more of an impact on the environment than recycling the water. A recent study on life-cycle net energy assessment for PEC hydrogen generation showed that 820 000 m³ of electrolyte would be required for 1GW facility (which

equals to 610 metric tons of H₂ per day) [109]. In view of this, applying wastewater as an electrolyte would be a promising approach to avoid freshwater scarcity whilst producing hydrogen. Pharmaceutical and surfactant pollutants in saltwater could be utilised as electrolytes for PEC hydrogen production. Previous reports have shown that PEC can degrade pollutants while simultaneously producing hydrogen gas [110-112]. Therefore, it is anticipated that hydrogen gas can be produced from ibuprofen and surfactant degradation processes.

During the PEC process hydrogen can be produced by the electrons on the platinum counter electrode being able to react with protons to produce hydrogen gas [70, 113, 114]. However, the amount produced relies heavily on the material utilised. This was demonstrated by Monfort et al, who utilising a BiVO₄ photoanode produced a higher amount of hydrogen than TiO₂ photoanodes [70]. While utilising BiVO₄ allows significant hydrogen production it does suffer from charge recombination. This is due to the electrons and holes being separated on the same surface, therefore, to help prevent this Li et al doped the BiVO₄ photoanodes with Bi [70, 113]. This resulted in the hydrogen production being enhanced by 3 μmol/cm² overall and demonstrates how effective doping is for charge separation and improved performance [113]. In addition Shen et al found utilising TiO₂, TiO₂CdSe, NTAs-Au-CdSe and NTAs-CdSe-Au as photoanodes in PEC resulted in hydrogen production of 0.184, 0.695, 0.43 and 1.742 mmol/hg respectively [114]. This evidences that hydrogen production is dependent on the photoanode material.

While the amount of hydrogen produced is dependent on the photocatalytic material, it still requires an applied potential to help drive the electrons from the photoanode surface to the counter electrode, thus reacting with the protons to produce hydrogen [45, 49]. This has been demonstrated by Monfort et al and Shen et al, who identified that increasing the bias potential increased the hydrogen production whilst the absence of bias potential failed to produce hydrogen [70, 114]. This is due to the applied potential helping to drive charge separation thus increasing the number of electrons available for hydrogen production [70, 114]. Therefore, PEC has the advantage over PC in that due to the applied potential it would be able to produce a higher amount of hydrogen and should be investigated more.

1.7. Aims of Thesis

This thesis will focus on demonstrating the PEC process in pollutants removal from water, examine its feasibility to replace current wastewater treatment technologies and determine its potential for hydrogen production. The following objectives will be examined in this thesis.

- Design and fabricate an effective heterostructure metal oxide photoanode
- Establish if the PEC can completely remove a model pharmaceutical compound from water without impacting the environment.
- Determine if PEC can completely remove a model surfactant pollutant compound (anionic and cationic) from water.
- Quantification of hydrogen gas produced via the developed PEC system and also verify if it can simultaneously produce hydrogen gas while degrading pollutants.

1.8 Bibliography

1. Organization, W.H. *Drinking-water*. Fact Sheets 2019.
2. Llopis, A. *Advanced technologies applied to wastewater treatment plant effluents*. 2015.
3. Meneses, M., J.C. Pasqualino, and F. Castells, *Environmental assessment of urban wastewater reuse: Treatment alternatives and applications*. Chemosphere, 2010. **81**(2): p. 266-272.
4. Briffa, J., E. Sinagra, and R. Blundell, *Heavy metal pollution in the environment and their toxicological effects on humans*. Heliyon, 2020. **6**(9): p. e04691.
5. Reddy, D.H.K. and S.-L. Lee, *Water Pollution and Treatment Technologies*. Journal of Environmental and Analytical Toxicology, 2012. **2**: p. 1-2.
6. Luo, Y., et al., *A review on the occurrence of micropollutants in the aquatic environment and their fate and removal during wastewater treatment*. Science of The Total Environment, 2014. **473-474**: p. 619-641.
7. Zhang, F., et al., *Increasing use of prescription drugs in the United Kingdom*. Pharmacoepidemiology and drug safety, 2016. **25**(6): p. 628-636.
8. OECD, *Pharmaceutical Residues in Freshwater*. 2019.
9. Liu, J.-L. and M.-H. Wong, *Pharmaceuticals and personal care products (PPCPs): A review on environmental contamination in China*. Environment International, 2013. **59**: p. 208-224.
10. Fursdon, J.B., et al., *The pharmaceutical pollutant fluoxetine alters reproductive behaviour in a fish independent of predation risk*. Science of The Total Environment, 2019. **650**: p. 642-652.
11. Sanderson, H., et al., *Ranking and prioritization of environmental risks of pharmaceuticals in surface waters*. Regulatory Toxicology and Pharmacology, 2004. **39**(2): p. 158-183.
12. Quinn, B., F. Gagné, and C. Blaise, *An investigation into the acute and chronic toxicity of eleven pharmaceuticals (and their solvents) found in wastewater effluent on the cnidarian, Hydra attenuata*. Science of The Total Environment, 2008. **389**(2): p. 306-314.
13. Gaworecki, K.M. and S.J. Klaine, *Behavioral and biochemical responses of hybrid striped bass during and after fluoxetine exposure*. Aquatic Toxicology, 2008. **88**(4): p. 207-213.
14. Nentwig, G., *Effects of Pharmaceuticals on Aquatic Invertebrates. Part II: The Antidepressant Drug Fluoxetine*. Archives of Environmental Contamination and Toxicology, 2007. **52**(2): p. 163-170.
15. Patneedi, C.B. and K. Prasadu, *Impact of pharmaceutical wastes on human life and environment*. 2015. **8**: p. 67-70.
16. Nakama, Y., *Chapter 15 - Surfactants*, in *Cosmetic Science and Technology*, K. Sakamoto, et al., Editors. 2017, Elsevier: Amsterdam. p. 231-244.
17. Ivanković, T. and J. Hrenović, *Surfactants in the environment*. Arh Hig Rada Toksikol, 2010. **61**(1): p. 95-110.
18. Ivanković, T. and J. Hrenović, *Surfactants in the Environment*. Archives of Industrial Hygiene and Toxicology, 2010. **61**(1): p. 95-110.
19. Crini, G. and E. Lichtfouse, *Advantages and disadvantages of techniques used for wastewater treatment*. Environmental Chemistry Letters, 2019. **17**(1): p. 145-155.
20. Zoomi, I., et al., *Biological Wastewater Treatment Technology: Advancement and Drawback*, in *Removal of Emerging Contaminants Through Microbial Processes*, M.P. Shah, Editor. 2021, Springer Singapore: Singapore. p. 207-216.

21. Campos, J.L., et al., *Greenhouse Gases Emissions from Wastewater Treatment Plants: Minimization, Treatment, and Prevention*. Journal of Chemistry, 2016. **2016**: p. 3796352.
22. Rashed, M.N., *Adsorption Technique for the Removal of Organic Pollutants from Water and Wastewater*. Organic Pollutants - Monitoring, Risk and Treatment, ed. M. Nageeb Rashed. 2012, <https://www.intechopen.com/chapters/42059>: IntechOpen.
23. Water, P.I. *Basics of Deionized Water by Ion Exchange*. 2012.
24. Wenten, I.G., *Ultrafiltration in Water Treatment and Its Evaluation as Pretreatment for Reverse Osmosis System*. 2008.
25. Premathilaka, R.W. and N.D. Liyanagedera, *Fluoride in Drinking Water and Nanotechnological Approaches for Eliminating Excess Fluoride*. Journal of Nanotechnology, 2019. **2019**: p. 2192383.
26. Chelliapan, S., T. Wilby, and P.J. Sallis, *Performance of an up-flow anaerobic stage reactor (UASR) in the treatment of pharmaceutical wastewater containing macrolide antibiotics*. Water Research, 2006. **40**(3): p. 507-516.
27. Ismail, Z.Z., U. Tezel, and S.G. Pavlostathis, *Sorption of quaternary ammonium compounds to municipal sludge*. Water Research, 2010. **44**(7): p. 2303-2313.
28. Mestre, A.S., et al., *Activated carbons for the adsorption of ibuprofen*. Carbon, 2007. **45**(10): p. 1979-1988.
29. Kimura, K., et al., *Rejection of neutral endocrine disrupting compounds (EDCs) and pharmaceutical active compounds (PhACs) by RO membranes*. Journal of Membrane Science, 2004. **245**(1): p. 71-78.
30. Landry, K.A. and T.H. Boyer, *Diclofenac removal in urine using strong-base anion exchange polymer resins*. Water Research, 2013. **47**(17): p. 6432-6444.
31. Daghrir, R., P. Drogui, and D. Robert, *Photoelectrocatalytic technologies for environmental applications*. Journal of Photochemistry and Photobiology A: Chemistry, 2012. **238**: p. 41-52.
32. Magara, Y., M. Itoh, and T. Morioka, *Application of ozone to water treatment and power consumption of ozone generating systems*. Progress in Nuclear Energy, 1995. **29**: p. 175-182.
33. Ma, D., et al., *Critical review of advanced oxidation processes in organic wastewater treatment*. Chemosphere, 2021. **275**: p. 130104.
34. Guo, Y., P.S. Qi, and Y.Z. Liu, *A Review on Advanced Treatment of Pharmaceutical Wastewater*. IOP Conference Series: Earth and Environmental Science, 2017. **63**: p. 012025.
35. Saravanan, A., et al., *Photocatalysis for removal of environmental pollutants and fuel production: a review*. Environmental Chemistry Letters, 2021. **19**(1): p. 441-463.
36. Hansen, K.M.S., et al., *Ozonation for source treatment of pharmaceuticals in hospital wastewater – Ozone lifetime and required ozone dose*. Chemical Engineering Journal, 2016. **290**: p. 507-514.
37. Khan, A.H., et al., *Toxicity reduction and improved biodegradability of benzalkonium chlorides by ozone/hydrogen peroxide advanced oxidation process*. Separation and Purification Technology, 2017. **185**: p. 72-82.
38. Alalm, M.G., A. Tawfik, and S. Ookawara, *Degradation of four pharmaceuticals by solar photo-Fenton process: Kinetics and costs estimation*. Journal of Environmental Chemical Engineering, 2015. **3**(1): p. 46-51.
39. Zhang, Q., Y.-F. Xia, and J.-M. Hong, *Mechanism and toxicity research of benzalkonium chloride oxidation in aqueous solution by H₂O₂/Fe²⁺ process*. Environmental Science and Pollution Research, 2016. **23**(17): p. 17822-17830.

40. Sabouni, R. and H. Gomaa, *Photocatalytic degradation of pharmaceutical micro-pollutants using ZnO*. Environmental Science and Pollution Research, 2019. **26**(6): p. 5372-5380.
41. López Loveira, E., et al., *TiO₂-photocatalytic treatment coupled with biological systems for the elimination of benzalkonium chloride in water*. Separation and Purification Technology, 2012. **91**: p. 108-116.
42. Chang, K.-L., et al., *Cu₂O loaded titanate nanotube arrays for simultaneously photoelectrochemical ibuprofen oxidation and hydrogen generation*. Chemosphere, 2016. **150**: p. 605-614.
43. Babu, B., et al., *Removal of pharmaceuticals from wastewater by electrochemical oxidation using cylindrical flow reactor and optimization of treatment conditions*. Journal of environmental science and health. Part A, Toxic/hazardous substances & environmental engineering, 2009. **44**: p. 985-94.
44. Peleyeju, M.G. and O.A. Arotiba, *Recent trend in visible-light photoelectrocatalytic systems for degradation of organic contaminants in water/wastewater*. Environmental Science: Water Research & Technology, 2018. **4**(10): p. 1389-1411.
45. Bessegato, G.G., et al., *Achievements and Trends in Photoelectrocatalysis: from Environmental to Energy Applications*. Electroanalysis, 2015. **6**(5): p. 415-441.
46. Fujishima, A. and K. Honda, *Electrochemical Photolysis of Water at a Semiconductor Electrode*. Nature, 1972. **238**(5358): p. 37-38.
47. Tazuke, S. and N. Kitamura, *Photofixation of carbon dioxide to formic acid in vitro using water as hydrogen source*. Nature, 1978. **275**(5678): p. 301-302.
48. Kawai, T. and T. Sakata, *Hydrogen evolution from water using solid carbon and light energy*. Nature, 1979. **282**(5736): p. 283-284.
49. Guilherme Garcia Bessegato, T.T.G.a.M.V.B.Z., *Enhancement of Photoelectrocatalysis Efficiency by Using Nanostructured Electrodes*, in *Modern Electrochemical Methods in Nano, Surface and Corrosion Science*, M. Aliofkhaezai, Editor. 2014, IntechOpen: <https://www.intechopen.com/chapters/46877>.
50. Zhou, X., et al., *Degradation Kinetics of Photoelectrocatalysis on Landfill Leachate Using Codoped TiO₂/Ti Photoelectrodes*. Journal of Nanomaterials, 2015. **2015**: p. 810579.
51. Garcia-Segura, S. and E. Brillas, *Applied photoelectrocatalysis on the degradation of organic pollutants in wastewaters*. Journal of Photochemistry and Photobiology C: Photochemistry Reviews, 2017. **31**: p. 1-35.
52. Lianos, P., *Review of recent trends in photoelectrocatalytic conversion of solar energy to electricity and hydrogen*. Applied Catalysis B: Environmental, 2017. **210**: p. 235-254.
53. Le Bahers, T. and K. Takanabe, *Combined theoretical and experimental characterizations of semiconductors for photoelectrocatalytic applications*. Journal of Photochemistry and Photobiology C: Photochemistry Reviews, 2019. **40**: p. 212-233.
54. Pinaud, B.A., et al., *Technical and economic feasibility of centralized facilities for solar hydrogen production via photocatalysis and photoelectrochemistry*. Energy & Environmental Science, 2013. **6**(7): p. 1983-2002.
55. Jiang, C., et al., *Photoelectrochemical devices for solar water splitting – materials and challenges*. Chemical Society Reviews, 2017. **46**(15): p. 4645-4660.
56. Ge, M.-Z., et al., *Synthesis, modification, and photo/photoelectrocatalytic degradation applications of TiO₂ nanotube arrays: a review*. Nanotechnology Reviews, 2016. **5**(1): p. 75-112.

57. Kalanur, S.S., L.T. Duy, and H. Seo, *Recent Progress in Photoelectrochemical Water Splitting Activity of WO₃ Photoanodes*. Topics in Catalysis, 2018. **61**(9): p. 1043-1076.
58. Zhang, H., G. Chen, and D.W. Bahnemann, *Photoelectrocatalytic materials for environmental applications*. Journal of Materials Chemistry, 2009. **19**(29): p. 5089-5121.
59. Hunge, Y.M., et al., *Photoelectrocatalytic degradation of oxalic acid using WO₃ and stratified WO₃/TiO₂ photocatalysts under sunlight illumination*. Ultrasonics Sonochemistry, 2017. **35**: p. 233-242.
60. Kalanoor, B.S., H. Seo, and S.S. Kalanur, *Recent developments in photoelectrochemical water-splitting using WO₃/BiVO₄ heterojunction photoanode: A review*. Materials Science for Energy Technologies, 2018. **1**(1): p. 49-62.
61. Zeng, Q., et al., *Synthesis of WO₃/BiVO₄ photoanode using a reaction of bismuth nitrate with peroxovanadate on WO₃ film for efficient photoelectrocatalytic water splitting and organic pollutant degradation*. Applied Catalysis B: Environmental, 2017. **217**: p. 21-29.
62. Mi, Q., et al., *A quantitative assessment of the competition between water and anion oxidation at WO₃ photoanodes in acidic aqueous electrolytes*. Energy & Environmental Science, 2012. **5**(2): p. 5694-5700.
63. Xu, S., et al., *One-dimensional WO₃/BiVO₄ heterojunction photoanodes for efficient photoelectrochemical water splitting*. Chemical Engineering Journal, 2018. **349**: p. 368-375.
64. Stoll, T., et al., *Visible-light-promoted gas-phase water splitting using porous WO₃/BiVO₄ photoanodes*. Electrochemistry Communications, 2017. **82**: p. 47-51.
65. Du, H., et al., *Synthesis of BiVO₄/WO₃ composite film for highly efficient visible light induced photoelectrocatalytic oxidation of norfloxacin*. Journal of Alloys and Compounds, 2019. **787**: p. 284-294.
66. Grigioni, I., et al., *Dynamics of Photogenerated Charge Carriers in WO₃/BiVO₄ Heterojunction Photoanodes*. Journal of Physical Chemistry C, 2015. **119**(36): p. 20792-20800.
67. Su, J., et al., *Nanostructured WO₃/BiVO₄ Heterojunction Films for Efficient Photoelectrochemical Water Splitting*. Nano Letters, 2011. **11**(5): p. 1928-1933.
68. Hong, S.J., et al., *Heterojunction BiVO₄/WO₃ electrodes for enhanced photoactivity of water oxidation*. Energy & Environmental Science, 2011. **4**(5): p. 1781-1787.
69. Selim, S., et al., *WO₃/BiVO₄: impact of charge separation at the timescale of water oxidation*. Chemical Science, 2019. **10**(9): p. 2643-2652.
70. Monfort, O., et al., *Photoelectrocatalytic hydrogen production by water splitting using BiVO₄ photoanodes*. Chemical Engineering Journal, 2016. **286**: p. 91-97.
71. Madhavi, V., et al., *Fabrication of porous 1D WO₃ NRs and WO₃/BiVO₄ heterojunction photoanode for efficient photoelectrochemical water splitting*. Materials Chemistry and Physics, 2021. **274**: p. 125095.
72. Fujimoto, I., et al., *WO₃/BiVO₄ composite photoelectrode prepared by improved auto-combustion method for highly efficient water splitting*. International Journal of Hydrogen Energy, 2014. **39**(6): p. 2454-2461.
73. Chae, S.Y., et al., *Insight into Charge Separation in WO₃/BiVO₄ Heterojunction for Solar Water Splitting*. ACS Applied Materials & Interfaces, 2017. **9**(23): p. 19780-19790.
74. Zhou, Y., et al., *Highly Efficient Photoelectrochemical Water Splitting from Hierarchical WO₃/BiVO₄ Nanoporous Sphere Arrays*. Nano Letters, 2017. **17**(12): p. 8012-8017.

75. Grigioni, I., et al., *Photoactivity and Stability of WO₃/BiVO₄ Photoanodes: Effects of the Contact Electrolyte and of Ni/Fe Oxyhydroxide Protection*. The Journal of Physical Chemistry C, 2018. **122**(25): p. 13969-13978.
76. Pedroni, M., et al., *Multilayer WO₃/BiVO₄ Photoanodes for Solar-Driven Water Splitting Prepared by RF-Plasma Sputtering*. Surfaces, 2020. **3**(1): p. 105-115.
77. Cao, Y., et al., *Surface Engineering of WO₃/BiVO₄ to Boost Solar Water-Splitting*. Catalysts, 2020. **10**(5): p. 556.
78. Grigioni, I., et al., *WO₃/BiVO₄ Photoanodes: Facets Matching at the Heterojunction and BiVO₄ Layer Thickness Effects*. ACS Applied Energy Materials, 2021. **4**(8): p. 8421-8431.
79. Zeradjanin, A., et al., *A Critical Review on Hydrogen Evolution Electrocatalysis: Re-exploring the Volcano-relationship*. Electroanalysis, 2016. **28**.
80. Xiao, S., et al., *Enhanced photoelectrocatalytic degradation of ammonia by in situ photoelectrogenerated active chlorine on TiO₂ nanotube electrodes*. Journal of Environmental Sciences, 2016. **50**: p. 103-108.
81. Zanoni, M.V.B., et al., *Photoelectrocatalytic Production of Active Chlorine on Nanocrystalline Titanium Dioxide Thin-Film Electrodes*. Environmental Science & Technology, 2004. **38**(11): p. 3203-3208.
82. Jo, W.-K. and R.J. Tayade, *New Generation Energy-Efficient Light Source for Photocatalysis: LEDs for Environmental Applications*. Industrial & Engineering Chemistry Research, 2014. **53**(6): p. 2073-2084.
83. Zhang, Y., et al., *Enhancing hydrogen evolution by photoelectrocatalysis of water splitting over a CdS flowers-loaded TiO₂ nanotube array film on the Ti foil substrate*. Ceramics International, 2020. **46**(11, Part A): p. 17606-17613.
84. Zhao, X., et al., *Photoelectrochemical degradation of anti-inflammatory pharmaceuticals at Bi₂MoO₆-boron-doped diamond hybrid electrode under visible light irradiation*. Applied Catalysis B: Environmental, 2009. **91**(1): p. 539-545.
85. Sun, Q., et al., *Photoelectrochemical oxidation of ibuprofen via Cu₂O-doped TiO₂ nanotube arrays*. Journal of Hazardous Materials, 2016. **319**: p. 121-129.
86. Liu, H., et al., *An Alternative Approach to Ascertain the Rate-Determining Steps of TiO₂ Photoelectrocatalytic Reaction by Electrochemical Impedance Spectroscopy*. The Journal of Physical Chemistry B, 2003. **107**(34): p. 8988-8996.
87. Chen, H., et al., *Enhanced photoelectrochemical degradation of Ibuprofen and generation of hydrogen via BiOI-deposited TiO₂ nanotube arrays*. Science of The Total Environment, 2018. **633**: p. 1198-1205.
88. Energy, O.o.E.E.R. *Hydrogen Production: Natural Gas Reforming*. Hydrogen and Fuel Cell Technologies Office.
89. Marchlewicz, A., U. Guzik, and D. Wojcieszńska, *Over-the-Counter Monocyclic Non-Steroidal Anti-Inflammatory Drugs in Environment-Sources, Risks, Biodegradation*. Water, air, and soil pollution, 2015. **226**(10): p. 355-355.
90. Chopra, S. and D. Kumar, *Ibuprofen as an emerging organic contaminant in environment, distribution and remediation*. Heliyon, 2020. **6**(6): p. e04087.
91. Gonzalez-Rey, M. and M.J. Bebianno, *Does non-steroidal anti-inflammatory (NSAID) ibuprofen induce antioxidant stress and endocrine disruption in mussel Mytilus galloprovincialis?* Environmental Toxicology and Pharmacology, 2012. **33**(2): p. 361-371.
92. Han, S., et al., *Endocrine disruption and consequences of chronic exposure to ibuprofen in Japanese medaka (Oryzias latipes) and freshwater cladocerans Daphnia magna and Moina macrocopa*. Aquatic Toxicology, 2010. **98**(3): p. 256-264.

93. De Lange, H.J., et al., *Behavioural responses of Gammarus pulex (Crustacea, Amphipoda) to low concentrations of pharmaceuticals*. Aquatic Toxicology, 2006. **78**(3): p. 209-216.
94. Letsinger, S., et al., *Spatial and temporal occurrence of pharmaceuticals in UK estuaries*. Science of The Total Environment, 2019. **678**: p. 74-84.
95. Sakai, N., et al., *Occurrence, fate and environmental risk of linear alkylbenzene sulfonate in the Langat and Selangor River basins, Malaysia*. Chemosphere, 2017. **172**: p. 234-241.
96. Venhuis, S.H. and M. Mehrvar, *Health effects, environmental impacts, and photochemical degradation of selected surfactants in water*. International Journal of Photoenergy, 2004. **6**: p. 631840.
97. Ahmari, H., S. Zeinali Heris, and M. Hassanzadeh Khayyat, *Photo catalytic degradation of linear alkylbenzene sulfonic acid*. Research on Chemical Intermediates, 2016. **42**(8): p. 6587-6606.
98. Hora, P.I. and W.A. Arnold, *Photochemical fate of quaternary ammonium compounds in river water*. Environmental Science: Processes & Impacts, 2020. **22**(6): p. 1368-1381.
99. Elersek, T., M. Ženko, and M. Filipič, *Ecotoxicity of disinfectant benzalkonium chloride and its mixture with antineoplastic drug 5-fluorouracil towards alga Pseudokirchneriella subcapitata*. PeerJ, 2018. **6**: p. e4986-e4986.
100. Kim, M., et al., *Widely Used Benzalkonium Chloride Disinfectants Can Promote Antibiotic Resistance*. Applied and Environmental Microbiology, 2018. **84**(17): p. e01201-18.
101. Martínez-Carballo, E., et al., *Determination of selected quaternary ammonium compounds by liquid chromatography with mass spectrometry. Part I. Application to surface, waste and indirect discharge water samples in Austria*. Environmental Pollution, 2007. **145**(2): p. 489-496.
102. Judkins, R.R., W. Fulkerson, and M.K. Sanghvi, *The dilemma of fossil fuel use and global climate change*. Energy & fuels, 1993. **7**(1): p. 14-22.
103. Ganguly, P., et al., *2D Nanomaterials for Photocatalytic Hydrogen Production*. ACS Energy Letters, 2019. **4**(7): p. 1687-1709.
104. Sfaelou, S., et al., *Mesoporous WO₃ photoanodes for hydrogen production by water splitting and PhotoFuelCell operation*. International Journal of Hydrogen Energy, 2016. **41**(14): p. 5902-5907.
105. Zhao, W., et al., *Hydrogen generation via photoelectrocatalytic water splitting using a tungsten trioxide catalyst under visible light irradiation*. International Journal of Hydrogen Energy, 2012. **37**(1): p. 908-915.
106. Li, F. and D.Y.C. Leung, *Highly enhanced performance of heterojunction Bi₂S₃/BiVO₄ photoanode for photoelectrocatalytic hydrogen production under solar light irradiation*. Chemical Engineering Science, 2020. **211**: p. 115266.
107. An, T., et al., *Photoelectrocatalytic degradation of quinoline with a novel three-dimensional electrode-packed bed photocatalytic reactor*. Journal of Photochemistry and Photobiology A: Chemistry, 2004. **161**(2): p. 233-242.
108. Alulema-Pullupaxi, P., et al., *Fundamentals and applications of photoelectrocatalysis as an efficient process to remove pollutants from water: A review*. Chemosphere, 2021. **281**: p. 130821.
109. Sathre, R., et al., *Life-cycle net energy assessment of large-scale hydrogen production via photoelectrochemical water splitting*. Energy & Environmental Science, 2014. **7**(10): p. 3264-3278.

110. Wu, Z., et al., *Simultaneous photoelectrocatalytic aromatic organic pollutants oxidation for hydrogen production promotion with a self-biasing photoelectrochemical cell*. *Electrochimica Acta*, 2017. **254**: p. 140-147.
111. Guaraldo, T.T., et al., *Hydrogen production and simultaneous photoelectrocatalytic pollutant oxidation using a TiO₂/WO₃ nanostructured photoanode under visible light irradiation*. *Journal of Electroanalytical Chemistry*, 2016. **765**: p. 188-196.
112. Wang, W., et al., *Photoelectrocatalytic hydrogen generation and simultaneous degradation of organic pollutant via CdSe/TiO₂ nanotube arrays*. *Applied Surface Science*, 2016. **362**: p. 490-497.
113. Li, F., W. Zhao, and D.Y.C. Leung, *Enhanced photoelectrocatalytic hydrogen production via Bi/BiVO₄ photoanode under visible light irradiation*. *Applied Catalysis B: Environmental*, 2019. **258**: p. 117954.
114. Shen, Q., et al., *Photoelectrocatalytic hydrogen production of heterogeneous photoelectrodes with different system configurations of CdSe nanoparticles, Au nanocrystals and TiO₂ nanotube arrays*. *International Journal of Hydrogen Energy*, 2020. **45**(51): p. 26688-26700.

Chapter 2 : Materials and Methodology

2.1 Laboratory Equipment

There was various laboratory equipment utilised for the numerous experiments, these were pipette tips (10 μ L, 100 μ L, 1 mL, 10 mL), Mettler Toledo EL240 analytical balance, vortex mixer, lyophiliser, desiccator, enclosed hotplate, rotary evaporator, spincoater, 200ml closed beaker, magnetic stirrer, ultrasonic sonicator, COD meter (multiparameter photometer kit, Hanna Instruments), two compartment photoelectrochemical cell with Nafion membrane and motor and pestle.

2.2 PEC Set-up

For all PEC experiments (including EIS and IMPS) a two-compartment photoelectrochemical cell was utilised and contained a Nafion membrane to separate the anodic and cathodic compartment (Figures 2.1 and 2.2). The anodic compartment contained the developed $\text{WO}_3/\text{BiVO}_4$ photoanode (will be stated which $\text{WO}_3/\text{BiVO}_4$ photoanode was utilised as it varied on the experiment) and Ag/AgCl reference electrode and the electrolyte spiked with the pollutant. While the cathodic compartment contained just a platinum wire as the counter electrode immersed in pure electrolyte. The electrodes were all connected to a potentiostat which controlled the applied potential. A magnetic stirrer was utilised to allow for constant stirring of the electrolyte.



Figure 2.1 - An image showing the two compartment PEC cell utilised for all PEC experiments.

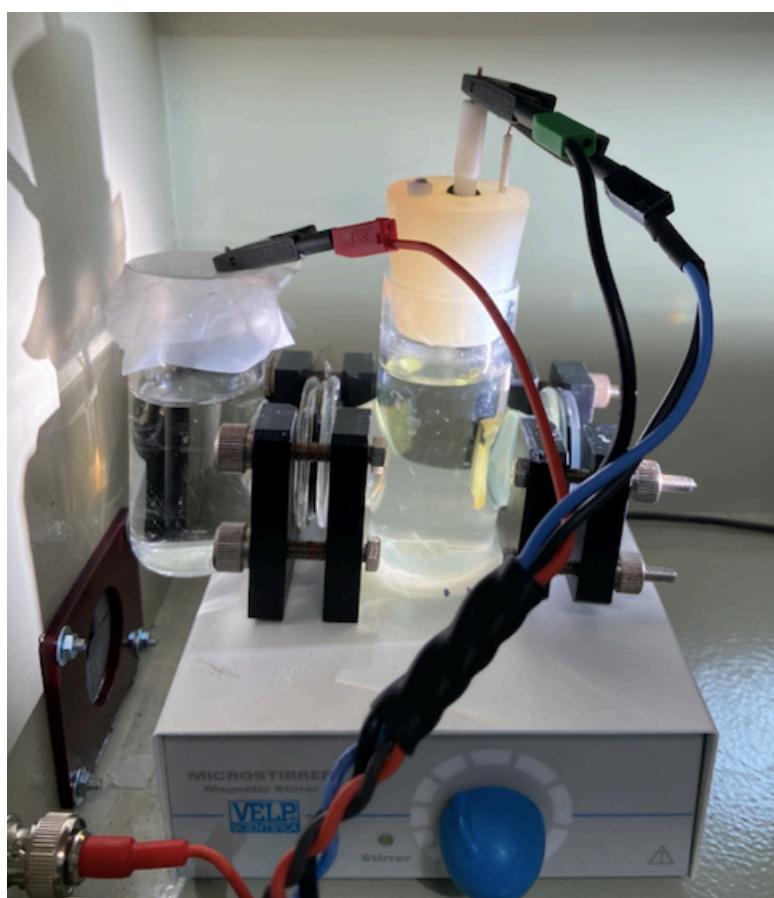


Figure 2.2 - An image showing the PEC cell during a pollutant degradation experiment.

2.3 Chemicals

A wide range of chemicals were utilised for various experiments conducted in this thesis. For the synthesis of WO_3 paste, the chemicals utilised were tungsten (VI) oxide (Sigma-Aldrich, 99.9%), ethanol (Fisher Scientific, HPLC Grade), acetic acid (Sigma-Aldrich, >99%), deionised water (Suez Environment, Purite, Ondeo IS), α -terpineol (Sigma-Aldrich, 90%), ethyl cellulose (Sigma-Aldrich, 48-49%). While for the synthesis of BiVO_4 the following chemicals were utilised ammonium metavanadate (Sigma-Aldrich, >99%), bismuth nitrate pentahydrate (Alfa Aesar, 98%), citric acid (Sigma-Aldrich, >99.5%), nitric acid (Sigma-Aldrich, 70%) and deionised water (Suez Environment, Purite, Ondeo IS).

For determining each synthesised photoanode's performance then the following chemicals were utilised for the PEC system to work which were sodium chloride (Arcos Organics, Extra Pure), sodium sulfate (Fisher Scientific, 99%), deionised water (Suez Environment, Purite, Ondeo IS).

While for pollutant degradation experiments, the following chemicals were utilised acetonitrile (Fisher Scientific, HPLC Grade), water (Fisher Scientific, HPLC Grade), sodium chloride (Arcos Organics, Extra Pure), ibuprofen (Sigma-Aldrich), benzyldimethyldodecylammonium chloride (SigmaAldrich, >99%) and sodium 2-naphthalenesulfonic acid (Sigma-Aldrich, >95%).

While for the LC-UV the mobile phases required the following chemicals which were acetonitrile (Fisher Scientific, HPLC Grade), water (Fisher Scientific, HPLC Grade) and formic acid (Fisher Scientific, >98%).

2.4 Photoanode Development

There were several techniques that could have been utilised for synthesising the WO_3 layer in the photoanodes. Here, the method utilised was adapted from O'Regan and Grätzel's method for TiO_2 paste for dye-sensitised solar cells and photoanodes due to its simplicity and its high reproducibility [1]. The method is outlined below:

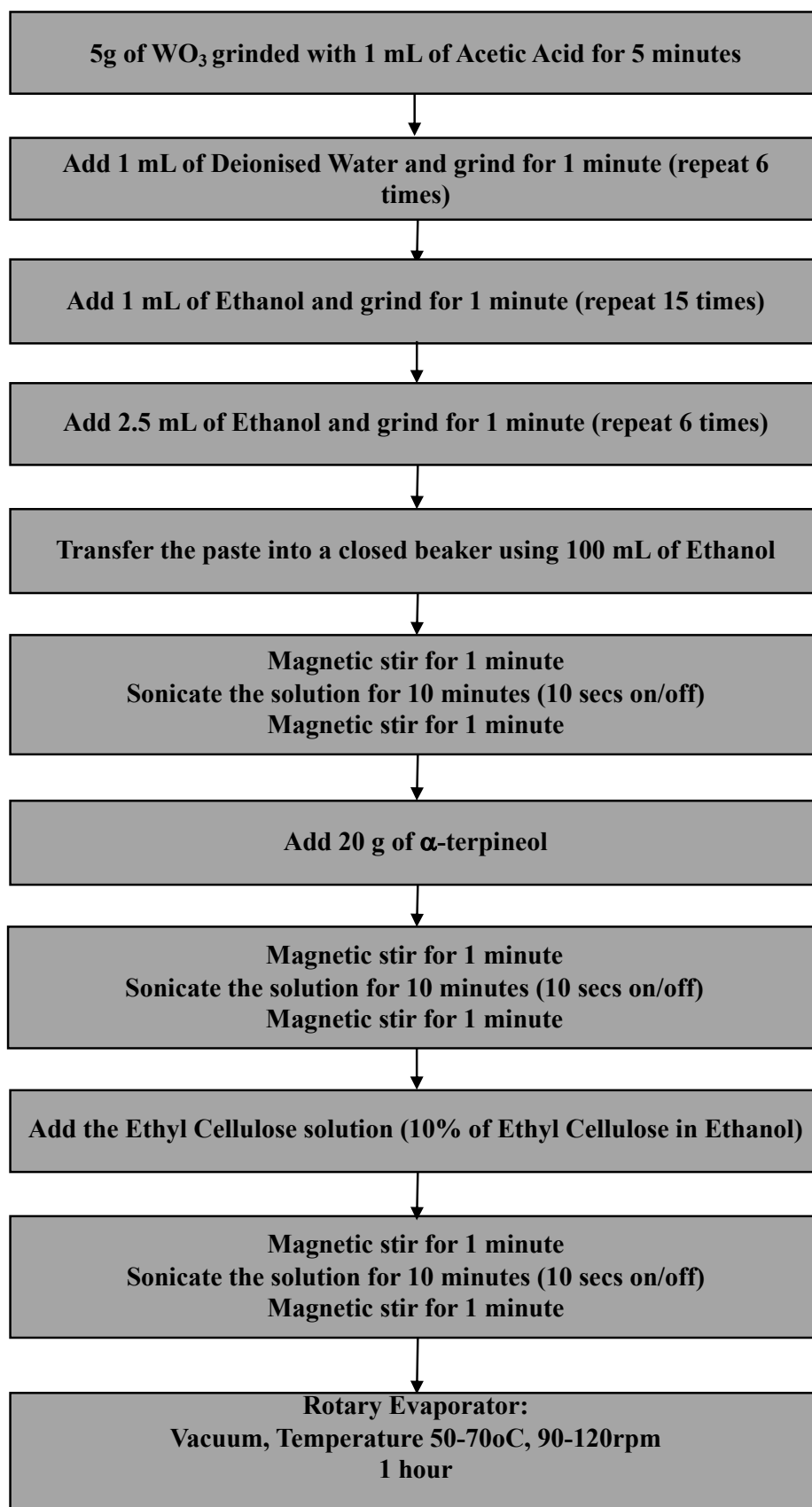


Figure 2.3 - The WO₃ paste synthesis method.

The doctor blade technique was then utilised to apply the WO_3 paste onto the FTO substrate. It worked by masking FTO glass substrate with scotch tape to expose 1 cm^2 of FTO area where the WO_3 paste was applied onto and spread across by utilising the doctor blade technique. Then an enclosed hotplate was utilised with the following conditions to anneal the WO_3 onto the FTO substrate: (a) Ramp time = 1 hour, (b) Set temperature = 450°C and (c) Annealing Time = 3 hours.

While the BiVO_4 thin films were prepared by adopting the method created by Choi et al [2]. It involved mixing together 0.1462 g of ammonium metavanadate, 0.6061 g of bismuth nitrate pentahydrate, 0.4803 g of citric acid, 0.825 g of nitric acid and 2.9 mL of deionised water [2]. Sonicate the mixture for 10 minutes. Once the solution was prepared then it was spin coated onto the FTO glass or the WO_3 surface with the settings of 500 rpm for 5 seconds, then 2000 rpm for 40 seconds. The photoanodes were then annealed in an enclosed hot plate using the following conditions: (a) ramp time = 2.5 hours, (b) Set temperature = 500°C and (c) annealing Time = 1 hour. Similarly, to WO_3 films the structure, surface morphology, chemical environment, and optical properties of the as-prepared BiVO_4 film were studied.

Once the desired number of cycles of WO_3 and BiVO_4 were applied then the ultrasonic solder was utilised to attach an insulated copper wire to the FTO glass, and the electrode was sealed using an epoxy resin glue.

To determine the effect of varying the thickness of WO_3 and BiVO_4 layers on the $\text{WO}_3/\text{BiVO}_4$ photoanode's performance then the number of deposition cycles were altered for each semiconductor onto the FTO glass. This was prepared by annealing each cycle before applying the next cycle.

Once the production of the photoanodes was done then several techniques were utilised to help determine and explain the photoanode performance. The best techniques for determining photoanode performance are chronoamperometry and linear sweep voltammetry (LSV), while electrochemical impedance (EIS) and intensity modulated photocurrent spectroscopy (IMPS) can help explain the behaviour of the photoanode.

2.4.1 Chronoamperometry

Chronoamperometry uses a constant applied potential to help to determine the photocurrent produced as a function of time. Photocurrent is produced when electrons travel from the photoanode to the cathode via an external circuit causing a flow of electrons (current). This method indicates how successful the photoanode is at producing electrons, as the higher the number of electrons produced the higher the photocurrent generated.

All chronoamperometry experiments were conducted on a Zahner potentiostat (Thales Zahner Zennium X) with the reference electrode being Ag/AgCl, the counter electrode being Pt wire and the working electrode being one of the synthesised photoanode (will be stated in results section). The chronoamperometry tests were ran by utilising 0.5 M sodium chloride as the supporting electrolyte in the anodic and cathodic compartment with 1.2 V applied potential and a chopped light (1 Sun of Solar Light (Solar Simulator 350-1800nm, HAL-320W, Asahi Spectra) with 30 seconds off/on) and a run time of 5 minutes.

As $2\text{WO}_3/1\text{BiVO}_4$ was found to be the optimised photoanode then this was utilised as the working electrode for all experiments going forward. The chronoamperometry function on the Zahner potentiostat was utilised to also help determine the effect of altering the operating parameters of the PEC system on the photocurrent production. Tables 2.1 - 2.3 summarises the PEC conditions utilised for each experiment.

The first set of experiments were conducted to determine how the type of supporting electrolyte effected the performance of the photoanode.

Table 2.1 - The method utilised for determining the best supporting electrolyte for the PEC system.

Condition	1	2	3
Supporting Electrolyte	Water	Na_2SO_4	NaCl
Concentration of Supporting Electrolyte (M)	n/a	0.5	0.5
Applied Potential (V vs Ag/AgCl)	+ 0.6	+ 0.6	+ 0.6
Light (suns)	1 (30 secs off/on)	1 (30 secs off/on)	1 (30 secs off/on)
Time (minutes)	5	5	5

The second set of experiments were conducted to determine the effect of the supporting electrolyte concentration on the performance of the photoanode.

Table 2.2 - The method utilised for determining the best supporting electrolyte concentration for the PEC system.

Condition	1	2	3
Supporting Electrolyte	NaCl	NaCl	NaCl
Concentration of Supporting Electrolyte (M)	0.1	0.5	1
Applied Potential (V vs Ag/AgCl)	+ 0.6	+ 0.6	+ 0.6
Light (suns)	1 (30 secs off/on)	1 (30 secs off/on)	1 (30 secs off/on)
Time (minutes)	5	5	5

The third set of experiments were conducted to determine the effect of the applied potential has on the performance of the photoanode.

Table 2.3 - The method utilised for determining the best applied potential for the PEC system.

Condition	1	2	3	4
Supporting Electrolyte	NaCl	NaCl	NaCl	NaCl
Concentration of Supporting Electrolyte (M)	0.5	0.5	0.5	0.5
Applied Potential (V vs Ag/AgCl)	+ 0.6	+ 0.9	+ 1.2	+ 1.5
Light (suns)	1 (30 secs off/on)	1 (30 secs off/on)	1 (30 secs off/on)	1 (30 secs off/on)
Time (minutes)	5	5	5	5

2.4.2 Linear Sweep Voltametry (LSV)

Linear sweep voltametry (LSV) is a simple sweep method which is commonly utilised to help determine the current response of a working electrode when a range of potentials are applied from a lower to an upper limit at a set scan rate. This results in a plot which exhibits the working electrode's photocurrent response vs the applied potential.

LSV was conducted like chronoamperometry by utilising the Zahner potentiostat with Ag/AgCl being the reference electrode, Pt wire being the counter electrode and the synthesised photoanodes as the working electrode in a two-compartment PEC cell with a Nafion membrane. The LSV experiments were ran utilising the LSV function on the Zahner system. The experiments were ran utilising the light and dark to help determine how much the light effects the photoanode's performance.

Table 2.4 - The method utilised for the LSV experiments.

Light	Dark	1 Sun
Lower Limit	- 0.5	- 0.5
Upper Limit	+ 1.5	+ 1.5
Scan rate	50 mV/secs	50 mV/secs
Supporting Electrolyte	NaCl	NaCl
Supporting Electrolyte Concentration (M)	0.5	0.5

2.4.3 Electrochemical Impedance Spectroscopy (EIS) and Intensity-Modulated Photocurrent Spectroscopy (IMPS)

The photoanode was assessed further by determining the resistance experienced in the photoanode and calculating the electron transit time. To do this then the EIS and IMPS functions of the Zahner system were utilised. Due to the measurement requirements of the Zahner system, the light source was changed from the solar simulator to a LS470 light in the Zahner PP211 potentiostat.

EIS was utilised to help understand the charge transfer occurring in the photoanode. This allowed the charge transfer resistance to be calculated. Due to the resistance in the photoanode it was important to help determine how altering the number of WO₃ and BiVO₄ deposition cycles affected the PEC performance. EIS works by applying a sinusoidal AC current to the photoanode with a set amplitude and measuring the response. The method utilised for the EIS experiment is explained in Table 2.5 below:

Table 2.5 - The method utilised for the EIS experiments.

Zahner Lamp	LS470	
Light Intensity (W/m²)	400	
Supporting Electrolyte	Sodium Chloride (NaCl)	
Concentration of Supporting Electrolyte (M)	0.5	
Applied Potential (V vs Ag/AgCl)	+ 0.3, + 0.6, + 0.9, + 1.2	
Amplitude for Potential (mV)	10	
Frequency Limits	Upper (Hz)	2 M
	Lower (Hz)	100 m
Steps per Decade	Upper	7
	Lower	7
Measure Periods	Upper	10
	Lower	1

The data recorded by the EIS experiment is plotted as a Nyquist plot where the Z'' (imaginary) is on the y-axis against Z' (real) on the x-axis. This plot is a result of the electrical circuit therefore, to help determine the charge transfer resistance then an equivalent electric circuit model was required which would fit the EIS data. The equivalent circuit utilised for fitting the EIS was as shown below [3]:

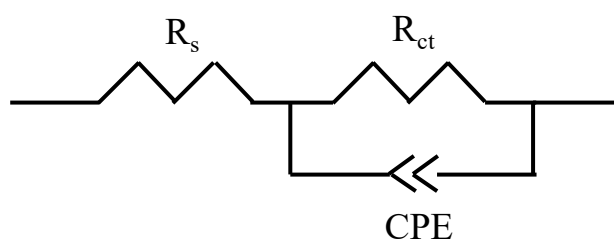


Figure 2.4 - The equivalent circuit utilised for resistance calculations [3].

Z' view was utilised to fit the equivalent circuit to the Nyquist plot. The R_{ct} value represents the charge transfer resistance and is the value taken for assessing the resistance the charge carriers need to overcome. While R_s and CPE are solution resistance and the constant phase element respectively [3].

IMPS was utilised to calculate the electron transit time. It works by the light intensity being modulated at a set amplitude and measuring the photocurrent response across a scope of frequencies. The IMPS method utilised for the photoanodes (detailed in Chapter 3) is highlighted below (Table 2.6):

Table 2.6 - The method utilised for the IMPS experiments.

Zahner Lamp	LS470	
Light Intensity (W/m²)	400	
Supporting Electrolyte	Sodium Chloride (NaCl)	
Concentration of Supporting Electrolyte (M)	0.5	
Applied Potential (V vs Ag/AgCl)	+ 0.3, + 0.6, + 0.9, + 1.2	
Light Amplitude (V)	0.230	
Frequency Limits	Upper (Hz)	100 K
	Lower (Hz)	100 m
Steps per Decade	Upper	7
	Lower	7
Measure Periods	Upper	10
	Lower	1

The data was analysed using Z view software which would plot Z'' (imaginary) on the y-axis against Z' (real) on the x-axis. This software allowed a circle to be fitted to the data which generated a value ω_{max} . This is important because the ω_{max} value is utilised in the transit time equation 2.1.

Electron Transit Time Calculation [4]:

$$\tau_D = \frac{1}{2\pi f} \quad (\text{Equation 2.1})$$

While [5]:

$$\omega_{max} = 2 \times \pi \times f \quad (\text{Equation 2.2})$$

Therefore, the equation becomes:

$$\tau_D = \frac{1}{\omega_{max}} \quad (\text{Equation 2.3})$$

2.4.4 Photoanode Characterisation

2.4.4.1 UV-Vis Spectroscopy

The UV-Vis spectrometer was utilised to help determine the wavelengths which could be absorbed by the different photoanodes. Due to the porosity of the solid films, back scattering of the light occurs which means absorbance is not able to be accurately recorded. Therefore, a diffuse reflection UV-Vis spectroscopy is utilised (DR-UV). Which is a UV-Vis spectrometer

with an integrating sphere which allows reflection values to be obtained. Table 2.7 below summarises the conditions of the DR-UV.

Table 2.7 - The UV method for photoanode analysis.

Instrument	Perkin Elmer Lambda 365
Wavelength Range (nm)	300 - 550

As this instrument obtains the reflection values then an equation is required to help convert these reflection values into the Kubelka-Munk value. Kubelka-Munk model is widely utilised for the diffuse reflection conversion to absorption and scattering coefficients (K/s).

The model is as follows [6]:

$$R_{\infty} = 1 + \frac{k}{s} - \sqrt{\frac{k}{s} \left(2 + \frac{k}{s} \right)} \quad (\text{Equation 2.4})$$

which can be re-arranged to [6]:

$$\frac{k}{s} = \frac{(1-R_{\infty})^2}{2R_{\infty}} \quad (\text{Equation 2.5})$$

These values are then plotted against the wavelength to help determine the wavelengths absorbed by the photoanode.

2.4.4.2 X-ray Powder Diffraction (XRD)

To help determine the crystal structure for each photocatalyst material on the photoanode then XRD was utilised. It utilises monochromatic x-rays to hit the sample at various directions. This causes x-rays to be diffracted by the atoms of the sample which are then detected and recorded as signals over a range of angles. This produces a diffraction pattern, which is compared to literature to help determine the crystallinity phases of the molecules. This will verify if the synthesis method was successful in producing photoanodes with high photoactivity.

The XRD analysis was conducted by Tom Dunlop (Specific Group in Swansea University). The instrument utilised was Bruker D8 Discover X-ray Diffractometer. It has a copper source (40kV, 40mA) with a 1D detector in Bragg-Brentao. The operating conditions were 0.03° step size with a step time of 0.7s and the scans were taken between 10 and 60° 2θ.

2.4.4.3 X-ray Photoelectron Spectroscopy (XPS)

XPS is utilised to help identify the atomic composition in the sample. It works by monochromatic x-rays being absorbed by the sample results in electrons being evicted from the atom. This produces an energy which is measured by a detector. This energy is the difference between the initial and final energies of the electron. The energy is dependent on the atom present in the sample and the environment around it. Finding the binding energy helps identify the composition of each element on the surface of the photoanode. Thus, making this a vital analysis tool for confirming WO_3 and/or BiVO_4 is present on the photoanode surface.

The XPS was performed by Tom Dunlop (Specific Group of Swansea University). The XPS was performed on a Kratos Axis Supra using a monochromatic Al $K\alpha$ X-ray source operated at 225W (15mA emission current). Each sample had wide scans performed at a pass energy of 160eV with a binding energy range of 1200-0eV to identify all the elements present. Then each element was recorded using a high-resolution spectroscopy with a pass energy of 40eV, step size of 0.1eV with a 1000ms dwell time and repeated sweeps (improves the signal:noise). A charge correction to the C_xH_y components of carbon components at 284.8eV was needed for the binding energy axis, while the Casa XPS with built in Kratos sensitivity factor library based on Shirley backgrounds was used to quantify the data.

2.4.4.4 Scanning Electron Microscopy (SEM)

SEM was utilised to show the morphology of the surface. This helps verify if the surface is porous and enables the grain size to be calculated. SEM works by using a beam of electrons hitting precise spots on the surface of the sample. The surface is scanned in a rectangular pattern using this beam which causes the back scattering (scattered out of the specimen – higher energy) and secondary electrons (from the specimen itself – lower energy) and the x-rays to hit the detector. This produces a signal which is measured and mapped as variation brightness thus creating an image. During the SEM analysis there is an EDS function which allows the identification of elements present on the photoanode surface.

Due to COVID restrictions limiting access to the laboratory and instruments the SEM analysis was conducted by James Russell (Advanced Imaging of Materials Facility in Swansea University). The SEM instrument was JEOL 7800F FEGSEM with an Oxford Instrument X-Max^N EDS Detector with a 50mm² window.

2.4.4.5 High Resolution Transmission Electron Microscopy (HR-TEM)

This technology produces an image of the crystallographic structure of a sample at its atomic level [7]. TEM works by an electron beam interacting with the sample which causes diffraction with its intensity varying on the plane's orientation with respect to the electron beam [7]. An aperture is utilised to block the deflected electrons and produce a contrast image [7].

Surface morphology of WO_3 and $\text{WO}_3/\text{BiVO}_4$ coatings were analysed by Chalmers University of Technology, Sweden utilising a HRTEM (FEI Technai F20) done through a collaboration. Typically, the coatings were scratched carefully and sonicated in ethanol for 15 min. The sonicated samples were coated on the copper TEM grid.

2.5 Pollutant Degradation

To help assess the pollutant degradation during the PEC process then it was necessary to monitor the concentration of the pollutant in the solution by utilising a liquid chromatography with an UV detector (LC-UV). LC-UV utilises a column to help separate each compound in the sample so each one is recorded by the UV detector separately. LC-UV works by the sample being injected into the system where it is carried down the non-polar column by the polar mobile phases. The sample should be completely miscible in the mobile phases so it flows down the column without causing any blocks or poor elution. The column interacts with the compounds in the sample and depending on the attraction between the column and compound the time spent in the column (retention time) changes. If the column has a strong attraction with the compound, then it will remain in the column longer than if there is a weak attraction. This allows the compounds to reach the UV detector separately. The UV detector then records the amount of light absorbed by each compound. This results in a peak or a series of peaks (depending on how many compounds are in the sample) being recorded as a chromatogram. The peak area is then utilised to calculate the concentration for compound as the intensity of the peaks relates to the amount of pollutant in the sample. Each pollutant requires different LC-UV methods as the eluting of the compounds (retention time) depends on the gradient pumping of the mobile phases, while the peak area depends on UV detection wavelength. Therefore, each method needs to be developed by trial and error of each method. The LC-UV utilised for all pollutant quantification was the Agilent 1200 LC-UV System with a Waters X-select C-18 column (2.1mm x 100mm).

2.5.1 Liquid Chromatography with UV detector (LC-UV) Methods

2.5.1.1 Ibuprofen

After some method development, the method which demonstrated the highest sensitivity for ibuprofen is summarised in Table 2.8. This method was assessed by reproducibility and calibrations. As the assessment showed excellent results this method was then utilised for analysing the samples collected during the ibuprofen degradation experiments.

Table 2.8 - The chosen method developed for ibuprofen analysis.

Column	Xselect C-18 column (2.1 mm x 100 mm)		
Injection Volume (µL)	5		
Flowrate (mL/min)	0.250		
UV Wavelength Detection (nm)	265		
Gradient Pumping	Time (minutes)	Mobile Phase A: 0.1% Formic Acid in Water (%)	Mobile Phase B: 100% Acetonitrile (%)
	0	75	25
	1	75	25
	17	0	100
	24	0	100
	25	75	25
	35	75	25

2.5.1.2 BAC-C12:

As BAC-C12 is a different compound then method development was needed again to help establish a method which resulted in high sensitivity. Therefore, the best method is summarised in the table below and was utilised for analysing the samples collected during the BAC-C12 degradation experiments.

Table 2.9 - The chosen method developed for BAC-C12 analysis.

Column	Xselect C-18 column (2.1 mm x 100 mm)		
Injection Volume (µL)	5		
Flowrate (mL/min)	0.250		
UV Wavelength Detection (nm)	260		
Gradient Pumping	Time (minutes)	Mobile Phase A: 0.1% Formic Acid in Water (%)	Mobile Phase B: 100% Acetonitrile (%)
	0	75	25
	1	75	25
	17	0	100
	24	0	100
	25	75	25
	35	75	25

2.5.1.3 S2NS:

Unlike the other two compounds S2NS did not require method development as the first method achieved high selectivity for S2NS. Therefore, the method which is summarised in Table 2.10 was utilised for quantifying the amount of S2NS in the samples collected from the degradation experiments.

Table 2.10 - The chosen method developed for S2NS analysis.

Column	Xselect C-18 column (2.1 mm x 100 mm)		
Injection Volume (µL)	5		
Flowrate (mL/min)	0.250		
UV Wavelength Detection (nm)	273		
Gradient Pumping	Time (minutes)	Mobile Phase A: 0.1% Formic Acid in Water (%)	Mobile Phase B: 100% Acetonitrile (%)
	0	75	25
	1	75	25
	17	0	100
	24	0	100
	25	75	25
	35	75	25

2.5.2 LC-UV Reproducibility and Calibration

2.5.2.1 Standards

a. Stock Solution

For each pollutant a stock solution was created. The method of the stock solution depends on the pollutant.

Ibuprofen: In an amber glass vial (15 mL) 5 mg of ibuprofen was weighed using an analytical weighing scale. Then 5 mL of acetonitrile was added to the vial using a pipette. The solution was mixed using a vortex and resulted in a concentration of 1 mg/mL.

BAC-C12: In an amber glass vial (15 mL) 5 mg of BAC-C12 was weighed using an analytical weighing scale. Then 5 mL of acetonitrile was added to the vial using a pipette. The solution was mixed using a vortex and resulted in a concentration of 1 mg/mL.

S2NS: In an amber glass vial (22 mL) 5 mg of S2NS was weighed using an analytical weighing scale. Then 5 mL of water was added to the vial using a pipette and vortexed. Then 5 mL of acetonitrile was added and vortexed and resulted in a concentration of 0.5 mg/mL.

b. Diluted Standards for Calibration and Reproducibility

To produce standards for the calibration and reproducibility then the stock solutions need to be diluted. This is done by adding a suitable amount of ACN/H₂O (50/50) to a 1 mL amber glass vial. Then adding an appropriate amount of the stock solution and vortex the solution.

2.5.2.2 Repeatability and Reproducibility

The repeatability and reproducibility were assessed by analysing the retention times and peak areas obtained from the consecutive injections (n=10 on day 1, and n=8 on day 2) of the same standard. The concentration for the standard utilised for ibuprofen, BAC-C12 and S2NS were 200 µg/mL, 200 µg/mL and 100 µg/mL, respectively. The reason these were the chosen concentrations was to ensure that the starting concentration of the degradation experiments would not cause carry over, thus affecting the analysis of the pollutant degradation samples.

In addition, a blank sample followed each set of injections to help identify any carry over which could occur. No carry over was identified for ibuprofen, BAC-C12 and S2NS thus verifying

that the selectivity of each method was sustained after multiple injections of high concentrations of each pollutant.

The coefficient of variation (CV%) was utilised to help determine the spread of the results from the reproducibility test. If the CV% is < 5% then the method produces repeatable results. The CV% is calculated using the equation below [8]:

$$\%CV = \frac{s}{x} \times 100 \quad (\text{Equation 2.6})$$

where: s = standard deviation

x = mean

The two tailed F-test was utilised to help determine if the results were reproducible. As it determines if there was a significant difference between the two sets of data. The equation below was utilised for calculating the F-test value [8]:

$$F - \text{Test} = \left(\frac{s_1^2}{s_2^2} \right) \quad (\text{Equation 2.7})$$

where: s₁ = the smaller standard deviation

s₂ = the larger standard deviation

The calculated F-test is then compared to the critical value to help determine if there is a significant difference between the two sets of data.

2.5.2.3 Calibration

A calibration graph is established to help quantify the ibuprofen concentration in the samples collected from the degradation experiments. It is achieved by running a set (n = 6) of calibration standards of known concentrations (Tables 2.11). This results in an analyte response (peak area) for each concentration. By applying regression statistics to the results then the coefficient of determination (R²), standard error, intercept and gradient values can be generated. These values are necessary to establish the linearity, instrument detection limit and actual concentrations of the analytes analysed. In addition, replicates of quality control standards (QCs) were utilised to determine the accuracy and precision of the method employed for analysing ibuprofen within the calibration range.

Table 2.11 - A table showing the concentrations of the calibration standards for each pollutant.

Standard	CC1	CC2	CC3	CC4	CC5	CC6	CC7	CC8
Ibuprofen Concentration ($\mu\text{g/mL}$)	10	30	50	70	100	130	160	200
BAC-C12 Concentration ($\mu\text{g/mL}$)	10	30	50	70	100	130	160	200
S2NS Concentration ($\mu\text{g/mL}$)	1	2	5	10	20	40	60	100

Table 2.12 - A table showing the concentrations of the QC standards for each pollutant.

QC (number of replicates = 5)	Low	Mid	High
Ibuprofen Concentration ($\mu\text{g/mL}$)	20	80	180
BAC-C12 Concentration ($\mu\text{g/mL}$)	20	80	180
S2NS Concentration ($\mu\text{g/mL}$)	1.5	15	80

To assess the data obtained from the calibration then it was necessary to calculate the accuracy and precision of the quality control standards (QCs). To do this then the first step was to calculate the actual concentration of the QCs. To achieve this the regression tool in excel was utilised. The regression tool helps to determine the linearity as well as generating values for the intercept and gradient of the line equation. The line equation was utilised to calculate the actual concentration of the pollutants in the samples.

$$y = mx + C \quad (\text{Equation 2.8})$$

where: y = peak area

m = gradient of the line

x = actual concentration

C = intercept

rearranged to make x the subject:

$$x = \frac{y-C}{m} \quad (\text{Equation 2.9})$$

Once the real concentrations were calculated then mean and standard deviations were calculated, using the formulas on excel. Once the mean and standard deviations of the QCs

were calculated then the accuracy and precision can be calculated using the equations below [8]:

$$\text{accuracy (\%)} = \frac{\text{theoretical concentration} - \text{real concentration}}{\text{theoretical concentration}} \times 100 \quad (\text{Equation 2.10})$$

$$\text{precision (\%)} = \frac{s}{x} \times 100 \quad (\text{Equation 2.11})$$

where: s = standard deviation

x = mean

2.5.2.4 Outliners

All quality control standards and experiments were carried out in triple replicates (unless stated) and then Grubb's test was utilised to determine any outliners. The Grubb's Test equation is as follows [8]:

$$\text{Grubb's Test} = \frac{(x - \bar{x})}{s} \quad (\text{Equation 2.12})$$

Where: s = standard deviation

x = mean

\bar{x} = average mean

2.5.2.5 Instrument Detection Limit (IDL)

It was necessary to establish the limit of detection of the LC-UV methods to ensure the lowest calibration standard was appropriate for the LC-UV system and method developed. The LC-UV detection limit can be calculated statistically by utilising the equation below [8]:

$$\text{IDL} = \frac{3.3 \times e_s}{m} \quad (\text{Equation 2.13})$$

where: e_s = standard error

m = gradient of the calibration line

2.5.4 Ibuprofen Degradation Experiment Conditions

There were several ibuprofen degradation experiments to determine if the optimised photoanode developed in chapter 3 ($2\text{WO}_3/1\text{BiVO}_4$) would be successful. These experiments

are classified as photoelectrocatalysis experiments and all involve the use of a working electrode ($2\text{WO}_3/\text{1BiVO}_4$), reference electrode (Ag/AgCl) and counter electrode (Pt wire). All the experiments were conducted on the Zahner potentiostat and conducted in a two-compartment PEC cell (with a Nafion membrane).

Table 2.13 - The PEC experiment method for ibuprofen degradation in the dark.

Ibuprofen Concentration ($\mu\text{g/ml}$)	100
Supporting Electrolyte	NaCl
Supporting Electrolyte Concentration (M)	0.5
Applied Potential (V vs Ag/AgCl)	+ 0.6
Time Ran in the Dark (minutes)	120
Light Used	0
Light Intensity	0
Time Ran in the Light (minutes)	0
Samples	1 mL taken every 10 minutes

Table 2.14 - The PEC experiment method for ibuprofen degradation in the light.

Ibuprofen Concentration ($\mu\text{g/ml}$)	100
Supporting Electrolyte	NaCl
Supporting Electrolyte Concentration (M)	0.5
Applied Potential (V vs Ag/AgCl)	+ 0.6
Time Ran in the Dark (minutes)	30
Light Used (HAL-320W, Ashai Spectra)	Solar Light (350nm-1800nm)
Light Intensity (sun)	1
Time Ran in the Light (minutes)	120
Samples	1 mL taken every 30 minutes

Table 2.15 - The PEC experiment method for optimising the applied potential.

Ibuprofen Concentration ($\mu\text{g/ml}$)	100			
Supporting Electrolyte	NaCl			
Supporting Electrolyte Concentration (M)	0.5			
Applied Potential (V vs Ag/AgCl)	+ 0.6	+ 0.9	+ 1.2	+ 1.5
Time Ran in the Dark (minutes)	30			
Light Used (HAL-320W, Ashai Spectra)	Solar Light (350nm-1800nm)			
Light Intensity (sun)	1			
Time Ran in the Light (minutes)	120			
Samples	1 mL taken every 30 minutes			

Table 2.16 - The PEC experiment method for optimising the supporting electrolyte concentration.

Ibuprofen Concentration ($\mu\text{g/ml}$)	100	
Supporting Electrolyte	NaCl	
Supporting Electrolyte Concentration (M)	0.5	1.0
Applied Potential (V vs Ag/AgCl)	+ 1.2	
Time Ran in the Dark (minutes)	30	
Light Used (HAL-320W, Ashai Spectra)	Solar Light (350nm-1800nm)	
Light Intensity (sun)	1	
Time Ran in the Light (minutes)	120	
Samples	1 mL taken every 30 minutes	

2.5.5 BAC-C12 Degradation Experiment Conditions

As the PEC operating conditions were optimised during the ibuprofen degradation chapter then there were only two different types of experiments run for the BAC-C12 degradation. These experiments were outlined in the tables below:

Table 2.17 - The PEC experiment method for the higher concentration of BAC-C12 degradation.

BAC-C12 Concentration ($\mu\text{g/ml}$)	100
Supporting Electrolyte	NaCl
Supporting Electrolyte Concentration (M)	1
Applied Potential (V vs Ag/AgCl)	+ 1.2
Time Ran in the Dark (minutes)	30
Light Used (HAL-320W, Ashai Spectra)	Solar Light (350nm-1800nm)
Light Intensity (sun)	1
Time Ran in the Light (minutes)	120
Samples	1 mL taken every 30 minutes

Table 2.18 - The PEC experiment method for the lower concentration of BAC-C12 degradation.

BAC-C12 Concentration ($\mu\text{g/ml}$)	50
Supporting Electrolyte	NaCl
Supporting Electrolyte Concentration (M)	1
Applied Potential (V vs Ag/AgCl)	+ 1.2
Time Ran in the Dark (minutes)	30
Light Used (HAL-320W, Ashai Spectra)	Solar Light (350nm-1800nm)
Light Intensity (sun)	1
Time Ran in the Light (minutes)	120
Samples	1 mL taken every 30 minutes

2.5.6 S2NS Degradation Experiment Conditions

The S2NS degradation was run using the optimised PEC operating conditions with the optimised concentration for complete removal of a surfactant.

Table 2.19 - The PEC experiment method for the of S2NS degradation.

S2NS Concentration (µg/ml)	50
Supporting Electrolyte	NaCl
Supporting Electrolyte Concentration (M)	1
Applied Potential (V vs Ag/AgCl)	+ 1.2
Time Ran in the Dark (minutes)	30
Light Used (HAL-320W, Ashai Spectra)	Solar Light (350nm-1800nm)
Light Intensity (sun)	1
Time Ran in the Light (minutes)	120
Samples	1 mL taken every 30 minutes

2.4.7 Analysis of the Pollutant Degradation

During the pollutant degradation, 1 mL samples were collected every 30 minutes. These samples were then filtered (using PVDF syringe filter) into 1.5 mL HPLC amber glass vials which were stored in the freezer overnight ready for the LC-UV analysis in Singleton Campus the next day.

2.5.7.1 Recovery Percentages

All standards and samples were required to be filtered to prevent any blockages in the column of the LC-UV. To help determine the recovery percentage of the pollutant when passed through the filter then the percentage yield formula was utilised. Percentage yield is the ratio between the amount of pollutant collected after and before filter and it is calculated as follows:

$$\text{recovery \%} = \frac{\text{concentration of pollutant after filtering}}{\text{concentration of pollutant before filtering}} \times 100 \quad (\text{Equation 2.14})$$

2.5.7.2 Calculation of Pollutant Degradation

To help calculate pollutant degradation, then it was necessary to run a calibration curve every time the samples were run on the LC-UV. Using the results from the calibration curve then the real concentrations were calculated for the pollutant in the samples utilising Eq 2.9 which allows pollutant degradation to be calculated.

$$\text{pollutant degradation} = \frac{C_i - C_c}{C_i} \times 100 \quad (\text{Equation 2.15})$$

where: C_i = initial concentration

C_c = current concentration

2.5.8 Reactive Species Identification

The PEC process generates several reactive species which have high oxidising properties which can degrade pollutants in water. There are several reactive species which can be produced they are hydroxyl radicals ($\bullet\text{OH}$) and active chlorine (Cl_2 , HClO , OCl^-). While hydrogen peroxide can also be produced due to some side reactions in the anodic compartment.

2.5.8.1 Hydroxyl Radical ($\bullet\text{OH}$) Quantification

There are several methods which can be utilised for the quantification $\bullet\text{OH}$ which involve emission spectroscopy, laser induced fluorescence, electron spin resonance, spin trap and chemical probes [9]. However due to its previous success in measuring the hydroxyl radical produced by a photocatalyst then the method chosen was one utilised by Sebastien J. De-Nasri et al [9]. It involved the utilisation of coumarin as the chemical probe which when degraded by $\bullet\text{OH}$ produces a florescent compound umbelliferone [9]. The coumarin can be measured by UV-Vis spectrometer while the umbelliferone is measured by photoluminescence (PL) spectrometer.

Before the $\bullet\text{OH}$ quantification experiment was able to be conducted then a calibration graph for coumarin and umbelliferone needed to be established. As mentioned, the coumarin concentration would be measured by the UV-Vis spectrometer (Perkin Elmer 9 Lambda) with a scan rate 240 nm/min and range of 250 – 500 nm. The calibration standards ranged from 5 μM to 100 μM . While the umbelliferone would be measured by photoluminescence (PL) spectrometer (Edinburgh Instruments, FS5 Spectrofluorometer) with the calibration standards ranging from 0.2 μM to 10 μM . The excitation wavelength was set to 332 nm (slit width 0.7 nm) and the emission wavelength range was set to 380 nm to 600 nm (slit width 0.7 nm).

The $\bullet\text{OH}$ quantification experiment method involved utilising the two compartment PEC cell (Nafion membrane) with the $2\text{WO}_3/1\text{BiVO}_4$ as the working electrode and the Ag/AgCl as the reference electrode in the anodic side with a Pt wire as the counter electrode in the cathodic side. The anodic side contained 100 μM of coumarin in 1 M NaCl while pure 1 M NaCl was in the cathodic side. The experiment was run utilising the Zahner potentiostat with an applied

potential of 1.2 V and 1 Sun of solar light for 1 hour after the 30 minutes in the dark while continuously being stirred magnetically. Samples were collected every 10 minutes for the UV-Vis spectrometer and PL spectrometer. The UV-Vis and PL spectrometer were ran the same as the settings utilised for the calibration. The degradation percentage of coumarin was calculated by determining the real concentrations utilising the calibration graph and Eq 2.9. Then utilising the real concentrations and Eq 2.15 then the degradation percentage was established. While the Eq 2.9 would have been utilised to calculate to the umbelliferone from the analyte's response and the calibration graph. Due to the results showing the quantification experiment was not adequate for this system then this experiment was only conducted once.

2.5.8.2 Hydrogen Peroxide (H_2O_2)

Hydrogen peroxide (H_2O_2) was measured due to the potential of it being produced as a side product. To help indicate how much H_2O_2 is present during the pollutant degradation then Quantofix 1138902 Peroxide Test Stick were utilised. This allowed the H_2O_2 to be measured by dipping the stick into the solution of the anodic compartment every 30 minutes for 5 seconds. Then comparing the stick to the chart to help determine an approximation of the concentration of H_2O_2 .

2.5.8.3 Active Chlorine (Cl_2 , $HClO$, ClO^-)

Active chlorine has been reported to be produced when utilising NaCl as the supporting electrolyte (Eq 1.14 – 1.18 in Chapter 1) [10, 11]. Therefore, it has been assumed in this study that they are produced. Monitoring the pH enables the determination of which active chlorine species are dominant. As active chlorine production is pH dependent hence this would be utilised to help indicate which active chlorine is present and could be responsible for pollutant degradation [11]. As Cl_2 is the dominant species for $pH < 3.3$, but $HClO$ starts to be dominate from $3.3 < pH < 7.5$ while OCl^- becomes the only active chlorine >7.5 [11].

The pH was determined by utilising a pH meter (Orion Star A211, Thermo Scientific) and was conducted by placing the pH probe in the solution of the anodic compartment before and after the PEC experiment. The pH probe was immersed in the solution until the pH was stable and recorded.

2.5.9 By-Product Identification

To identify the by-products, present in the solution then the liquid chromatography coupled with a mass spectrometer (LC-MS) were utilised. It works by the LC helping to separate the

compounds in the sample, so they enter the MS separately. This is achieved by utilising a reverse-phase column that contains a non-polar stationary phase while a polar mobile phase is utilised to help the sample travel down the column. As the Agilent 1200 LC-UV system (utilised for quantifying pollutant degradation) was very successful in separating all the compounds in the samples collected from the pollutant degradation experiments then this was the LC system utilised for the LC-MS. The difference was that the outlet line was then attached to the inlet of the MS. In terms of MS there were several available however only one type of MS which was able to identify the ibuprofen standard which was the Waters Xevo TQ-S. The MS is broken into three main components which are the ionisation, mass analyser and detector. The ionisation section utilises electrospray ionisation (ESI) to produce gaseous ions from the compounds in the samples introduced by the inlets. The gaseous ions are then analysed by the quadrupole mass analyser which enables the separation of the ions depending on their m/z values. These ions then get detected by the detector which produces a signal for a mass spectrum.

2.5.9.1 Sample Preparation

Sample preparation for the LC-MS was the same as for the LC-UV analysis however the filtered samples from the pollutant degradation experiments were reduced to a concentration of 10 $\mu\text{g/mL}$ and 50 $\mu\text{g/mL}$ by diluting with ACN/0.1% Formic Acid in water (50/50). The only samples which were analysed were the samples collected from the ibuprofen degradation experiments.

2.5.9.2 LC Method

There was no need to develop a LC method as the LC-UV method developed previously showed significant separation of the compounds in the degradation samples. However, it was found that when developing the LC-MS method, the injection volume needed to be increased to 20 μL .

Table 2.20 - The method utilised for the LC part of the LCMS.

HPLC Settings			
Column	Xselect C-18 column (2.1 mm x 100 mm)		
Flowrate (mL/min)	0.250		
Injection Volume (µL)	20		
UV Detection Wavelength (nm)	265		
Gradient Pumping	Time (mins)	0.1% Formic Acid in Water	100% Acetonitrile
	0	75	25
	1	75	25
	17	0	100
	24	0	100
	25	75	25
	35	75	24

2.5.9.3 MS Method

The MS settings followed the recommended method provided by the MS's operating manual when the inlet flowrate was 0.250 mL/min. This allowed the inlet to be turned completely into a gaseous sample. It was also established that during the method development the electrospray mode had to be positive to ensure ibuprofen could be identified.

Table 2.21 - The method utilised for the MS part of the LCMS.

MS Setting	
Electrospray mode	Positive
Capillary (kV)	3.50
Cone (V)	5
Desolvation Temperature (°C)	500
Desolvation Gas Flowrate (L/hr)	600
Cone Gas Flowrate (L/hr)	150
Mass Scan Range	50 - 500
Sample Concentration (ug/mL)	10

2.5.9.4 Fragmentation in MS

Running a mass scan can help identify the m/z values for all the compounds present in the sample. However, these values cannot be utilised to identify the compounds as several different compounds could have the same m/z values. Therefore, fragmentation can be utilised to help break the ionised compounds into smaller product ions by utilising a cone energy specified by the user. These product ions go through the mass analyser and are identified by the detector which produces a fragmentation pattern. These fragmentation patterns then display all m/z values corresponding to the product ions which could be produced by the breakdown of the original compound. The success of the fragmentation relies heavily on the collision energy

utilised for each of the compound, as this controls how much the compound is broken down. Too low of an energy result in insufficient breakdown of the compound, while too high of an energy, results in complete breakdown but with less fragmentation. The first and successful fragmentation is outlined below:

Table 2.22 - The collision energies chosen for the fragmentation of the by-product compounds.

LC-MS Method	Table 2.18 and 2.19	
Fragmentation Method		
Compound <i>m/z</i>	First Collision Energy (eV)	Optimised Collision Energy (eV)
251	+30	n/a
239	+30	+25
223	+30	+30
221	+30	+30
177	+30	+30

2.6 Hydrogen Production

The GC utilised for the hydrogen production analysis was provided by the Dr. Mortiz Group in the Chemistry Department in Singleton Campus of Swansea University. The GC utilised was Shimadzu Nexis GC-2030 with a barrier-discharge ionisation detector (BID) and a molecular sieve column with an internal diameter of 530 μm and a length of 30 m. The capillary column temperature was set to 140 $^{\circ}\text{C}$ with the BID set to 250 $^{\circ}\text{C}$. The run time of the injection method was 5 minutes, programmed with an auto-injection time after 2 minutes and a backflash at 2.29 minutes to avoid moisture and CO_2 to be injected into the column. The gas samples were carried by the purge gas (nitrogen, BOC) via mass flow chamber (Bronkhorst) to the injection port of the GC, the gas mixture (sample and purge gas) is then carried through the GC column to the detector by the carrier gas (helium, BOC). The H_2 evolution rates were determined from the concentration of H_2 measured from the gas mixture and the gas flowrate (10 mL/min).

All the hydrogen production experiments were conducted in the two compartment PEC cell with the $2\text{WO}_3/1\text{BiVO}_4$ photoanode and Ag/AgCl reference electrode in the anodic side (where pollutant degradation occurs), while the Pt mesh counter electrode was in the cathodic side with a sealed lid that had an inlet and outlet line for the nitrogen gas and GC, respectively. The light illumination was provided by a solar light simulator (Thermo Oriel 92194-1000) equipped with an AM 1.5G filter (Newport) with 1 sun light intensity. While the applied potential was provided by the EmStat 3+ Potentiostat (PalmSens). The cathodic side was purged for 10

minutes with nitrogen (flowrate 20 mL/min) before the PEC experiment. The PEC experiment was conducted the same as previously mentioned but summarised in Table 2.23.

Table 2.23 - The PEC experiments ran for hydrogen production.

Anodic Compartment	0.5M NaCl	0.5M NaCl	100 µg/mL of ibuprofen in 0.5M NaCl	100 µg/mL of ibuprofen in 1M NaCl	50 µg/mL of BAC-C12 in 1M NaCl	50 µg/mL of S2NS in 1M NaCl
Cathodic Compartment	0.5M NaCl	0.5M NaCl	0.5M NaCl	1M NaCl	1M NaCl	1M NaCl
Applied Potential (V vs Ag/AgCl)	+1.2	+1.2	+1.2	+1.2	+1.2	+1.2
Time Ran in the Dark (minutes)	120	30	30	30	30	30
Light Used	0					
Light Intensity	0	1 Sun	1 Sun	1 Sun	1 Sun	1 Sun
Time Ran in the Light (minutes)	0	120	120	120	120	120

2.6 Bibliography

1. O'Regan, B. and M. Grätzel, *A low-cost, high-efficiency solar cell based on dye-sensitized colloidal TiO₂ films*. *Nature*, 1991. **353**(6346): p. 737-740.
2. Choi, J., et al., *WO₃/W:BiVO₄/BiVO₄ graded photoabsorber electrode for enhanced photoelectrocatalytic solar light driven water oxidation*. *Physical Chemistry Chemical Physics*, 2017. **19**(6): p. 4648-4655.
3. Chatchai, P., et al., *Enhanced photoelectrocatalytic activity of FTO/WO₃/BiVO₄ electrode modified with gold nanoparticles for water oxidation under visible light irradiation*. *Electrochimica Acta*, 2010. **55**(3): p. 592-596.
4. Su, J., et al., *Nanostructured WO₃/BiVO₄ Heterojunction Films for Efficient Photoelectrochemical Water Splitting*. *Nano Letters*, 2011. **11**(5): p. 1928-1933.
5. Bernhardsgrütter, D. and M.M. Schmid, *Modeling of Intensity-Modulated Photocurrent/Photovoltage Spectroscopy: Effect of Mobile Ions on the Dynamic Response of Perovskite Solar Cells*. *The Journal of Physical Chemistry C*, 2019. **123**(50): p. 30077-30087.
6. Harrick Scientific Products, I., *What is Kubelka-Munk*, in *FAQs*, H.S. Products, Editor.: <https://harricksci.com/faqs/>.
7. Titus, D., E. James Jebaseelan Samuel, and S.M. Roopan, *Chapter 12 - Nanoparticle characterization techniques*, in *Green Synthesis, Characterization and Applications of Nanoparticles*, A.K. Shukla and S. Iravani, Editors. 2019, Elsevier. p. 303-319.
8. James N Miller, J.C.M., *Statistics and Chemometrics for Analytical Chemistry*. Vol. Six. 2010, Essex: Pearson Education Limited.
9. De-Nasri, S.J., et al., *Quantification of hydroxyl radicals in photocatalysis and acoustic cavitation: Utility of coumarin as a chemical probe*. *Chemical Engineering Journal*, 2021. **420**: p. 127560.
10. Xiao, S., et al., *Enhanced photoelectrocatalytic degradation of ammonia by in situ photoelectrogenerated active chlorine on TiO₂ nanotube electrodes*. *Journal of Environmental Sciences*, 2016. **50**: p. 103-108.
11. Zaroni, M.V.B., et al., *Photoelectrocatalytic Production of Active Chlorine on Nanocrystalline Titanium Dioxide Thin-Film Electrodes*. *Environmental Science & Technology*, 2004. **38**(11): p. 3203-3208.

Chapter 3 : Photoanode Development

3.1 Introduction

The aim of this chapter is to synthesise a $\text{WO}_3/\text{BiVO}_4$ photoanode which resembles a porous nanocrystalline structure that can produce a high photocurrent. This chapter will also investigate how altering the WO_3 and BiVO_4 thickness effects its performance and what is the optimum thickness for this study. The final part of this chapter will establish how the operating parameters of the PEC system can impact on the photocurrent production.

3.2 Results and Discussion

3.2.1 Preparing the Primary Semiconductor WO_3

It was decided that WO_3 would be the primary semiconductor for the heterostructure photoanode configuration. This is due to several reasons, such as narrow bandgap energy, high abundance (in the earth), highly tuneable configuration, high stability in moderate pH, excellent electrical conductivity, good hole diffusion length (~ 150 nm) and good electron transport ($12 \text{ cm}^2\text{V}^{-1}\text{s}^{-1}$) [1-3]. However currently many methods involve complicated routes or hazardous chemicals, making them less than ideal for upscaling in industry. Therefore, a simple method was utilised (described in section 2.4) to create two different types of WO_3 pastes, which had different ethyl cellulose amounts. Ethyl cellulose is utilised as an eco-friendly binder for producing mesoporous metal oxide electrodes for dye-sensitised solar cells or photoanodes [4]. A binder is necessary to ensure the photoanodes were crack-free and the film thickness could be controlled [4]. The benefit of using a binder is that during the sintering process, the binder combusts, thus creating a porous surface [4]. Therefore, it is necessary to determine the optimal amount of ethyl cellulose that would create a high porosity for effective photodegradation but not too high that it causes any naked sites of conducting substrate to be exposed to the electrolyte. This would cause photoelectrons from the semiconductor to leak or back travel from the FTO substrate to the electrolyte, thus reducing the charge collection rate at the FTO substrate. To determine the optimal binder concentration, two types of pastes were synthesised. Paste 1 had a lower ethyl cellulose content (15 g of 10% ethyl cellulose solution), while Paste 2 had a higher ethyl cellulose content (30 g of 10% ethyl cellulose solution). It would be assumed that Paste 2 should obtain the better photocurrent production due to the higher porosity facilitating a higher amount of water splitting reaction [5].

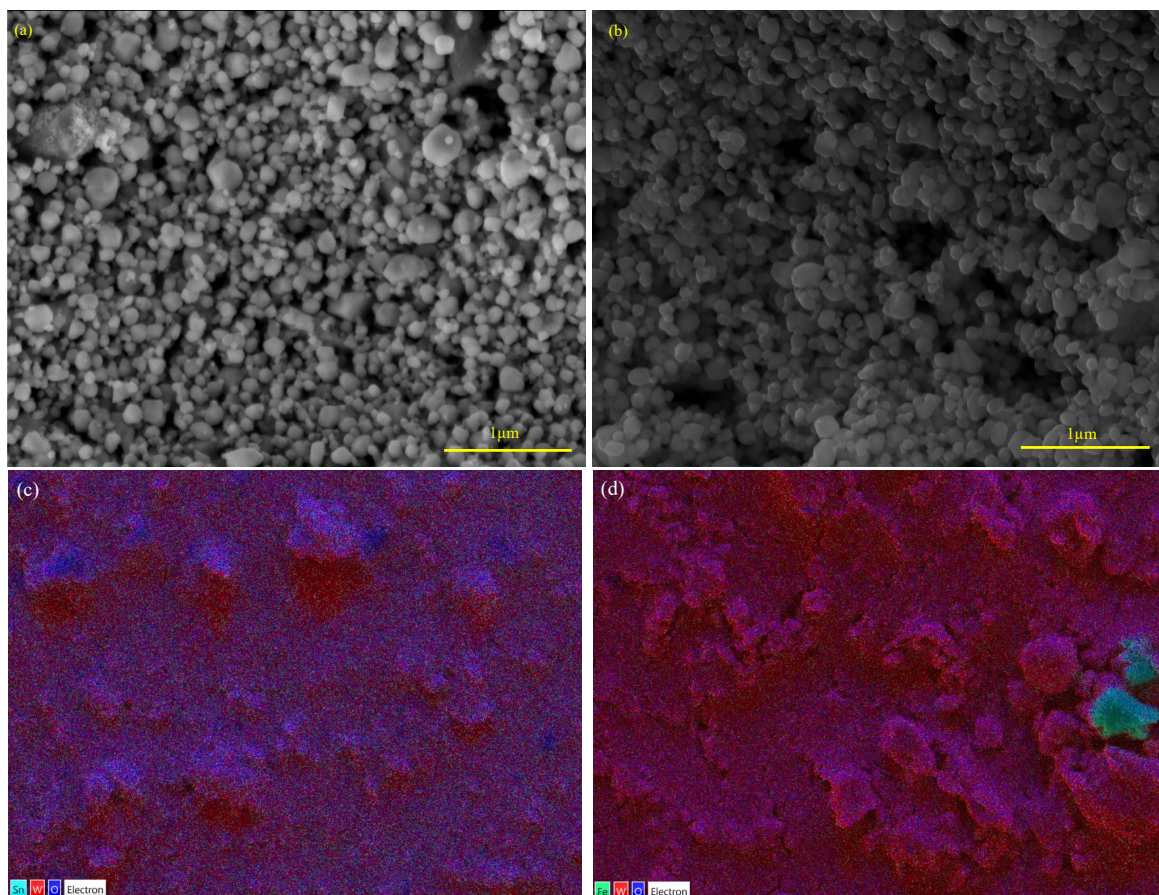


Figure 3.1 – SEM images for WO_3 film fabricated using (a) Paste 1, (b) Paste 2, EDS analysis of (c) Paste 1 and (d) Paste 2.

The surface morphology and porous distribution was determined by utilising scanning electron microscopy (SEM). The SEM analysis (Figure 3.1(a) and 3.1(b)) confirmed that both pastes were successful in creating a porous structure as both images show particles with grain sizes between 66.7 and 333.3 nm. This indicates that varying the ethyl cellulose amount does not significantly affect the grain size. However, the EDS analysis (Figure 3.1(c) and 3.1(d)) did show that the ethyl cellulose content in Paste 1 was not sufficient to bind the WO_3 nanoparticles onto the FTO substrate. Indicated by figure 3.1(c) showing exposure of Sn which is an element present in FTO substrates, thus verifying that the WO_3 paste does not completely cover the FTO substrate. However, for Paste 2 Sn was absent thus demonstrating that the ethyl cellulose content was an appropriate amount for WO_3 to completely cover the FTO substrate.

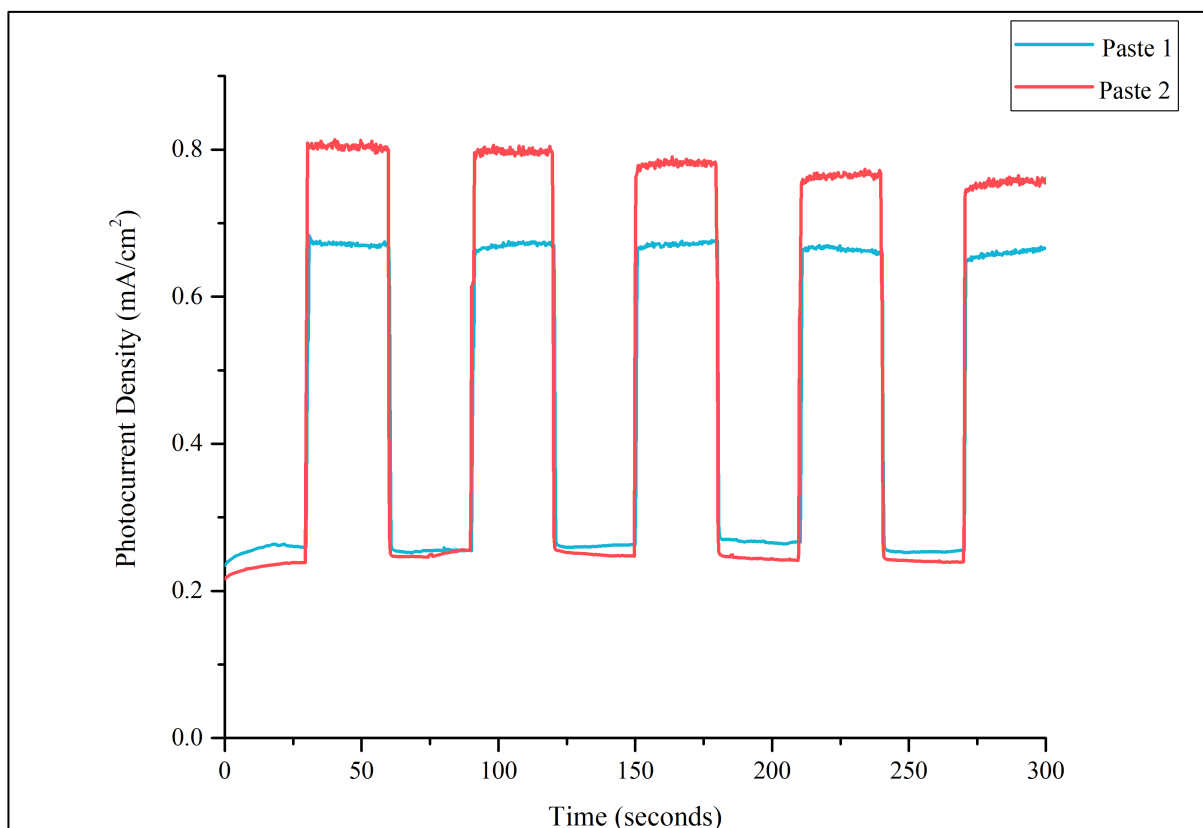


Figure 3.2 - The chronoamperometry results for Paste 1 and Paste 2, the experiment was run by utilising 2 layer pristine WO_3 as the working electrode, Pt wire as the counter electrode, Ag/AgCl as reference electrode, +1.2 V (vs Ag/AgCl) potential, 0.5 M NaCl electrolyte and a chopped light (30 seconds on/off) with a solar light intensity of 1 Sun.

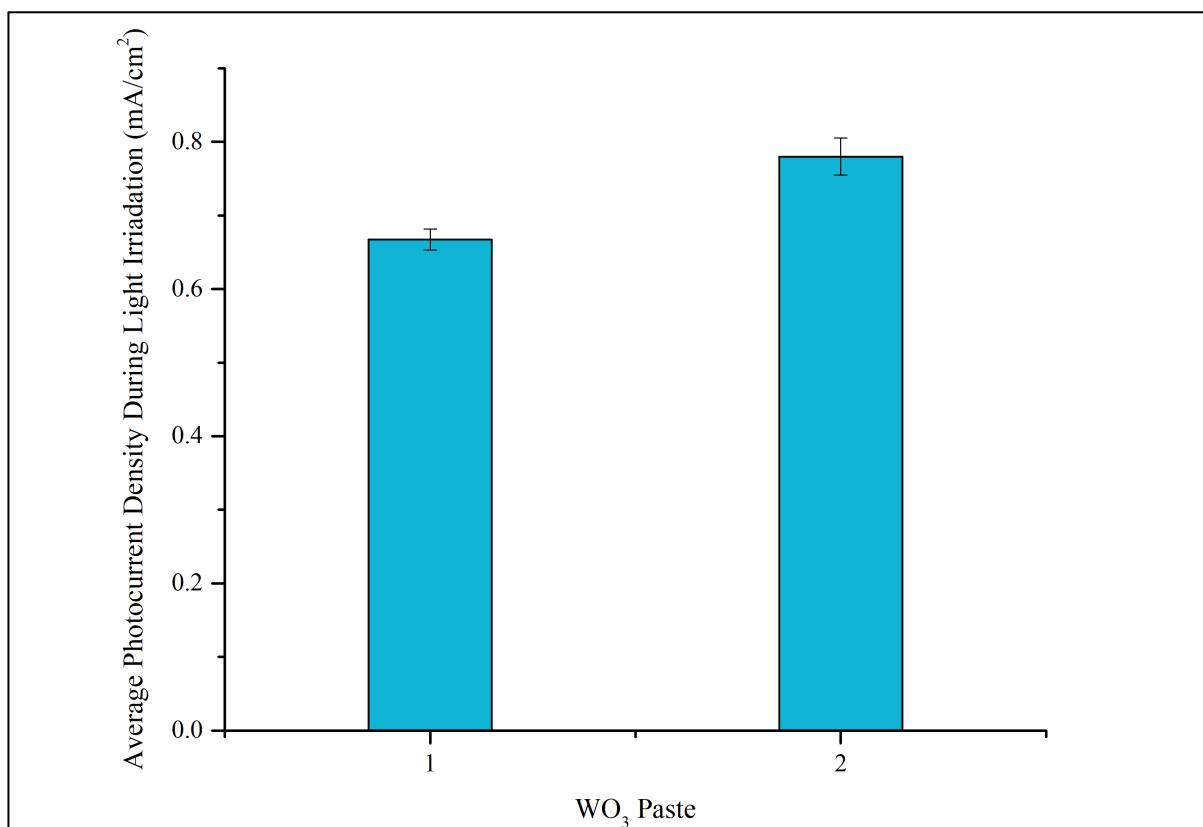


Figure 3.3 - A plot displaying the average photocurrent density produced for each WO_3 paste type.

To further assess the influence of the ethyl cellulose concentration on the WO_3 photoanodes, then it was necessary to establish the photoelectrochemical performance of each paste. Figures 3.2 and 3.3 showed that Paste 2 obtained a significantly higher photocurrent than Paste 1. Several reasons contribute to this. The first reason is that the higher concentration of ethyl cellulose helps achieve a homogenous paste. This results in WO_3 nanoparticles to uniformly spread over the FTO substrate thus avoiding naked sites. Therefore, no back electron flow from the FTO substrate to the electrolyte occurring thus a higher photocurrent production. Usually having a higher binder concentration can result in higher porosity thus more active sites for photon absorption [6]. However, the SEM images did not support this, but it did confirm that Paste 2 synthesised a porous WO_3 structure. Based on these results it was decided to utilise Paste 2 for manufacturing the WO_3 layer.

3.2.2 Crystalline Structure Analysis of WO_3

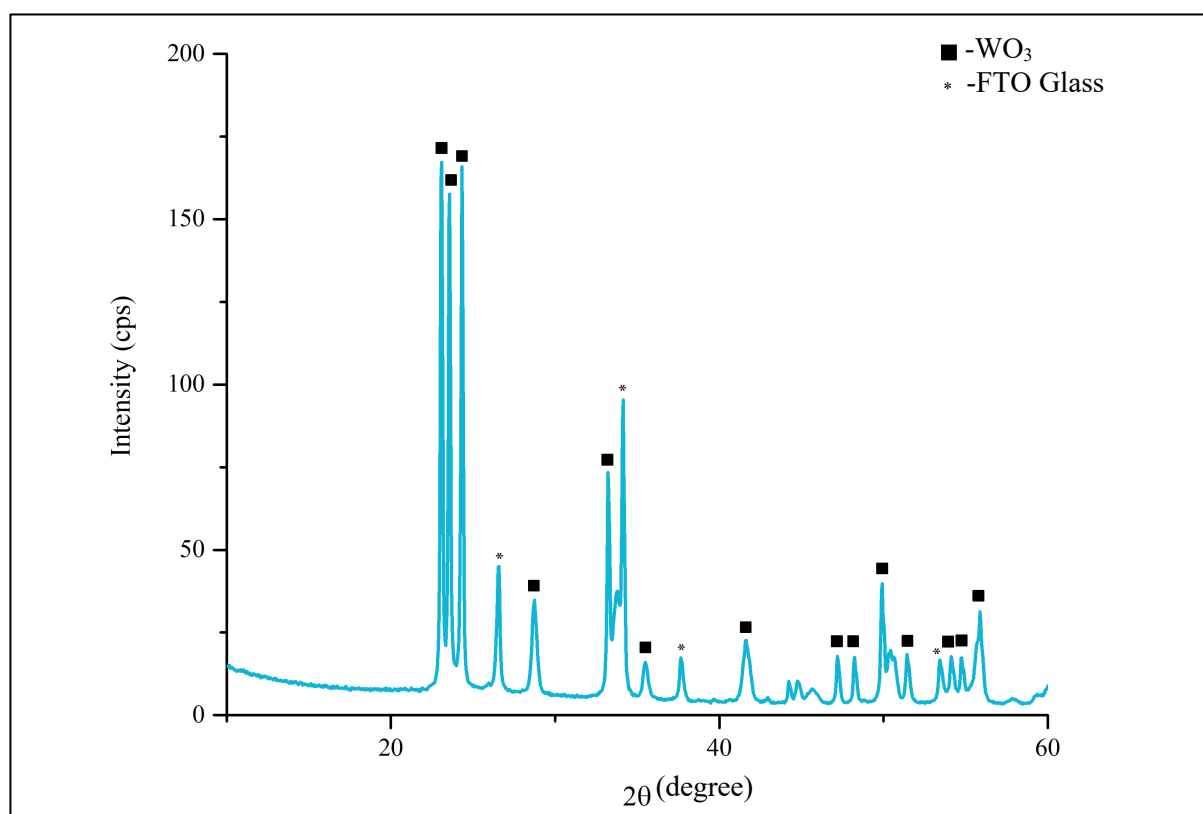


Figure 3.4 - The XRD diffraction pattern of pristine WO_3 .

The crystallinity phase of a semiconductor is critical in governing its PEC performance. Therefore, it is vital to identify the crystallinity phase of the WO_3 photoanode to ensure it will achieve the highest photocurrent production. To help determine the crystalline structure of the

WO₃ photoanode then X-Ray Powder Diffraction (XRD) was utilised. The XRD analysis showed strong peaks at 23.1°, 23.6° and 24.1° which corresponds to the phases (002), (020) and (200), thus confirming that monoclinic WO₃ is present on the photoanode surface [2, 3, 7-9]. This was the aim as according to literature, the crystallinity phase which exhibits the highest photocatalytic activity and stability for WO₃ is the monoclinic phase [2, 3, 7]. This signifies that the method developed above created WO₃ photoanodes with high photoactivity capabilities. This was expected as the annealing temperature utilised was 450 °C which in literature has proven to produce monoclinic WO₃ [2].

3.2.3 Chemical Environment of WO₃

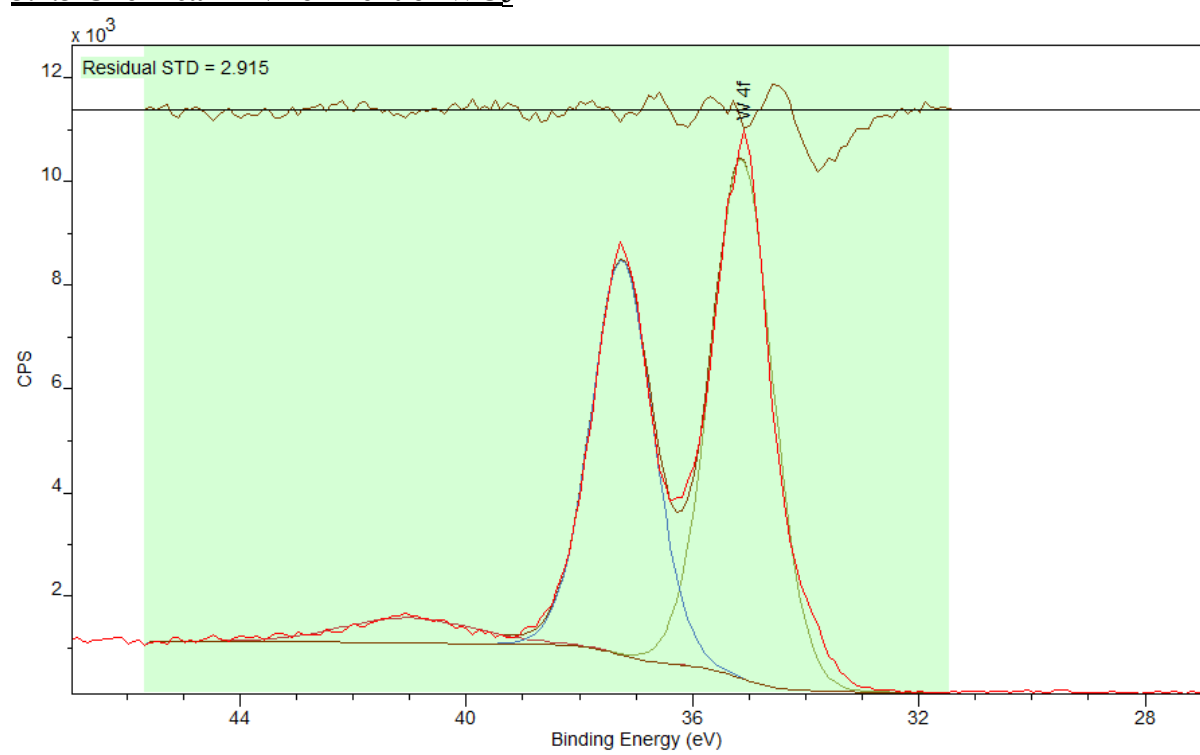


Figure 3.5 - The XPS core spectra results of pristine WO₃. The experimental results of W4f core spectra (red colour) are fitted with CasaXPS software.

The chemical environment of the WO₃ photoanode was studied utilising X-ray Photoelectron Spectroscopy (XPS). The XPS identifies the compound present on the surface as it can measure the elemental composition with the chemical and electronic state of the atoms. From Figure 3.5 peaks were established at binding energies of 35.18 and 37.29 eV which corresponds to W4f_{7/2} and W4f_{5/2}, respectively [10, 11]. These peaks confirm that W⁶⁺ is present on the surface of the photoanode, thus verifying WO₃ was present [10, 11]. Since WO₃ has been confirmed to be present on the photoanode then further characterization needs to be conducted to help explain its photocurrent production.

3.2.4 Optical Property of WO₃

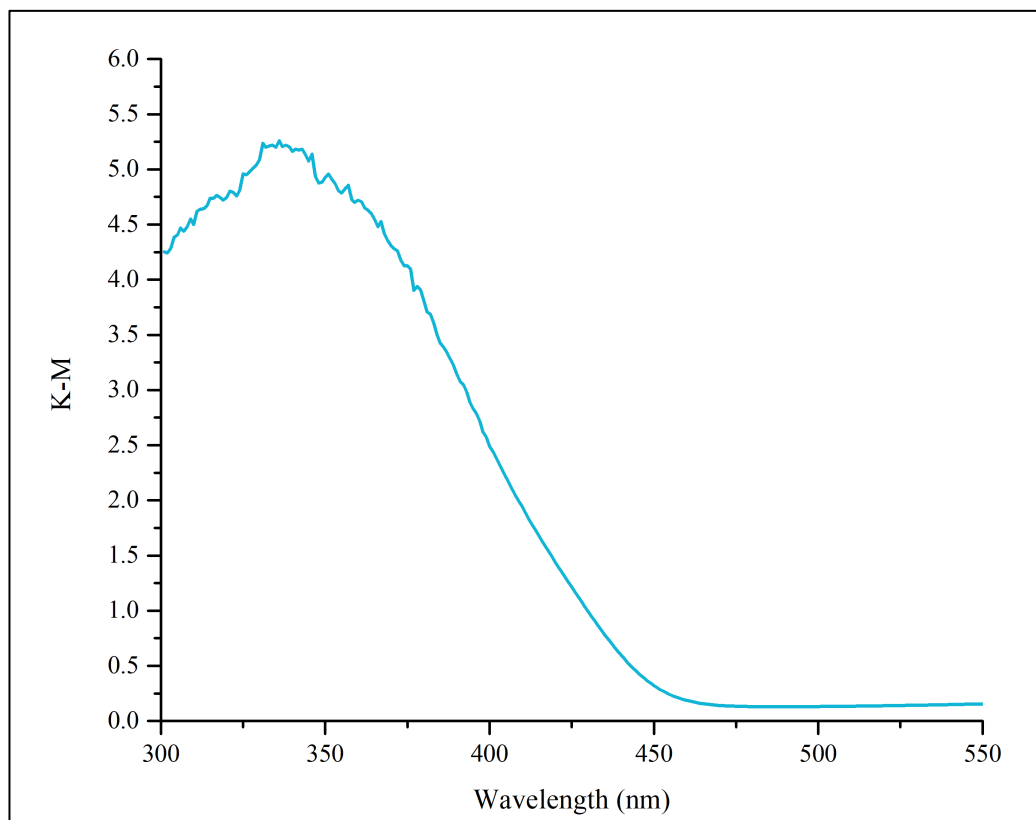


Figure 3.6 – The K-M spectra obtained for pristine WO₃.

To determine the optical properties of WO₃ photoanode than a DR-UV was utilised. This results in the reflectance to be measured and recorded. These reflectance values allow the Kubelka-Munk value to be calculated by utilising the equation below [12]:

$$F(R) = \frac{K}{s} = \frac{(1-R_{\infty})^2}{(2 \times R_{\infty})} \quad (\text{Equation 3.1})$$

Plotting the Kubelka-Munk value against the wavelength allows the wavelength absorption range to be determined as the Kubelka-Munk value represents the absorption and scattering coefficients of the photoanode. Figure 3.6 establishes the WO₃ photoanode can absorb wavelengths up to 450 nm. This is excellent as it translates to the synthesis WO₃ photoanode being a visible light absorbing photoanode. This confirms that the method developed for WO₃ was successful in creating a visible light absorbing photoanode. Thus, a higher number of photons are absorbed compared to TiO₂ photoanodes, which can only utilise wavelengths in the UV range.

Whilst it is important to know the wavelength absorption range it is equally important to calculate the bandgap. The band gap energy can be calculated using the Tauc plot with the Kubelka-Munk function [13].

The Tauc plot is based on the equation below:

$$(\alpha hv)^{\frac{1}{\gamma}} = A(hv - E_g) \quad (\text{Equation 3.2})$$

where:

α - absorption coefficient

h - Planck constant

ν - photon's frequency

γ - $\frac{1}{2}$ for direct or 2 for indirect transition band gaps

A - constant usually 1

E_g - bandgap energy

As K and S are the absorption and scattering coefficients respectively then the Kubelka-Munk function can be substituted into Eq 3.2 for α . While γ was equal to 2 for WO_3 and BiVO_4 as both have indirect bandgaps [14, 15]. Therefore, making the equation:

$$(F(R) \times hv)^{1/2} = (hv - E_g) \quad (\text{Equation 3.3})$$

Using this equation then a graph is plotted with $(F(R)hv)^{1/2}$ vs hv and a tangent line was utilised to determine the bandgap energy (Figure 3.6). From this the calculated bandgap was 2.6 eV. This is a narrow bandgap and is the reason why the synthesis WO_3 photoanode can absorb wavelengths up to 450 nm.

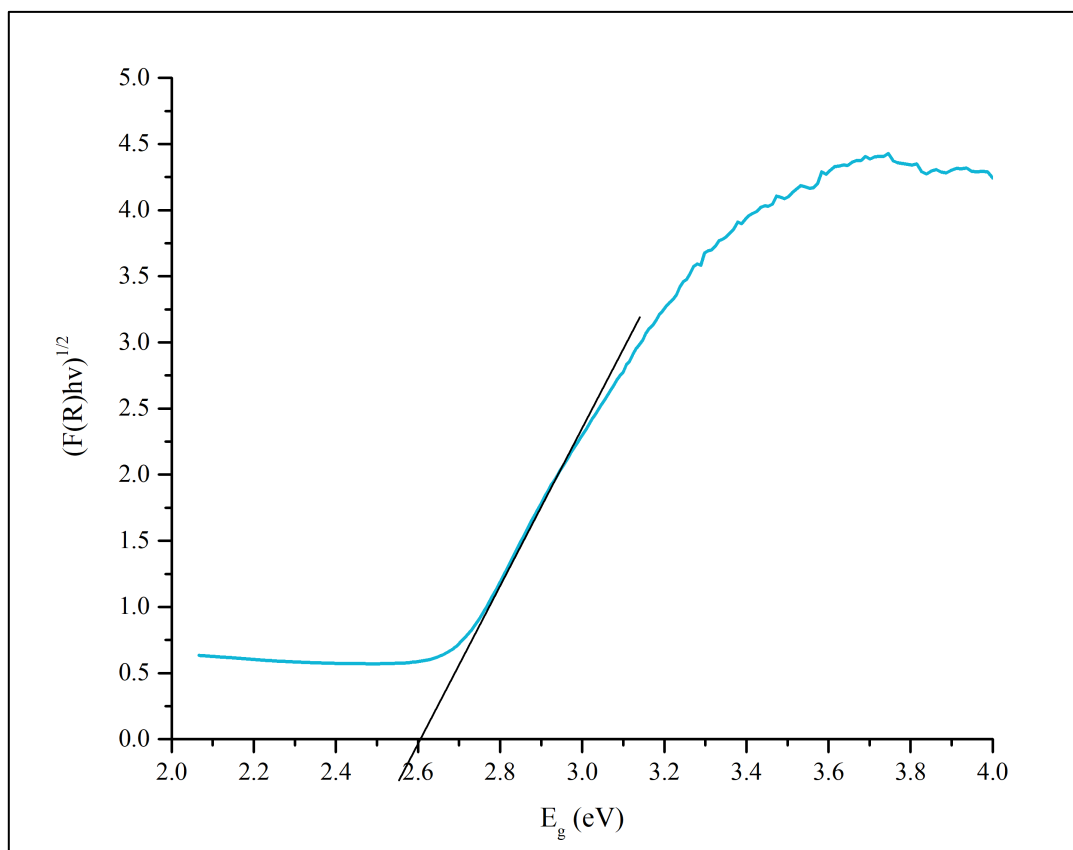


Figure 3.7 – The Tauc plot of WO_3 .

Whilst Figures 3.1 to 3.7 demonstrated that the WO_3 photoanodes synthesized exhibited properties which enable them to have high photoactivity. The photoelectrochemical study (Figures 3.2 and 3.3) demonstrated that the WO_3 photoanodes produced by Paste 2 were only able to generate a photocurrent of 0.8 mA/cm^2 at 1.2 V (vs Ag/AgCl). This is low but is expected for a pristine WO_3 photoanode as unfortunately pristine WO_3 photoanodes suffer from charge recombination, thus lower photocurrent production. This demonstrates that a heterostructure is necessary for achieving high photocurrents as it enables charge separation thus enabling more electrons to travel the counter electrode while more holes are available for pollutant degradation [3, 8, 16-19]. To make a successful heterojunction then $BiVO_4$ was the chosen semiconductor to couple with the developed WO_3 . However, before the heterojunction could be formed it was essential to find a successful method for manufacturing $BiVO_4$.

3.2.5 Preparation and Investigation of BiVO₄ Film

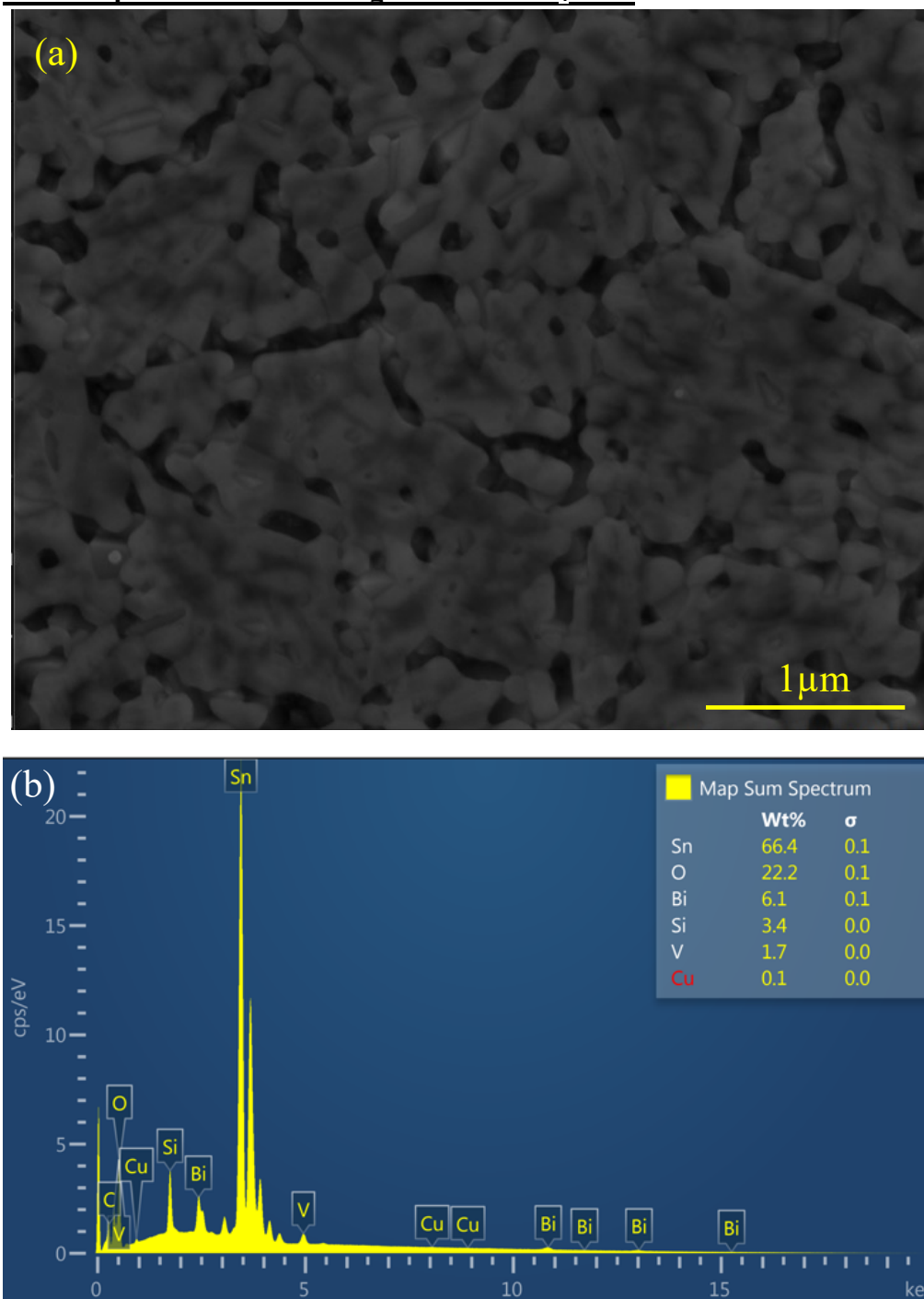


Figure 3.8 - Images obtained for thin film BiVO₄ during (a) SEM analysis and (b) EDS analysis.

The SEM analysis demonstrated that the BiVO₄ films have a morphology that contains a high pore network. Whilst the EDS analysis (Figure 3.8 (b)) confirms the presence of Bi, V and O species thus verifying that the method was successful in creating a BiVO₄ film. However, it also showed a high peak for “Sn” element, thus indicating the FTO substrate was exposed. This could be due to the porosity of the thin films exposing the FTO glass. This would mean that if

using the above method for pure BiVO_4 photoanodes then the photoanode must contain multiple layers of BiVO_4 to lower the exposure of the FTO glass.

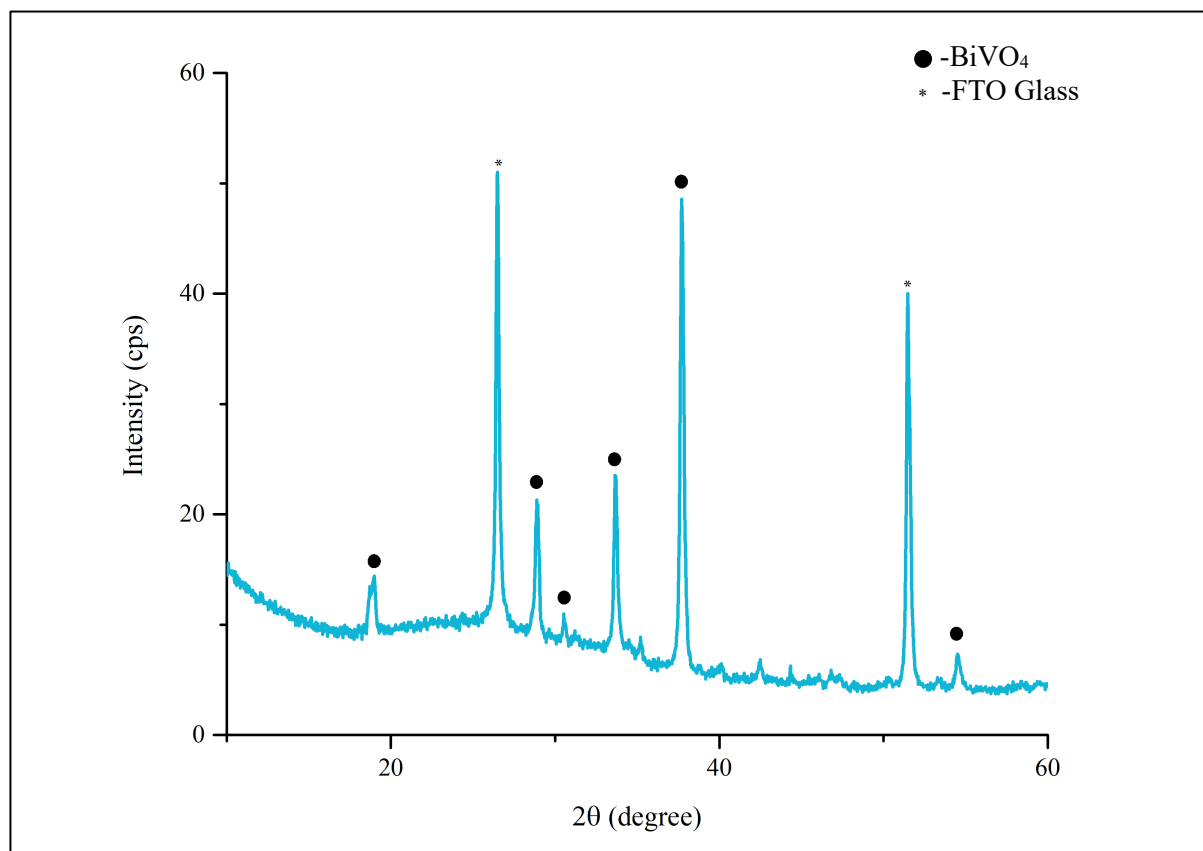


Figure 3.9 – The XRD diffraction pattern of pristine BiVO_4 .

Similarly, to WO_3 the crystallinity phases which demonstrates the highest photocatalytic activity for BiVO_4 was monoclinic [3, 7, 20]. The results from the XRD analysis (Figure 3.9) established peaks at 18.9° , 28.9° and 30.5° which are associated with diffraction facets of (101), (112) and (004) [20]. These diffraction peaks correspond to monoclinic BiVO_4 thus verifying that this method was very successful in producing high photoactivity BiVO_4 photoanodes [33].

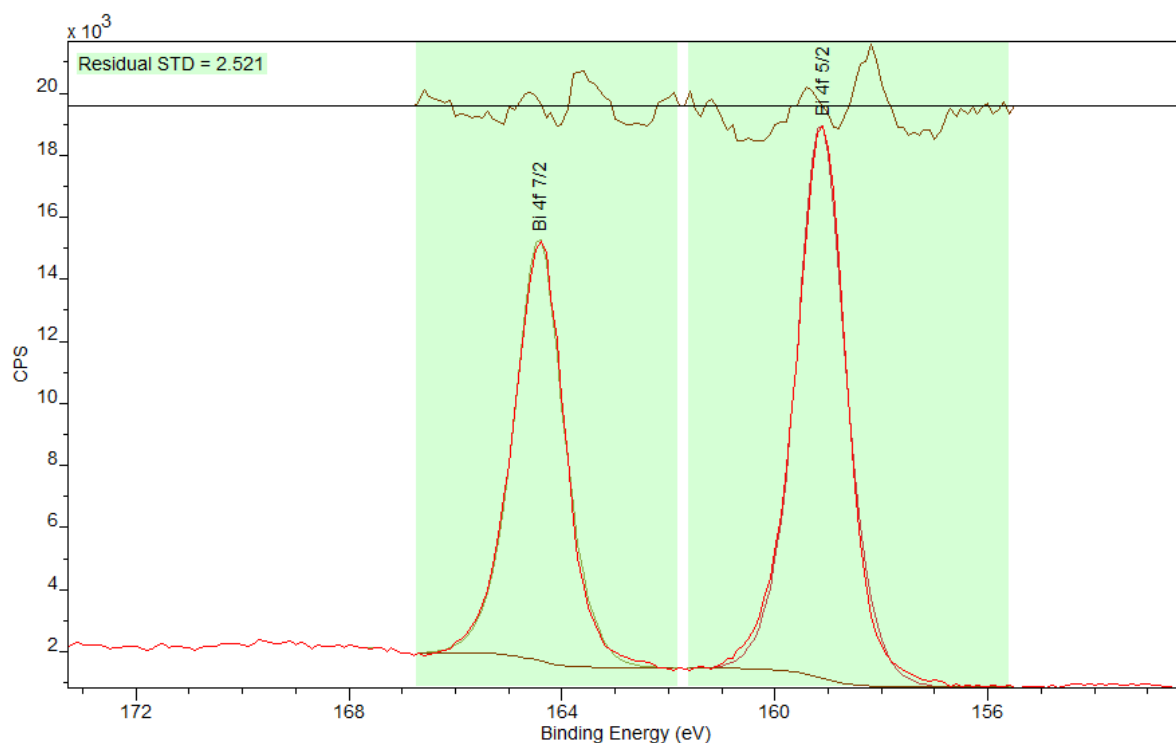


Figure 3.10 - The XPS obtained for pristine BiVO_4 focused on the $\text{Bi}4f$ signals. The experimental results of $\text{Bi}4f$ core spectra (red colour) are fitted with CasaXPS software.

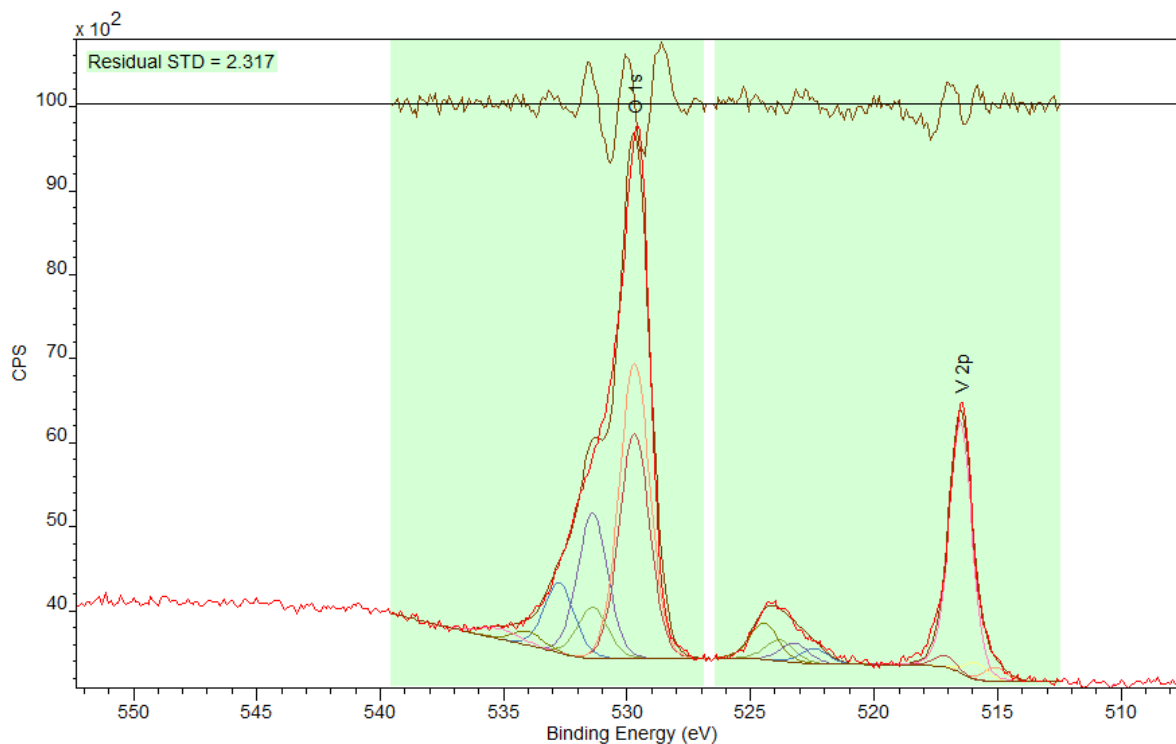


Figure 3.11 - The XPS obtained for pristine BiVO_4 focused on the $\text{O}1s$ and $\text{V}2p$ signals. The experimental results of $\text{O}1s$ and $\text{V}2p$ core spectra (red color) are fitted with CasaXPS software.

The XPS analysis confirmed the presence of BiVO_4 . Figure 3.10 identified two strong signals with binding energies of 159.16 eV and 164.45 eV. These correspond to $\text{Bi}4f_{7/2}$ and $\text{Bi}4f_{5/2}$ which verify that Bi^{3+} was present on the photoanode surface and is the element state in BiVO_4

[11]. While Figure 3.11 displays a peak at a binding energy of 516.5 eV that corresponds to $V2p_{3/2}$ which confirms that V^{5+} is present [11]. While the peak at 529.64 eV indicates that oxygen species in a metal oxide ($BiVO_4$) are present on the surface. There are multiple peaks in O1s which were theoretically fitted by utilising the XPS fitting software and taking references from the XPS knowledge base created by Thermo Fisher Scientific [21]. There are multiple peaks as not only is there oxygen associated with a metal oxide being present, but also oxygen associated with water and/or organic contamination, thus there will always be oxygen peaks when samples are exposed to the atmosphere [21]. These results verify that $BiVO_4$ was successfully synthesized [11].

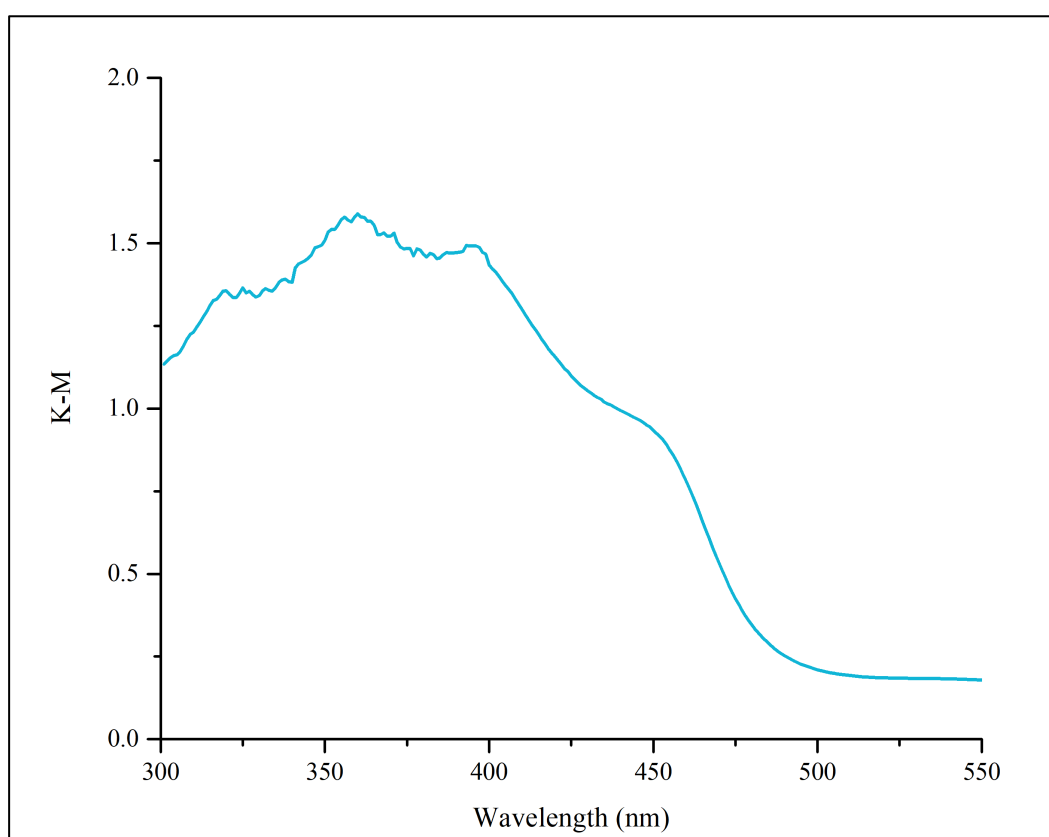


Figure 3.12 – The K-M spectra of pristine $BiVO_4$.

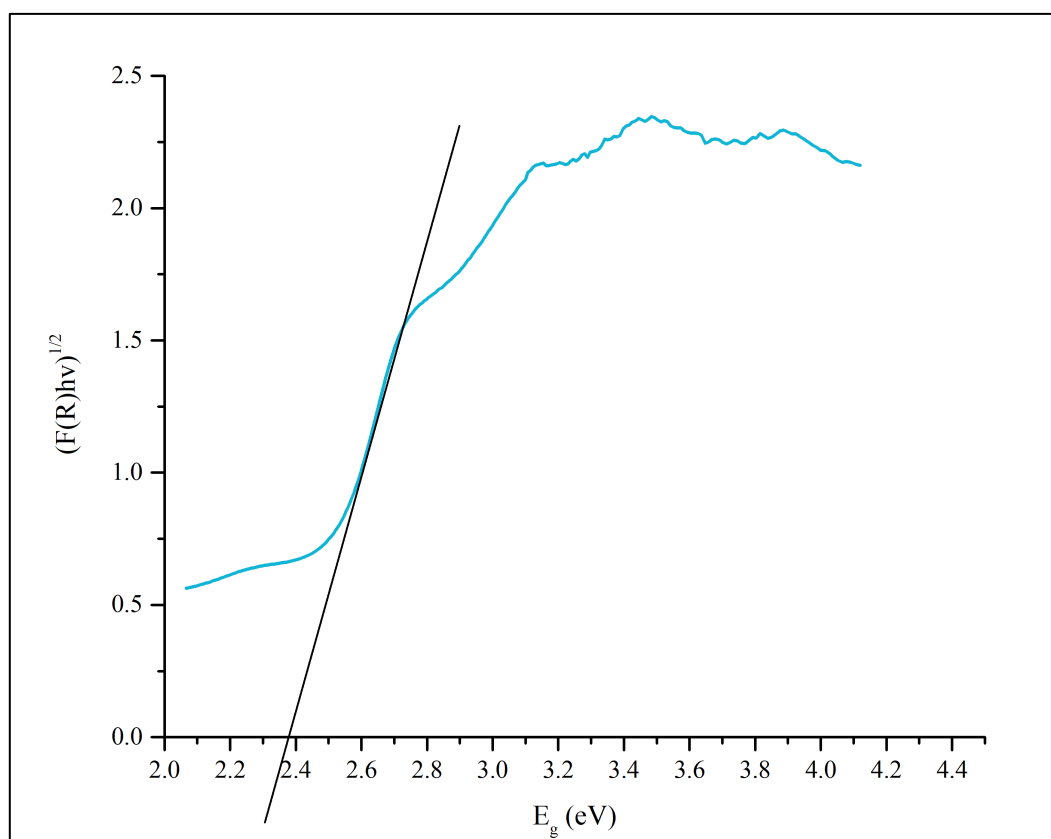


Figure 3.13 – The Tauc plot of BiVO₄.

The results from the DR UV-Vis analysis of pristine BiVO₄ (Figure 3.12) revealed that the band edge lies around 490 nm. This extended absorbance wavelength range is due to BiVO₄ having a narrower bandgap than WO₃ [22]. Utilising the Eq 3.1 – 3.3 and the plotted graph (Figure 3.13) the calculated bandgap of BiVO₄ was 2.4 eV which is significantly lower than WO₃ (2.6 eV). Therefore, coating WO₃ with BiVO₄ should extend the solar light absorbance from 450 nm to 490 nm. Thus, resulting in a higher number of photons being absorbed and producing more electron/hole pairs.

3.2.6 Creating a Heterostructure Metal Oxide Photoanode

To create WO₃/BiVO₄ photoanode then the pre-synthesised BiVO₄ solution was spin coated onto the 2 layered WO₃ electrode and annealed utilising the method for the pristine BiVO₄ photoanode.

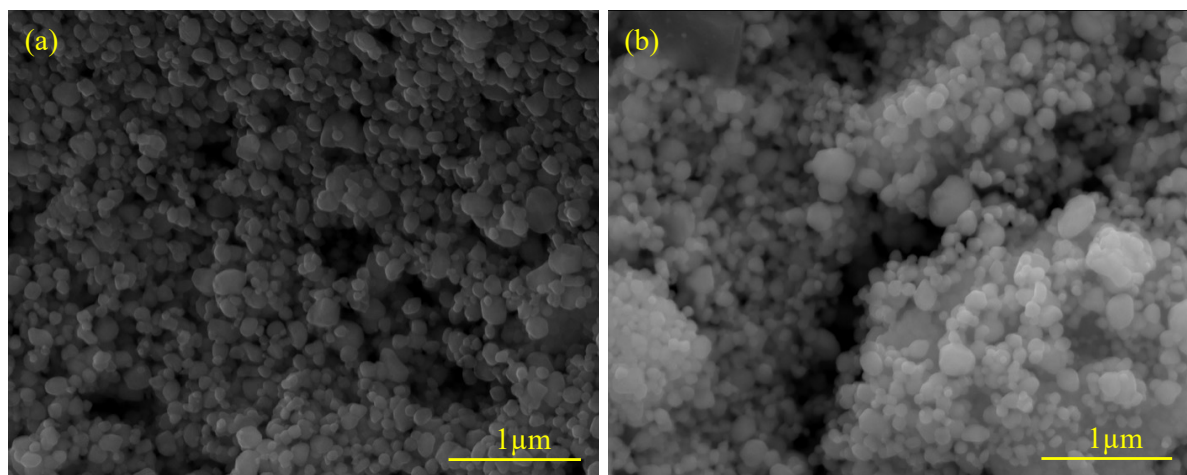
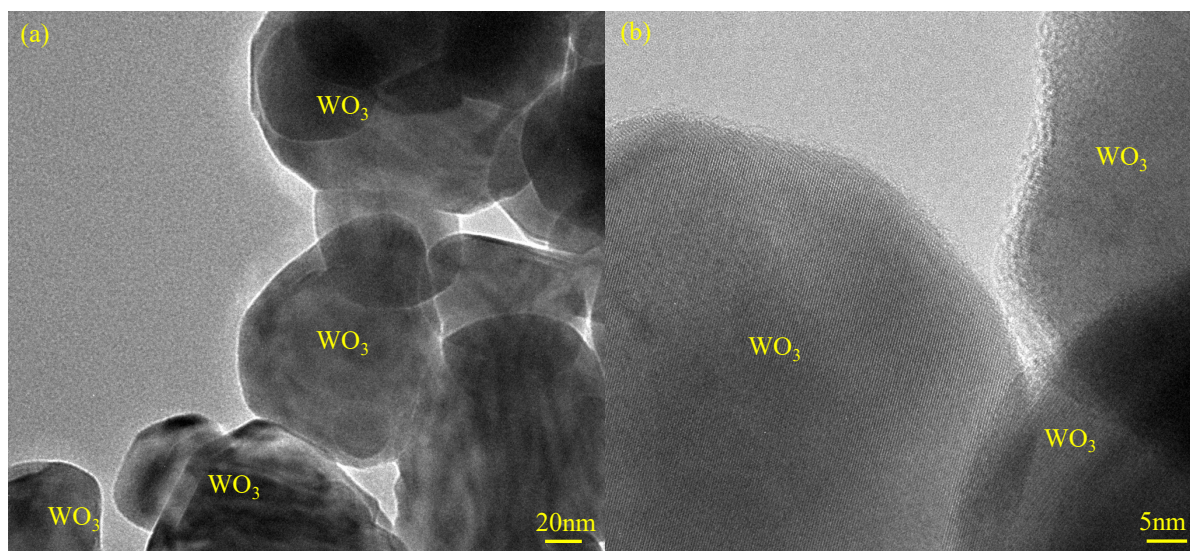


Figure 3.14 - The images obtained during the SEM analysis for (a) Pristine WO_3 and (b) $\text{WO}_3/\text{BiVO}_4$

The surface morphology of the synthesised $\text{WO}_3/\text{BiVO}_4$ photoanode was studied via SEM and HR-TEM. The Figures 3.14(a) and 3.14(b) show that adding the BiVO_4 layer did not greatly affect the porous structure as the images show that nanoparticles are still present on the photoanode surface without huge variation in grain size. This was because the BiVO_4 layer was discovered to be ultra-thin (3 nm - 12.5 nm) by the HR-TEM analysis (Figures 3.15 c-d). Hence, coating the WO_3 particles with a single layer would not significantly vary the nanoparticle size or cause any active sites to become block. It was necessary to create an ultra-thin layer of BiVO_4 because it has poor electron mobility, which means electrons take a long time to travel in the BiVO_4 layer. Consequently, if it is too thick then there is high probability of charge recombination.



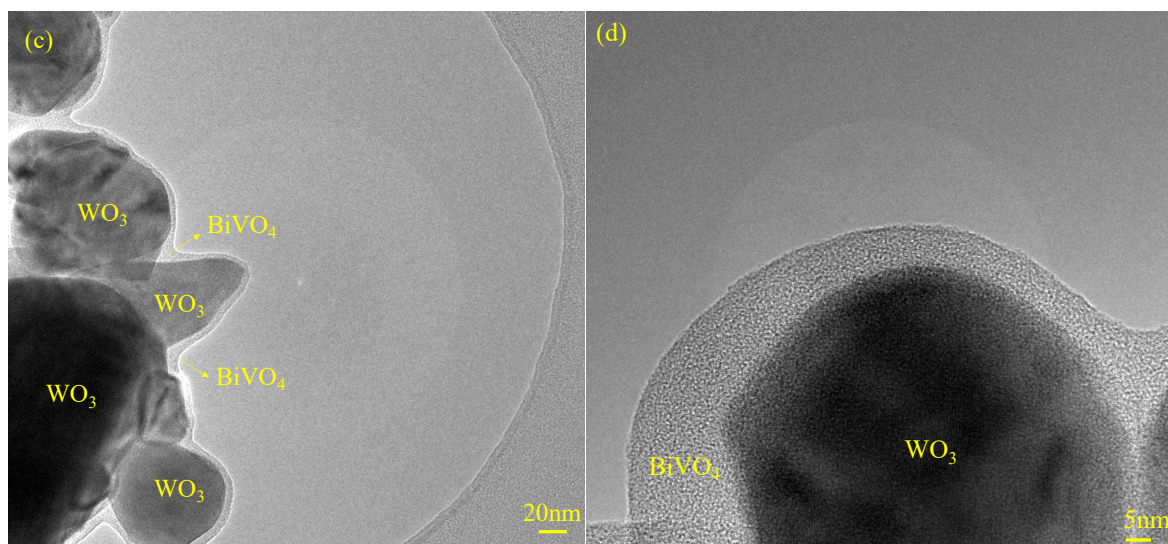


Figure 3.15 - HR-TEM analysis of (a-b) of pristine WO_3 and (c-d) of $WO_3/BiVO_4$ photoanodes.

3.2.7 Characterization of $WO_3/BiVO_4$

To ensure that the addition of $BiVO_4$ onto the WO_3 did not affect the crystallinity or chemical environment of the photoanode then it was essential to run characterise the $WO_3/BiVO_4$ photoanode by surface analytical tools (XRD and XPS).

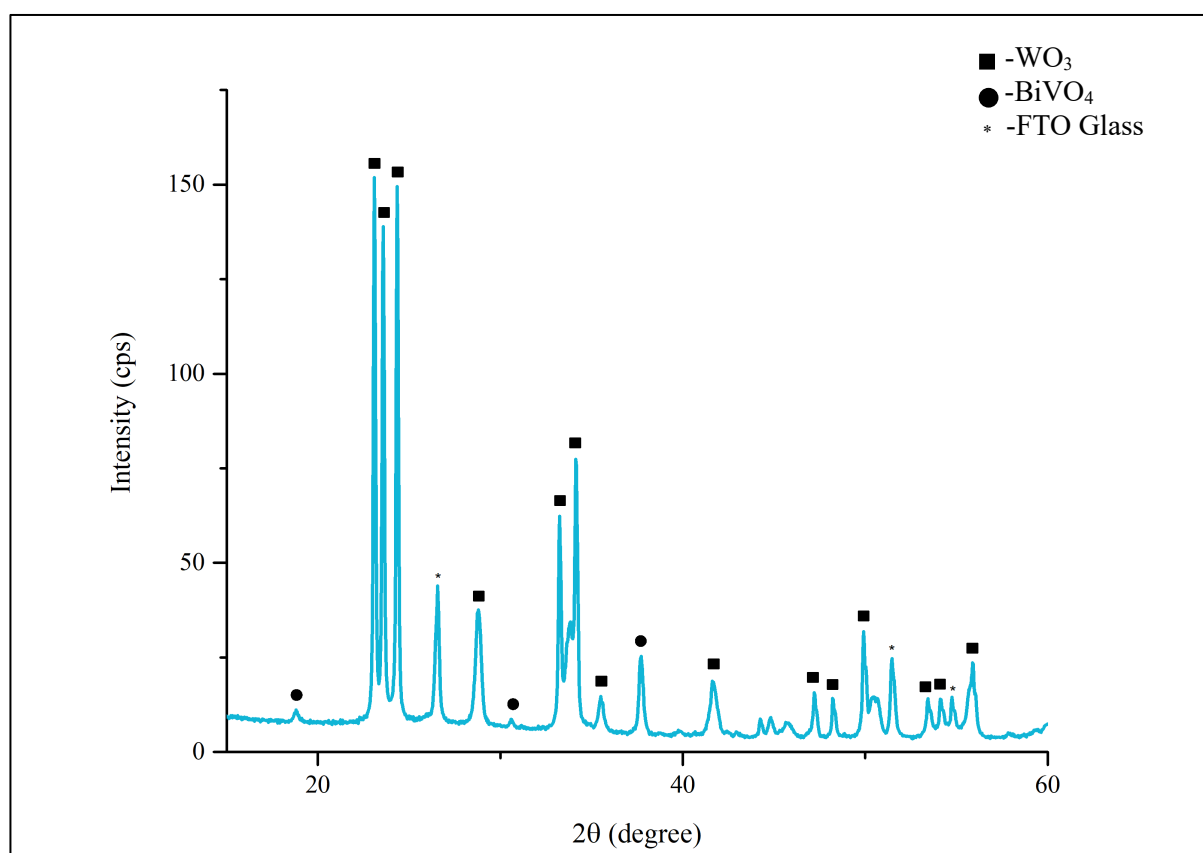


Figure 3.16 - The XRD diffraction pattern obtained for the synthesised $WO_3/BiVO_4$ photoanode.

As previously mentioned, it was important that the crystallinity phases of both WO_3 and BiVO_4 were monoclinic. The XRD analysis (Figure 3.16) of the synthesised $\text{WO}_3/\text{BiVO}_4$ established signals at 18.8° , 28.8° and 30.5° which were associated with the diffraction peaks of (101), (112) and (004) of BiVO_4 and signals at 23.1° , 23.6° , 24.3° which were associated with the diffraction peaks of (002), (020), (200) of WO_3 [2, 7, 11, 20]. These diffraction peaks verified that both monoclinic BiVO_4 and WO_3 were present in the synthesised $\text{WO}_3/\text{BiVO}_4$ and that the heterojunction did not affect the crystallinity.

The XPS was utilised to examine the chemical environment of $\text{WO}_3/\text{BiVO}_4$ heterostructure photoanode. It was essential to determine any metal ion diffusion or oxygen vacancies that could occur at the $\text{WO}_3/\text{BiVO}_4$ interface.

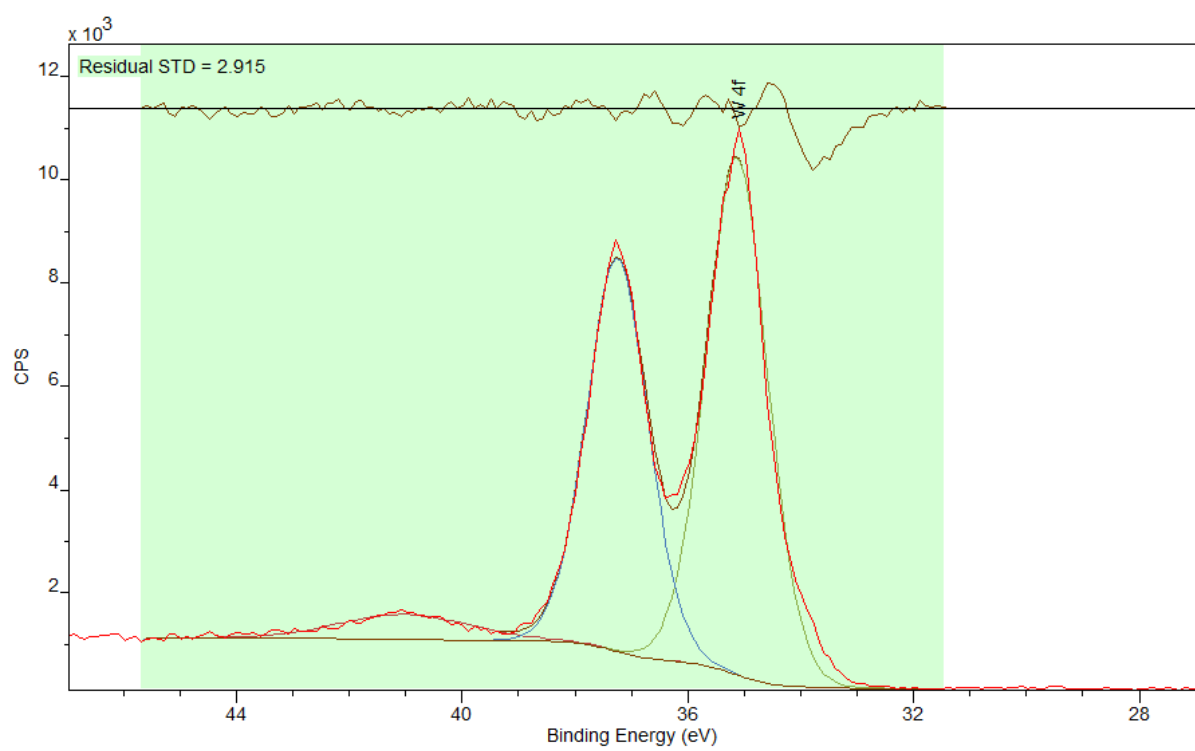


Figure 3.17 - The XPS spectra obtained for pristine WO_3 focused on W4f peaks. The experimental results of W4f core spectra (red colour) are fitted with CasaXPS software.

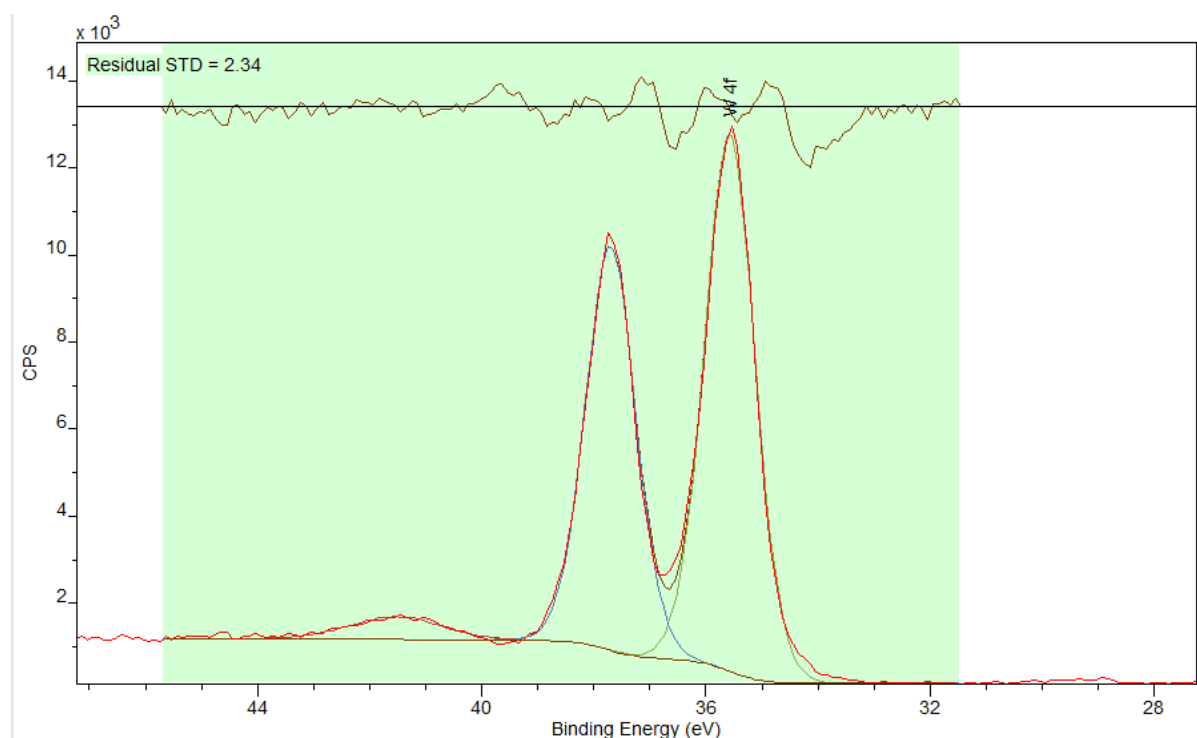


Figure 3.18 - The XPS spectra obtained for $WO_3/BiVO_4$ focused on $W4f$ peaks. The experimental results of $W4f$ core spectra (red colour) are fitted with CasaXPS software.

For both WO_3 and $WO_3/BiVO_4$ there were signals at 35.18 eV and 35.55 eV which are associated with $W4f_{5/2}$ for WO_3 and $WO_3/BiVO_4$, respectively [11, 23]. Whilst also having signals at 37.29 eV and 37.66 eV which are associated with $W4f_{7/2}$ for WO_3 and $WO_3/BiVO_4$ respectively [11, 23]. This verifies that both photoanodes contain W^{6+} which is part of WO_3 [11, 23]. There was a slight positive shift in the binding energies associated with W in $WO_3/BiVO_4$. A shift in binding energies usually suggests that there is a chemical shift due to the oxidation state of the atom or the physical environment changing. This would suggest that the W oxidation state in $WO_3/BiVO_4$ is higher than in WO_3 or that the chemical environment has changed. However, looking at literature for WO_3 , the $W4f_{5/2}$ and $W4f_{7/2}$ associated with W^{6+} have binding energies between 35.1-35.4 eV and 37.2-37.6 eV [11, 23, 24]. Therefore, this would suggest the oxidation state has not changed but instead adding the $BiVO_4$ changes the chemical environment causing this shift in binding energy.

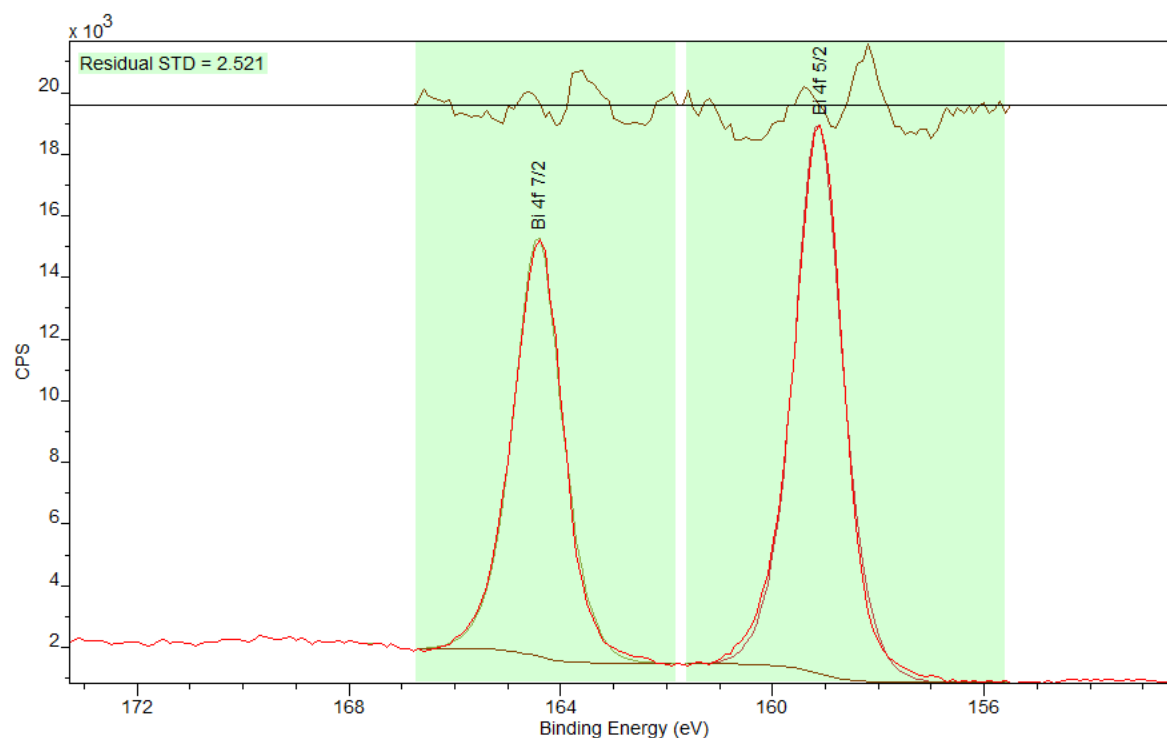


Figure 3.19 - The XPS spectra obtained for BiVO_4 focused on $\text{Bi}4f$ peaks. The experimental results of $\text{Bi}4f$ core spectra (red colour) are fitted with CasaXPS software.

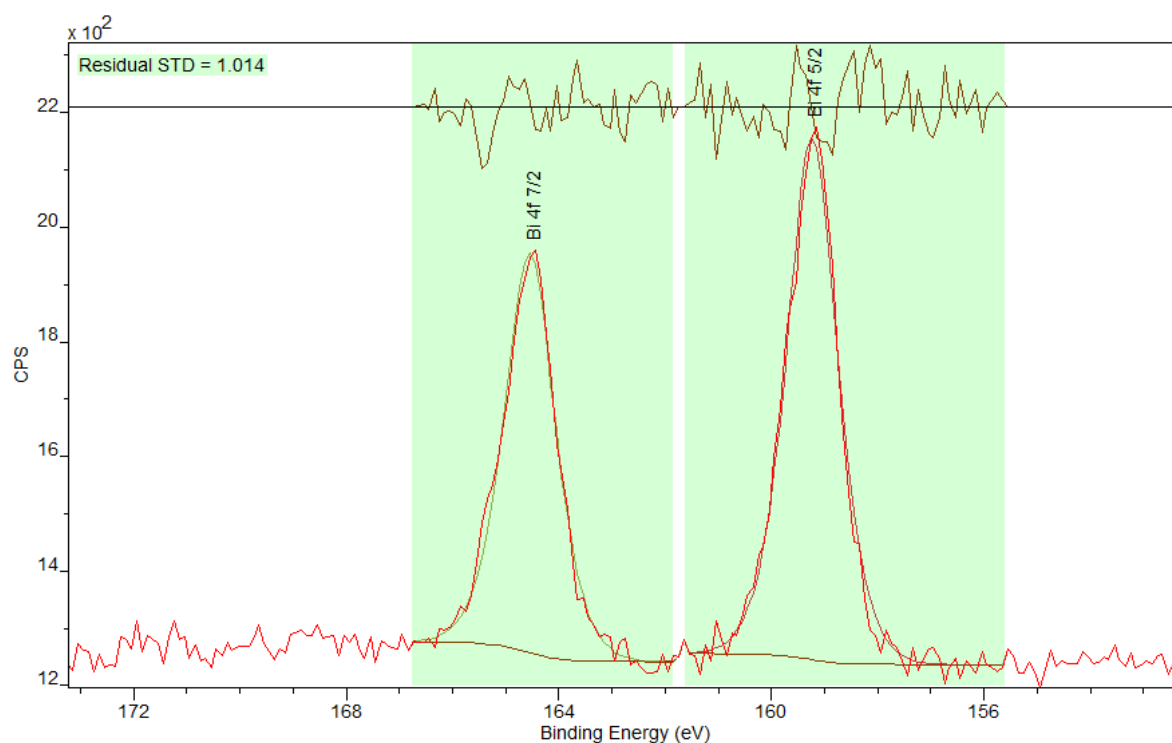


Figure 3.20 - The XPS spectra obtained for $\text{WO}_3/\text{BiVO}_4$ focused on $\text{Bi}4f$ peaks. The experimental results of $\text{Bi}4f$ core spectra (red colour) are fitted with CasaXPS software.

Again, both BiVO_4 and $\text{WO}_3/\text{BiVO}_4$ photoanodes exhibited peaks 159.16 eV and 159.21 eV (respectively) associated with $\text{Bi}4f_{5/2}$ [3]. As well as signals at 164.45 eV and 164.52 eV for

Bi4f_{5/2} [3]. This helps demonstrate that Bi³⁺ is present thus verifying that BiVO₄ was successfully synthesized for WO₃/BiVO₄ and did not cause the oxidation state of Bi to change.

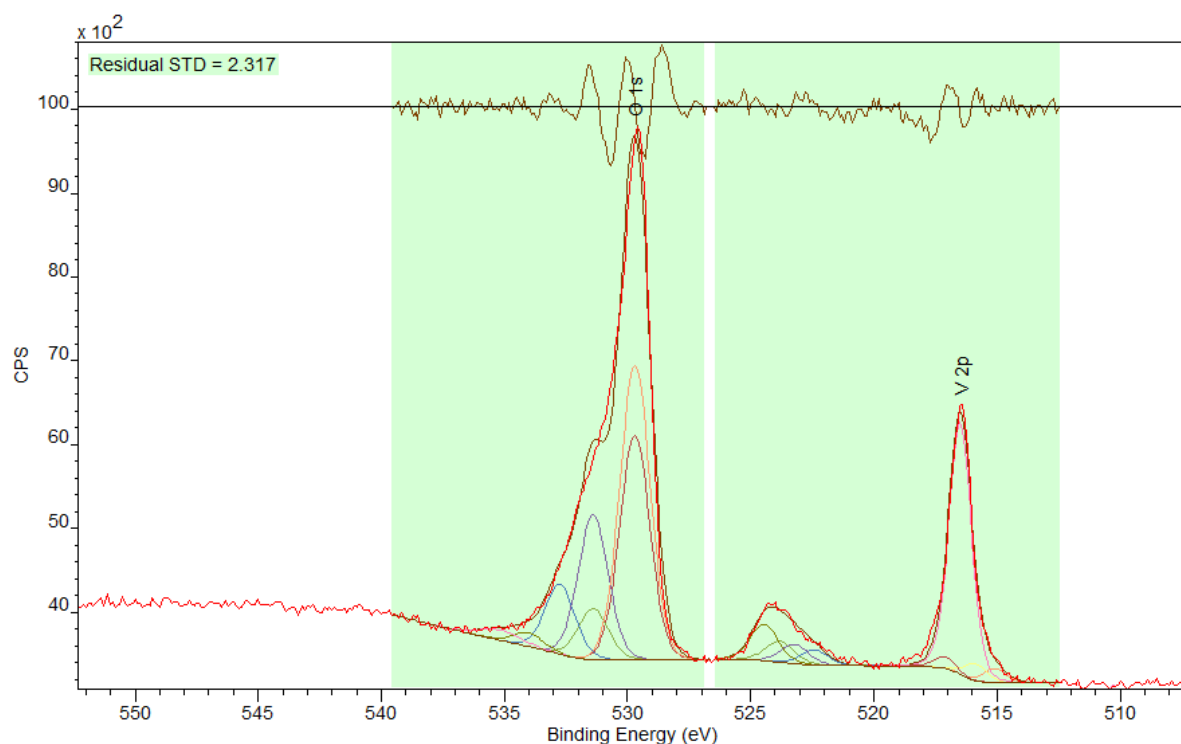


Figure 3.21 - The XPS spectra obtained for BiVO₄ focused on O1s and V2p peaks. The experimental results of O1s and V2p core spectra (red colour) are fitted with CasaXPS software.

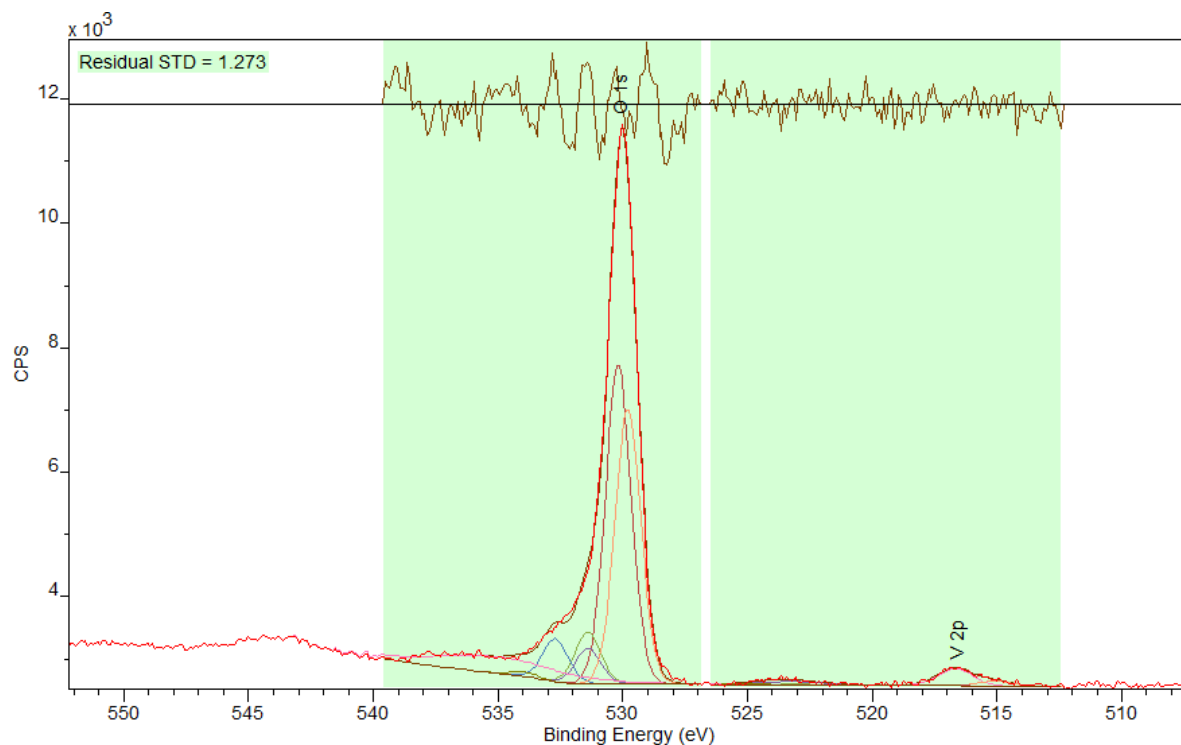


Figure 3.22 - The XPS spectra obtained for WO₃/BiVO₄ focused on O1s and V2p peaks. The experimental results of O1s and V2p core spectra (red colour) are fitted with CasaXPS software.

As previously mentioned BiVO_4 contains V^{5+} which is associated with $\text{V}2\text{p}_{3/2}$ [11]. As both the spectra show that pristine BiVO_4 and $\text{WO}_3/\text{BiVO}_4$ photoanodes had peaks at binding energies of 5.16.5 eV and 516.55 eV, respectively, then V^{5+} is present [11]. The $\text{V}2\text{p}$ peak in $\text{WO}_3/\text{BiVO}_4$ is much lower compared to the BiVO_4 as the $\text{O}1\text{s}$ peak is stronger due to the higher presence of oxygen associated with WO_3 and BiVO_4 . There was no shift to the binding energies of the $\text{O}1\text{s}$ associated with BiVO_4 peaks which would indicate that the heterojunction does not affect the oxygen absorption sites.

3.2.8 The Photoelectrochemical Activity of $\text{WO}_3/\text{BiVO}_4$

To assess the benefit of creating a heterostructure the photoelectrochemical activity and optical absorbance was assessed.

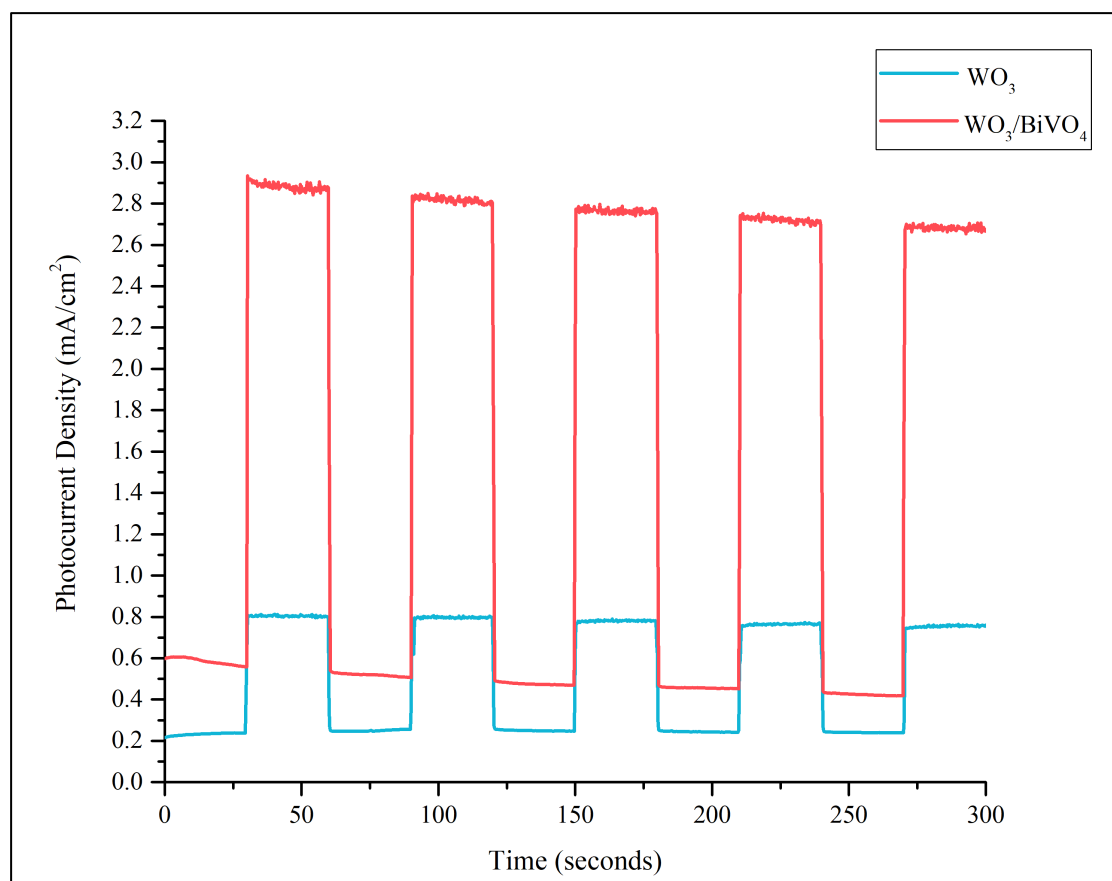


Figure 3.23 - A graph displaying the production of photocurrent by pristine WO_3 (2 layers) and $\text{WO}_3/\text{BiVO}_4$ (2 layers of WO_3 and 1 BiVO_4) with a chopped light (30 secs off/on for 5 minutes), 1.2 V applied potential and 0.5 M NaCl supporting electrolyte.

The photoelectrochemical analysis (Figure 3.23) established that adding the layer of BiVO_4 onto the WO_3 photoanode helped to increase the photocurrent density produced by 3.44-fold. There are several reasons creating this heterostructure resulted in an increase in photocurrent production, these are:

- The onset potential could shift lower thus a higher number of electrons are produced at lower potentials.
- The heterojunction helped achieve effective charge separation thus extending the electron's lifetime.
- The BiVO₄ helps to narrow the bandgap energy thus allowing a higher range of wavelengths to be absorbed.

To determine which of these reasons were truly responsible for this increase in performance then further investigations were conducted.

The onset potential was examined by linear sweep voltammetry (LSV) (Table 2.4) that generated a plot of photocurrent density produced as a function of the applied potential. The onset potential is the potential at which the photocurrent production increases significantly due to it going above the flat band potential.

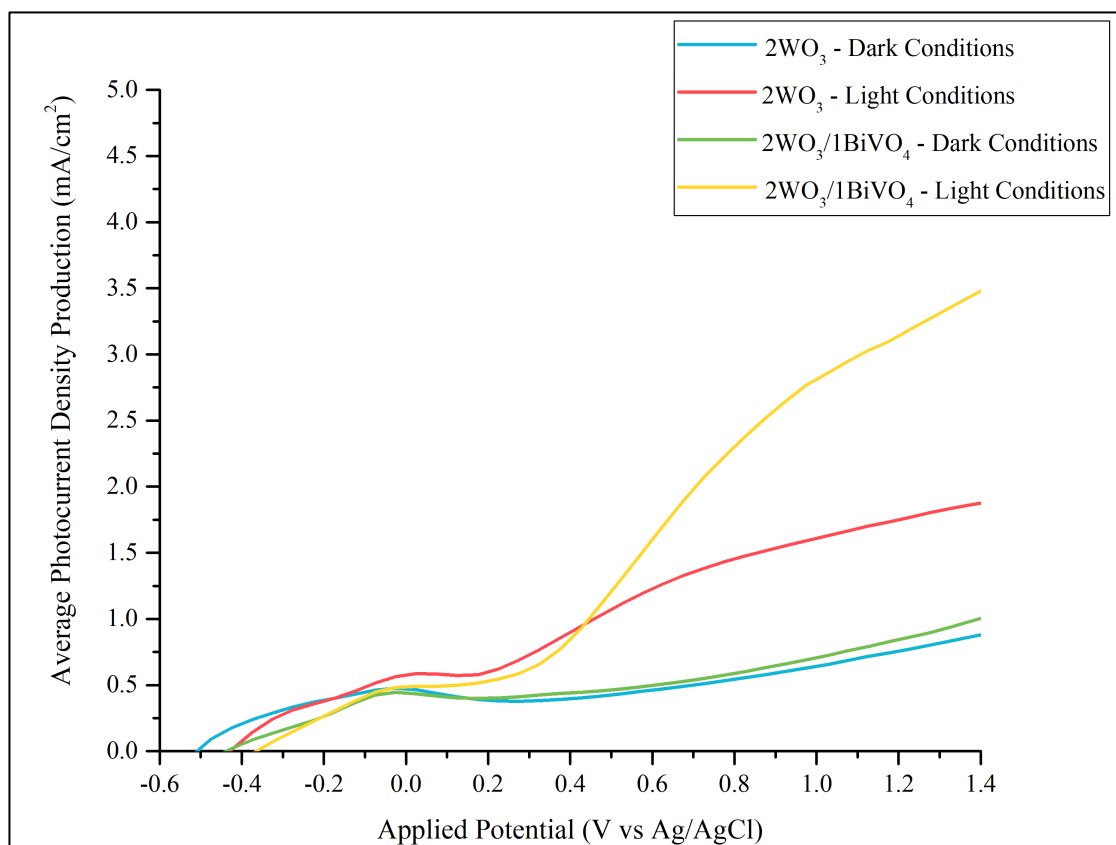


Figure 3.24 - The LSVs for Pristine WO₃ and WO₃/BiVO₄ the experiment details were that the electrolyte was 0.5M NaCl, 1 sun of solar light (when light was turned on), scan limit from -0.5 V to 1.5 V.

Unexpectedly it was established that the onset potential did not alter when adding the BiVO_4 layer onto the WO_3 photoanode. This confirmed that the onset potential was not responsible for the increase in photoactivity.

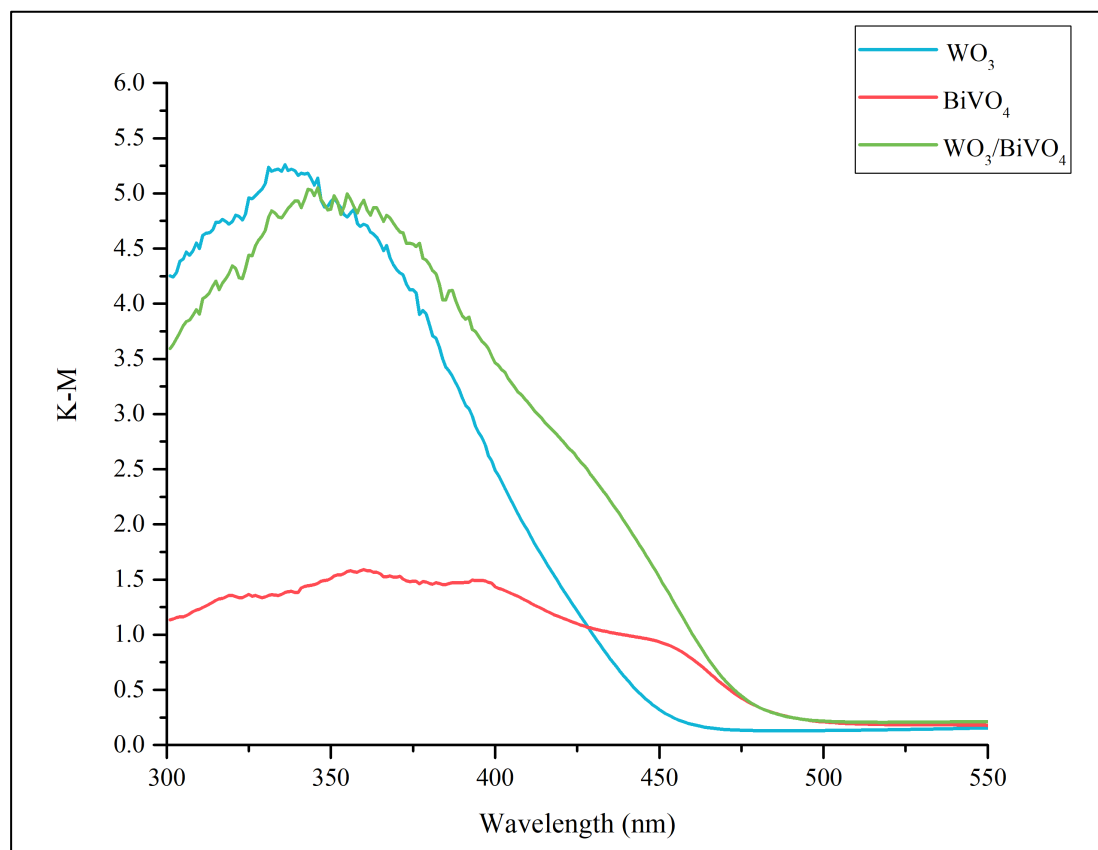


Figure 3.25 – The K-M spectra of (blue) WO_3 , (red) BiVO_4 and (green) $\text{WO}_3/\text{BiVO}_4$.

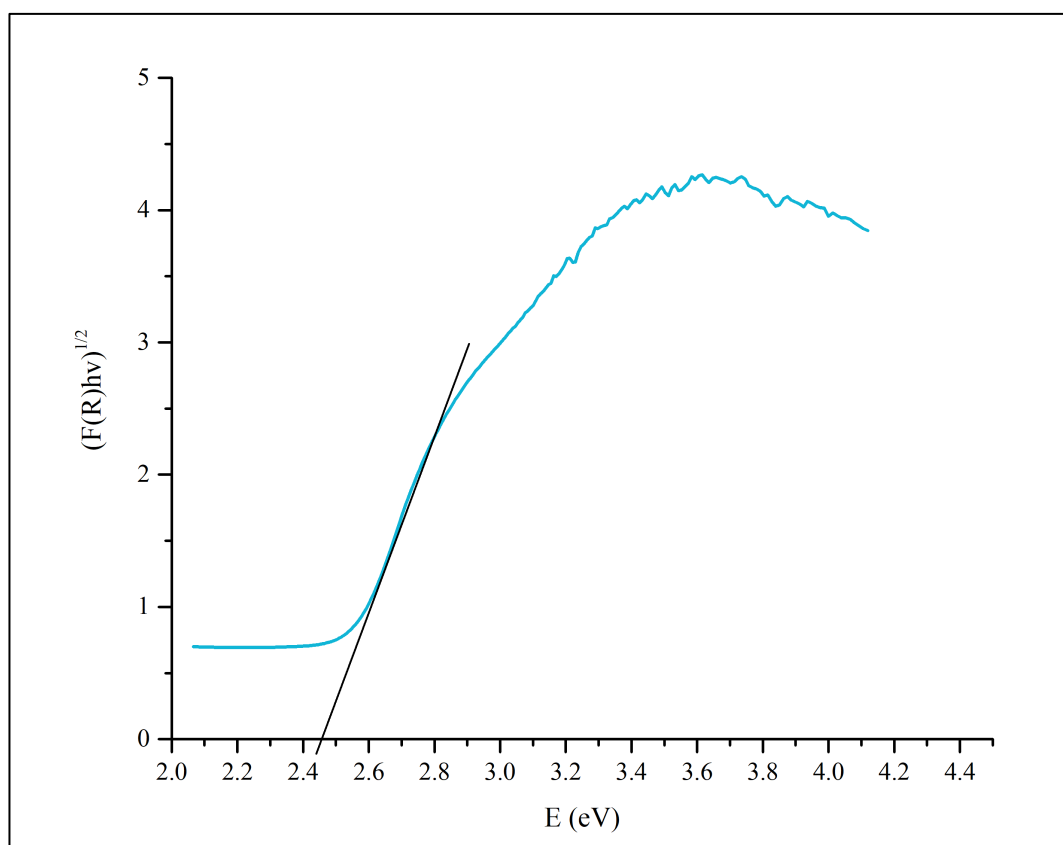


Figure 3.26 - The Tauc plot of $\text{WO}_3/\text{BiVO}_4$.

The DR UV-Vis analysis (Figure 3.25) exhibits that the $\text{WO}_3/\text{BiVO}_4$ photoanode absorbs wavelengths up to 490 nm. This is significantly higher than the maximum wavelength absorption of pristine WO_3 . This is due to the BiVO_4 layer having a narrower bandgap thus allowing a higher proportion of solar light to be absorbed [10, 22]. From the bandgap energy calculations, the bandgap of $\text{WO}_3/\text{BiVO}_4$ was 2.45 eV, which is narrower than WO_3 . Resulting in the wavelength absorption range increasing thus helping to increase the photoactivity of the photoanode as it allows a more electrons to be excited, thus a higher production of photocurrent.

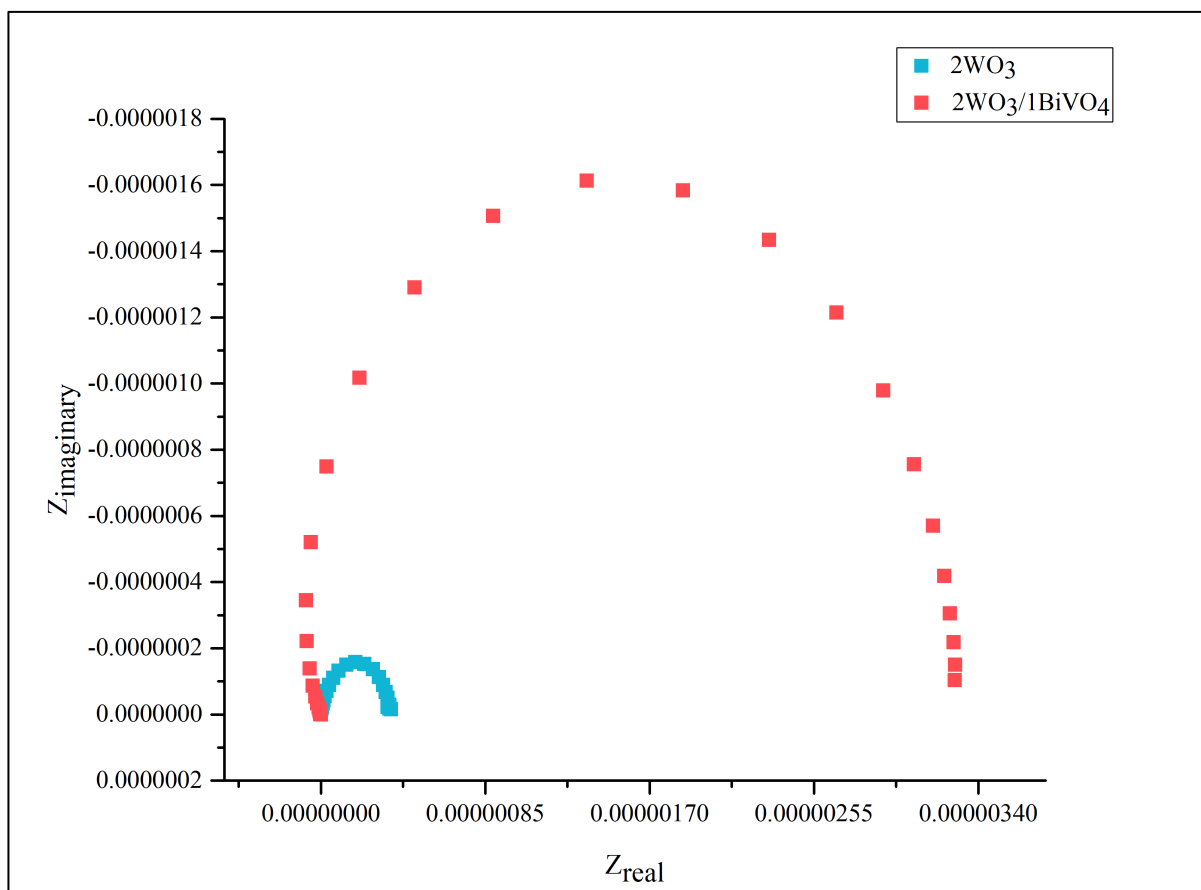


Figure 3.27 - The Nyquist plot obtained from the IMPS analysis of (blue) WO_3 and (red) $WO_3/BiVO_4$. The experimental details summarised in Table 2.6.

Intensity-modulated photocurrent spectroscopy (IMPS) is commonly utilised to assess the dynamics of the charge carriers [25]. Therefore, it was utilised to help assess the electron transfer time from the photoanode surface to the FTO substrate. The IMPS experiment produced a Nyquist plot which is utilised for calculation of the electron transit time (τ_D) as the electron transit time (τ_D) is estimated to be ω_{max}^{-1} generated from the Nyquist plot. The τ_D for WO_3 and $WO_3/BiVO_4$ was calculated as 22.97 ms (to 2 d.p) and 2.44 ms (to 2d.p), respectively. This verified that the electrons were travelling faster in the $WO_3/BiVO_4$ photoanode compared to the WO_3 photoanode. This could be because there is effective charge separation in $WO_3/BiVO_4$ and as result then the electrons are not being trapped in charge recombination reactions, resulting in more electrons traveling to the FTO substrate.

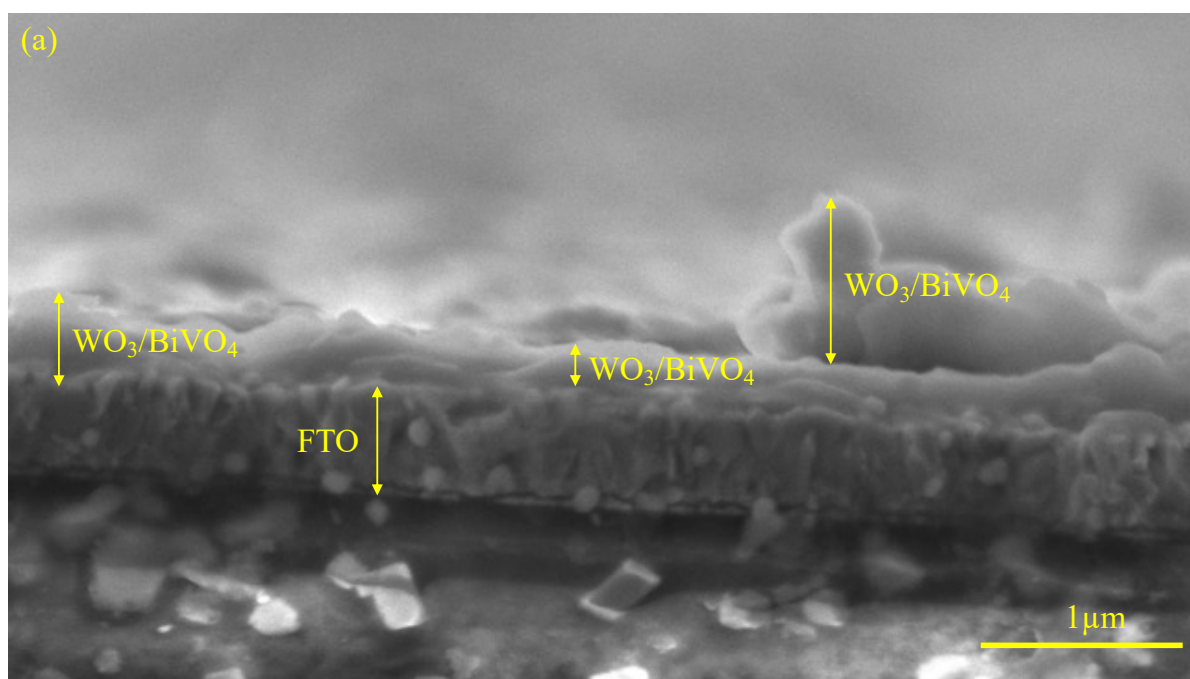
3.2.9 The Effect of Varying the Semiconductors' Thickness on The Heterostructure Photoanode's Performance

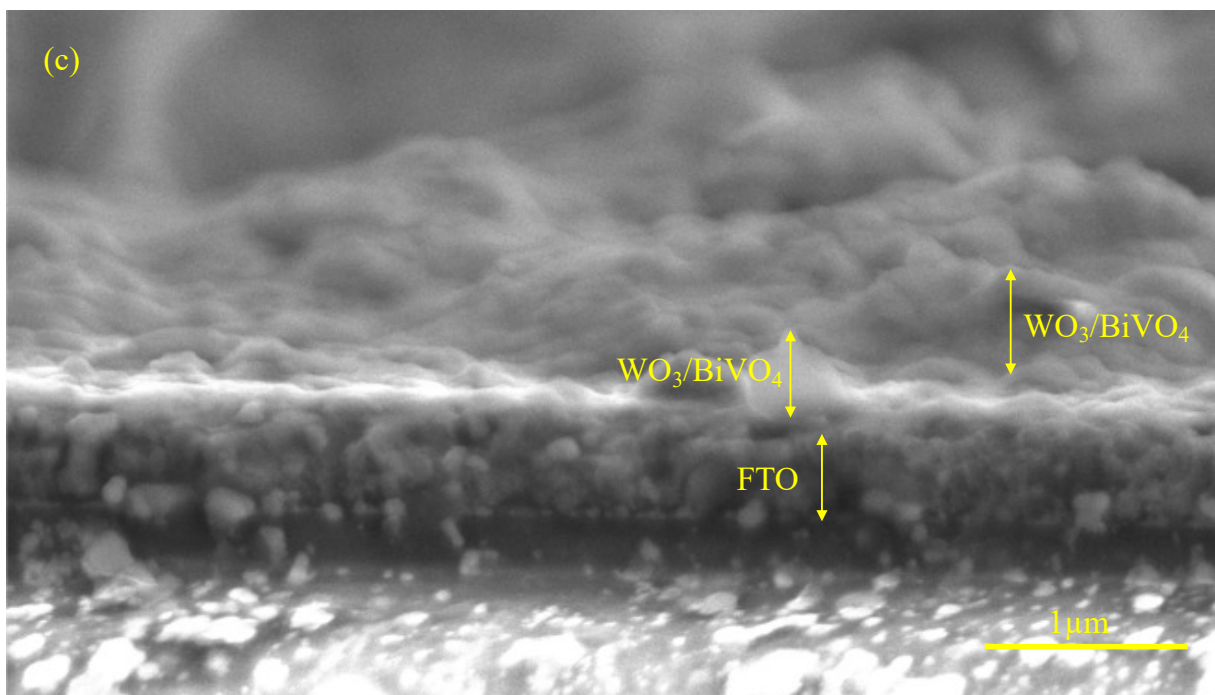
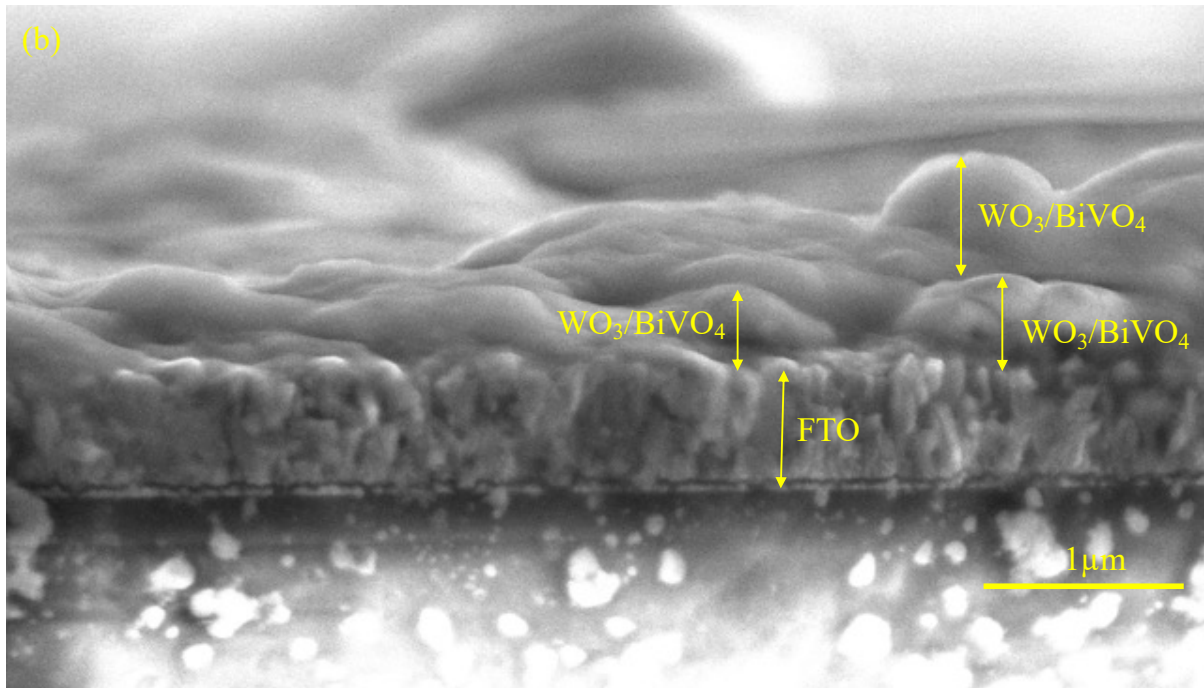
There is very limited research on how each semiconductor's layer could affect the performance of the photoanode. However there has been some studies which looked into the effect of altering the WO_3 thickness in $WO_3/BiVO_4$ [19, 26-29]. It showed that increasing the WO_3

thickness decreases the performance of $\text{WO}_3/\text{BiVO}_4$ [19, 26]. This is because the BiVO_4 layer starts becoming less effective in charge separation as it is small compared to the WO_3 layer [26]. Thus more charge recombination occurs [26]. However, another study showed in increasing the WO_3 thickness increased the performance, due to WO_3 having good light absorption thus resulting in more photon absorption [19]. Therefore, to help add value to either argument then in this thesis the effect of the WO_3 thickness on the heterostructure photoanode's performance was investigated.

3.2.9.1 Influence of WO_3 Coating Cycles in the $\text{WO}_3/\text{BiVO}_4$ Photoanode

The WO_3 layer is an essential layer in the photoanode as not only does it absorb visible light, but it also exhibits excellent electron mobility and stability in low pH [2, 10, 30]. To help understand the influence of the WO_3 thickness on the photoanode performance then different coating cycles (1, 2, 3 and 4) of WO_3 were annealed onto the FTO glass and subsequently a single coating cycle of BiVO_4 was sintered on top of the desired number of cycles of WO_3 .





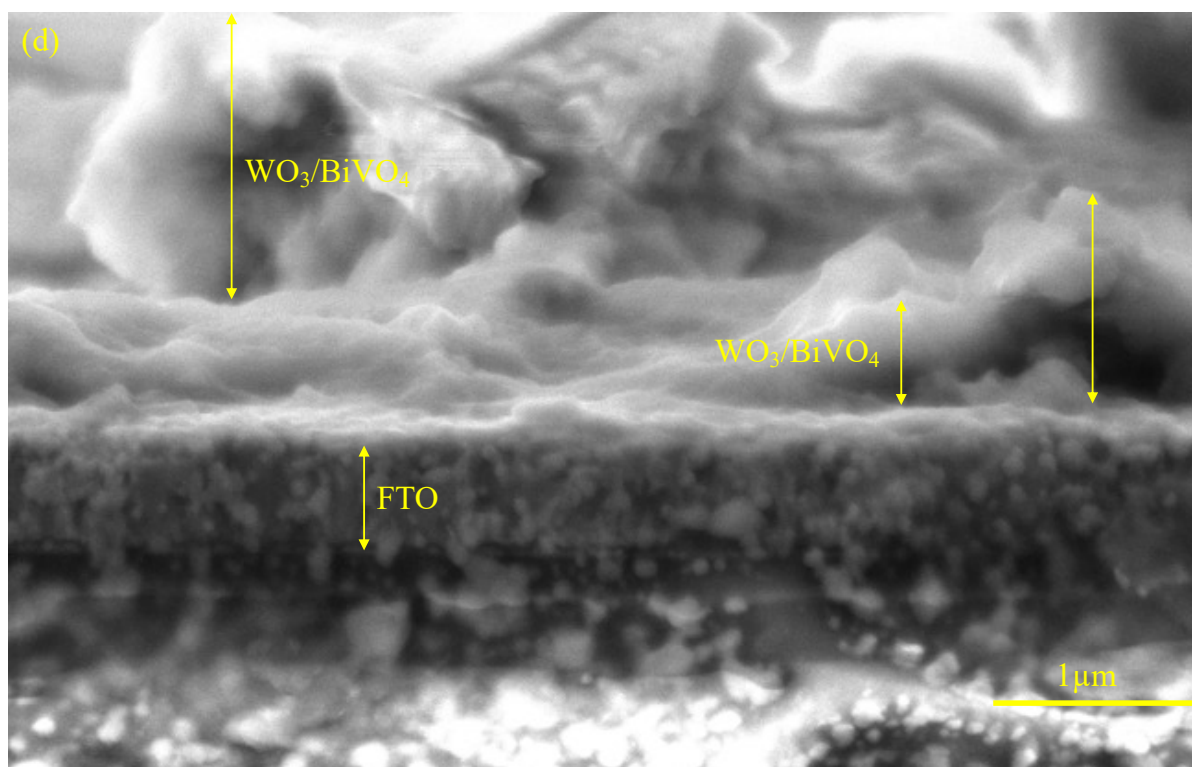


Figure 3.28 - Transverse SEM analysis of (a) 1 Layer of WO_3 with $BiVO_4$, (b) 2 Layers of WO_3 with $BiVO_4$, (c) 3 Layers of WO_3 with $BiVO_4$ and (d) 4 Layers of WO_3 with $BiVO_4$.

The cross section of each photoanode was analysed utilising SEM to help determine the effect of the number of the WO_3 cycles has on the thickness. Figures 3.28 a-d demonstrated that none of the photoanodes displayed a non-uniform surface as several different thicknesses were established for each photoanode. This implies that the method developed for WO_3 synthesis created a random arrangement of WO_3 nanoparticles. It also demonstrated that increasing the number does not always increase the thickness of the $WO_3/BiVO_4$ thickness. This indicates that increasing the WO_3 cycles results in any naked FTO sites or pores being filled. Filling any naked FTO sites would improve the photocurrent production, however filling any pores will reduce the surface area thus reducing photocurrent production (Figure 3.29). To help determine this then photoelectrochemical analysis was conducted.

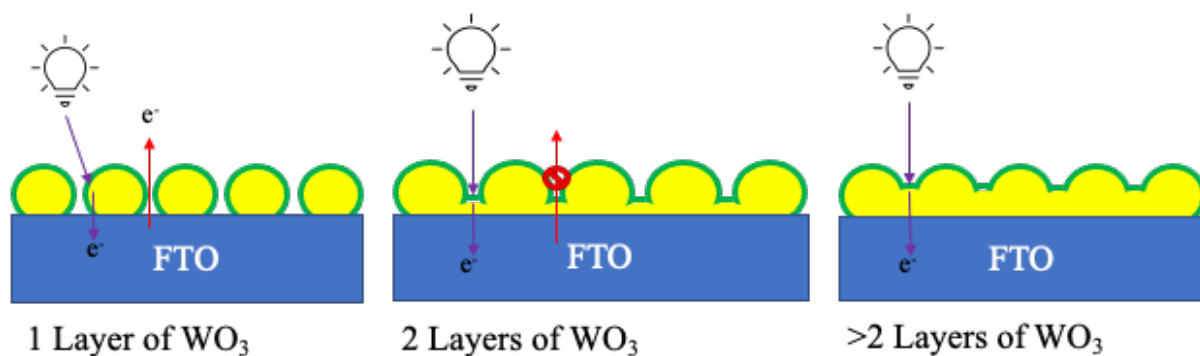


Figure 3.29 - A schematic illustration of how altering the WO_3 cycles effects the cross-sectional surface morphology

The EDS mapping (Figure 3.30) verifies that there is no electron leakage when increasing the number of WO_3 cycle, as only $1WO_3/BiVO_4$ photoanode (Figure 3.30a) has Sn exposed. Therefore, it is good to have more than one cycle of WO_3 to help ensure that no electron leakage (lower photocurrent) occurs.

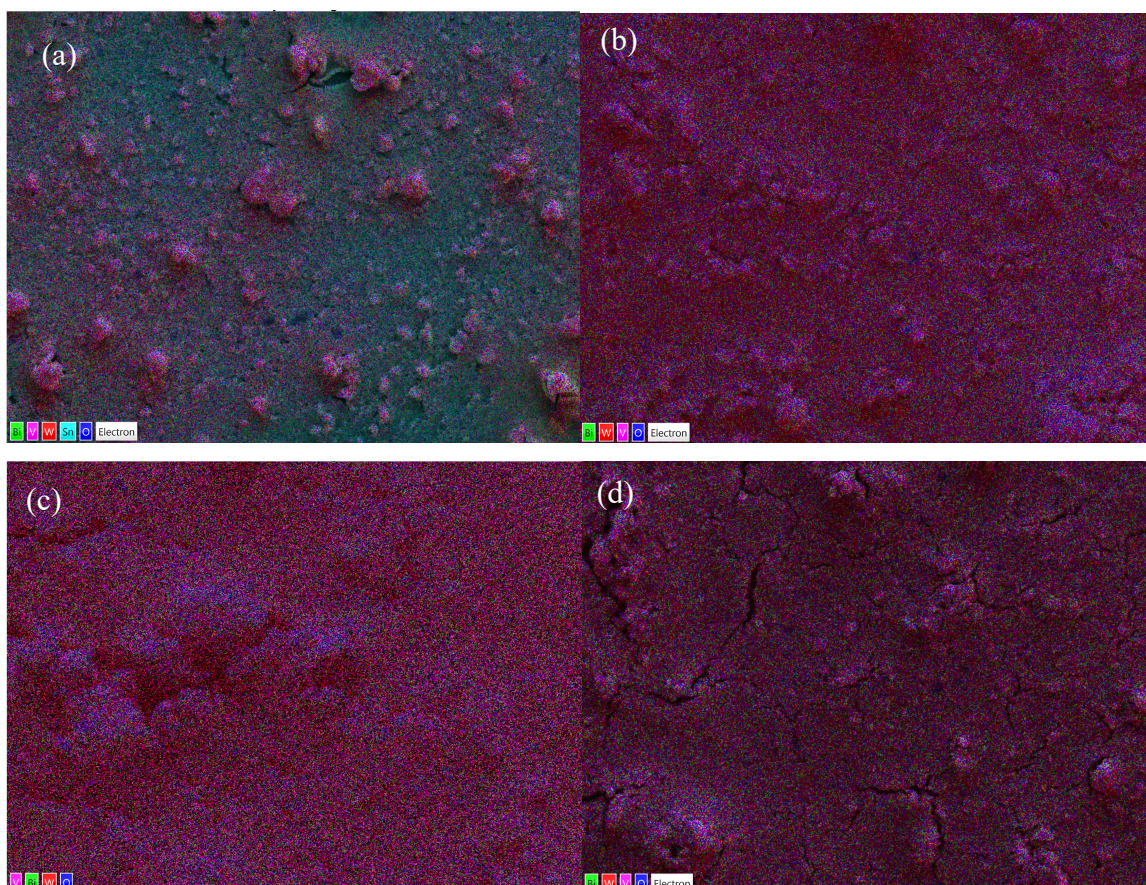


Figure 3.30 - The EDS mapping obtained for (a) $1WO_3/1BiVO_4$, (b) $2WO_3/1BiVO_4$, (c) $3WO_3/1BiVO_4$ and (d) $4WO_3/1BiVO_4$.

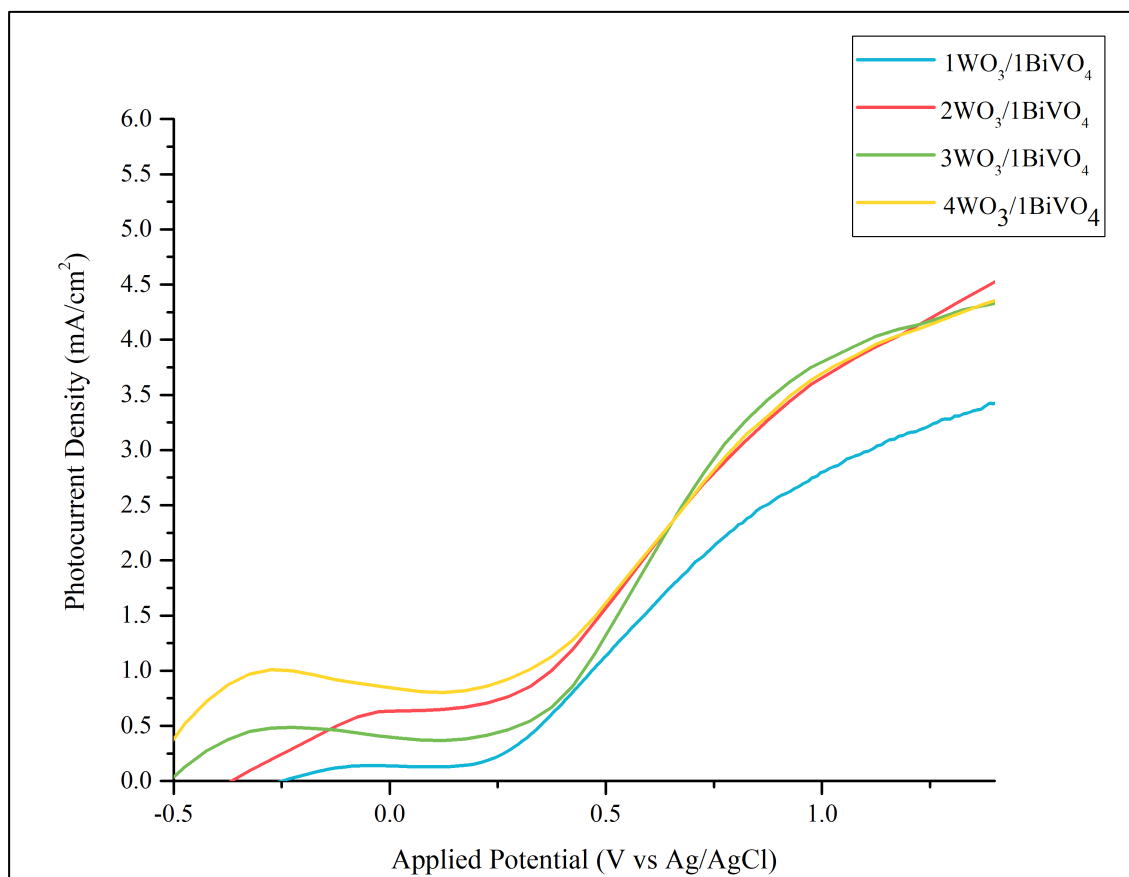


Figure 3.31 - The LSV analysis of (a) $1\text{WO}_3/1\text{BiVO}_4$, (b) $2\text{WO}_3/1\text{BiVO}_4$, (c) $3\text{WO}_3/1\text{BiVO}_4$ and (d) $4\text{WO}_3/1\text{BiVO}_4$. Note that the experiment details were that the electrolyte was 0.5M NaCl , 1 sun of solar light, scan limit from -0.5 V to 1.5 V .

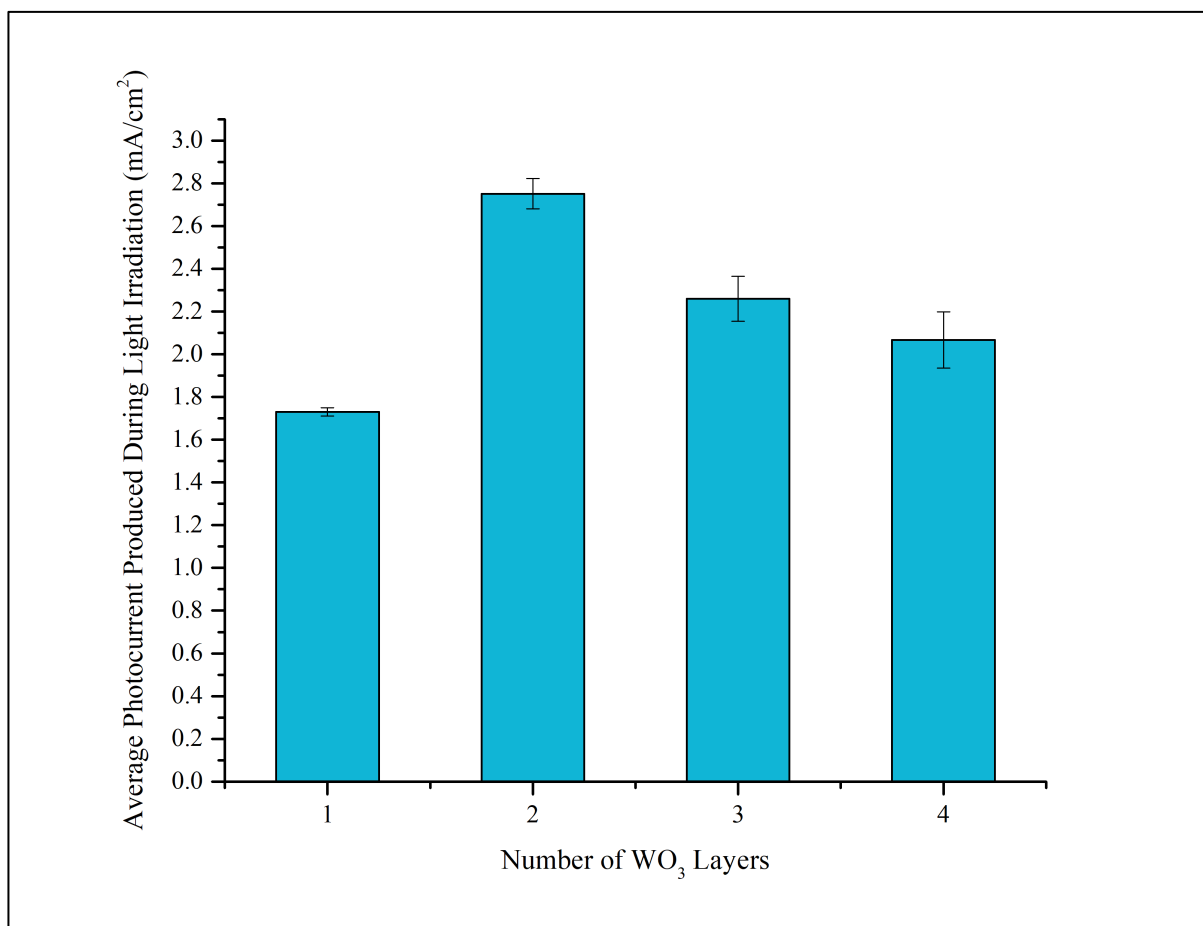


Figure 3.32 - A plot displaying the average photocurrent densities for each synthesised WO₃/BiVO₄ photoanode.

The LSV analysis (Figure 3.31) demonstrated that under light illumination all photoanodes produced a significant photocurrent. It demonstrated that increasing the number of WO₃ cycles above 1 significantly improved the photocurrent production of the WO₃/BiVO₄ photoanode. This could be due to no electron leakage as the EDS showed no exposure of Sn in the photoanodes with more than 1 WO₃ cycle. Beyond 2 cycles of WO₃ the difference in photocurrent is negligible this could be while higher content of WO₃ allows for higher photon absorption there is a higher resistance for electron transfer due to a longer diffusion length [19, 26]. The photoelectrochemical analysis (Figure 3.32) demonstrated that increasing the number of WO₃ cycles from 1 to 2 increased the performance of WO₃/BiVO₄. According to literature the reason this occurs is because WO₃ has good absorption capabilities meaning more photons are absorbed thus generating more electrons [19, 26]. However, from the EDS mapping it showed that adding an extra cycle of WO₃ helped prevent exposure of the FTO “naked” sites to the electrolyte, thus stopping any back flow of electrons from the FTO substrate to the electrolyte (Figure 3.30 b). This means all electrons travel to the counter electrode resulting in a higher current. Figure 3.32 also identified that increasing the WO₃ cycles beyond 2 cycles

caused the photocurrent production to decrease significantly. According to literature this is due to the BiVO_4 layer being insufficient to achieve charge separation, as increasing the WO_3 increases the resistance for the photogenerated charges to travel through thus causing more charge recombination to occur in the WO_3 layer [26]. There is also the possibility that increasing the number of WO_3 cycles can decrease the diameter of the pores thus lowering the surface area of the photoanode resulting in lower photon absorption. This is due to the doctor blade technique allowing for WO_3 to fill the pores. This contradicts the study of Pedroni et al who concluded that increasing the WO_3 helped increase the photocurrent production due to the increase in absorption capabilities [19].

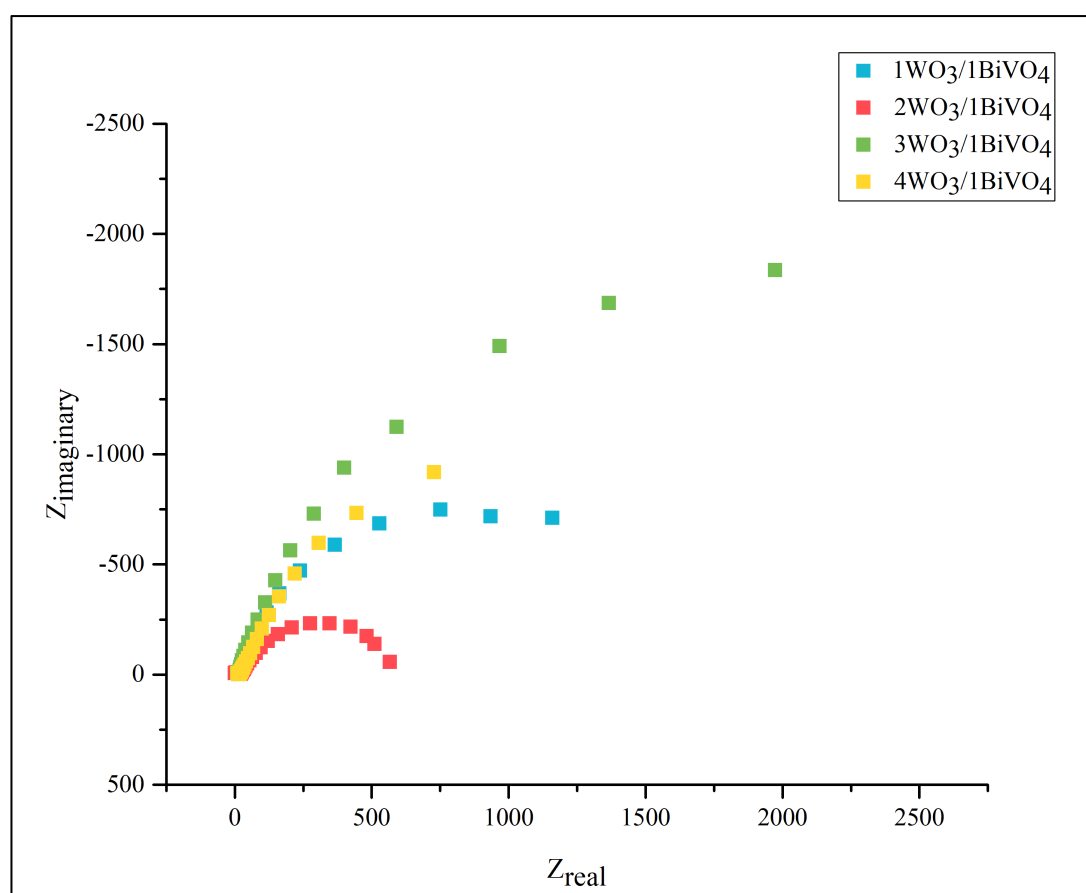


Figure 3.33 - The EIS Nyquist plots for $\text{WO}_3/\text{BiVO}_4$ photoanodes with varying WO_3 thickness. The experimental details are summarised in Table 2.5.

This study utilised electrochemical impedance spectroscopy (EIS) to determine the resistance of the photoanode. The EIS analysis (Figure 3.33) produced Nyquist plots which with the equivalent circuit establishes the charge transfer resistance (R_{ct}) that the electron faces in the photoanode. Increasing the number of cycles from 1 to 2 decreased the R_{ct} from 1719.1Ω to 563.25Ω . The reason why 1 cycle has a higher R_{ct} is because there is an inadequate amount of

WO₃ present to achieve good transfer of electrons from BiVO₄ to the FTO substrate [1, 2]. As WO₃ has good electron mobility then a significant amount needs to present to help drive the electrons from the BiVO₄ to the FTO glass substrate. The EIS study also identified that increasing the number of cycles from 2 to 3 increased the R_{ct} value to 4487. The increase R_{ct} could be due to the electrons transfer length increasing which results in charge recombination and lowers the number of electrons. The interesting discovery of this EIS study however, is that even though the optimal WO₃/BiVO₄ photoanode contained 2 cycles when increasing the cycles from 3 to 4 the R_{ct} value decreased to 3564. This has not been witnessed in literature but would suggest that 4 cycles achieve a lower resistance as it has a higher absorption capability that enables effective electron transfer.

IMPS was utilised again to help determine if increasing the WO₃ thickness helped increase the electron mobility.

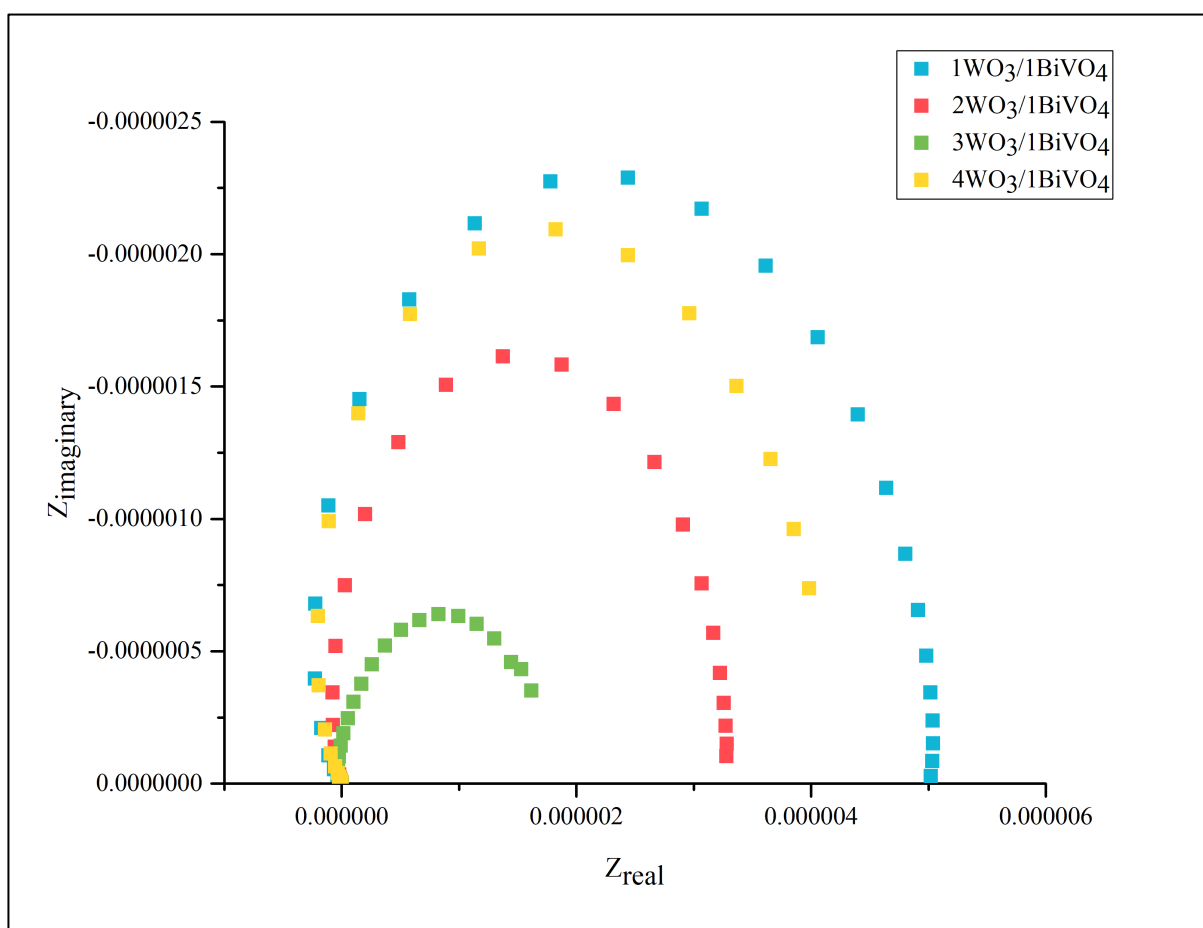


Figure 3.34 - The IMPS Nyquist plot for each WO₃/BiVO₄ photoanode with varying WO₃ thickness. The experimental details summarised in Table 2.6.

The data obtained showed that the increasing the number of WO_3 cycles increases the electron transfer time with 3 cycles of WO_3 having the worst electron transfer as the transfer electron time goes from 1.01 ms for 1 cycle WO_3 to 12.36 ms for 3 cycle WO_3 . This is due to the electrons have a longer distance to travel. When there were 4 cycles of WO_3 in the photoanode the electron transit time decreased slightly to 11.27 ms which could be due to the lower resistance thus allowing the electron to travel faster to the FTO substrate.

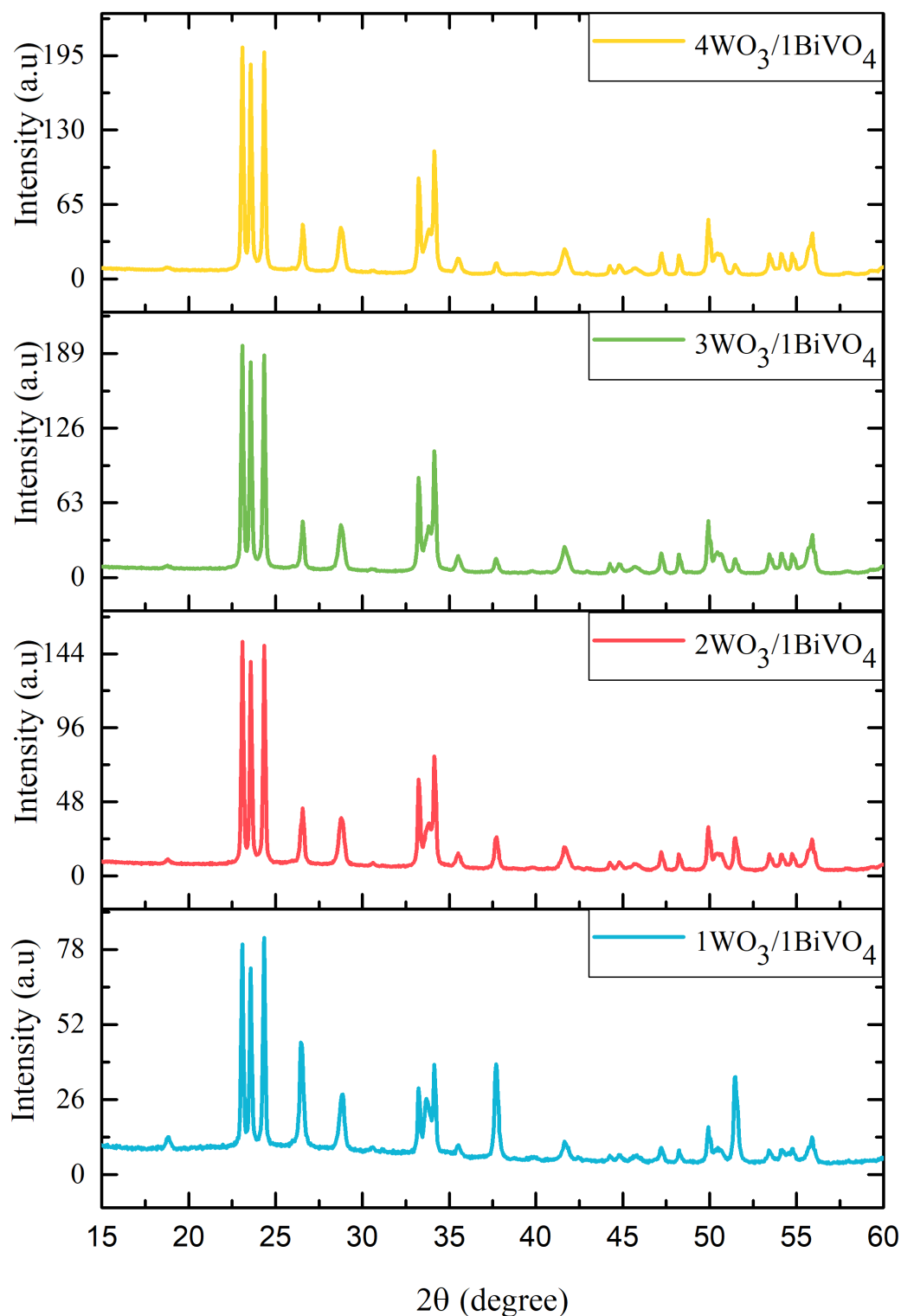


Figure 3.35 - The XRD diffraction pattern obtained for each $\text{WO}_3/\text{BiVO}_4$ photoanode with different WO_3 thickness.

According to the XRD analysis altering the number of WO_3 cycles does not affect crystallinity as all the $\text{WO}_3/\text{BiVO}_4$ photoanodes had phase peaks of 002, 020, 200 associated with monoclinic WO_3 and 101, 112, 004 associated with monoclinic BiVO_4 [2, 7, 11, 20]. This is important as the monoclinic phase for WO_3 and BiVO_4 has demonstrated the highest

photocatalytic activity [2, 7, 11, 20]. Hence it was important to ensure this crystallinity was not affected.

Since $2\text{WO}_3/1\text{BiVO}_4$ achieved the highest photocurrent then the next step was to determine how altering the thickness of BiVO_4 altered the performance of this photoanode.

3.2.9.2 Influence of BiVO_4 Coating Cycles in the $\text{WO}_3/\text{BiVO}_4$ Photoanode

There have been some studies on how increasing the BiVO_4 thickness effects the $\text{WO}_3/\text{BiVO}_4$ performance. From the studies it was evidenced that the $\text{WO}_3/\text{BiVO}_4$ photoanode performance increases with increasing the thickness of BiVO_4 to an optimal [29]. Beyond this optimal thickness however the performance decreases, the photogenerated charges recombine as BiVO_4 has poor electron mobility thus taking longer to get to the WO_3 layer [27, 29].

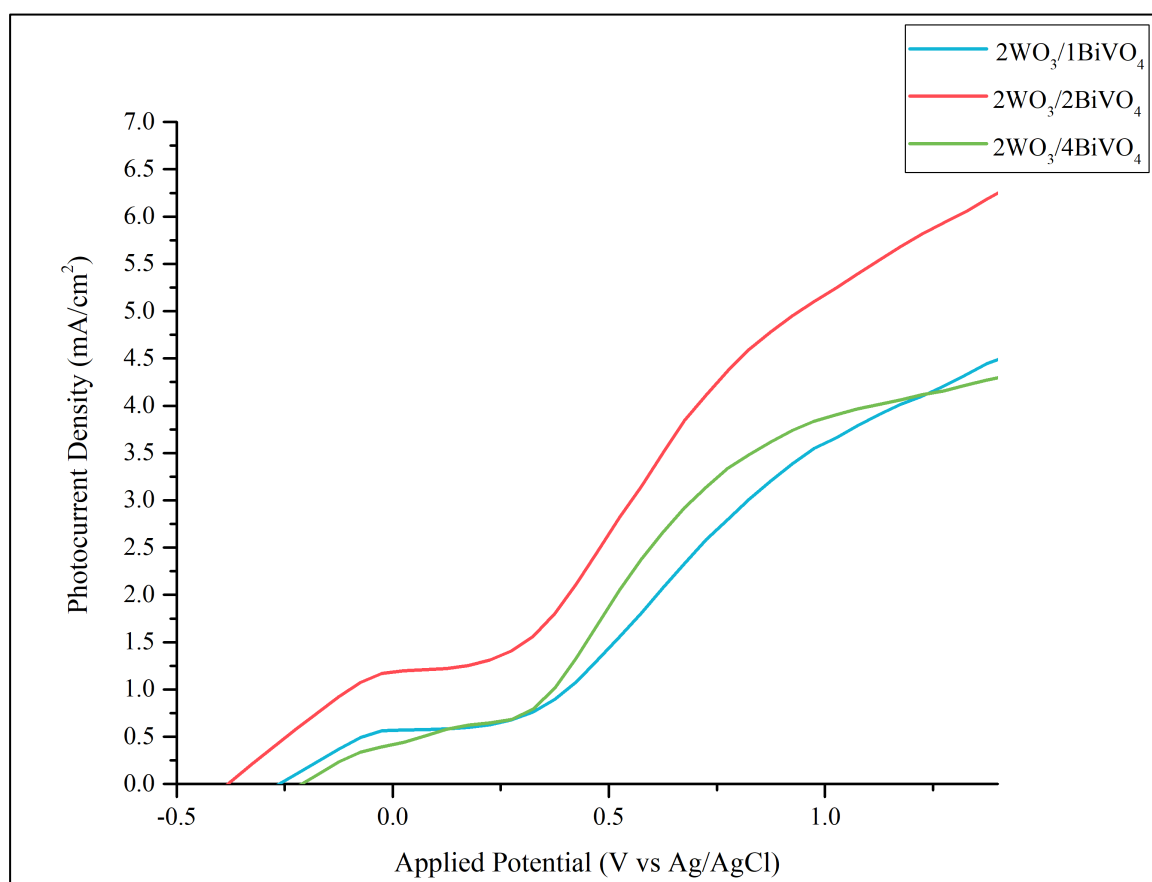


Figure 3.36 - LSV analysis of (a) $2\text{WO}_3/1\text{BiVO}_4$, (b) $2\text{WO}_3/2\text{BiVO}_4$ and (c) $2\text{WO}_3/4\text{BiVO}_4$. Note that the experiment details were that the electrolyte was 0.5M NaCl , 1 sun of solar light, scan limit from -0.5 V to 1.5 V .

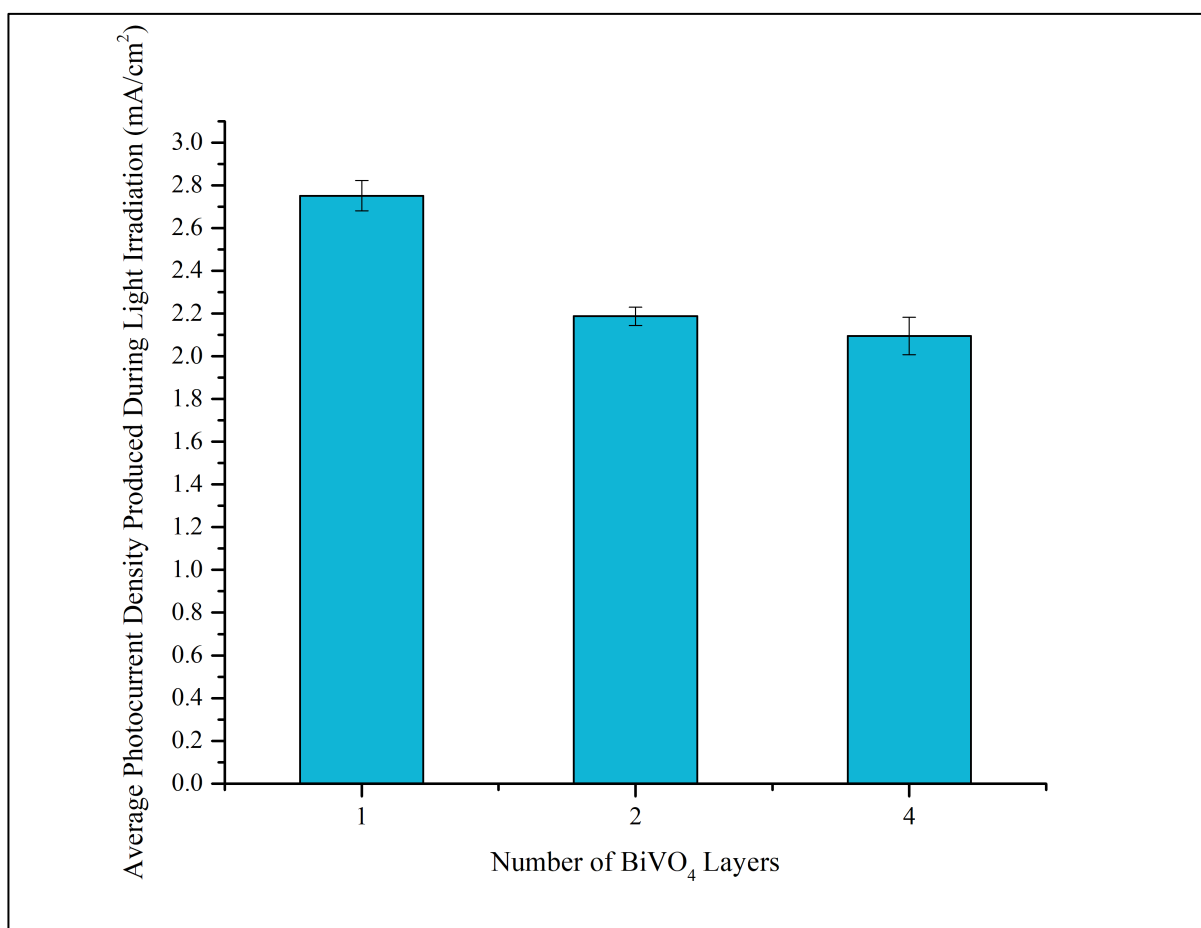


Figure 3.37 - A plot displaying the amount of photocurrent density produced by each $WO_3/BiVO_4$ of varying $BiVO_4$ thickness.

The LSV analysis (Figure 3.36) demonstrated that the $WO_3/BiVO_4$ electrode with 2 layers of $BiVO_4$ improved the photocurrent density production compared to 1 and 4 layers. However, the photoelectrochemical analysis (Figure 3.37) showed that the $WO_3/BiVO_4$ photocurrent production decreases as the thickness of the $BiVO_4$ layer increases and that one layer of $BiVO_4$ was the optimum thickness. This is due to $BiVO_4$ having poor electron mobility thus encouraging charge recombination at the photoanode's surface [31]. This means that there is a lower number of electrons traveling to the counter electrode. The photoelectrochemical analysis results are more reliable as it is a more in-depth study of the photoactivity of the photoanodes.

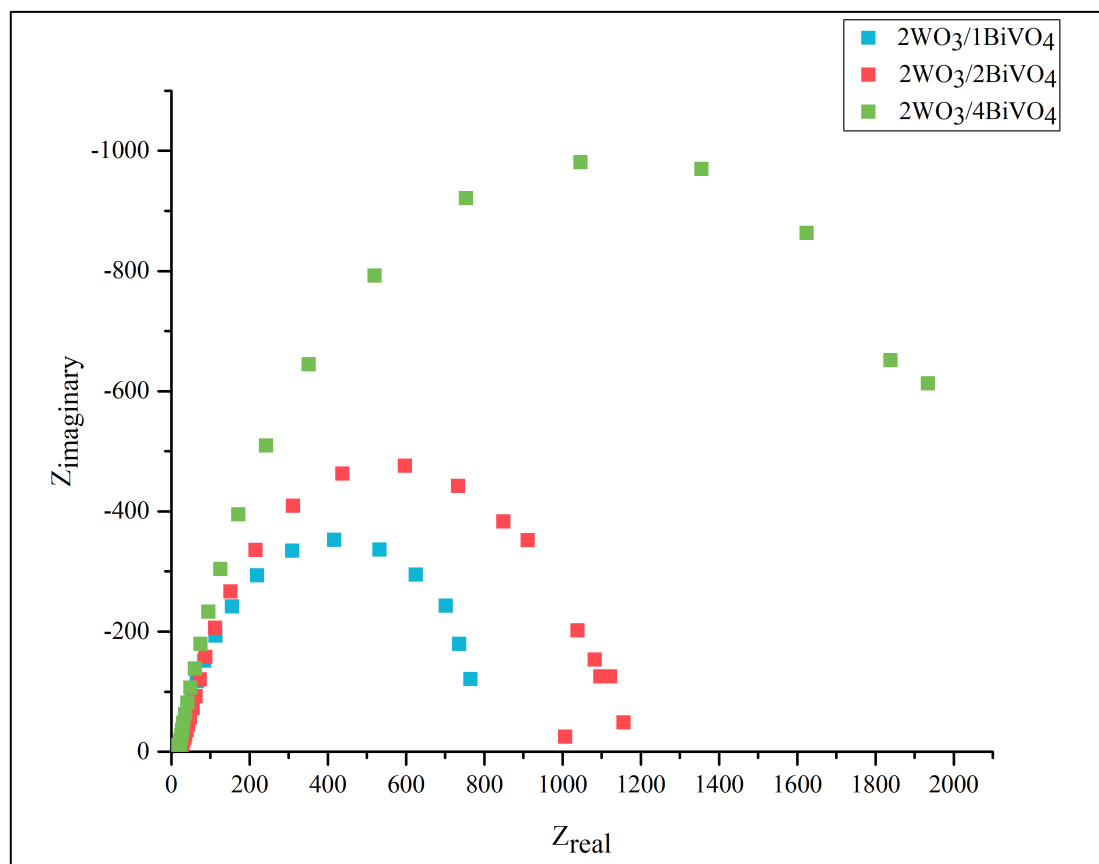


Figure 3.38 - The EIS Nyquist plot for each $\text{WO}_3/\text{BiVO}_4$ with varying BiVO_4 thickness. The experimental details are summarised in Table 2.5.

Again, EIS was utilised to help determine the resistance in each photoanode. As the data shows increasing the BiVO_4 layer increases the R_{ct} from 563.25Ω to 2442Ω . This is due to a higher amount of the poor electron mobility BiVO_4 causing the electrons to move slower from the photoanode surface to the FTO substrate [29]. Hence, only one cycle of BiVO_4 is sufficient for effective charge separation [28].

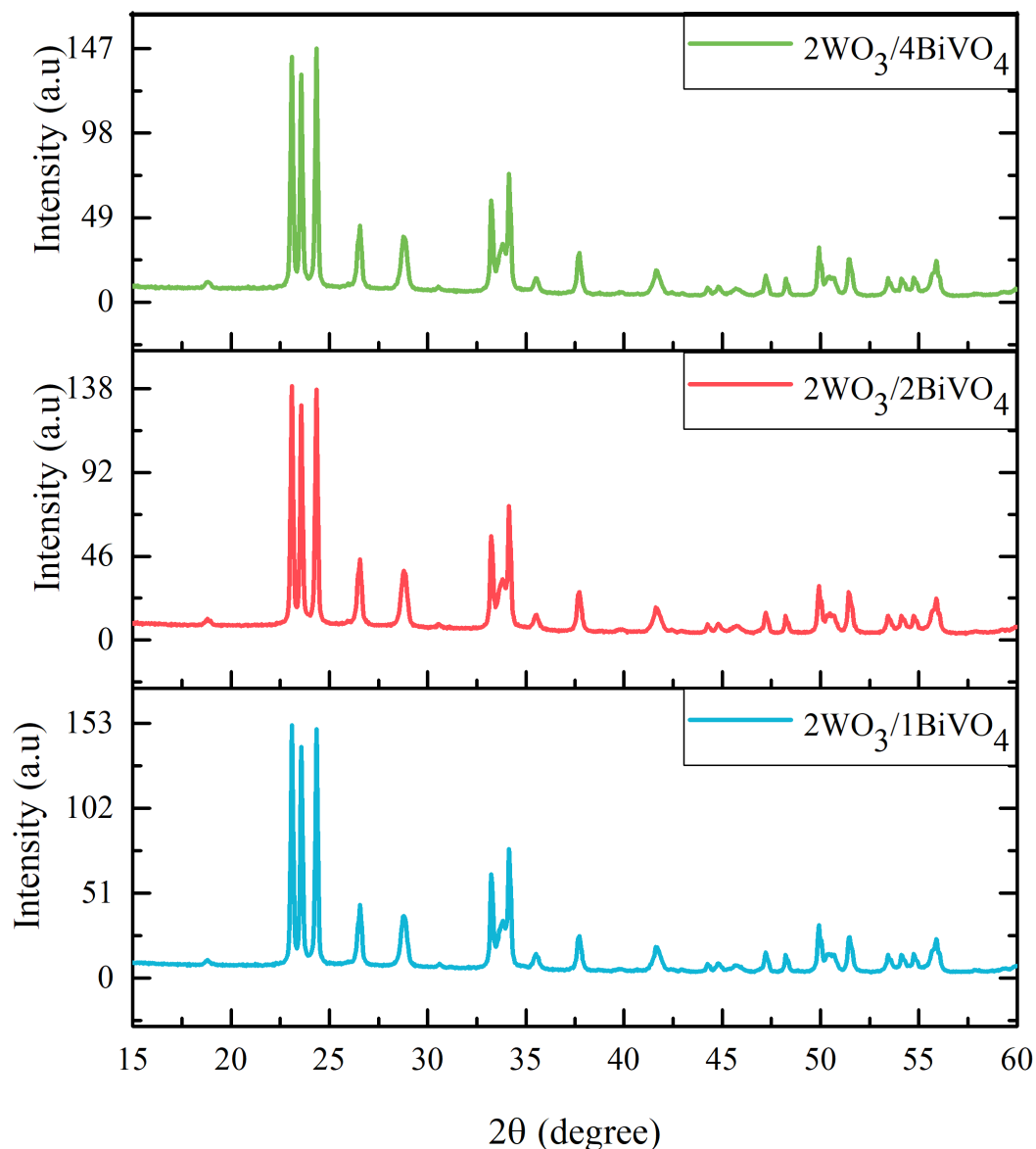


Figure 3.39 - The XRD diffraction pattern obtained for each $WO_3/BiVO_4$ photoanode with varying $BiVO_4$ thickness.

Again, XRD was utilised to ensure that altering the $BiVO_4$ thickness did not affect the crystallinity of the WO_3 and $BiVO_4$ in the $WO_3/BiVO_4$ photoanode. Figure 3.39 showed that monoclinic WO_3 and $BiVO_4$ were both present in the photoanodes as there were peaks at approximately 18.8° , 23.1° , 23.6° , 24.3° , 28.8° and 30.5° [7, 20]. This confirms that adding various layers of $BiVO_4$ did not affect the crystallinity of WO_3 or $BiVO_4$ in the photoanode. The only change relates to more $BiVO_4$ layers resulting in more intensity for the peaks associated with $BiVO_4$.

These results showed that increasing the $BiVO_4$ causes a decrease in photocurrent production for $WO_3/BiVO_4$. This is due to a higher percentage of electrons recombining with holes. This

recombination occurs due to the higher resistance causing electrons to remain in the BiVO₄ for a longer time. It was therefore, decided that 2 layers of WO₃ and 1 layer of BiVO₄ created the optimum WO₃/BiVO₄ photoanode with an average photocurrent of 2.75 mA/cm². This photoanode will be known as 2WO₃/1BiVO₄ as it is the optimum photoanode and as a result is the photoanode which will be utilised in all experiments going forward.

3.2.11 How Do the Operating Conditions Effect the Photocurrent Production

The photocurrent production is heavily dependent on the semiconductor material used for the photoanode. As found in the previous section utilising the 2WO₃/1BiVO₄ photoanode with a 0.5 M NaCl supporting electrolyte and 1 sun of solar light then a high photocurrent of 2.75 mA/cm² was produced higher than utilising pristine WO₃ which resulted in 0.8 mA/cm². However, while 2WO₃/1BiVO₄ achieved elevated photocurrent production compared to other studies, the operating parameters can also be altered to improve the photocurrent production. It was necessary to determine how these factors influence the photocurrent production to help explain decisions made in future work.

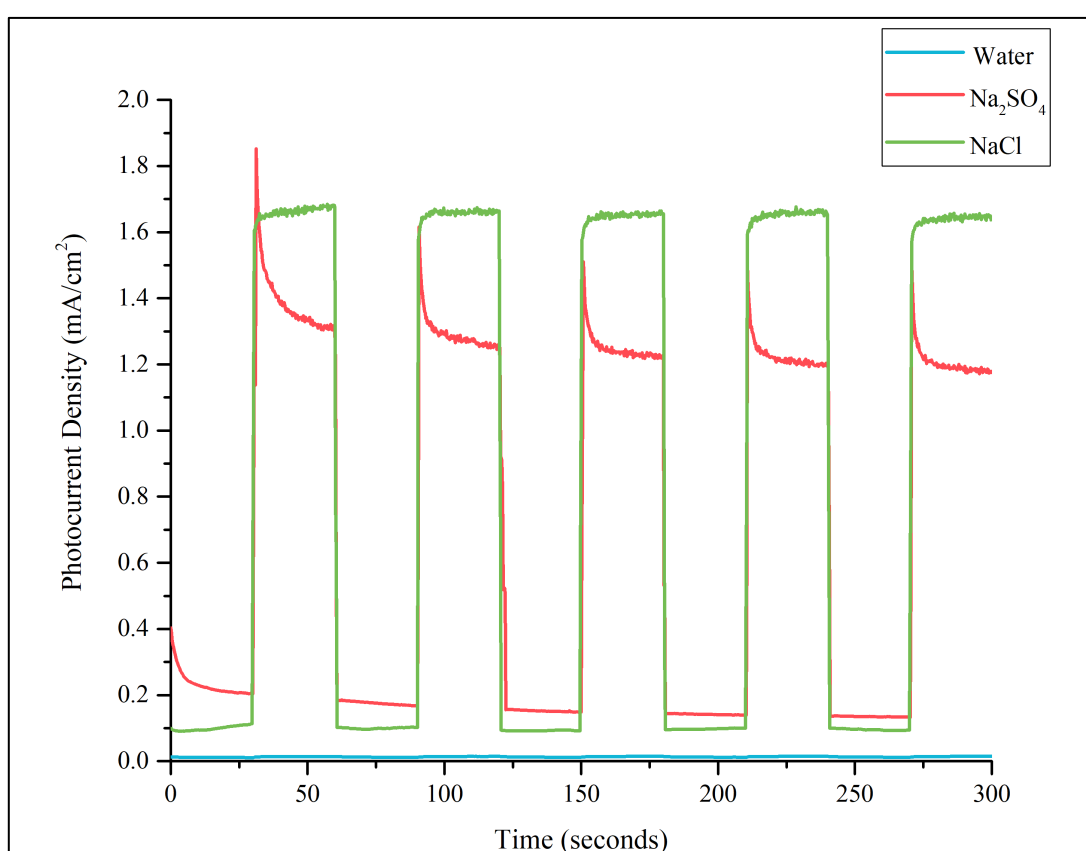


Figure 3.40 - The chronoamperometry obtained for the optimised photoanode with (blue) pure water, (red) 0.5 M Na₂SO₄ and (green) 0.5 M NaCl. Note that all the experiments had an applied potential + 0.6 V with a chopped light (30 secs off/on for 5 minutes).

The first operating parameter tested was the supporting electrolyte type, as it is important to use an electrolyte to help provide the system with conductivity. As no supporting electrolyte (pure water) resulted in zero photocurrent production (Figure 3.40). The addition of a supporting electrolyte such as NaCl or Na₂SO₄ helps create a conductivity in the solution [32]. Forming a conductivity in the solution enables an electrical current solution which prevents recombination of the photogenerated electrons and holes [32]. This is due to the electrical current reducing the resistance in the solution to help drive ions transfer [32].

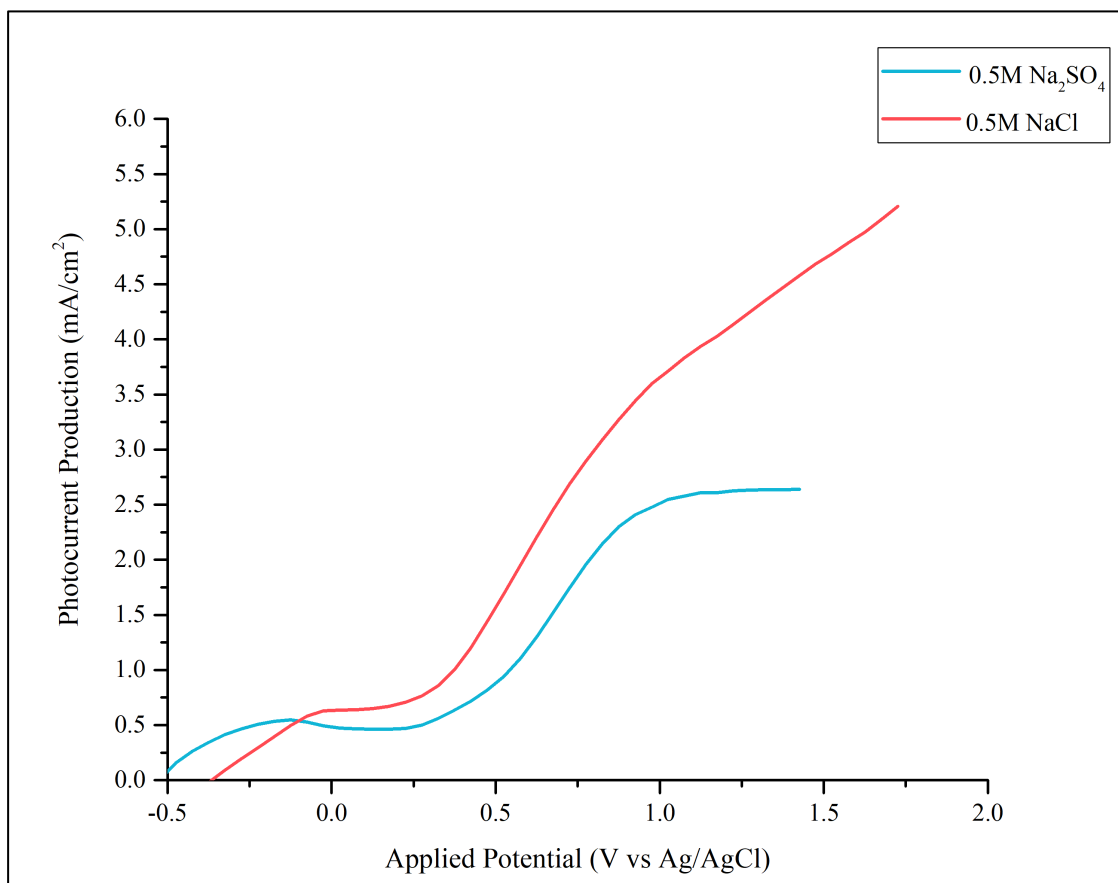


Figure 3.41 - The J-V plots when utilising 0.5 M Na₂SO₄ electrolyte (blue) and 0.5 M NaCl (red). Note that the experiment details were that 1 sun of solar light was utilised with a scan limit from -0.5 V to 1.5 V at a rate of 50 mV/s.

The electrolyte effects the onset potential of the PEC system, which in turn effects the photocurrent production. Sodium chloride (NaCl) electrolyte shows a lower onset potential than sodium sulphate (Na₂SO₄) which means NaCl is able to achieve higher photocurrents at a lower applied potential than Na₂SO₄ [33]. However, Figure 3.41 demonstrated that this was not true when utilising 2WO₃/1BiVO₄ as the photoanode. As the onset potential was the same for Na₂SO₄ and NaCl. Therefore, the reason for the increase in photocurrent production when utilising NaCl is because it enables higher charge separation, due to the negative chloride ions having a higher absorption rate on the semiconductor surface than sulphate ions [33]. Hence

the chloride ions act as a hole scavenger thus lowering and charge recombination [33]. The other benefit of utilising NaCl as a supporting electrolyte is that it's cheap, abundant and has shown great photodegradation for pollutants. Due to this reason, it was decided that this would be the supporting electrolyte of choice.

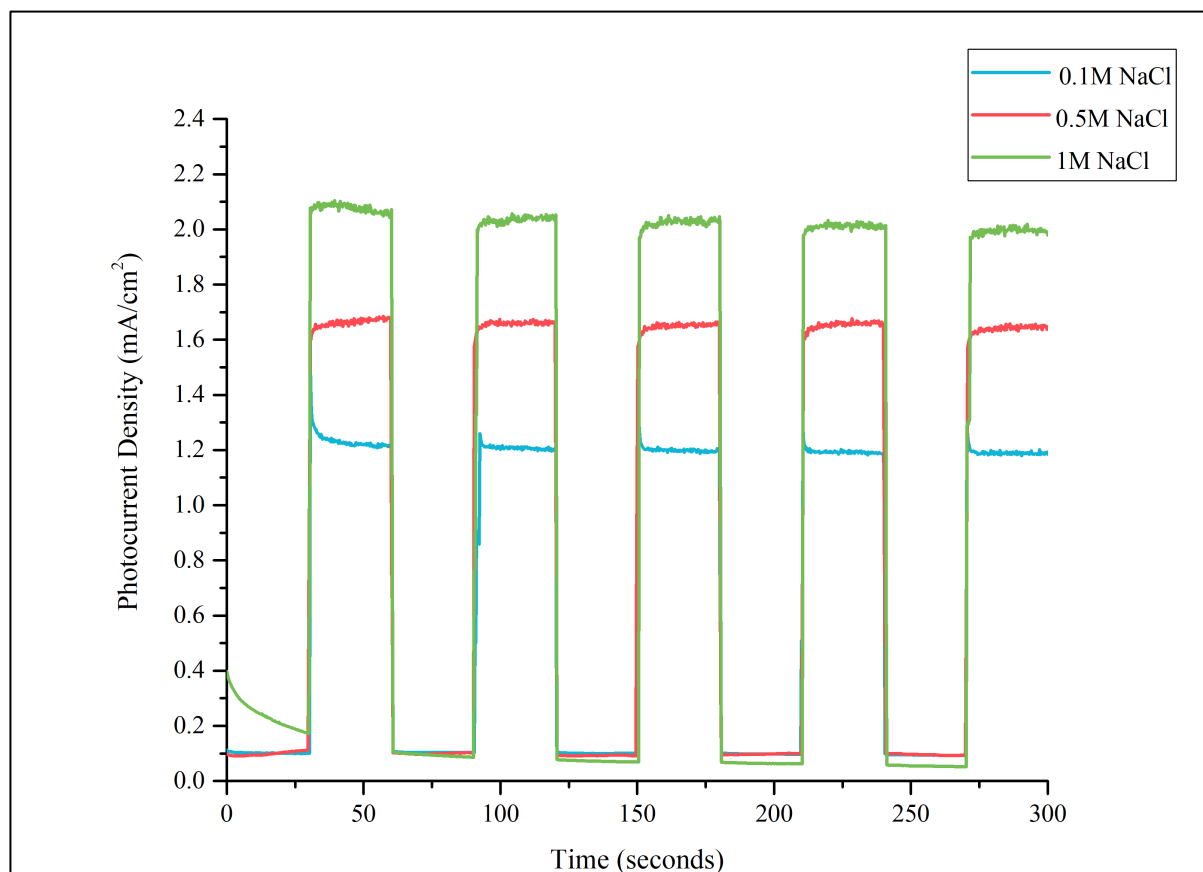


Figure 3.42 - The chronoamperometry obtained for the optimised photoanode with (blue) 0.1 M NaCl, (red) 0.5 M NaCl and (green) 1 M NaCl supporting electrolyte. Note that the constant experimental details were that an applied potential of 0.6 V was utilised with a chopped 1 Sun of solar light (on/off, 30 s each) for 5 minutes.

Not only does the type of electrolyte utilised affect the photocurrent production but so does the concentration. This is because the higher the concentration the greater the conductivity. As previously mentioned, increasing the conductivity of the solution results in the resistance reducing, thus fast ion transfer [32]. It was identified that increasing the NaCl concentration from 0.1 M to 1 M resulted in the photocurrent density production to increase by approximately 0.8 mA/cm². This demonstrates how important the conductivity is in achieving high photocurrents.

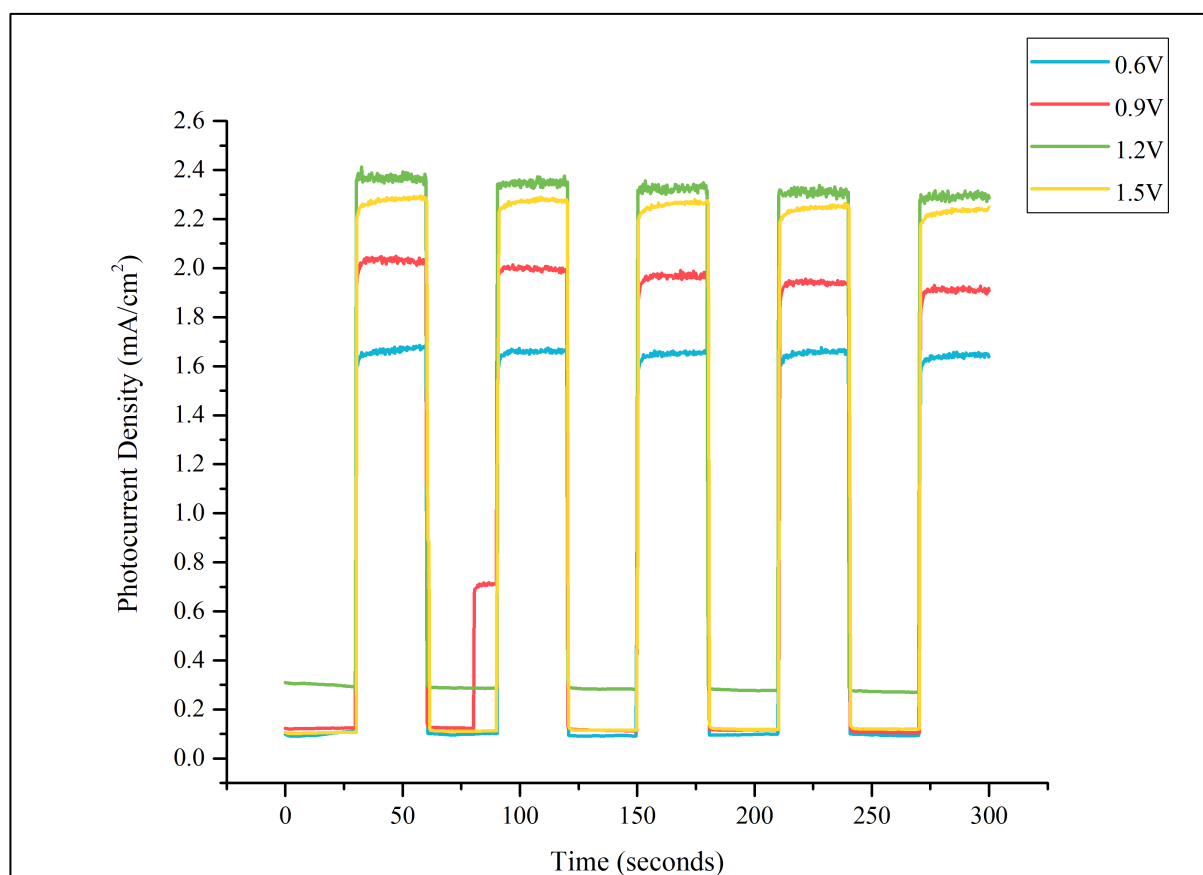


Figure 3.43 - The chronoamperometry obtained for the optimised photoanode with (blue) 0.6 V, (red) 0.9 V, (green) 1.2 V and (yellow) 1.5 V. Note that the constant experimental details were that an 0.5 M NaCl supporting electrolyte was utilised with a chopped 1 Sun of solar light (on/off, 30 s each) for 5 minutes.

The benefit of utilising PEC is that it combines electrochemistry with photocatalysis [32]. This method results in the separation of the photogenerated electrons and holes which improves the efficiency of the process [32]. It achieves this by the applied potential causing band-bending to occur in the semiconductor material [34]. The band-bending creates a gradient which drives the electrons away from the photoanode surface to the FTO substrate, where it travels via an external circuit and into the counter electrode [34, 35]. This band-bending effect only occurs when the potential is above the flat band potential [34]. Therefore, from the LSV it was shown that the flat-band potential for this system was approximately 0.25 - 0.3 V (Figure 3.24), thus the applied potential needed to be above this value for effective charge separation.

As Figure 3.43 demonstrates increasing the applied potential increases the photocurrent production due to the band-bending driving the electrons to the counter electrode [34]. By driving the electrons from the photoanode surface the photogenerated holes have longer lifetime to split water molecules or degrade pollutants [36]. However, as the data showed the

increase in applied potential only enhances the photocurrent production to a certain value, namely 1.2 V (vs Ag/AgCl) for this PEC system. Beyond 1.2 V (vs Ag/AgCl) the photocurrent generated decreases, due to the light intensity being fixed at a permanent intensity [36]. This means only a finite number of electrons can be produced, as electron excitation depends on the amount of photons absorbed [36]. Another reason why increasing the applied potential above this limit can cause a decrease in performance is due to the space charge layer. The space charge layer becomes nearly the same thickness as the film at the optimum applied potential but beyond this then the space charge layer is relocated thus decreasing the amount of photogenerated carriers [36]. The maximum applied potential varies for each system or pollutant it is therefore key to identify the maximum potential was for this system [32, 37, 38]

3.3 Conclusion

A monoclinic crystalline WO_3 layer was successfully synthesised on a conductive substrate. In literature monoclinic WO_3 crystallinity phase has displayed the highest photocatalytic activity. Also, it was able to absorb visible wavelengths up to 450 nm which means it is a visible light absorber. This achieved the aim of producing a visible light photoanode. However, the photocurrent production was low (0.8 mA/cm^2) meaning that the photoanode experienced high charge recombination due to poor electron-hole separation at the photoanode/electrolyte interface.

The BiVO_4 was successfully optimised and XRD showed a monoclinic crystalline phase. A monoclinic BiVO_4 usually exhibits the highest photocatalysis activity among its other phases. Whilst the DR UV-Vis analysis also showed that the synthesised BiVO_4 was able to absorb wavelengths up to 490 nm. This meant that when adding BiVO_4 layer to WO_3 the light absorbance range increased for the photoanode, while also enhancing the charge separation and preventing charge recombination, thus increasing the photocurrent.

It was hypothesised that creating a $\text{WO}_3/\text{BiVO}_4$ photoanode should result in an increase of the photocurrent as it enables charge separation. This hypothesis was met as adding a BiVO_4 layer to the WO_3 photoanode increased the photocurrent by a 3.44 -fold. This would indicate that the heterojunction helped prevent any charge recombination occurring thus helping electrons to travel faster to the FTO substrate. While the DR UV-Vis analysis exhibited that adding BiVO_4 helped increase the wavelength absorption range by 40 nm. This meant that the $\text{WO}_3/\text{BiVO}_4$

photoanode could utilise a higher portion of visible light, resulting in this photoanode being a visible light absorber. This demonstrated that the aim was met during this chapter.

To help optimise the $\text{WO}_3/\text{BiVO}_4$ photoanode then it was necessary to determine the effect of altering each semiconductor's coating cycles separately. It was found that increasing the layer from 1 to 2 increased the photocurrent production as there was more WO_3 (good electron mobility) to help effectively transfer the electrons from BiVO_4 to the FTO substrate and absorb more electrons. However, increasing the WO_3 coating cycles above 2 resulted in a decrease in performance. This is due to a higher resistance in the WO_3 layer thus allowing the electrons to recombine with the holes. It was found that 1 layer of BiVO_4 was optimum for $2\text{WO}_3/\text{BiVO}_4$ as any further increase caused a decrease in performance. This is due to poor electron mobility of BiVO_4 which means its more susceptible to charge recombination, which lowers the photocurrent. Therefore, the optimised photoanode was 2 layers of WO_3 with 1 layer of BiVO_4 and it achieved a high photocurrent of 2.75 mA/cm^2 .

It is known that the effects of the operating parameters can help influence the photoanode's performance. Therefore, to help ensure decisions for optimising pollutant degradation would result in positive results it was important to investigate how these parameters affected the $2\text{WO}_3/1\text{BiVO}_4$ photoanode. It was demonstrated that a supporting electrolyte was required for PEC to be successful and the best electrolyte for this system was 1 M NaCl. A high concentration of NaCl allowed the photocurrent production to increase significantly as it increases ion transfer. It was also found that increasing the applied potential increased the photocurrent production as it helped improve charge separation. However, this was only to 1.2 V (vs Ag/AgCl) as beyond this the applied potential decreased slightly. This is due to the light intensity being fixed which resulting in 1.2 V (vs Ag/AgCl) transferring the maximum number of electrons possible.

3.4 Bibliography

1. Mi, Q., et al., *A quantitative assessment of the competition between water and anion oxidation at WO₃ photoanodes in acidic aqueous electrolytes*. Energy & Environmental Science, 2012. **5**(2): p. 5694-5700.
2. Kalanur, S.S., L.T. Duy, and H. Seo, *Recent Progress in Photoelectrochemical Water Splitting Activity of WO₃ Photoanodes*. Topics in Catalysis, 2018. **61**(9): p. 1043-1076.
3. Zeng, Q., et al., *Synthesis of WO₃/BiVO₄ photoanode using a reaction of bismuth nitrate with peroxovanadate on WO₃ film for efficient photoelectrocatalytic water splitting and organic pollutant degradation*. Applied Catalysis B: Environmental, 2017. **217**: p. 21-29.
4. Holliman, P.J., et al., *Low temperature sintering of binder-containing TiO₂/metal peroxide pastes for dye-sensitized solar cells*. Journal of Materials Chemistry A, 2014. **2**(29): p. 11134-11143.
5. Reyes-Gil, K.R., et al., *Comparison between the Quantum Yields of Compact and Porous WO₃ Photoanodes*. The Journal of Physical Chemistry C, 2013. **117**(29): p. 14947-14957.
6. Singh, P., et al., *Review on various strategies for enhancing photocatalytic activity of graphene based nanocomposites for water purification*. Arabian Journal of Chemistry, 2020. **13**(1): p. 3498-3520.
7. Wei, P., et al., *2D/3D WO₃/BiVO₄ heterostructures for efficient photoelectrocatalytic water splitting*. International Journal of Hydrogen Energy, 2021. **46**(54): p. 27506-27515.
8. Du, H., et al., *Synthesis of BiVO₄/WO₃ composite film for highly efficient visible light induced photoelectrocatalytic oxidation of norfloxacin*. Journal of Alloys and Compounds, 2019. **787**: p. 284-294.
9. Madhavi, V., et al., *Fabrication of porous 1D WO₃ NRs and WO₃/BiVO₄ hetero junction photoanode for efficient photoelectrochemical water splitting*. Materials Chemistry and Physics, 2021. **274**: p. 125095.
10. Xu, S., et al., *One-dimensional WO₃/BiVO₄ heterojunction photoanodes for efficient photoelectrochemical water splitting*. Chemical Engineering Journal, 2018. **349**: p. 368-375.
11. Chatchai, P., et al., *Efficient photocatalytic activity of water oxidation over WO₃/BiVO₄ composite under visible light irradiation*. Electrochimica Acta, 2009. **54**(3): p. 1147-1152.
12. Harrick Scientific Products, I., *What is Kubelka-Munk*, in *FAQs*, H.S. Products, Editor.: <https://harricksci.com/faqs/>.
13. Makuła, P., M. Pacia, and W. Macyk, *How To Correctly Determine the Band Gap Energy of Modified Semiconductor Photocatalysts Based on UV-Vis Spectra*. The Journal of Physical Chemistry Letters, 2018. **9**(23): p. 6814-6817.
14. Poongodi, S., et al., *Synthesis of hierarchical WO₃ nanostructured thin films with enhanced electrochromic performance for switchable smart windows*. RSC Advances, 2015. **5**(117): p. 96416-96427.
15. Cooper, J.K., et al., *Indirect Bandgap and Optical Properties of Monoclinic Bismuth Vanadate*. The Journal of Physical Chemistry C, 2015. **119**(6): p. 2969-2974.
16. Stoll, T., et al., *Visible-light-promoted gas-phase water splitting using porous WO₃/BiVO₄ photoanodes*. Electrochemistry Communications, 2017. **82**: p. 47-51.

17. Grigioni, I., et al., *Dynamics of Photogenerated Charge Carriers in WO₃/BiVO₄ Heterojunction Photoanodes*. Journal of Physical Chemistry C, 2015. **119**(36): p. 20792-20800.
18. Su, J., et al., *Nanostructured WO₃/BiVO₄ Heterojunction Films for Efficient Photoelectrochemical Water Splitting*. Nano Letters, 2011. **11**(5): p. 1928-1933.
19. Pedroni, M., et al., *Multilayer WO₃/BiVO₄ Photoanodes for Solar-Driven Water Splitting Prepared by RF-Plasma Sputtering*. Surfaces, 2020. **3**(1): p. 105-115.
20. Liu, Y., et al., *Facet effect on the photoelectrochemical performance of a WO₃/BiVO₄ heterojunction photoanode*. Applied Catalysis B: Environmental, 2019. **245**: p. 227-239.
21. Scientific, T.F. *Oxygen*. XPS Knowledge Base 2013.
22. Kalanoor, B.S., H. Seo, and S.S. Kalanur, *Recent developments in photoelectrochemical water-splitting using WO₃/BiVO₄ heterojunction photoanode: A review*. Materials Science for Energy Technologies, 2018. **1**(1): p. 49-62.
23. Nareejun, W. and C. Ponchio, *Novel photoelectrocatalytic/solar cell improvement for organic dye degradation based on simple dip coating WO₃/BiVO₄ photoanode electrode*. Solar Energy Materials and Solar Cells, 2020. **212**: p. 110556.
24. Darmawi, S., et al., *Correlation of electrochromic properties and oxidation states in nanocrystalline tungsten trioxide*. Physical Chemistry Chemical Physics, 2015. **17**(24): p. 15903-15911.
25. Rodríguez-Gutiérrez, I., et al., *An intensity-modulated photocurrent spectroscopy study of the charge carrier dynamics of WO₃/BiVO₄ heterojunction systems*. Solar Energy Materials and Solar Cells, 2020. **208**: p. 110378.
26. Grigioni, I., M.V. Dozzi, and E. Selli, *Photoinduced electron transfer in WO₃/BiVO₄ heterojunction photoanodes: effects of the WO₃ layer thickness*. Journal of Physics: Condensed Matter, 2019. **32**(1): p. 014001.
27. Cao, Y., et al., *Surface Engineering of WO₃/BiVO₄ to Boost Solar Water-Splitting*. Catalysts, 2020. **10**(5): p. 556.
28. Hong, S.J., et al., *Heterojunction BiVO₄/WO₃ electrodes for enhanced photoactivity of water oxidation*. Energy & Environmental Science, 2011. **4**(5): p. 1781-1787.
29. Grigioni, I., et al., *WO₃/BiVO₄ Photoanodes: Facets Matching at the Heterojunction and BiVO₄ Layer Thickness Effects*. ACS Applied Energy Materials, 2021. **4**(8): p. 8421-8431.
30. Lianos, P., *Review of recent trends in photoelectrocatalytic conversion of solar energy to electricity and hydrogen*. Applied Catalysis B: Environmental, 2017. **210**: p. 235-254.
31. Tolod, K.R., S. Hernández, and N. Russo, *Recent Advances in the BiVO₄ Photocatalyst for Sun-Driven Water Oxidation: Top-Performing Photoanodes and Scale-Up Challenges*. Catalysts, 2017. **7**(1): p. 13.
32. Daghrrir, R., P. Drogui, and D. Robert, *Photoelectrocatalytic technologies for environmental applications*. Journal of Photochemistry and Photobiology A: Chemistry, 2012. **238**: p. 41-52.
33. Xiao, S., et al., *Enhanced photoelectrocatalytic degradation of ammonia by in situ photoelectrogenerated active chlorine on TiO₂ nanotube electrodes*. J Environ Sci (China), 2016. **50**: p. 103-108.
34. Guilherme Garcia Bessegato, T.T.G.a.M.V.B.Z., *Enhancement of Photoelectrocatalysis Efficiency by Using Nanostructured Electrodes*, in *Modern Electrochemical Methods in Nano, Surface and Corrosion Science*, M. Aliofkhazraei, Editor. 2014: IntechOpen,.

35. Bessegato, G.G., et al., *Achievements and Trends in Photoelectrocatalysis: from Environmental to Energy Applications*. *Electrocatalysis*, 2015. **6**(5): p. 415-441.
36. Liang, F. and Y. Zhu, *Enhancement of mineralization ability for phenol via synergetic effect of photoelectrocatalysis of g-C₃N₄ film*. *Applied Catalysis B: Environmental*, 2016. **180**: p. 324-329.
37. Zhao, X., et al., *Photoelectrocatalytic degradation of 4-chlorophenol at Bi₂WO₆ nanoflake film electrode under visible light irradiation*. *Applied Catalysis B: Environmental*, 2007. **72**(1): p. 92-97.
38. Sun, J., et al., *H₂O₂ assisted photoelectrocatalytic degradation of diclofenac sodium at g-C₃N₄/BiVO₄ photoanode under visible light irradiation*. *Chemical Engineering Journal*, 2018. **332**: p. 312-320.

Chapter 4 : Ibuprofen Degradation

4.1 Introduction

The aim of this chapter is to establish if PEC can completely remove a model pharmaceutical compound from water without impacting on the environment. The model pharmaceutical compound chosen for this study was ibuprofen because as mentioned in Chapter 1 it is one of the most popular pharmaceutical compounds and it can cause various side effects to aquatic life. Therefore, it was necessary to see if this PEC system utilising a $\text{WO}_3/\text{BiVO}_4$ photoanode was able to completely remove ibuprofen from water. The work in this chapter involved; the optimisation of the PEC system to maximise the ibuprofen degradation, provide an explanation of how ibuprofen is degraded by identifying the reactive oxidising species involved and finally identified by-products produced during the degradation of ibuprofen via PEC.

4.2 Results and Discussion

4.2.1 Development of Ibuprofen Analysis

Due to the physical properties of ibuprofen many researchers have utilised liquid chromatography coupled with a UV detector (also known as LC-UV) to quantify its concentration in target samples. LC-UV has recently become a popular analytical tool due to several reasons namely its rapid, automatic, high precision and reproducibility.

The LC-UV system (Agilent 1200 LC-UV) was utilised with a Waters Xselect C-18 column (2.1 mm x 100 mm) which was constant for all methods and analysis work. To ensure that the LC-UV system was able to detect and quantify ibuprofen then the *sensitivity* was determined through method development. For all methods developed the mobile phases were kept constant and were 0.1% formic acid in water (Mobile A) and 100% acetonitrile (Mobile B) with starting ratios of 75% and 25% respectively.

Method I was developed using the LC-UV settings highlighted below (Table 4.1). The chromatogram (Figure 4.1) demonstrates that the method was successful as there was a sharp peak present at a retention time of 14.3 minutes. It demonstrates that the sensitivity was high for ibuprofen and the gradient pumping was adequate in eluting the ibuprofen at one time as

there was only one sharp peak. Agreeably, the blank sampled displayed no signal at the target detection conditions, thus verifying the selectivity of the method.

Table 4.1 - The first method developed for detection of ibuprofen via LC-UV.

Column	Xselect C-18 column (2.1 mm x 100 mm)		
Injection Volume (µL)	5		
Flowrate (mL/min)	0.250		
UV Wavelength Detection (nm)	260		
Gradient Pumping	Time (minutes)	Mobile Phase A: 0.1% Formic Acid in Water (%)	Mobile Phase B: 100% Acetonitrile (%)
	0	75	25
	1	75	25
	17	0	100
	24	0	100
	25	75	25
	35	75	25

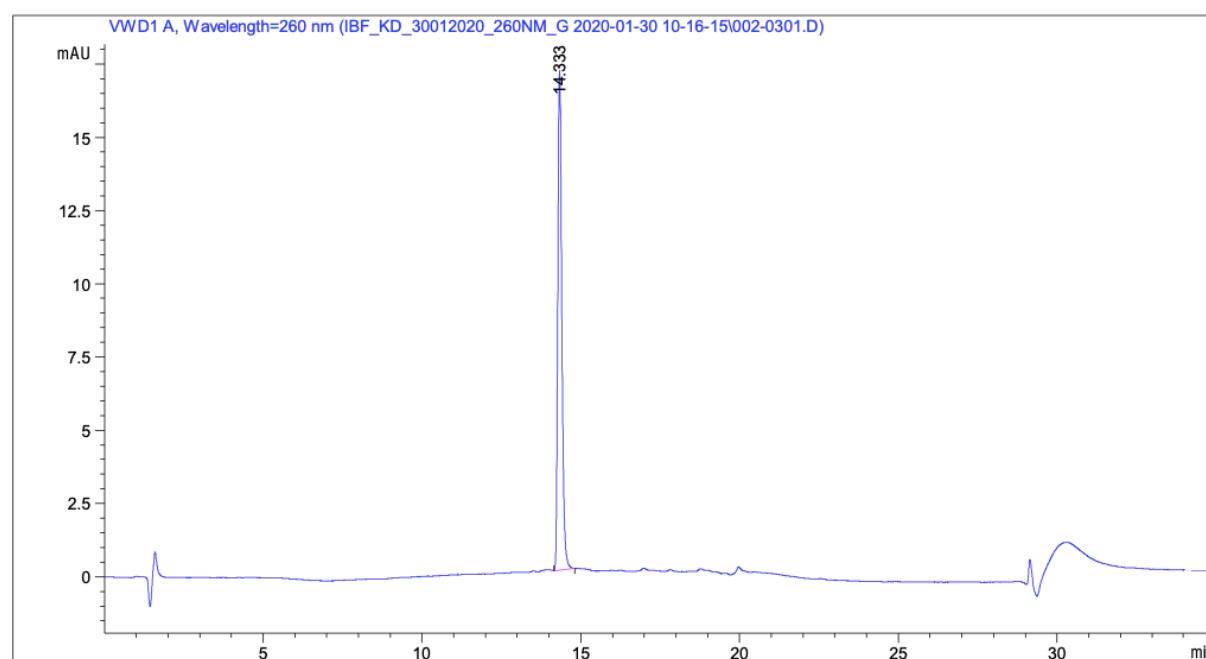


Figure 4.1 - Chromatogram of the ibuprofen standard when utilising LC-UV method 1.

To help increase the peak area the UV detection wavelength was changed to 265nm as ibuprofen has high absorption between wavelengths of 260-270 nm [1]. Utilising **Method II** (Table 2.8 in Chapter 2) resulted in a higher peak area for ibuprofen. Therefore, this method was chosen to quantify the amount of ibuprofen present in the sample. However, it was essential to determine the repeatability, accuracy, and precision of the method in quantifying ibuprofen.

4.2.1.2 Repeatability and Reproducibility of Ibuprofen LC-UV Method

Once the method for the LC-UV had been developed, a reproducibility (Section 2.5.2.2) and calibration test (Section 2.5.2.3) was conducted to ensure the system produced an accurate and precise analysis of the ibuprofen samples.

Table 4.2 - The calculated CV% and F-test value obtained for the retention time reproducibility.

Compound	CV% Day 1	CV% Day 2	F-Test Value
Ibuprofen	0.19	0.05	12.23

The assessment of the obtained retention times (Table 4.2) showed that they were highly repeatable as the CV% calculated for each day was < 1%. Thus, demonstrating there was very low variation in the retention times. The calculated F-test value (12.23) was significantly higher than the critical value (4.30) indicating a significant difference between the two sets of data. There is a significant difference due to the spread of the results being much lower on the second day ($CV\%_{\text{day 1}} > CV\%_{\text{day 2}}$). This reveals that the stability of LC-UV improves with longer runtime. Since both CV% values are < 5%, the retention times are found to have high repeatability [2].

Table 4.3 - The calculated CV% and F-test value for the injection repeatability of ibuprofen.

Compound	CV% Day 1	CV% Day 2	F-Test Value
Ibuprofen	0.18	0.89	3.89

The injection repeatability was determined to establish the stability of the analyte response (peak area), through the comparison of the peak areas obtained between the two days. The CV% for each was less than < 1% which translates to there being low variation of the peak areas obtained. This was also confirmed by the F-test value which was less than the critical value. Thus, confirming there was no significant difference between the two sets of data. This validates that the method developed for ibuprofen analysis, was able to produce repeatable and reproducible results.

4.2.1.3 Calibration Graph

The calibration was important to help determine the accuracy and precision of the method while also being used to calculate the concentration of ibuprofen in the samples.

Table 4.4 - A table displaying the values obtained from the regression statistics analysis.

R² Value	0.99
Standard Value	4.33
Intercept	-0.92
Gradient	1.32

The results from the calibration showed excellent linearity as the R² was > 0.99, as the closer the R² value is to 1 the closer the calibration trend is to a perfect line.

To help determine the accuracy and precision of the method developed for ibuprofen analysis, the concentrations of the QCs needed to be established, through the utilisation of Eq 2.9 (Chapter 2) and the values obtained from the regression statistics of the calibration results. The FDA bioanalytical method validation criteria was utilised to determine if the accuracy and precision of the QCs could be accepted. They state that QCs can only be accepted when they are within 15% of the known concentration except for the low concentration QCs where it should be within 20% [3]. As the accuracy and precision for all QCs (Table 4.5) were < 8% then the method demonstrates it is suitable for producing accurate and reliable concentrations within this calibration range.

Table 4.5 - A table displaying the calculated mean concentrations, accuracy % and precision % of the QCs.

QC Sample Name	Theoretical Concentration (µg/mL)	Actual Concentration (µg/mL)	Accuracy %	Precision %
QC Low	20	21.46	7.30	4.61
QC Mid	80	80.30	0.37	0.59
QC High	180	182.48	1.38	0.65

4.2.1.4 Instrument Detection Limit

The instrument detection limit (IDL) was assessed to evaluate the minimum concentration, which could be accurately quantified for the chosen test material by the developed LC-UV method. There are two methods for quantifying the IDL. The IDL value calculated via the statistical method (Eq 2.13) was 12.79 µg/mL which is higher than the lowest concentration of the calibration range. Therefore, as it is a more robust approach, the empirical method was utilised, which demonstrated the lowest (10 µg/mL) concentration showed a signal-to-noise (S/N) ratio of 20:1. A S/N ratio of > 3:1 means that the analyte's signal response is more significant than the background signal. This demonstrates that 10 µg/mL is an appropriate low

concentration for the calibration as it results in a significantly bigger signal than the blank signal.

The instrument quantification limit (IQL) also confirms that the instrument can quantify ibuprofen concentrations less than the low QC concentration (20 µg/mL) due to the QC's accuracy and precision being much less than < 20%.

4.2.1.5 Sample Preparation

LC-UV is an excellent analytical tool however, it is an extremely sensitive instrument due to the column containing a very narrow diameter and particles. Therefore, it is at risk of becoming blocked by insoluble particles in the samples. This would suggest that target samples should be filtered before running them on the LC-UV system to prevent any of these issues.

There are many different filters that can be used to help filter samples for the LC-UV analysis. However, due to availability, the selection was narrowed down to PTFE hydrophobic (0.45 µm), PTFE hydrophilic (0.45 µm), PVDF hydrophilic (0.45 µm) and Regenerated Cellulose (0.45 µm). To validate the suitability of the filter for ibuprofen, then all five filters were tested and compared to the calibration standards.

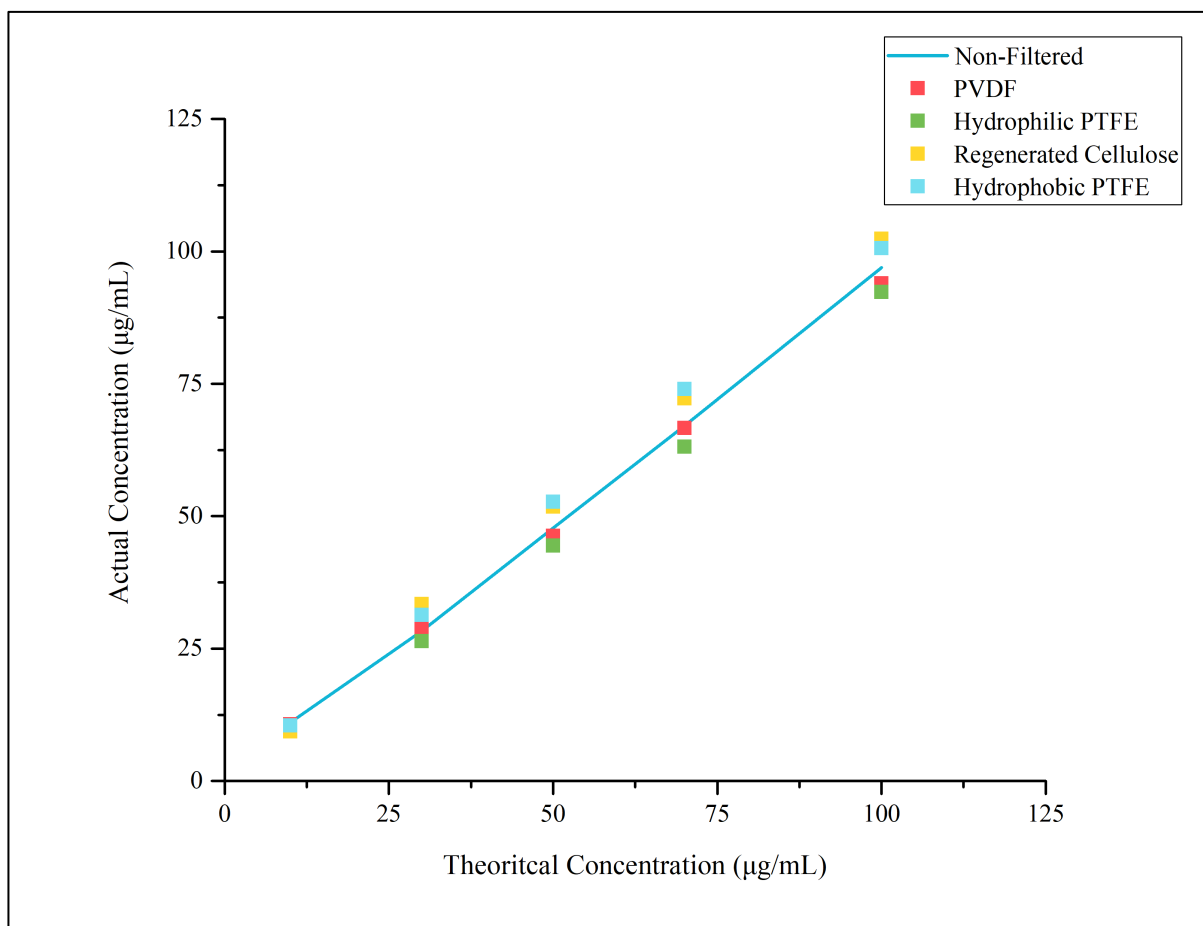


Figure 4.2 - A graph showing the ibuprofen concentration achieved for each filter.

Table 4.6 - A table displaying the difference in ibuprofen concentration between the filtered samples and the non-filtered standards.

Sample Name	Concentration difference (%) between Filtered Sample and Standard (to 2 d.p)
IBF 10 μ g PVDF	2.92
IBF 30 μ g PVDF	-1.51
IBF 50 μ g PVDF	3.09
IBF 70 μ g PVDF	0.65
IBF 100 μ g PVDF	3.06
IBF 10 μ g Hydrophilic PTFE	7.17
IBF 30 μ g Hydrophilic PTFE	6.56
IBF 50 μ g Hydrophilic PTFE	6.96
IBF 70 μ g Hydrophilic PTFE	5.96
IBF 100 μ g Hydrophilic PTFE	4.70
CC 1 10 μ g RC	14.94
CC 1 30 μ g RC	-18.20
CC 1 50 μ g RC	-8.41
CC 1 70 μ g RC	-7.68
CC 1 100 μ g RC	-5.63
CC 1 10 μ g Hydrophobic PTFE	4.89
CC 1 30 μ g Hydrophobic PTFE	-10.80
CC 1 50 μ g Hydrophobic PTFE	-10.42
CC 1 70 μ g Hydrophobic PTFE	-10.35
CC 1 100 μ g Hydrophobic PTFE	-3.83

The filter showing the closest ibuprofen concentrations to the calibration trend was the PVDF hydrophilic filter. It is known that PVDF hydrophilic filters are compatible with aqueous and organic samples, which the sample solution contains to help dissolve the ibuprofen. It is worth mentioning that any ibuprofen captured in the PVDF hydrophilic filter can result in degradation errors when analysing the target samples. Therefore, it was vital to calculate the *recovery percentage* of ibuprofen achieved by the filter to help minimise these errors in the degradation calculations. To determine recovery (%) then the percentage yield formula (the ratio between the amount of ibuprofen collected after filter and the amount of ibuprofen present before the filter) was utilised. Therefore, it was essential to prepare a non-filtered and filtered standard using the same 100 μ g/mL ibuprofen solution. This would help calculate the ibuprofen concentration before and after filtering. Thus, demonstrating the amount of ibuprofen if there

was no filter. For the filter analysis experiments it was essential to prepare two types of ibuprofen solutions. One solution was made up in 0.5 M NaCl while the other solution was made up in 1 M NaCl. This was necessary to see if the supporting electrolyte concentration influences the ibuprofen recovery in the filters.

Table 4.7 - A table displaying the calculated percentage yields and loss (%).

Sample Name	Percentage Yield (%)	Average Recovery (%)	Precision (%)
0.5M NaCl IBF 1	96.19	96.43	0.36
0.5M NaCl IBF 2	96.27		
0.5M NaCl IBF 3	96.83		
1M NaCl IBF 1	95.06	94.76	0.28
1M NaCl IBF 2	94.58		
1M NaCl IBF 3	94.64		

The recoveries (%) achieved from the filtering of ibuprofen were 96.43% and 94.76% for 0.5 M NaCl and 1 M NaCl respectively with high precision. This demonstrates that while high recoveries were achieved, the ibuprofen interacts with the filter, thus causing a small amount of ibuprofen to remain in the filter. These values need to be taken into consideration when calculating the ibuprofen degradation percentage. Unexpectedly slightly lower recoveries were established for the 1 M of NaCl ibuprofen standards than 0.5 M NaCl. Therefore, it was important to test the two different supporting concentrations to ensure the proper recovery percentages were utilised in the ibuprofen degradation calculations.

4.2.2 Ibuprofen Degradation Via Photoelectrocatalysis

Previous studies have demonstrated the success of utilising PEC in the degradation of ibuprofen [4-7]. Therefore, this PEC system should be able to degrade ibuprofen. However, there are no existing reports to explain how the operating parameters effect the ibuprofen degradation.

4.2.2.1 The Effect of Light Irradiation

The PEC performance is highly dependent on the light absorption behaviour of the photoanode. Hence it was valuable that this photoanode (2WO₃/1BiVO₄) was able to absorb wavelengths up to 490 nm (utilising UV and visible light). A higher absorbance of light photons results in higher photocharge carrier generation (electrons and holes) for catalysis reactions, as electrons are excited when photons (from light) with energies the same or higher than the bandgap energy of the photoanode are absorbed by the photoanode [8-11]. This electron excitation produces

holes in the valance band which can either degrade ibuprofen directly or split water to produce reactive species that degrade ibuprofen [4, 5]. Therefore, it would be expected that ibuprofen degradation occurs when light irradiates the photoanode surface.

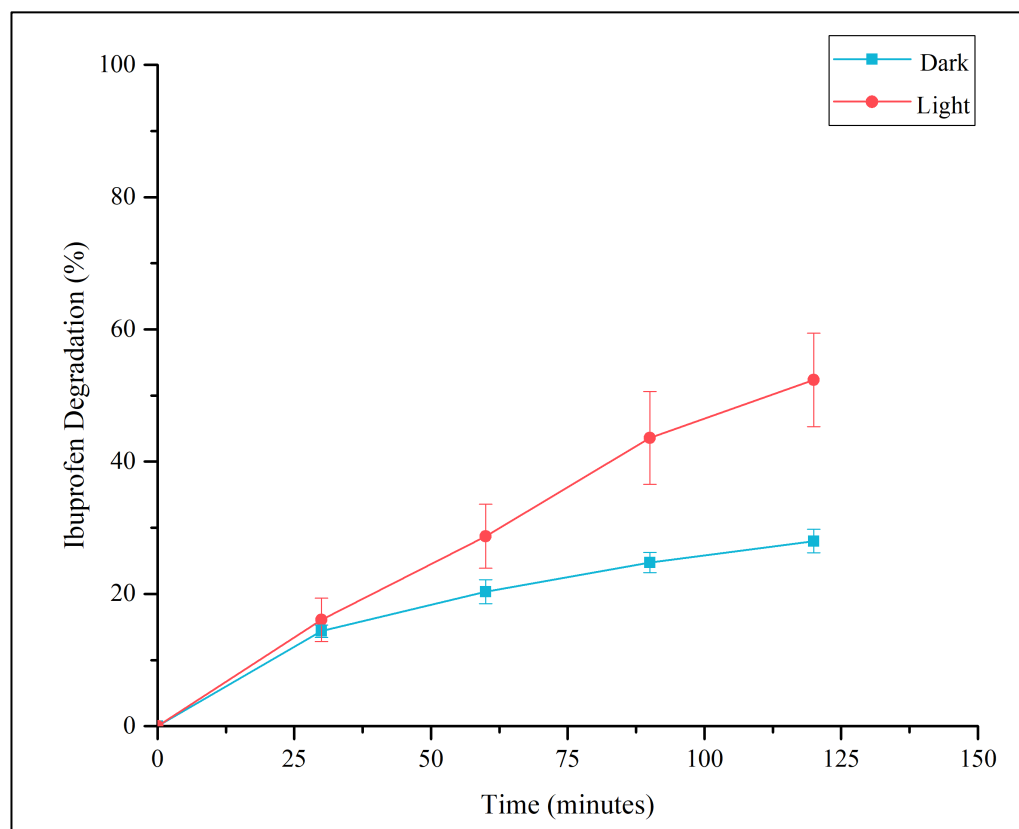


Figure 4.3 - A graph showing the ibuprofen degradation during the dark and light (1 Sun of solar light) PEC process with the following conditions 0.5 M NaCl as supporting electrolyte, 0.6 V (vs Ag/AgCl) as an applied potential and 2 hours of run time.

To establish the adsorption equilibrium time for ibuprofen onto the photoanode surface then the PEC experiment (0.5 M NaCl, 0.6 V vs Ag/AgCl, 2 hours runtime) was ran in the dark. Figure 4.3 demonstrates the adsorption equilibrium is achieved within the first 30 minutes as the slope of the degradation went from being sharp to gradual which implies the absorption equilibrium was saturated after 30 minutes. Another indication that the degradation in ibuprofen was related to the absorption of ibuprofen onto the photoanode surface is that the chromatogram obtained for the 120-minute treatment sample (Figure 4.5) indicated no by-products. As no additional peaks were observed when comparing to the 0-minute treatment sample (Figure 4.4). However, after 30 minutes of PEC treatment utilising light there was by-product formation at 15.49 minutes (Figure 4.6). Therefore, all ibuprofen degradation experiments conducted in this thesis required an initial 30 minutes in the dark to achieve absorption equilibrium.

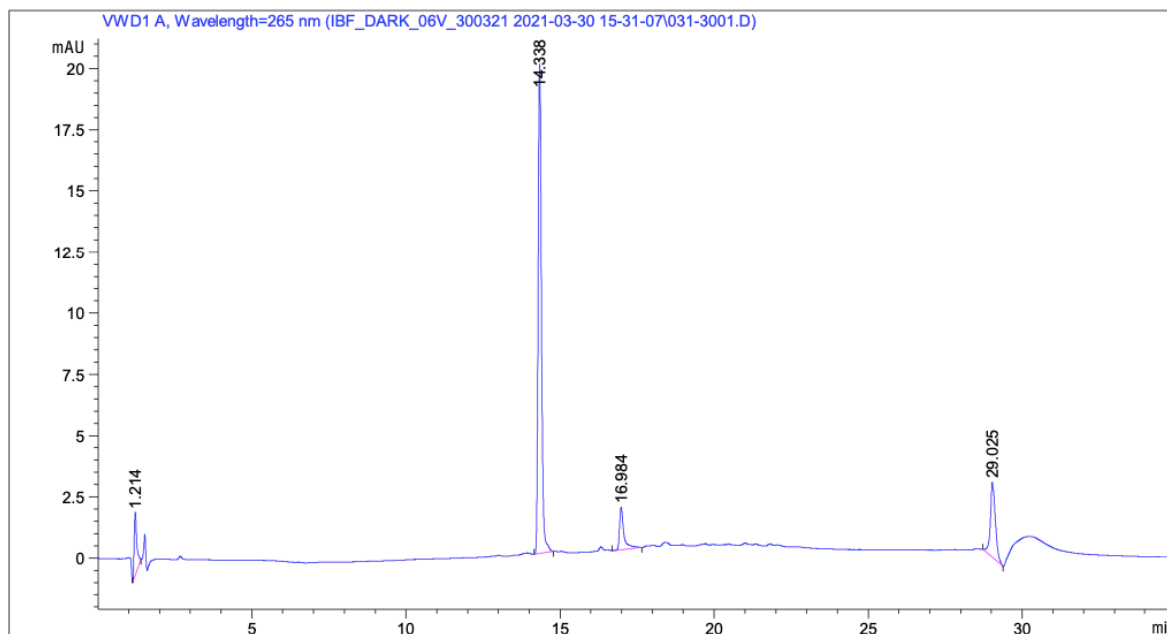


Figure 4.4 - Chromatogram obtained from the LC-UV analysis of 0-minute dark sample.

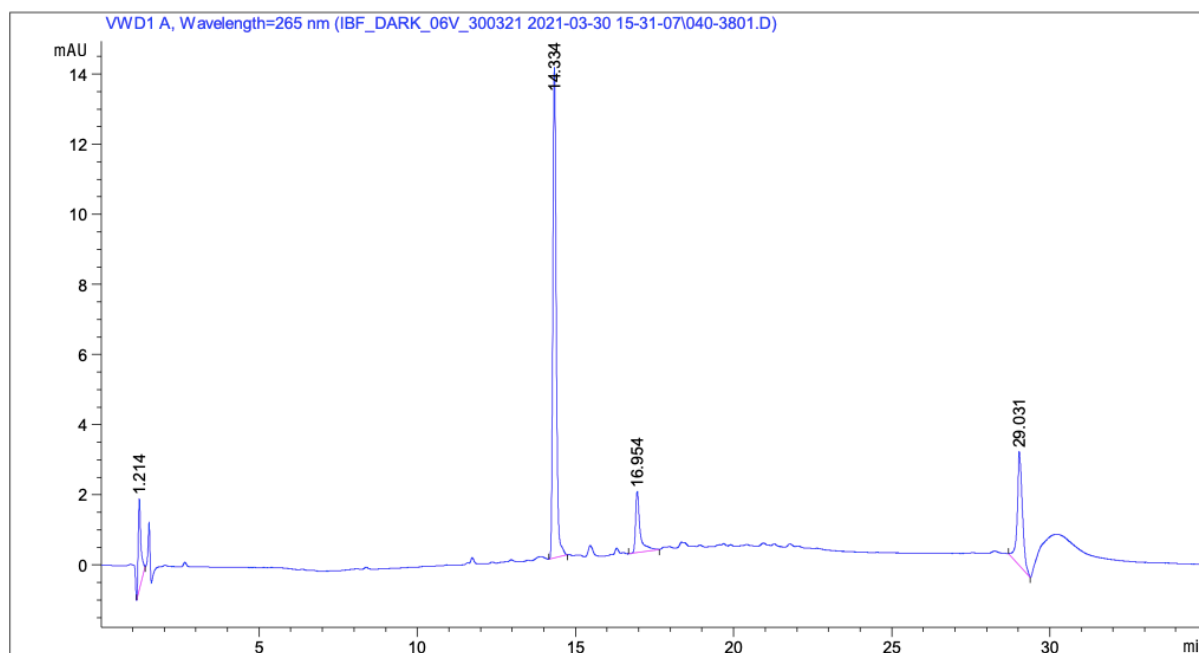


Figure 4.5 - Chromatogram obtained from the LC-UV analysis of 120-minute dark sample.

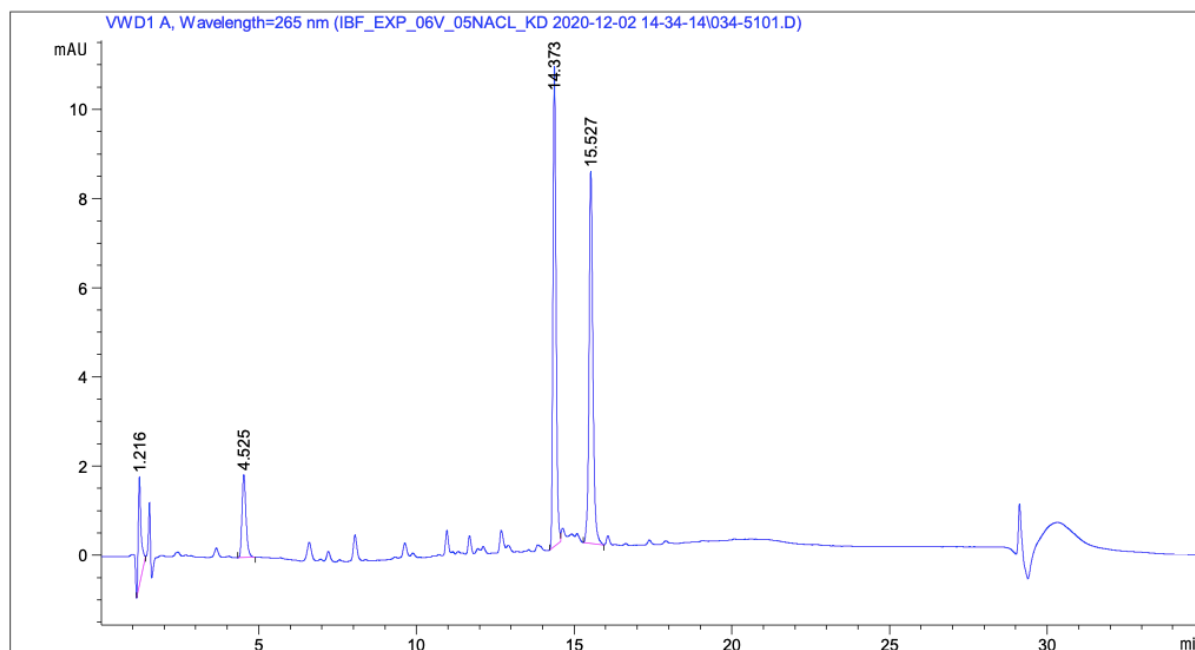


Figure 4.6 - Chromatogram obtained from the LC-UV analysis of 30-minute light sample.

As Figure 4.3 demonstrates the ibuprofen degradation increases from 27.99% to 52.38% when the photoanode is irradiated by simulated solar light. The enhancement of ibuprofen degradation under light irradiation conditions is due to combining photocatalysis and electrochemical oxidation [5-7]. It is expected that the photoanode, generates holes which produces reactive species such as hydroxyl radicals and active chlorine (from the NaCl supporting electrolyte) to degrade ibuprofen when irritated by light. As the result of ibuprofen degradation is linearly dependent on the light duration. This demonstrated that light irradiation is key for driving the PEC ibuprofen degradation process.

Importantly, the results confirmed that PEC is successful in ibuprofen degradation, but it does not achieve 100% degradation. It is therefore crucial to alter another operating parameter to help maximise the degradation of ibuprofen for this system. As it has been previously shown that increasing the applied potential helps to improve charge separation, it was decided to vary the applied potential and evaluate whether it increases ibuprofen degradation.

4.2.2.1 The Effect of Applied Potential

Evidence exists that the applied potential to the circuit affects the pollutant degradation [12]. Applying an electric potential to the system helps increase band-bending in the photoanode, thus driving the electrons from the photoanode surface to the counter electrode via an external circuit [13-15]. Thus lowering the charge recombination rate and resulting in the holes' lifetime

extending for hydroxy radical production (indirect pollutant degradation) or direct pollutant degradation [13-15]. To define the influence of the applied potential on the PEC ibuprofen degradation performance, then the PEC experiment was carried out with different applied potentials (0.6 V to 1.5 V).

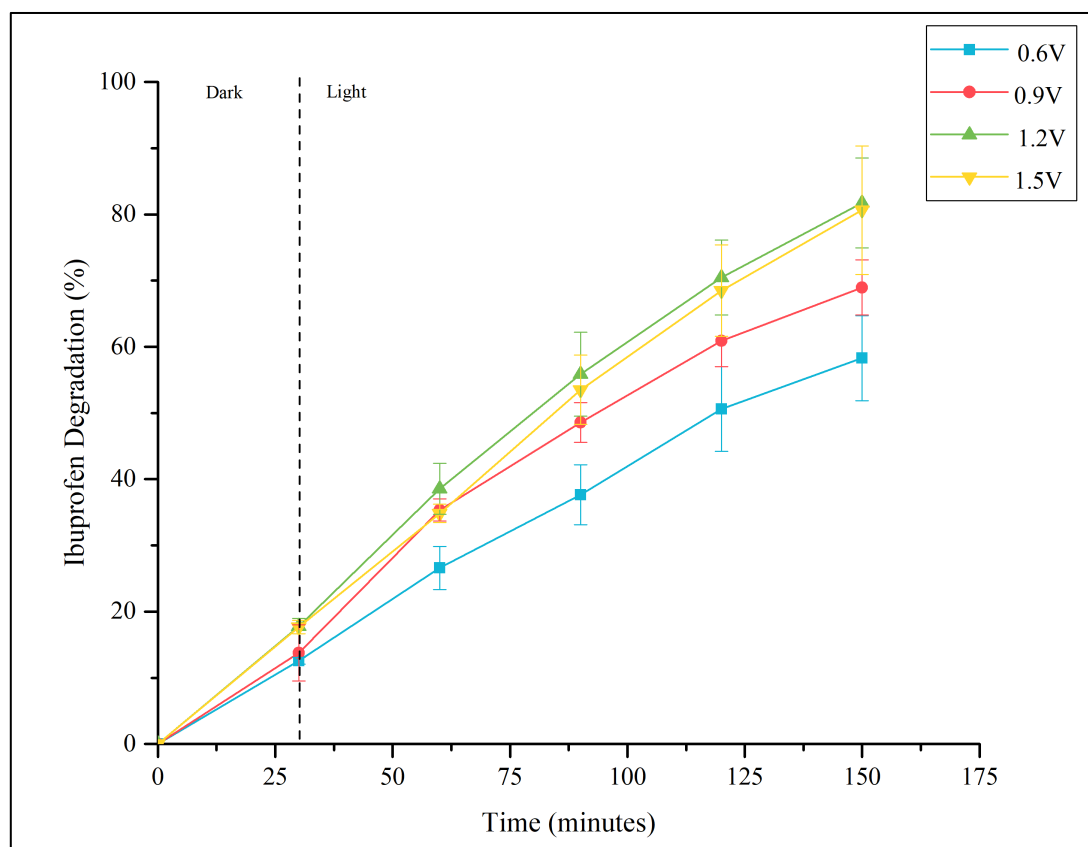


Figure 4.7 - A graph demonstrating the ibuprofen degradation achieved for each PEC experiment with the following conditions 0.5 M NaCl, 30 minutes in dark then 2 hours with 1 Sun of Simulated Solar Light (blue) 0.6 V vs Ag/AgCl, (red) 0.9 V vs Ag/AgCl, (green) 1.2 V vs Ag/AgCl and (yellow) 1.5 V vs Ag/AgCl.

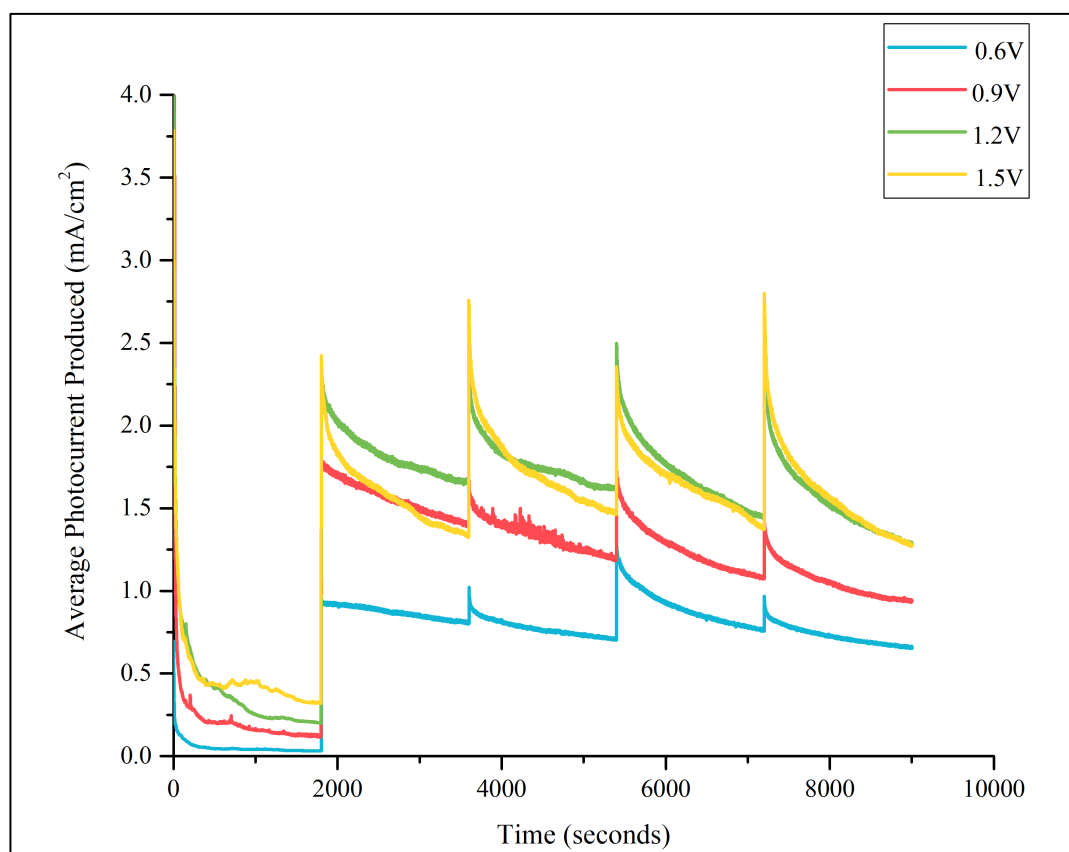


Figure 4.8 - The photocurrent produced by the photoanode during the ibuprofen degradation experiments in Figure 4.7.

The results presented in Figure 4.7 advocate that the ibuprofen degradation was distinctly affected by the applied potential. As expected, increasing the applied potential from 0.6 to 1.2 V (vs Ag/AgCl) resulted in the ibuprofen degradation enhancing from 58.28% to 81.73%. This is due to the charge carrier separation effect caused by the applied potential which controls the band-bending in the photoanode. Increasing the band-bending by increasing the applied potential drives the electrons from the photoanode surface to the counter electrode thus separating them from the reaction sites and allowing more holes to be available for ibuprofen degradation [13-15]. The chronoamperometry studies (Figure 4.8) demonstrate that increasing the applied potential from 0.6 V to 1.2 V (vs Ag/AgCl) promotes the photocurrent production due to charge separation affect. This results in more holes being available on the photoanode surface for either degrading the ibuprofen directly or producing reactive species for ibuprofen degradation.

The photocurrent generation was slightly reduced after increasing the applied potential 1.2 V to 1.5 V (vs Ag/AgCl). The reduction in photocurrent generation maybe due to several reasons. Firstly, there can only be a maximum amount of electrons produced as the light intensity is

fixed at 1 Sun. It means the applied potential can only drive the electrons available on the photoanode surface. Hence continually increasing the applied potential cannot constantly increase the ibuprofen degradation as there are no extra electrons available on the surface. This was shown in Figure 4.8 as the photocurrent produced was slightly lower for 1.5 V than 1.2 V (vs Ag/AgCl). Secondly at the optimal applied potential, the space charge layer becomes nearly the same thickness as the photoanode thus achieving complete charge carrier separation [16]. Beyond this optimal value the space charge layer has to relocate thus causing charge recombination to occur and lowering pollutant degradation [16]. Thirdly at higher applied potentials the formation of intermediates occurs at faster rates [17]. Therefore, there is more competition for the active sites which can be blocked by some intermediates resulting in a reduction in ibuprofen degradation [17]. Finally increasing the applied potential above the optimal can result in a competitive reaction i.e generation of oxygen (O_2), thus reducing the availability of reactive species for ibuprofen degradation [15].

Both Figure 3.43 (in Chapter 3) and Figure 4.8 suggested that $2WO_3/1BiVO_4$ photoanode based PEC cells function at high rate of ibuprofen degradation under optimal applied potential 1.2 V (vs Ag/AgCl). Therefore, this value was chosen as the optimum applied potential and was utilised for the other ibuprofen degradation experiments to help optimise the additional operating parameters. Note that even this applied potential did not result in complete degradation (81.73%). Therefore, the next step was to alter the concentration of the supporting electrolyte (NaCl) as it can help improve conductivity thus enhancing the ion transfer.

4.2.2.3 The Effect of Electrolyte Concentration

The ionic species present in the electrolyte provide a conductivity which enables good transfer of ions to the photoanode and cathode surfaces as the ions scavenge the photocharge carriers to the electrolyte [13]. There are several different types of supporting electrolytes that have been tested by other researchers. However, sodium chloride (NaCl) based aqueous electrolyte was selected for several reasons. Firstly utilising NaCl as the supporting electrolyte enables the production of active chlorine, which can degrade pollutants [18]. Secondly in Chapter 3, it was demonstrated that utilising NaCl resulted in a higher photocurrent production due to enhanced charge separation when compared to Na_2SO_4 (Figure 3.40). This indicates that NaCl helps the photoanode achieve higher electron hole separation at electrode/electrolyte interfaces, thus improving reactive species production.

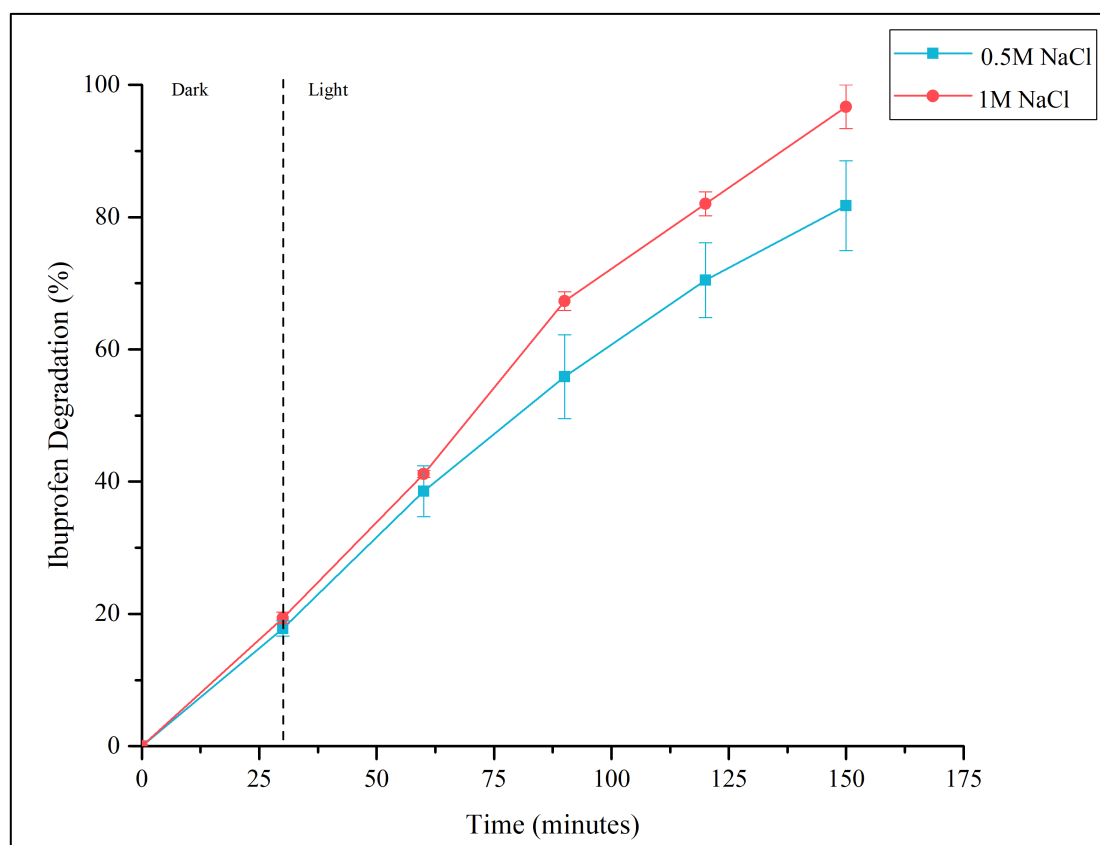


Figure 4.9 - PEC ibuprofen degradation vs time plot for different concentrations of the NaCl electrolyte. Note that the PEC experiment was conducted at applied potential 1.2 V Vs Ag/AgCl). The simulated solar light irradiation (1 Sun) was used for PEC experiments.

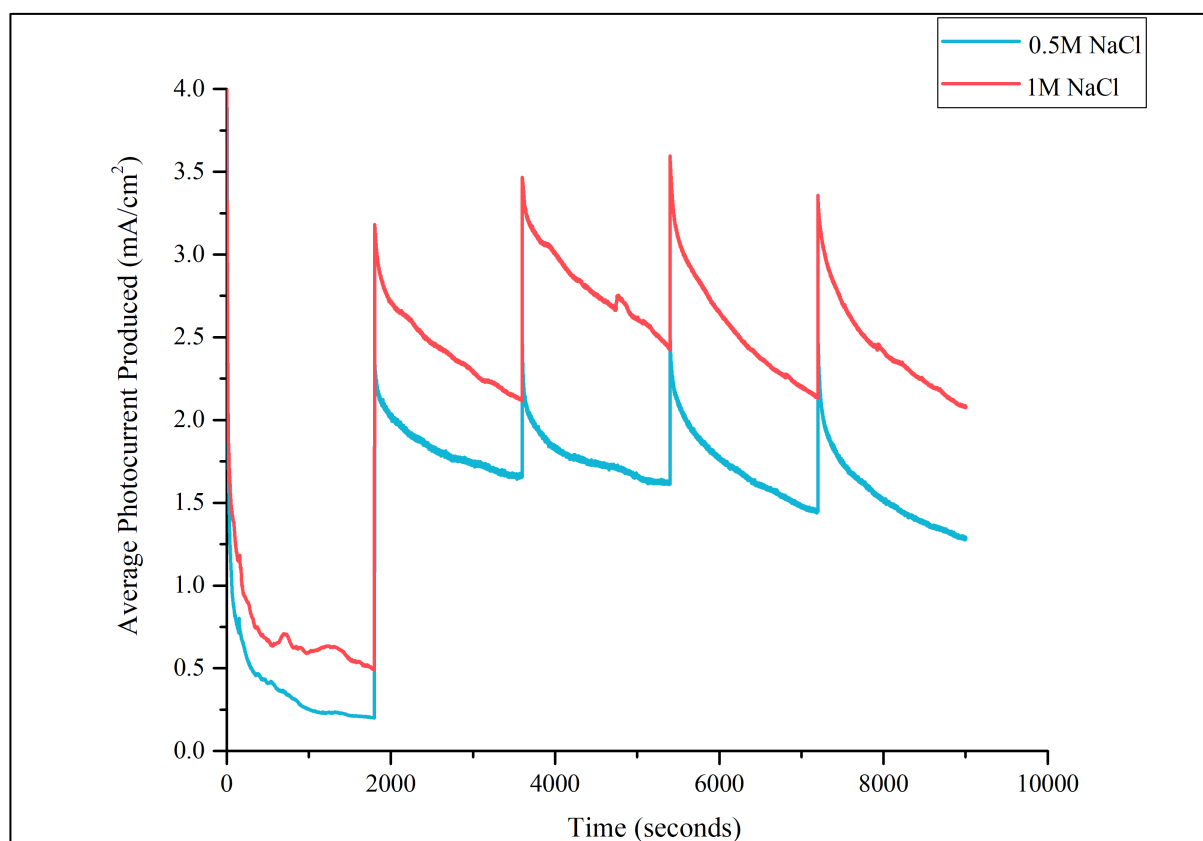


Figure 4.10 - The photocurrent produced by the photoanode during the ibuprofen degradation experiments in Figure 4.9.

As expected, the ibuprofen degradation has increased by 13.06% when doubling the sodium chloride (NaCl) concentration from 0.5 M to 1 M (Figure 4.9). Figure 4.10 demonstrates how increasing the supporting electrolyte's concentration promoted photocurrent production. The higher concentration of NaCl in the electrolyte significantly improves ionic conductivity of the electrolyte, thus facilitating faster ion transfer and resulting in more holes being transferred to the electrolyte for ibuprofen degradation. Also, a higher amount of chlorine ions in the solution results in a higher amount of active chlorine (Eq 4.3 - 4.5) such as Cl_2 , HClO , OCl^- being produced during the PEC process. As active chlorine species have disinfecting properties, it has been anticipated they degrade pollutants [18, 19]. It is suggested that higher production of active chlorine is responsible for the increase in ibuprofen degradation. Overall increasing the electrolyte concentration to 1 M resulted in an average ibuprofen degradation of 96.70%. It has been demonstrated by other studies that a further increase of the concentration may decrease the ibuprofen degradation. This is due to chloride ions reacting with the holes and hydroxyl radicals instead of the ibuprofen, because the absorption of chloride ions is faster than pollutants onto the photoanode surface [19, 20]. It was therefore decided to keep the electrolyte concentration at 1 M. To further achieve complete ibuprofen degradation then it would be recommended to extend the light irradiation duration or increase the photoanode surface area.

Increasing light irradiation duration would enhance the number of light photons absorbed thus extending the electron excitation which allows more holes for ibuprofen degradation. For instance, it would be expected that extending the light irradiation to 150 minutes (initial 30 minutes in the dark) could achieve complete ibuprofen degradation. In view of reproducibility the experiments were repeated three times. The repeats of the optimised ibuprofen degradation experiment resulted in two out of the three experiments achieving complete degradation within 2 hours of light irradiation while one achieved 90.09%. Thus, to ensure complete degradation for each run then 2.5 hours of light irradiation would be recommended

Alternatively, the pollutant degradation could be improved through enhancing the photoanode active area. Increasing the photoanode's surface area can help increase in the light photon absorption and improve the number of active sites for ibuprofen degradation. This PEC system utilises a photoanode with an active area of 1 cm² which is less compared to previous reports of PEC ibuprofen degradation [4, 5, 7]. It indicates that this study of PEC ibuprofen degradation (Figure 4.9) is very effective in degrading ibuprofen as it achieved an average of 96.70% ibuprofen degradation with only an active area of 1 cm² with 2 hours of treatment. At the same time, the other studies utilised photoanode active areas of 2 cm² and 3 cm² to achieve complete ibuprofen degradation within 1.5 hours and 2 hours of treatment respectively [5, 7].

4.2.3 The Degradation Pathway of Ibuprofen via The Optimised PEC System

Table 4.8 below is based on the previous information (see section 4.2.2.3) and shows the optimum operating parameters for this photoelectrocatalysis system.

Table 4.8 - The optimised photoelectrocatalysis method.

Ibuprofen concentration (µg/ml)	100
Electrolyte Concentration (M)	1
Light Irradiation Intensity (suns)	1 Suns Solar Light
Light Duration (mins)	120
Dark Duration (mins)	30 minutes
Samples Collection Period	1ml every 30 minutes
Syringe Filter for Sample	PVDF Hydrophillic

Utilising the parameters above for PEC ibuprofen degradation experiments achieved an average of 96.70% of degradation. However, degrading ibuprofen via PEC produced several by-products as the chromatogram (Figure 4.11) established several peaks at retention times of 3.61, 6.39, 9.61, 10.93, 15.48, 17.29. This implies that after the PEC process, the ibuprofen was transformed into other organic species, which would need to be defined in order to

determine the safety of this water treatment process. If these by-products are harmless than there is no issue in terms of releasing the solution into the environment. However, if the by-products are more hazardous then maybe another water treatment route or post treatment would be necessary. To further investigate the by-products then a mass spectrometer is required. To determine the by-products then it was essential to analyse which reactive species could be involved in the degradation of ibuprofen.

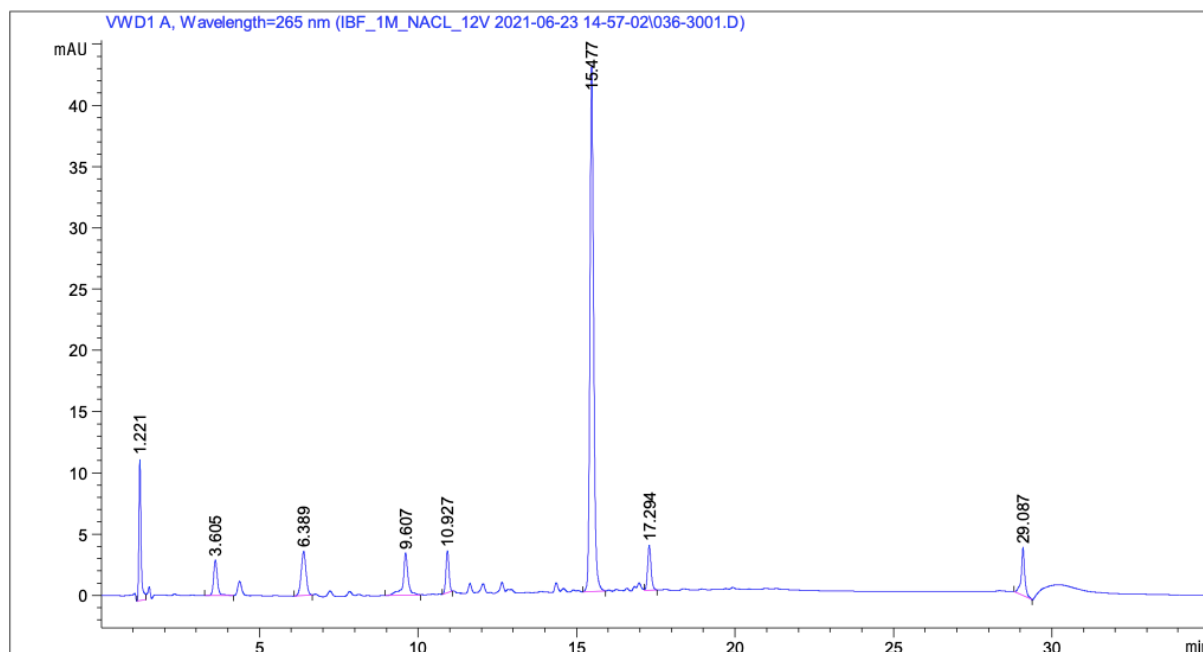


Figure 4.11 - The chromatogram obtained from the final sample of the optimised PEC ibuprofen degradation experiment.

4.2.4 Species Responsible for Ibuprofen Degradation

During the PEC process, there are several possible species which could be involved in pollutant degradation which are holes (h^+), hydroxyl radicals ($\bullet OH$) and active chlorine species [4-7, 13, 18]. The by-product varies depending on the reactive species responsible for ibuprofen degradation, so it was decided to determine which reactive species were produced. It was hypothesised that the main reactive species produced by the PEC system and would be responsible for ibuprofen degradation would be $\bullet OH$ and active chlorine.

4.2.4.1 Hydroxyl Radical Quantification

The problem found in several reports of ibuprofen degradation via PEC is that the species responsible is usually assumed to be hydroxyl radicals ($\bullet OH$). Previous theories have suggested that $\bullet OH$ is produced during the PEC system. Therefore, it was essential to check

that this system was able to produce $\bullet\text{OH}$. To do this then a previously successful quantification method was employed to analyse this PEC system [21, 22].

The experiment utilises $100\ \mu\text{M}$ of Coumarin as the target pollutant (full description in Chapter 2 Methods and Materials) that when degraded by $\bullet\text{OH}$ produces umbelliferone (also known as 7-hydroxycoumarin) which enables to indirectly measure the amount of $\bullet\text{OH}$ produced [21, 23]. Due to umbelliferone being a fluorescence compound it is measured via the photoluminescence (PL) spectrophotometer while the coumarin is measured by a UV-Vis spectrophotometer.

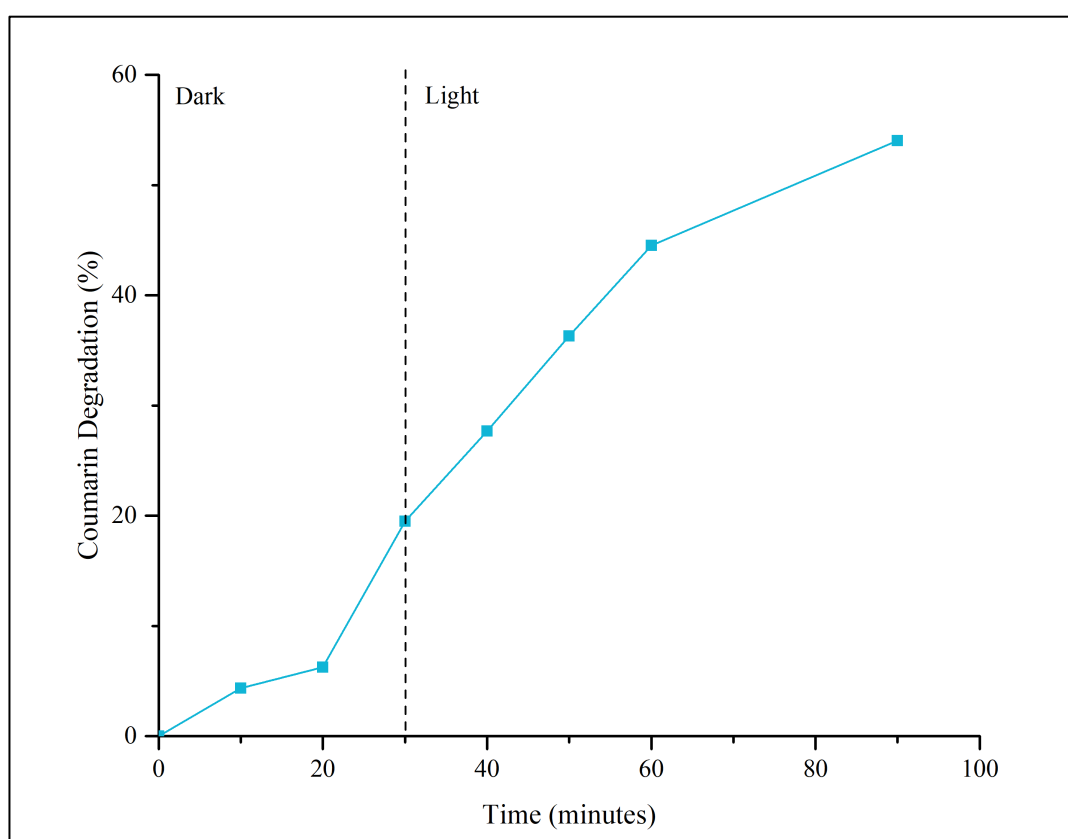


Figure 4.12 - A graph displaying the coumarin degradation achieved by the utilisation of the optimised PEC system. Note that the experiment was run with $2\text{WO}_3/1\text{BiVO}_4$ as the photoanode, Pt wire as the counter electrode, Ag/AgCl as the reference electrode, 1 M NaCl as the supporting electrolyte, 1.2 V applied potential and 1.5 hr of 1 Sun solar light irradiation.

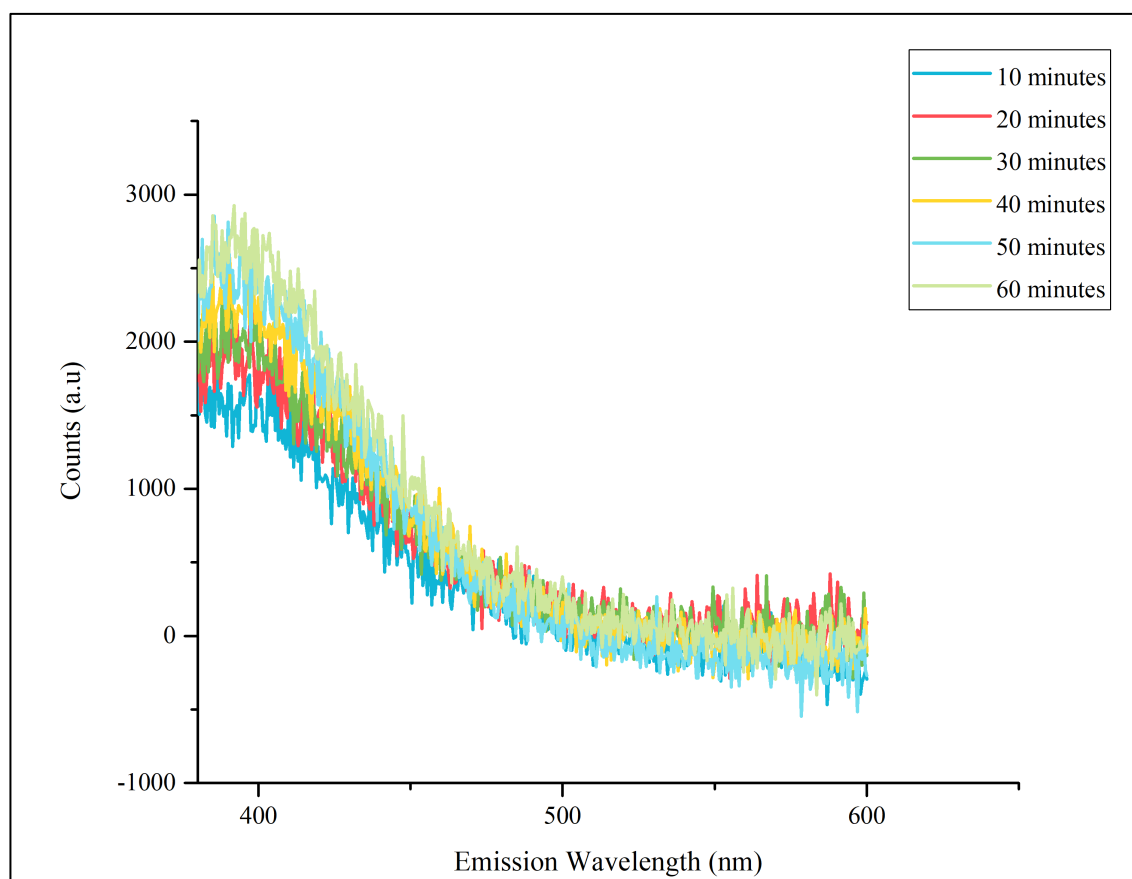
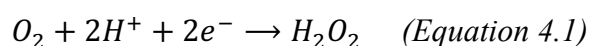


Figure 4.13 - The PL spectra obtained during the coumarin degradation experiment.

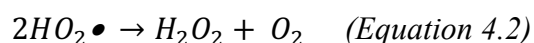
The system was very effective in degrading Coumarin (Figure 4.12) achieving 50% degradation. However, the PL spectra showed no umbelliferone was formed (figure 4.13) during the degradation of Coumarin as there was no peak at 450 nm. During the calibration of umbelliferone it was found that the emission wavelength was 450 nm. It means that the $\text{WO}_3/\text{BiVO}_4$ photoanode developed did not produce $\bullet\text{OH}$ to degrade Coumarin. This means the hypothesis was not met.

4.2.4.2 Hydrogen Peroxide Production

It has been demonstrated that hydrogen peroxide (H_2O_2) can be produced during the PEC process, following the reactions below [14, 24]:



or



H₂O₂ has a low oxidation-reduction potential (1.77 V) which means it cannot degrade ibuprofen directly [25]. However, UV light is able to split H₂O₂ into •OH which is able to degrade ibuprofen [4-6, 25]. However, the coumarin degradation experiment suggests that •OH are not produced directly by the PEC process. It does not suggest that •OH could be produced via the UV degradation of H₂O₂. Therefore, it was necessary to establish if there was H₂O₂ being produced during the PEC process when degrading ibuprofen.

The Quantofix H₂O₂ stripes were utilised to quantify the H₂O₂ being produced during the PEC ibuprofen degradation experiment. These stripes can only give an approximation; thus, the results have low precision for the H₂O₂ concentrations. The stripes were dipped into the electrolyte periodically every 30 minutes and examined against the colour chart.

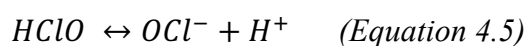
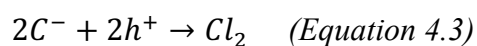
Table 4.9 - A table displaying rough approximations of the hydrogen peroxide concentration in the solution during the ibuprofen degradation process.

Sample Collection Time (min)	Average H ₂ O ₂ Concentration (mg/L)	Precision (%)
0	0	0
30	0	0
60	1.67	69.28
90	1.67	69.28
120	2.33	49.49
150	2.33	49.49

During the ibuprofen degradation process, H₂O₂ was produced in an abundance (approximately 2.33 mg/L) in the electrolyte. The quantity of H₂O₂ gradually increased with reaction time and became saturated after 120 minutes. This endorses would suggest that H₂O₂ is not degrading into •OH or degrading ibuprofen itself as it is accumulating in the solution. The other benefit of producing H₂O₂ is that it can be utilised as a fuel in H₂O₂ fuel cell [26]. Utilising H₂O₂ as a fuel instead of H₂ is a much safer option as it can be stored as liquid in a much safer way [26]. This means that this PEC system has other benefits above and beyond just ibuprofen degradation.

4.2.4.3 Active Chlorine

The utilisation of NaCl as the supporting electrolyte enables active chlorine species (Cl₂, HClO and OCl⁻) to be formed as the following reactions [18]:



It was assumed that when utilising NaCl as the electrolyte then active chlorine species are formed which is a benefit for pollutant degradation as active chlorine species have disinfectant properties and can degrade pollutants from water [18]. As the formation of the active chlorine species are dependent on the pH level in the solution then pH was monitored to indicate which possible active chlorine species are being produced [18]. At room temperature, Cl_2 is prominently produced at $\text{pH} < 3.3$, while HClO starts to dominate for $\text{pH} > 3.3$ [18]. However, beyond $\text{pH} 7.5$ then the OCl^- starts to be produced and becomes the only active species in alkaline solutions [18]. Therefore, establishing the pH level of the solution can help indicate what active chlorine species could be responsible for the ibuprofen degradation, but it cannot quantify the amount.

Table 4.10 - A table displaying the pH of the solution in the anodic compartment before and after treatment.

	Average pH	Precision (%)
Before PEC Treatment	4.05	0.14
After PEC Treatment	2.75	5.76

The pH of the solution decreases from 4.05 to 2.75 indicating the solution is being acidified during the PEC process. Acidification occurs when there is a high amount of H^+ present in the solution. This would imply that the system is producing H^+ which can be from the water oxidation process and the production of either HClO or OCl^- as during their production they generate H^+ . Since the pH is < 7.5 , the only active chlorine species present which could be Cl_2 and HClO [18]. Thus, suggesting these two species are involved in ibuprofen degradation.

4.2.4.4 Holes

As this $\text{WO}_3/\text{BiVO}_4$ photoanode was unsuccessful in producing $\bullet\text{OH}$ then the holes generated by electron excitation are able to directly oxidise ibuprofen. It has been demonstrated that the holes have strong enough oxidising properties to effectively degrade various pollutants [27-

29]. Therefore, holes play an important role in degrading ibuprofen for this system. However, time of flight experiments are necessary in understanding the hole pathway mechanisms.

4.2.5 Identification of By-Products

To identify the possible by-products formed when the ibuprofen was degraded then LC-MS was utilised. The LC-MS couples a liquid chromatography (LC) with a mass spectrometer (MS) to help separate each compound in the sample and introduce them separately into the MS. The MS can then determine the mass/charge ratio of each compound. During the MS analysis, fragmentation can be utilised to help produce a product ion spectrum which helps determine the chemical structure of the compound identified. Identifying the by-products is essential to determine if ibuprofen degradation via PEC is safe for the environment. Therefore, it is important to utilise the LC-MS correctly to obtain accurate data.

4.2.5.1 Method Development

Similar to the LC-UV, the mass spectrometer needed a method that would allow it to identify ibuprofen and its' degradation by-products. As the method for the LC-UV was successful in the identification of ibuprofen and its degradation by-products then it was decided to keep these settings for the LC part of the LC-MS system (Table 2.18 - Chapter 2 Materials and Methodology).

For analysing ibuprofen via mass spectrometry, the electrospray ionisation mode is usually operated in negative [30]. This is due to ibuprofen's acidic pKa of 4.3, indicating that ionisation happens when a proton in the carboxylic acid group is lost [30]. However, in this work both positive and negative modes were investigated to find out which mode produced the highest sensitivity for ibuprofen. Comparing the obtained chromatograms, it was found that the positive mode helped achieve better sensitivity. To help improve the sensitivity then it was necessary to prepare the ibuprofen standard to have a concentration of 10 µg/mL using a diluting solution of ACN/0.1% Formic Acid in H₂O (50/50) as well as increasing the injection volume from 5 to 20 µL. The optimised LC-MS method was summarised in Table 4.11.

Table 4.11 - A table displaying the LC-MS method operating parameters.

HPLC Settings			
Column	Xselect C-18 column (2.1 mm x 100 mm)		
Flowrate (mL/min)	0.250		
Injection Volume (uL)	20		
UV Detection Wavelength (nm)	265		
Gradient Pumping	Time (mins)	0.1% Formic Acid in Water	100% Acetonitrile
	0	75	25
	1	75	25
	17	0	100
	24	0	100
	25	75	25
	35	75	24
MS Setting			
Electrospray mode	Positive		
Capillary (kV)	3.50		
Cone (V)	5		
Desolvation Temperature (°C)	500		
Desolvation Gas Flowrate (L/hr)	600		
Cone Gas Flowrate (L/hr)	150		
Mass Scan Range	50 - 500		
Sample Concentration (ug/mL)	10		

Table 4.12 - A table displaying the m/z values and their retention times obtained from the mass scan.

Ibuprofen Degradation Experiment (Run 3)	
m/z Value	Mass Spectrometer Retention Time (minutes)
251	11.95 and 14.42
239	4.15 and 13.90
223	11.26-11.63, 14.25, 15.8 and 17.87
221	17.84
177	15.58

The utilisation of the LC-MS method helped obtain m/z values with retention times similar to the peak obtained in the LC-UV, thus indicating the presence of by-product. To ensure the repeatability of m/z values at least three samples were collected from different ibuprofen degradation runs (with the same operating parameters). The LC-MS results of these samples are displayed in Table 4.13.

Table 4.13 - A table showing the retention times for each peak associated with the individual m/z ratios.

Run 1		Run 2		Run 3	
m/z	MS RT	m/z	MS RT	m/z	MS RT
251	11.95	251	11.96 and 14.40	251	11.95 and 14.42
239	4.16 and 13.80	239	4.19, 13.80 and 15.55	239	4.15 and 13.90
223	11.35, 15.62	223	11.464, 14.15, 15.435 and 17.871	223	11.26-11.63, 14.25, 15.8 and 17.87
221	11.01 and 17.90	221	17.87	221	17.84
177	15.54	177	15.55	177	15.58

Table 4.13 showed that the same m/z values were found in each sample at similar retention times. This implies that these by-products are consistent for every run of ibuprofen degradation. Their retention times are also similar to the retention times found in the LC-UV chromatogram. This indicates that these are the by-products stemming from the ibuprofen degradation.

The LC-MS results expressed that some of the compounds, were not completely eluted from the column. Therefore, there could be a possible contamination on the guard column causing a slight blockage. This would result in the compounds not eluting individually and at one time, hence multiple retention times. Another indication that the guard column was contaminated was that the blanks were starting to have peaks appearing in the chromatogram. Therefore, the guard column was changed to help remove these contaminants and improve the eluting of the by-products in the sample.

Once the guard column was changed, then the sample was reanalysed to see if the eluting of the compounds improved. As table 4.14 demonstrates all the compounds elute at one time, except for compound 177. This would imply that the elution for the by-products improved which means all the compound is entering the MS at one time. As the m/z ratios were determined then fragmentation could be done to produce a product ion spectrum which can be used to determine the chemical structures for each compound.

Table 4.14 - A table showing the retention times of each compound obtained by the LC-MS.

Sample R3 150mins	
<i>m/z</i>	MS RT
251	14.48
239	4.34
223	11.26
221	11
177	7.28 and 15.57

4.2.5.2 MS/MS Fragmentation

The fragmentation in LC-MS helps break down each compound in the sample into product ions, thus creating a spectrum with several peaks which correspond to an ion of the original compound. This identifies the chemical structure of the compound. Note that the success of fragmentation depends on the collision energy, because the collision energy controls the breakdown of the compound. For instance, too high of a collision energy causes a complete breakdown of the target analyte while too low of a collision energy can result in insufficient fragmentation of the precursor ion. Therefore, some method development was required to help determine the optimal collision energy for each by-product.

Table 4.15 - A table showing the optimised collision energy for each compound found.

LC-MS Method	Table 4.11
Fragmentation Method	
Compound <i>m/z</i>	Optimised Collision Energy (eV)
251	n/a
239	+25
223	+30
221	+30
177	+30

During the fragmentation optimisation, it was found that compound 251 was not present in the product ion scan. This indicates that *m/z* 251 may have been a background ion or in too low an abundance to fragment. However, the other compounds achieved great fragmentation utilising the optimised collision energies (Table 4.15). Table 4.16 below summarises the *m/z* compounds with their corresponding product ion peaks obtained by the fragmentation.

Table 4.16 - A table displaying each compound with their corresponding peaks.

Compound <i>m/z</i>	Product Ion Peaks
239	167, 157, 147 139, 129, 121, 116, 111, 95, 93, 87, 81, 75, 73, 71, 67, 57, 55.
223	191, 149, 141, 123, 121, 97, 93, 91, 67, 65, 57, 55
221	163, 159, 143, 142, 139, 133, 131, 121, 117, 106, 105, 93, 91, 81, 79, 77, 67, 57
177	135, 128, 119, 103, 92, 91, 77, 65, 59, 57

As the product ion peaks have been established for each by-product compound then they need to be compared to literature to identify the structure of the compound.

4.2.5.3 Comparison with Literature

Previous literature is utilised to determine if the compounds present in the sample are the same as other ibuprofen degradation experiments. The benefits of confirming the chemical structure of the compounds are:

- It defines the species responsible for the ibuprofen degradation.
- It establishes if the PEC process is safe for ibuprofen degradation or if it causes more hazards.

There is only one report that identifies by-products produced during the ibuprofen degradation via PEC [4]. Therefore, irrespective of treatment technique, it is necessary to look other studies of ibuprofen degradation that involve the same reactive species produced by PEC. This would then help identify other possible by-products formed due to ibuprofen reacting with these species. Table 4.27 outlines all the possible by-products with their monoisotopic mass obtained from the various ibuprofen degradation experiments.

Table 4.17 - A table summarising the possible by-products from ibuprofen degradation experiments by PEC and other techniques.

Experiment	Reactive Oxidising Species Responsible	Possible By-Products	By-products' Monoisotopic Mass	Ref
Photoelectrocatalysis	•OH	2-hydroxyl-propanoic acid Hydroxyl-acetic acid Pentanoic acid Malonate Phenol 1,4-benzenecarboxylic acid	90.031694049 76.016043985 102.068079557 101.99530854 94.041864811 164.01095860	[4]
Photocatalysis	•OH, h+	C ₁₃ H ₁₈ O ₂ C ₁₃ H ₁₈ O ₃ C ₁₃ H ₁₈ O ₃ C ₁₃ H ₁₈ O ₃ C ₁₂ H ₁₈ C ₁₀ H ₁₄ C ₁₃ H ₁₈ O ₄ C ₁₂ H ₁₉ O C ₁₂ H ₁₉ O	206 222 222 222 163 135 239 179 179	[31]
Photocatalysis	•OH	4'-Isobutylacetophenone (C ₁₂ H ₁₆ O) 1-(4-Isobutylphenyl)ethanol (C ₁₂ H ₁₈ O) C ₁₂ H ₁₈ O ₃ C ₁₂ H ₁₆ O ₂ C ₁₂ H ₁₆ O ₃ C ₁₁ H ₁₆ O	176.12 178.14 210.13 192.12 208.11 164.12	[27]
Photocatalysis	•OH	2-hydroxy-2-(4-isobutyl phenyl) propanoic acid 2-(4-(1-hydroxy-2-methyl propyl) phenyl) propanoic acid 1-(4-ethyl phenyl)-2-methyl propan-1-ol 4-isobutylacetophenone Isobutylbenzene	222.28 222.13 178.27 176.25 134.22	[32]
UV/chlorine advanced oxidation process	•OH, active chlorine	C ₁₃ H ₁₈ O ₃ C ₁₃ H ₁₈ O ₄ C ₁₃ H ₁₇ O ₂ Cl C ₁₃ H ₁₆ O ₆ C ₁₂ H ₁₈ O ₆ C ₉ H ₈ O ₄ C ₉ H ₁₀ O C ₅ H ₁₀ O ₃ C ₆ H ₁₀ O ₃ C ₈ H ₁₂ O ₄ C ₃ H ₄ O ₂ Cl ₂ C ₅ H ₉ O ₃ Cl	222 238 240 268 258 180 134 118 130 172 142 152	[33]

Electro-peroxone (E- peroxone) treatment	•OH	2-(3-Hydroxy-4- isobutylphenyl)propanoic acid (C ₁₃ H ₁₈ O ₃)	222	[34]
		2-Hydroxy-ibuprofen (C ₁₃ H ₁₈ O ₃)	222	
		1-Hydroxy-ibuprofen (C ₁₃ H ₁₈ O ₃)	222	
		2-Hydroxy-2-(4- isobutylphenyl)propanoic acid (C ₁₃ H ₁₈ O ₃)	222	
		Dihydroxylated ibuprofen (C ₁₃ H ₁₈ O ₄)	238	
		4-(1-Hydroxyethyl)benzaldehyde (C ₉ H ₁₀ O ₂)	150	
		2-(4-Methylphenyl)propanoic acid (C ₉ H ₈ O ₃)	164	
		1-(4-Isobutylphenyl)ethanol (C ₁₁ H ₁₃ O ₂)	178	
		4-Isobutylacetophenone (C ₁₂ H ₁₆ O)	176	
		1-(4-(1-Hydroxyethyl)phenyl)-2- methylpropan-1-one (C ₁₂ H ₁₆ O ₂)	192	
		4-(1-Hydroxy-2- methylpropyl)acetophenone (C ₁₂ H ₁₆ O ₂)	192	
		2-(4- (Carboxycarbonyl)phenyl)propanoic acid (C ₁₃ H ₁₈ O ₃)	222	
		1,2,4-Benzenetriol (C ₆ H ₆ O ₃)	126	
		Catechol (C ₆ H ₆ O ₂)	110	
		4-Ethylphenol (C ₈ H ₁₀ O)	122	
		Hydroquinone (C ₆ H ₆ O ₂)	110	
		4-Ethylbenzaldehyde (C ₉ H ₁₀ O)	134	

The compounds which had matching molecular mass to the compounds obtained from this chapter's ibuprofen degradation experiments were 2-hydroxy-2-[4-(2-methylpropyl)phenyl]propanoic acid, 4'-Isobutylacetophenone (C₁₂H₁₆O) C₁₃H₁₈O₃ , C₁₃H₁₈O₄, 2-(3-Hydroxy-4-isobutylphenyl)propanoic acid (C₁₃H₁₈O₃), 2-Hydroxy-ibuprofen (C₁₃H₁₈O₃), 1-Hydroxy-ibuprofen (C₁₃H₁₈O₃), 2-Hydroxy-2-(4-isobutylphenyl)propanoic acid (C₁₃H₁₈O₃), Dihydroxylated ibuprofen (C₁₃H₁₈O₄) and 2-(4-

(Carboxycarbonyl)phenyl)propanoic acid (C₁₃H₁₈O₃). However, the m/z values alone cannot confirm these compounds are present because compounds can have identical m/z values. Therefore, the fragmentation data was needs to be compared to confirm if the compounds are present.

Table 4.18 - A table comparing the product ion peaks obtained for the samples and the literature for each compound [27, 32, 34].

Compound m/z	Product Ion Peaks From The Sample	Product Ion Peaks From Literature				
239	167, 157, 147 139, 129, 121, 116, 111, 95, 93, 87, 81, 75, 73, 71, 67, 57, 55	237.0802, 221.0783, 195.0995				
223	191, 149, 141, 123, 121, 97, 93, 91, 67, 65, 57, 55	221.1172, 205.0894, 159.1188	221.1147, 177.1295	221.1123, 177.1257, 149.0417	221.1132, 203.1060, 159.1143	221.1166, 133.065
		149, 133	177, 149			
221	163, 159, 143, 142, 139, 133, 131, 121, 117, 106, 105, 93, 91, 81, 79, 77, 67, 57	n/a				
177	135, 128, 119, 103, 92, 91, 77, 65, 59, 57	177.12 121.06 57.07 43.02		175, 103		

The major issue in finding fragmentation data for each compound is that there is limited fragmentation data available for each compound. In addition, some compounds only had fragmentation data using negative electrospray ionisation mode. Therefore, when comparing these fragmentation peaks the literature peaks would have m/z values slightly less than the thesis obtained fragmentation.

The only compound in literature which has some of the same product ion peaks as the sample was 177. This was identified as 4-Isobutylacetophenone. There were some peaks that were different to each other, but this could be due to the different fragmentation conditions. The literature shows they were unable to achieve complete fragmentation as they still had a peak at 177. This explains why more peaks were attained for the PEC treated sample's product scan as complete fragmentation was achieved thus producing more product ions. The issue with

producing 4-Isobutylacetophenone as a by-product after PEC ibuprofen degradation is that it has many hazards such as skin irritant, toxic to aquatic life and flammable as liquid or vapour. Therefore, running the PEC system with the optimised conditions degraded the ibuprofen to a toxic pollutant 4-Isobutylacetophenone. In a previous study, the formation of 4-Isobutylacetophenone indicates that h^+ are the prominent reactive species in ibuprofen degradation due to the decarboxylation of ibuprofen by hole oxidation forming a benzyl radical [27]. Subsequently the benzyl radical then reacts with $\bullet OH$ to produce 4-Isobutylacetophenone [27]. This demonstrates that this PEC system produces $\bullet OH$ to degrade ibuprofen and indicates that the method utilised for quantifying $\bullet OH$ was not appropriate for this PEC process. In general, the original organic species were degraded quickly by PEC or PC process however the by-products will take longer, possibly a few hours to completely degrade into toxic-free species. This would indicate a longer treatment time might help to degrade 4-Isobutylacetophenone as there would be more $\bullet OH$ formed. However, further research would be needed to confirm this.

The problem with compounds 239 and 223 is that the only fragmentation data available is data obtained through negative electrospray ionisation. It means there would be a slight difference between the m/z values of the product ion peaks. However, Table 4.18 shows there is a big difference between the two sets of fragmentation data. This implies these by-products are not present in the sample. Therefore, to precisely determine the by-products then the samples should be run on a mass spectrometer with an accurate mass function. This demonstrates the importance of fragmentation in identifying compounds.

4.2.6 The Feasibility of Utilising PEC for Ibuprofen Degradation

To assess the feasibility of using PEC as a water treatment technology, then the pH of the resulting solution needs to be established. This would help determine if a post-treatment was required. It is essential to consider the pH of treated solutions before releasing them into freshwater sources as too acidic or too alkaline solutions could cause harm to aquatic life and plants. In nature there are some lakes that have become either alkaline or acidic [35]. This is due to evaporation causing an accumulation of minerals or concentrating the sulfates and acids already in the water [35]. This only occurs in certain regions of the world such as the alkaline Lake Natron in Tanzania and acidic lakes in Dallol in Ethiopia [35]. These lakes demonstrate

how dangerous it is for aquatic animals when the pH is too high or too low. Therefore, it is crucial to ensure the pH of the water released into the environment is neutral.

Adding ibuprofen to the saltwater solution resulted in a pH of 4 (Table 4.13) in the solution, which is due to ibuprofen having a pK_a of 4 in its natural form [36]. Therefore, the anodic side is already acidic before the treatment process. However, during the PEC ibuprofen degradation process the solution acidifies to a pH of 2.75. This pH would be too low for release into the environment. This means a post-treatment step is necessary to help neutralise the solution before it can be released to the environment. This is a drawback as it would add to the cost of utilising PEC and would need to be considered if PEC were to be adopted by industry.

During the ibuprofen degradation via PEC, the pH of the solution is constantly acidic. This means that the photoanode needs to be stable in acidic conditions. WO₃ has proven to be stable in acidic conditions hence the stability of the photoanode should allow it to be reused. In order to verify the sustainability of the photoanode then the PEC ibuprofen degradation was repeated 3 times with the same photoanode. This would help demonstrate if the photoanode could be reused and achieve high degradation each time.

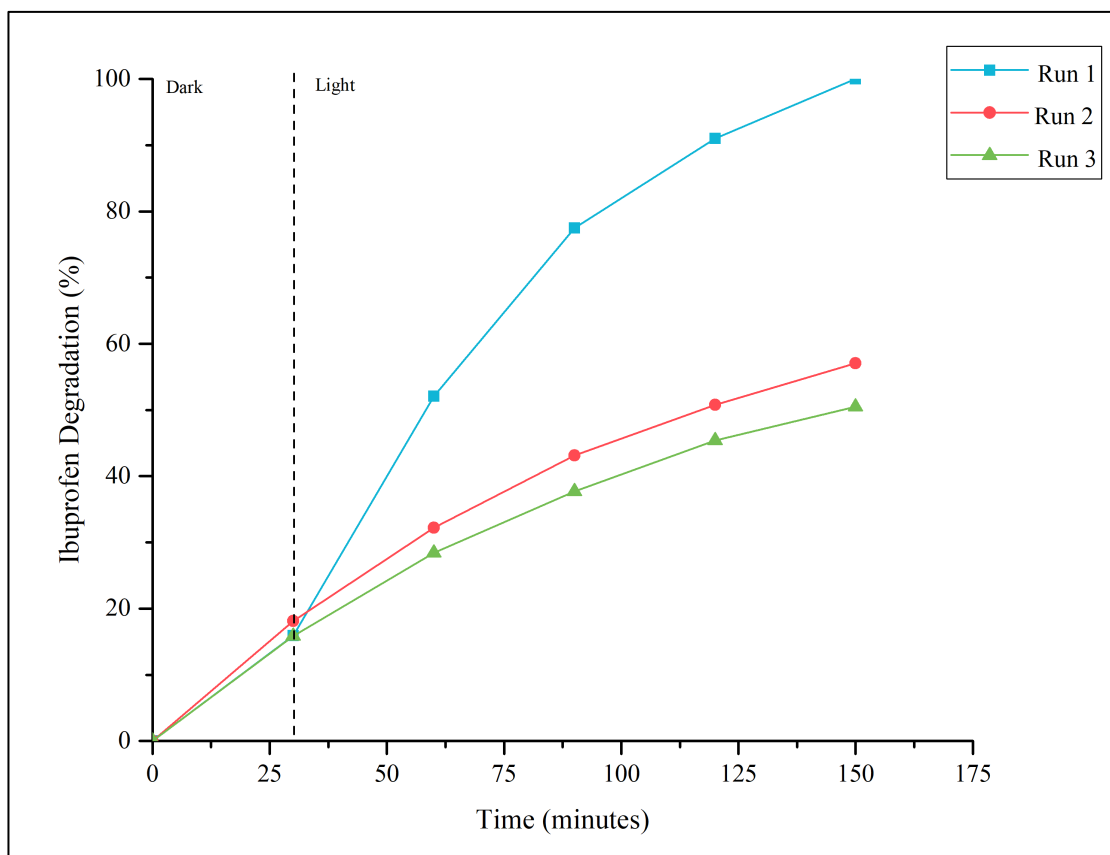


Figure 4.14 - A graph of the ibuprofen degradation achieved during each run of the optimised PEC system while utilising the same $2WO_3/1BiVO_4$ photoanode.

From Figure 4.14, unexpectedly the photoanode showed significant difference in ibuprofen degradation performance between run 1 and 2. This would imply that the $WO_3/BiVO_4$ photoanode undergoes photocorrosion which affects the stability at low pH. This was not expected as WO_3 has good stability in low pH [10, 37]. However, this issue could be resolved by the addition of a passivation layer coating with another metal oxide.

Chemical oxygen demand (COD) is an indirect measurement method in determining the amount of organic contaminants in the solution. It is widely utilised in wastewater plants to help determine the efficiency of the water treatment process [38]. The COD analysis was done on the solution before and after treatment to help determine if there was any decrease in organic compounds in the solution.

Table 4.19 - Display of the COD values obtained before and after treatment.

	Ibuprofen (100ug/ml) in 1M NaCl	Treated Water Average
COD (mg/L)	144	144.67

From the COD results (Table 4.19) the optimised method does not affect the organic compounds in the solution. This could be due to the production of several by-products during the process. Therefore, it is recommended that the experiment is repeated but with a longer treatment time to see if this helps degrade the by-products. Consequently, reducing the COD and improving the efficiency of the process.

4.3 Conclusion

Ibuprofen is a popular pharmaceutical compound which due to its excessive use, improper disposal and inability of current water cleaning technologies to eradicate, means it enters our freshwater supplies. This has many complications for the health of humans and aquatic life. Therefore, it is crucial to develop a water cleaning treatment which completely eliminates ibuprofen.

The method developed for quantifying the ibuprofen degradation via LC-UV was successful. It demonstrated excellent repeatability and the results were reproducible. In addition, the established calibration graph demonstrated high accuracy and precision for calculating the ibuprofen concentrations of the QCs. This proves how successful the method was in determining the ibuprofen concentrations.

PEC is a sustainable process and was optimised to degrade an average of 96.70% of (100 µg/mL) ibuprofen from water. This was achieved using the optimised PEC conditions which were $2\text{WO}_3/1\text{BiVO}_4$ photoanode (1 cm^2) with a 1.2 V (vs Ag/AgCl) potential, 1 M NaCl supporting electrolyte and 1 sun of solar light irradiation for 2 hours (30 minutes in the dark). This PEC system demonstrated extremely high ibuprofen degradation whilst utilising a smaller surface area compared to previous studies which utilised larger surface areas to achieve 100% degradation within the same 1.5 – 2 hr treatment time. Therefore, demonstrating that this system is very successful over a short period. However, a longer duration of reaction is essential to degrade the by-products completely.

Despite its advantages there are some challenges such as the very low pH of the treated solution. This means that the treated solution is very acidic and would require a post treatment step to ensure the solution is neutralised before being released into the environment.

The other obstacle relates to the formation of by-products confirmed by the LC-UV, LC-MS and COD. Due to the minimal fragmentation data available, only one by-product could be identified, namely 4-isobutylacetophenone. 4-Isobutylacetophenone is a more hazardous material than ibuprofen therefore it would be important to see if increasing the treatment time or photoanode active area would result in degrading this by-product. Thus, decreasing the environmental impact of the PEC system. As the other by-products detected in the sample are unidentifiable via the fragmentation data, it is suggested that the sample analysis is repeated on a mass spectrometer with accurate mass identification function. This will determine other by-products' chemical structures to be determined. In addition this would help determine other possible by-products which could be formed, as it is often assumed that hydroxyibuprofen is produced during ibuprofen degradation via PEC or photocatalysis.

It was established that several reactive species such as holes, $\bullet\text{OH}$, H_2O_2 and active chlorine was produced during the PEC process which are responsible for ibuprofen degradation. However, the quantification experiment for $\bullet\text{OH}$ was not appropriate for this system as it indicated no $\bullet\text{OH}$ was produced. In contrast, the MS identified that 4-isobutylacetophenone was produced this is due to the benzyl radical (from holes reacting with ibuprofen directly) reacting with $\bullet\text{OH}$, thus indicating $\bullet\text{OH}$ is being produced by the system and is responsible for ibuprofen degradation. However more research is needed to quantify the amount. It is also suggested that while stripes and pH indicate that H_2O_2 and active chlorine are produced during the ibuprofen degradation, it does not quantify the amount. Therefore, more quantification tests for H_2O_2 and active chlorine are required to establish the amounts produced. This demonstrates the need for more research to determine the quantities produced for each reactive species, thus confirming the species responsible for ibuprofen degradation and if this differs for different photoanodes utilised.

4.4 Bibliography

1. Moore, D., *Photophysical and Photochemical Aspects of Drug Stability*. 2004. p. 9-40.
2. James N Miller, J.C.M., *Statistics and Chemometrics for Analytical Chemistry*. Vol. Six. 2010, Essex: Pearson Education Limited.
3. Administration, U.S.D.o.H.a.H.S.F.a.D., *Bioanalytical Method Validation - Guidance for Industry*. 2018, The Food and Drug Administration (FDA): <https://www.fda.gov/regulatory-information/search-fda-guidance-documents/bioanalytical-method-validation-guidance-industry>.
4. Zhao, X., et al., *Photoelectrochemical degradation of anti-inflammatory pharmaceuticals at Bi₂MoO₆-boron-doped diamond hybrid electrode under visible light irradiation*. Applied Catalysis B: Environmental, 2009. **91**(1): p. 539-545.
5. Sun, Q., et al., *Photoelectrochemical oxidation of ibuprofen via Cu₂O-doped TiO₂ nanotube arrays*. Journal of Hazardous Materials, 2016. **319**: p. 121-129.
6. Chen, H., et al., *Enhanced photoelectrochemical degradation of Ibuprofen and generation of hydrogen via BiOI-deposited TiO₂ nanotube arrays*. Science of The Total Environment, 2018. **633**: p. 1198-1205.
7. Chang, K.-L., et al., *Cu₂O loaded titanate nanotube arrays for simultaneously photoelectrochemical ibuprofen oxidation and hydrogen generation*. Chemosphere, 2016. **150**: p. 605-614.
8. Ye, S., et al., *Simultaneous removal of organic pollutants and heavy metals in wastewater by photoelectrocatalysis: A review*. Chemosphere, 2021. **273**: p. 128503.
9. Alulema-Pullupaxi, P., et al., *Fundamentals and applications of photoelectrocatalysis as an efficient process to remove pollutants from water: A review*. Chemosphere, 2021. **281**: p. 130821.
10. Lianos, P., *Review of recent trends in photoelectrocatalytic conversion of solar energy to electricity and hydrogen*. Applied Catalysis B: Environmental, 2017. **210**: p. 235-254.
11. Peleyeju, M.G. and O.A. Arotiba, *Recent trend in visible-light photoelectrocatalytic systems for degradation of organic contaminants in water/wastewater*. Environmental Science: Water Research & Technology, 2018. **4**(10): p. 1389-1411.
12. Wang, N., et al., *Evaluation of bias potential enhanced photocatalytic degradation of 4-chlorophenol with TiO₂ nanotube fabricated by anodic oxidation method*. Chemical Engineering Journal, 2009. **146**(1): p. 30-35.
13. Daghri, R., P. Drogui, and D. Robert, *Photoelectrocatalytic technologies for environmental applications*. Journal of Photochemistry and Photobiology A: Chemistry, 2012. **238**: p. 41-52.
14. Garcia-Segura, S. and E. Brillas, *Applied photoelectrocatalysis on the degradation of organic pollutants in wastewaters*. Journal of Photochemistry and Photobiology C: Photochemistry Reviews, 2017. **31**: p. 1-35.
15. Orimolade, B.O., et al., *Visible light driven photoelectrocatalysis on a FTO/BiVO₄/BiOI anode for water treatment involving emerging pharmaceutical pollutants*. Electrochimica Acta, 2019. **307**: p. 285-292.
16. Liang, F. and Y. Zhu, *Enhancement of mineralization ability for phenol via synergetic effect of photoelectrocatalysis of g-C₃N₄ film*. Applied Catalysis B: Environmental, 2016. **180**: p. 324-329.

17. Liu, D., et al., *Enhanced visible light photoelectrocatalytic degradation of organic contaminants by F and Sn co-doped TiO₂ photoelectrode*. Chemical Engineering Journal, 2018. **344**: p. 332-341.
18. Zaroni, M.V.B., et al., *Photoelectrocatalytic Production of Active Chlorine on Nanocrystalline Titanium Dioxide Thin-Film Electrodes*. Environmental Science & Technology, 2004. **38**(11): p. 3203-3208.
19. Fang, T., C. Yang, and L. Liao, *Photoelectrocatalytic degradation of high COD dipterex pesticide by using TiO₂/Ni photo electrode*. J Environ Sci (China), 2012. **24**(6): p. 1149-56.
20. Cardoso, J.C., T.M. Lizier, and M.V.B. Zaroni, *Highly ordered TiO₂ nanotube arrays and photoelectrocatalytic oxidation of aromatic amine*. Applied Catalysis B: Environmental, 2010. **99**(1): p. 96-102.
21. De-Nasri, S.J., et al., *Quantification of hydroxyl radicals in photocatalysis and acoustic cavitation: Utility of coumarin as a chemical probe*. Chemical Engineering Journal, 2021. **420**: p. 127560.
22. Hirano, K. and T. Kobayashi, *Coumarin fluorometry to quantitatively detectable OH radicals in ultrasound aqueous medium*. Ultrason Sonochem, 2016. **30**: p. 18-27.
23. Zhang, J. and Y. Nosaka, *Quantitative Detection of OH Radicals for Investigating the Reaction Mechanism of Various Visible-Light TiO₂ Photocatalysts in Aqueous Suspension*. The Journal of Physical Chemistry C, 2013. **117**(3): p. 1383-1391.
24. Papagiannis, I., et al., *Photoelectrocatalytic production of hydrogen peroxide using a photo(catalytic) fuel cell*. Journal of Photochemistry and Photobiology A: Chemistry, 2020. **389**: p. 112210.
25. Peng, M., et al., *Photo-degradation ibuprofen by UV/H₂O₂ process: response surface analysis and degradation mechanism*. Water Science and Technology, 2017. **75**(12): p. 2935-2951.
26. Mase, K., et al., *Seawater usable for production and consumption of hydrogen peroxide as a solar fuel*. Nature Communications, 2016. **7**(1): p. 11470.
27. Arthur, R.B., et al., *Photocatalytic degradation of ibuprofen over BiOCl nanosheets with identification of intermediates*. Journal of Hazardous Materials, 2018. **358**: p. 1-9.
28. Wang, D., et al., *Simultaneously efficient adsorption and photocatalytic degradation of tetracycline by Fe-based MOFs*. Journal of Colloid and Interface Science, 2018. **519**: p. 273-284.
29. Chen, F., et al., *Visible-light photocatalytic degradation of multiple antibiotics by AgI nanoparticle-sensitized Bi₅O₇I microspheres: Enhanced interfacial charge transfer based on Z-scheme heterojunctions*. Journal of Catalysis, 2017. **352**: p. 160-170.
30. Townsend, R., *Mass Spectrometric Investigation of Pharmaceuticals in Environmental Matrices: Homogenate Analysis*. 2019, Swansea University: Swansea.
31. Wang, J., et al., *Atomic scale g-C₃N₄/Bi₂WO₆ 2D/2D heterojunction with enhanced photocatalytic degradation of ibuprofen under visible light irradiation*. Applied Catalysis B: Environmental, 2017. **209**: p. 285-294.
32. Liu, S.-H. and W.-T. Tang, *Photodecomposition of ibuprofen over g-C₃N₄/Bi₂WO₆/rGO heterostructured composites under visible/solar light*. Science of The Total Environment, 2020. **731**: p. 139172.
33. Xiang, Y., J. Fang, and C. Shang, *Kinetics and pathways of ibuprofen degradation by the UV/chlorine advanced oxidation process*. Water Research, 2016. **90**: p. 301-308.
34. Li, X., et al., *Degradation of the anti-inflammatory drug ibuprofen by electro-peroxone process*. Water Research, 2014. **63**: p. 81-93.

35. Fondriest Environmental, I. *pH of Water*. Fundamentals of Environmental Measurements 2013.
36. Oh, S., W.S. Shin, and H.T. Kim, *Effects of pH, dissolved organic matter, and salinity on ibuprofen sorption on sediment*. Environmental science and pollution research international, 2016. **23**(22): p. 22882-22889.
37. Zeng, Q., et al., *Synthesis of WO₃/BiVO₄ photoanode using a reaction of bismuth nitrate with peroxovanadate on WO₃ film for efficient photoelectrocatalytic water splitting and organic pollutant degradation*. Applied Catalysis B: Environmental, 2017. **217**: p. 21-29.
38. Zarka, E., et al. *Correlation between Biochemical Oxygen Demand and Chemical Oxygen Demand for Various Wastewater Treatment Plants in Egypt to Obtain the Biodegradability Indices*. 2014.

Chapter 5 : Surfactant Degradation

5.1 Introduction

The aim of this chapter was to determine if PEC could completely remove a model surfactant pollutant compound (anionic and cationic) from water. The model surfactants chosen for this study were BAC-C12 which is a cationic surfactant and S2NS which is an anionic surfactant. This chapter looked at utilising the optimised PEC system from Chapter 4 to remove BAC-C12 at a high concentration 100 $\mu\text{g/mL}$ and low concentration 50 $\mu\text{g/mL}$. Then the same PEC system was utilised to remove S2NS at a low concentration of 50 $\mu\text{g/mL}$ and the results were compared to help determine which type of surfactant was favoured for degradation via PEC. This chapter is of importance as currently no research exists in relation to a technology that can completely remove an anionic and cationic surfactant.

5.2 Results and Discussion

5.2.1 Quantification of Surfactant Degradation

To monitor and quantify the amount of surfactant present in the sample, then a LC-UV method was developed for the two surfactants, BAC-C12 and S2NS. Based on the chemical properties of these surfactants, the reversed phase column and methodology applied for ibuprofen was tested for these analytes. However, due to the differences in chemical structure then these compounds displayed two different maximum wavelength absorption thus two different wavelengths were utilised. The UV wavelength detections for BAC-C12 and S2NS were 260 nm and 273 nm, respectively. To test if the methods developed (Table 2.9 and Table 2.10) achieved good selectivity, a known concentration standard (BAC-C12 = 50 $\mu\text{g/mL}$ and S2NS = 20 $\mu\text{g/mL}$) was injected for each analyte to establish its retention time. The obtained chromatograms were then compared to a blank sample to find the selectivity of the method. As expected, these compounds showed significant sharp peaks at retention time indicative of their hydrophobicity at 14.163 (BAC-C12) and 2.6 (S2NS) minutes, thus showing great sensitivity at the target wavelengths. Pleasingly, no signal was observed within the blank sample at the target detection conditions, supporting the selectivity of the method.

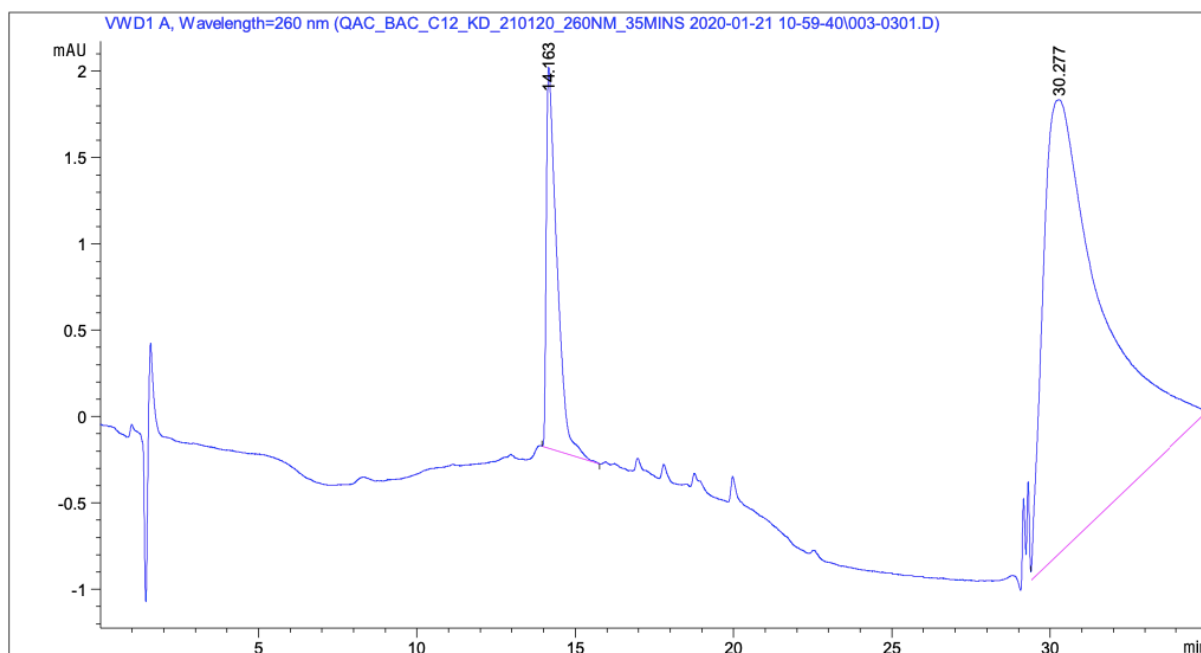


Figure 5.1 - The chromatogram obtained for a pure BAC-C12 standard utilising the best method developed.

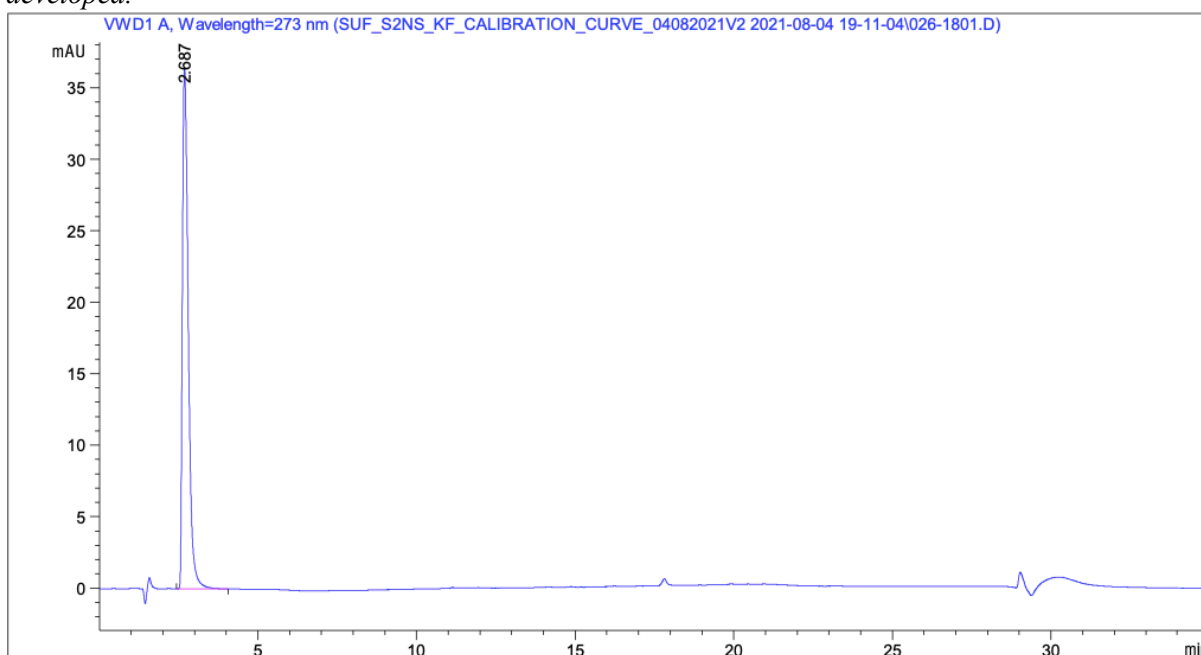


Figure 5.2 - The chromatogram obtained for a pure S2NS standard utilising the best method developed.

5.2.1.1 Repeatability and Reproducibility of Methods

As the LC-UV methods for BAC-C12 and S2NS showed great selectivity then it was important to determine whether the methods were repeatable and reproducible.

Table 5.1 - Results for retention times repeatable for each surfactant.

Compound	CV% for Day 1	CV% for Day 2	F-Test Value
BAC-C12	0.11	0.14	1.79
S2NS	0.54	2.02	13.82

The retention times of BAC-C12 and S2NS were highly repeatable as the CV% values were < 0.2% and < 3% respectively across each day. This indicates a minor variation in retention times as the CV% was < 5%. This was also confirmed for BAC-C12 as the F-test value was determined to be 1.79 (to 2 d.p) which is far less than the critical value of 4.3, thus showing no significant difference between the two days. It ensures that the method (Table 2.9) achieved repeatable retention times running over a 2-day period. However, for S2NS, the F-test calculated was 13.82 (to 2 d.p) which is much higher than the critical value. It implies that there is a significant difference between the two sets of data. However, as the CV was < 5% then the retention times are repeatable [1].

Table 5.2 - Results for the injection repeatability for each surfactant.

Compound	CV% for Day 1	CV% for Day 2	F-Test Value
BAC-C12	0.23	0.26	1.27
S2NS	0.22	2.44	125.32

The stability of the integrated analyte response was explored by determining the injection repeatability. It involved comparing the peak areas across both days. Again, good injection repeatability was observed as both compounds achieved CV% < 0.3% (BAC-C12) and < 3% (S2NS). Thus, a low variation in the results (Table 5.2). Interestingly, a higher CV% was observed for S2NS for day 2 which would indicate there is carryover. However, the blank signal obtained after the samples would suggest this increase in CV% is due to random error during the LC-UV analysis. The F-test value calculated for BAC-C12 was 1.27 (to 2 d.p) which is much lower than the critical value of 4.3. This suggests that there is no significant difference in variation between days 1 and 2. This further verifies this method (Table 2.9) and the LC-UV can achieve outstanding injection repeatability for BAC-C12. However, the F-test value of S2NS was 125.32 (to 2 d.p), which signifies a significant difference between the two sets of data. As previously mentioned, this could be due to day 2 having a higher variation as a result of some random errors. However, as both CV% were < 5%, the injection is repeatable for each method [1].

5.2.1.2 Calibration Graph

Again similar to ibuprofen it was necessary to assess the calibration graph to determine if the methods were accurate and precise and if so then it could be utilised to calculate BAC-C12 and S2NS concentration in the samples.

Table 5.3 - The values obtained from the regression of the calibration graph.

Compound	R ² (to 3 d.p)	Standard Error (to 2 d.p)	Intercept (to 2 d.p)	Gradient (to 2 d.p)
BAC-C12	0.999	1.74	0.32	1.08
S2NS	0.999	17.20	-0.28	23.67

The linearity for both compounds were > 0.99, which shows that the calibration graph has excellent linearity and enables the use of the line equation to calculate the actual concentrations of the QCs.

Table 5.4 - The average accuracy and precision calculated for the QCs of BAC-C12 and S2NS.

Compound	QC Type	Accuracy (%) (to 2 d.p)	Precision (%) (to 2 d.p)
BAC-C12	Low	4.38	2.56
BAC-C12	Mid	0.05	1.01
BAC-C12	High	0.08	2.62
S2NS	Low	24.09	10.96
S2NS	Mid	3.19	0.38
S2NS	High	1.20	0.97

The precision and accuracy for the quantitation of BAC-C12 was excellent as the values obtained were < 5% across the concentration range. It fulfilled the acceptance criteria set out by the FDA bioanalytical method validation. This set a threshold value of 15% for mid and high QC concentrations and 20% for the low QC concentration [2]. Thus, confirming that the method was able to quantify BAC-C12 accurately and precisely across the tested concentration range. However, for S2NS, only the mid and high concentration QCs were acceptable accuracy and precision (< 15%) values [2]. The low concentration QC was > 20%. Therefore, to establish statistically if there were any outliers within the data set then Grubb's Test (Eq 2.12 in Chapter 2) was utilised. Interestingly, a replicate QC sample (QC_Low_4) was an outlier. Removing this outlier from the accuracy and precision calculations resulted in the values being 18.81% (to 2 d.p) and 6.57% (to 2 d.p), respectively. Therefore, meeting the acceptance criteria. This data shows that the method can accurately and precisely quantify S2NS concentrations within the tested concentration range.

5.2.1.3 Instrumentation Detection Limit

The calibration graph was assessed further by determining the instrument detection limit (IDL), which indicates the minimum concentration that could be accurately quantified for the chosen test material by the preferred method. There are two methods to calculate this value which are either a statistical approach (Eq 2.13 in Chapter 2) or an empirical approach. Utilising the statistical approach the IDL values for BAC-C12 and S2NS were 5.31 $\mu\text{g/mL}$ and 2.40 $\mu\text{g/mL}$, respectively. However, as demonstrated for ibuprofen the empirical method is a more robust approach. Therefore, this method was chosen to verify if the lowest concentrations on the calibration graphs of BAC-C12 and S2NS were appropriate. For BAC-C12 and S2NS the signal to noise ratio (S/N) was calculated as 7:1 and 33:1 (respectively), thus demonstrating that both of the analytes' signal response is more significant than the background signal. This confirms that 10 $\mu\text{g/mL}$ and 1 $\mu\text{g/mL}$ are appropriate low concentrations for the calibration as it results in significantly higher signal than the blank signal. Due to both low QC concentrations achieving accuracy and precision of less than $< 20\%$ then it is confirmed that the instrument quantification limit (IQL) is less than the low QC concentration.

5.2.1.4 Sample Preparation

Similar to ibuprofen degradation, the samples collected during the BAC-C12 and S2NS degradation were filtered to ensure no particulates would enter the column of the LC-UV. The filter was kept the same as the ibuprofen degradation due to its availability and high pollutant recovery (for ibuprofen). The recovery % was calculated by utilising the percentage yield (Eq 2.14 in Chapter 2) achieved from comparing the difference in concentration with and without a filter.

Table 5.5 - The obtained recovery percentages of the surfactants after filtering.

	Average Recovery % (to 2 d.p)	Precision % (to 2 d.p)
BAC-C12	93.80	0.30
S2NS	100.02	1.04

The filtration process showed high average recoveries of 93.80 % (to 2 d.p) and 100.02 % (to 2 d.p) for BAC-C12 and S2NS, respectively, with excellent repeatability (precision $< 2\%$). This implies that there is some minimal interaction of BAC-C12 with the filter. However, given the excellent precision ($< 2\%$) of the data this minimal loss can be accounted for when calculating the final degradation percentage. There was no loss witnessed for S2NS, implying S2NS did not interact with the filter.

5.2.2 BAC-C12 Degradation

The results from the PEC degradation of 100 $\mu\text{g/mL}$ BAC-C12 (Figure 5.3) showed poor degradation (52.9%) after 2 hours of treatment. The poor performance could be due to several reasons which are inadequate light intensity, reaction duration or too high an initial concentration. As this system was operating with maximum light intensity and a long reaction time, then the pollutant concentration was reduced to 50 $\mu\text{g/mL}$. The results showed that lowering the initial BAC-C12 concentration by half and maintaining the identical the PEC experiment then the system achieved complete degradation, thus demonstrating its effectiveness for removal pollutants at low concentrations. Previous reports have established that reducing the initial pollutant concentration facilitates higher degradation due to the formation of reactive species being constant for a given PEC system [3, 4]. Therefore, when the initial pollutant concentration decreases the ratio of reactive species to pollutant increases. This results in more pollutant degradation due to the increased availability of active sites [3, 4]. The other issue with high initial pollutant concentration is there is an increased production of by-products which compete with the active sites, thus lowering the number of active sites available for the initial pollutant [3, 4]. This was demonstrated as Figure 5.4 shows that during the degradation of 100 $\mu\text{g/mL}$ BAC-C12 there was by-product formed (retention time of 15.46 minutes). However, the chromatogram obtained at the end of the PEC degradation of 50 $\mu\text{g/mL}$ of BAC-C12 showed no by-product peak. These results support the hypothesis that degradation is more efficient at lower initial pollutant concentrations. In addition, demonstrating that cationic surfactants such as QACs are able to be completely degraded by this PEC system at low concentrations. This report is the first of its kind in literature on PEC surfactant degradation. As discussed in the introduction, current wastewater treatment technologies can only degrade QACs to 50 $\mu\text{g/mL}$ [5]. Therefore, it is suggested to utilise PEC technology as a polishing step to degrade the QACs remaining after wastewater treatment.

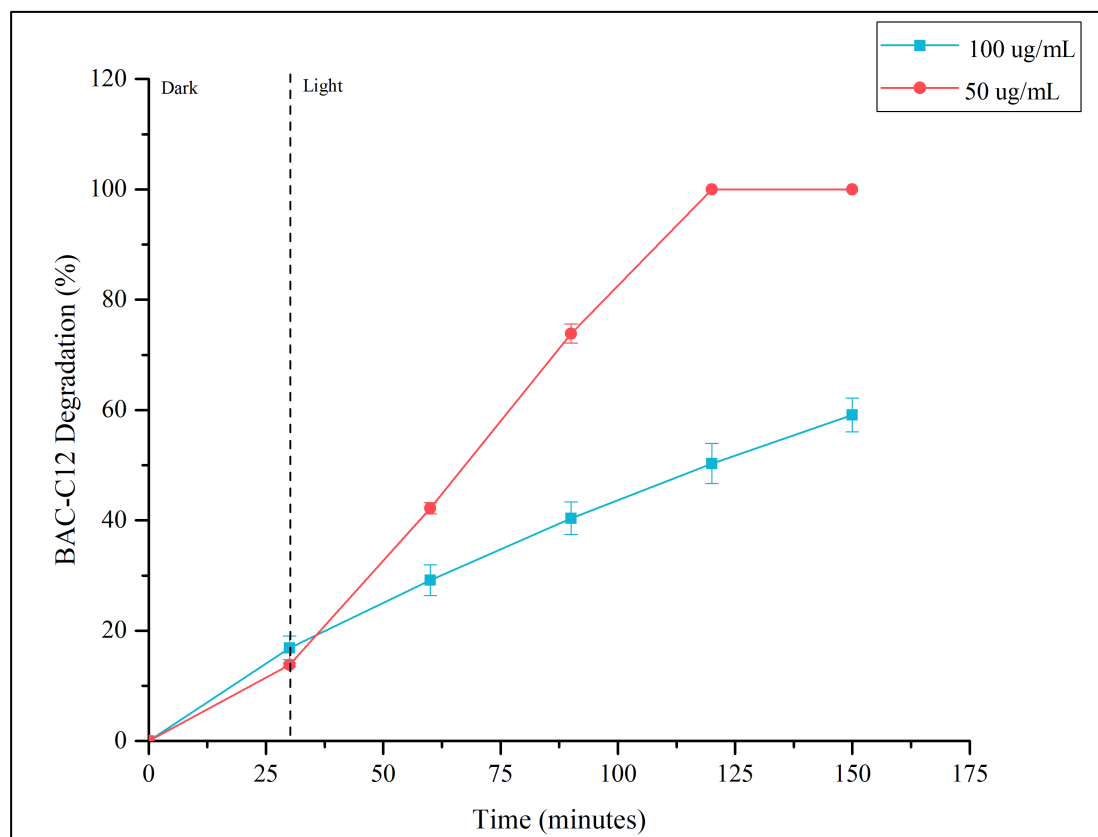


Figure 5.3 - A plot comparing the degradation of high concentration (100 $\mu\text{g/mL}$) vs low concentration (50 $\mu\text{g/mL}$) of BAC-C12 during the PEC experiment. The experiment details are the supporting electrolyte was 1 M NaCl, with 1.2 V (vs Ag/AgCl) and 2 hours of 1 Sun solar light irradiation with an initial 30 minutes in the dark.

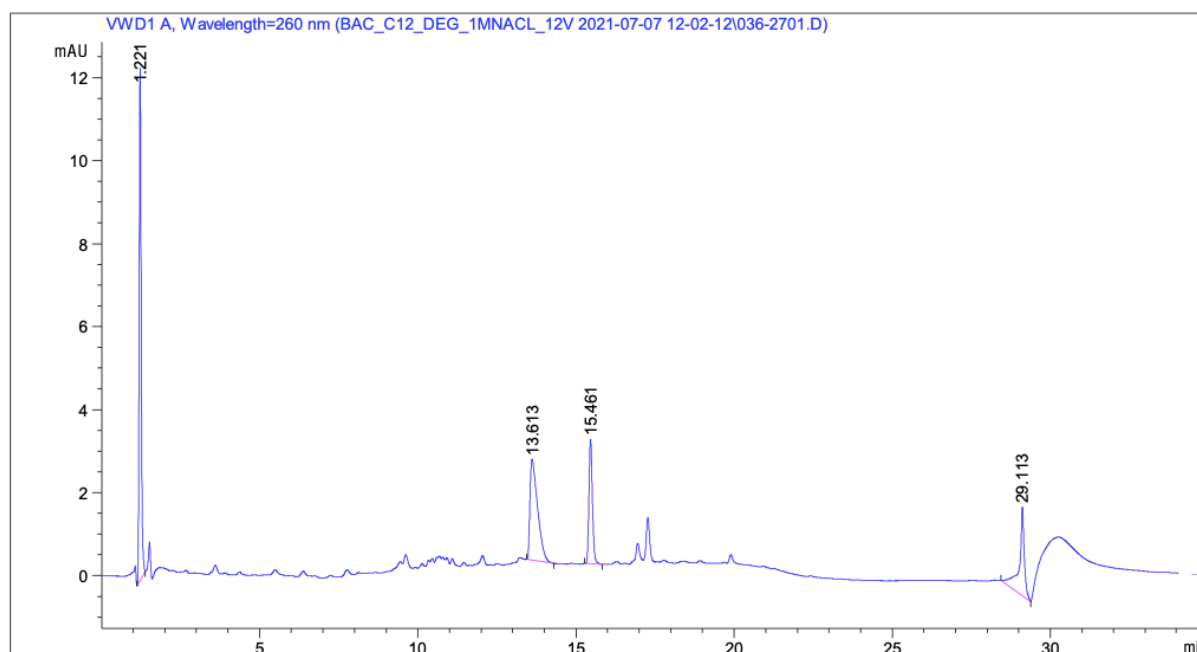


Figure 5.4 - The chromatogram obtained for the analysis of 150-minute sample from the PEC degradation of 100 $\mu\text{g/mL}$ BAC-C12.

To verify the influence of surfactant pollutants concentration on the photoanode activity, chronoamperometry studies were carried out (Figure 5.5). Figure 5.5 shows that there was

similar photocurrent generation for both concentrations. This reveals that the number of holes available for pollutant degradation is the same for both concentrations. Therefore, confirming that there is less competition when there is a lower pollutant concentration hence higher degradation rate.

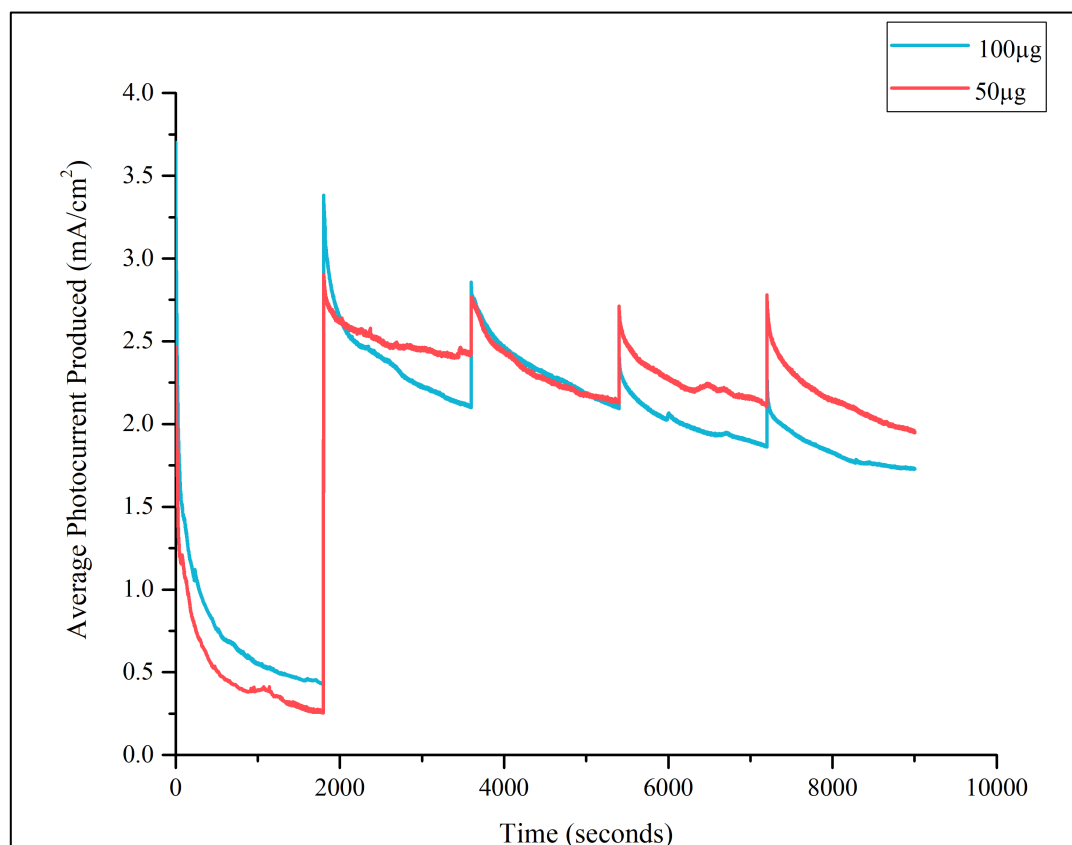


Figure 5.5 - A plot showing the photocurrent produced during the BAC-C12 degradation experiments.

5.2.3 S2NS Degradation

The PEC system was shown to be effective for degrading a cationic surfactant (BAC-C12), so it was decided to utilise it to determine if anionic surfactants could be degraded by this technology. There have been several previous reports which have achieved degradation of anionic surfactants utilising photocatalysis [6]. Therefore, it was hypothesised that PEC should be able to degrade S2NS as it utilises photocatalysis with an applied potential thus resulting in improved pollutant degradation.

The PEC system was very successful in completely degrading 50 µg/mL S2NS from water, as Figure 5.6 showed 100% degradation was achieved within 1 hour of light irradiation (plus the 30 minutes absorption equilibrium). Figure 5.6 also established that the PEC system favoured

the anionic surfactant as the degradation was more rapid for S2NS compared to BAC-C12. This is due to the fundamentals of the electrolysis process in the cell which is when the anode is under an anodic potential the electrons are driven away from the anode to the cathode, thus making the anode positively charged which attracts the negatively charged heads of the anionic compounds towards it [7]. Hence the negatively charged S2NS is more attracted to the positively charged photoanode surface. In comparison the BAC-C12 is degraded slower as it is attracted to the reactive oxidising species produced after water oxidation reactions.

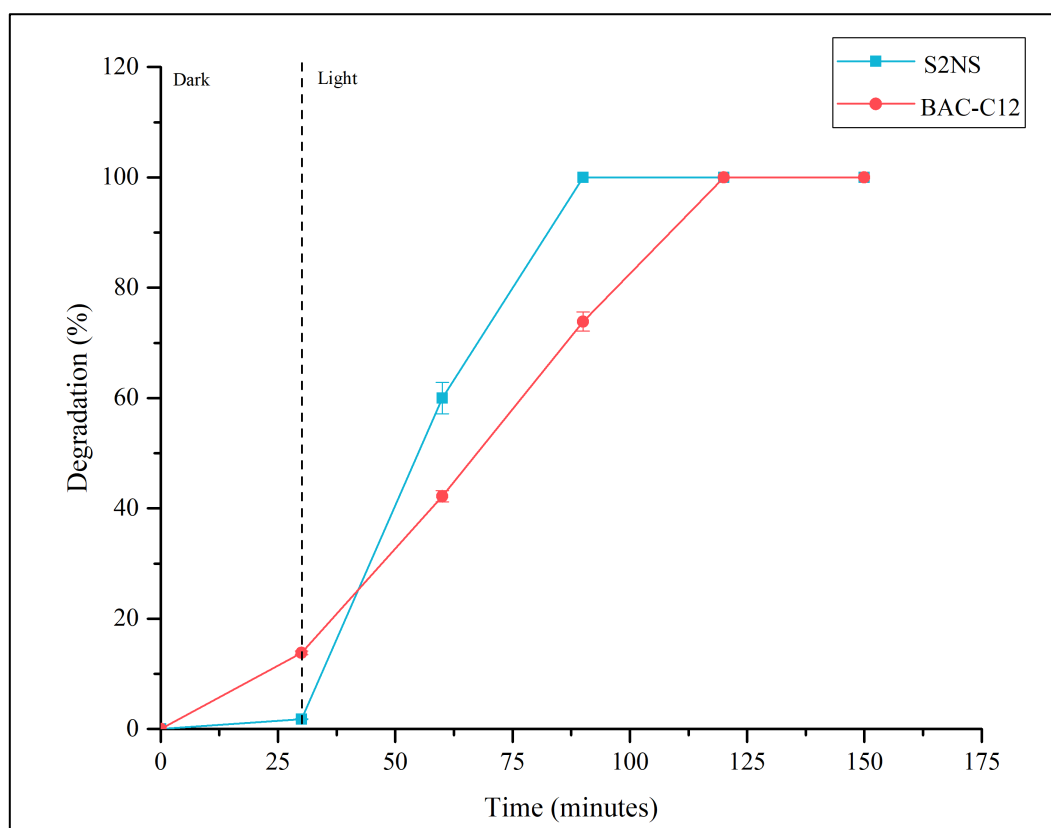


Figure 5.6 - A plot comparing the degradation of (red) $50 \mu\text{g/mL}$ BAC-C12 vs (blue) $50 \mu\text{g/mL}$ S2NS during the PEC process. The experiment details are the supporting electrolyte was 1 M NaCl , with 1.2 V (vs Ag/AgCl) and 2 hours of 1 Sun solar light irradiation with an initial 30 minutes in the dark.

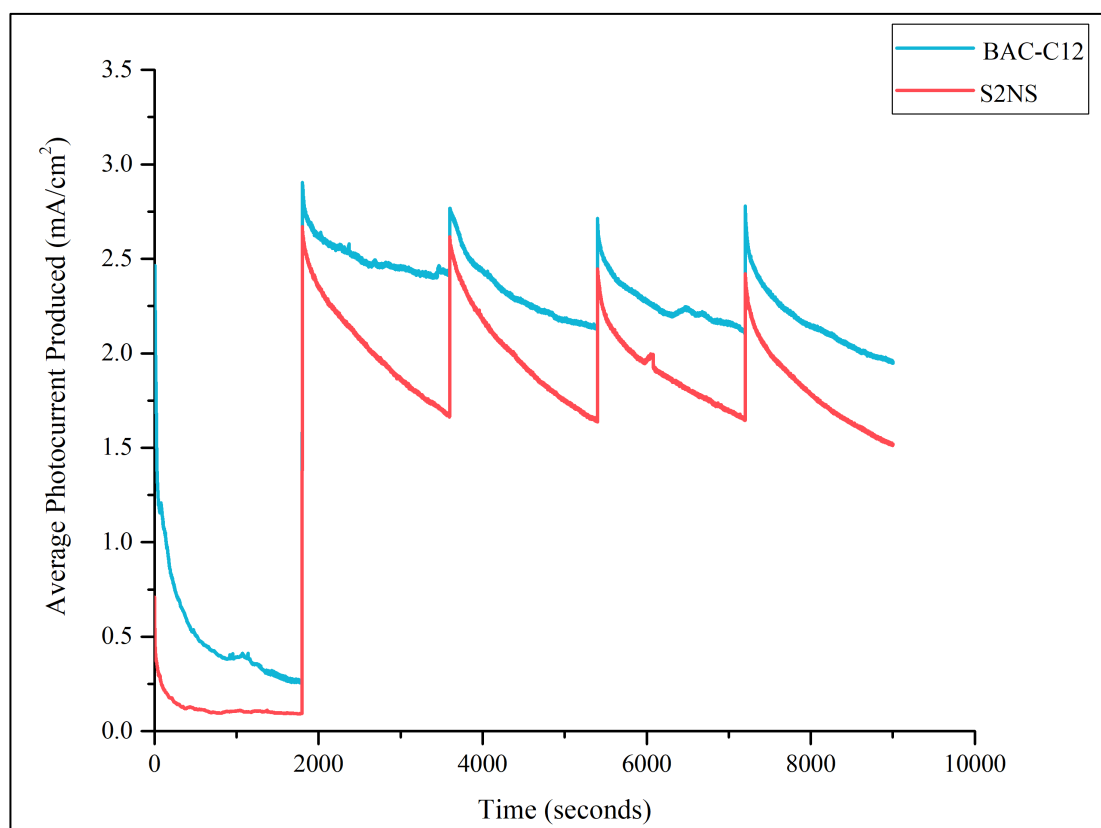


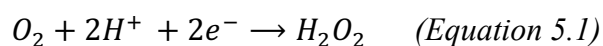
Figure 5.7 - The photocurrent produced by the photoanode during the two surfactant degradation experiments.

The chronoamperometry results (Figure 5.7) showed that the surfactant degradation was not dependent on the photocurrent production but was dependent on the charge of the photoanode. As the average photocurrent produced during S2NS degradation was 0.39 V less than during BAC-C12 degradation. This would suggest there's less holes available for S2NS degradation thus the degradation should be lower. However, that is not the case hence demonstrating that the charge of the photoanode and pollutants are more important factors to take in consideration for pollutant degradation.

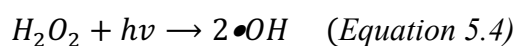
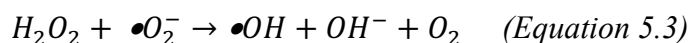
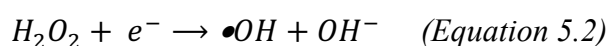
5.2.4 Degradation Pathway Explained

It is well recognised that during PEC, hydroxy radicals ($\bullet\text{OH}$) are formed from water splitting reactions [3, 8, 9]. These hydroxyl radicals have strong oxidising properties that are able to react with pollutants to degrade them [10]. Whilst the free radical analysis in Figure 4.13 (Chapter 4) implied that $\bullet\text{OH}$ was not produced during the PEC process the LC-MS data showed there must have been $\bullet\text{OH}$ produced due to the formation of 4-Isobutylacetophenone from ibuprofen. Hence, $\bullet\text{OH}$ is likely to be responsible for some surfactant degradation.

During the PEC process H_2O_2 has been generated due to the reduction of oxygen [11]:



The production of H₂O₂ is beneficial for several reasons, namely it is able to degrade into hydroxyl radicals under UV light or reduction by electrons/superoxide in the cathode and be used as an alternative fuel [12]:



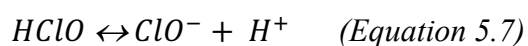
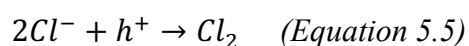
The amount of H₂O₂ produced during the surfactant degradation experiments was determined using Quantofix H₂O₂ stripes. These stripes were utilised to give an approximation of how much H₂O₂ was produced. The drawback of utilising these stripes is the precision is very low as a chart with set concentrations was used with the stripes to determine the H₂O₂ concentration.

Table 5.6 - The H₂O₂ concentration monitored from PEC cell throughout the surfactant degradation process.

Time (minutes)	BAC-C12 - H ₂ O ₂ Concentration (mg/L)	Precision (%)	S2NS - H ₂ O ₂ Concentration (mg/L)	Precision (%)
0	0	0	0	0
30	0	0	0	0
60	2.33	49.49	0	0
90	5.33	75.78	0	0
120	5.33	75.78	3	0
150	5.33	75.78	7.67	52.72

Interestingly, a significant amount of H₂O₂ was generated from the 2WO₃/BiVO₄ photoanode during the BAC-C12 degradation experiment which would indicate H₂O₂ was not involved in BAC-C12 degradation. However, during the PEC S2NS degradation process, H₂O₂ was generated after S2NS was completely degraded by the other reactive species. This would imply that H₂O₂ was involved in S2NS degradation. It has been demonstrated by literature that H₂O₂ can improve the amount of pollutant degradation [13, 14]. Therefore, the presence of H₂O₂ can improve pollutant degradation.

Sodium chloride (NaCl) was the supporting electrolyte utilised in this PEC system for two reasons. Firstly, as in Chapter 3 utilising NaCl as the supporting electrolyte resulted in higher photocurrent production compared to sodium sulphate (Na₂SO₄) due to improved charge separation. Thus, indicating more h⁺ would be available for pollutant degradation. Secondly other reports suggest that utilising NaCl as a supporting electrolyte helps generate active chlorine species such as Cl₂, HClO and Cl⁻ [15, 16]. This is due to the chlorine ions reacting with the holes available on the photoanode's surface. Therefore, the active chlorine species are produced by the following reactions [15, 16]:



Active chlorine species has previously been demonstrated to have disinfection properties [15]. Therefore, it has been evidenced that utilising NaCl as a supporting electrolyte compared to other electrolytes has improved the pollutant degradation [16].

It was assumed that active chlorine was produced during the PEC process due to the utilisation of NaCl as the electrolyte. While pH cannot dictate the presence of active chlorine it can indicate the dominant species as the amount of each active chlorine produced during the PEC process varies on the pH and temperature of the solution [15]. At room temperature, Cl₂ is the dominant species in very acidic conditions (< 3.3), while HClO dominates at 3.3 < pH < 7.5 and as OCl⁻ dominates in pH > 7.5 [15]. Therefore, determining the pH of the solution will identify the type of active chlorine species present.

Table 5.7 - The pH of the solution during the surfactant degradation experiments

	BAC-C12 Average	Precision (%)	S2NS Average	Precision
pH Before	5.80	2.00	5.98	1.42
pH After	2.60	4.12	2.59	1.61

The repeatability of the pH was very good as the precision of the measurements were < 5% for both before and after BAC-C12 and S2NS degradation experiments.

During the degradation of BAC-C12 the average pH of the solution decreased from 5.80 to 2.60. This indicates that the solution is becoming acidic. Acidification occurs due to the increase of protons in the solution which can occur from the water oxidation process and the hydrolysis of dissolved chlorine (Eq 5.6). Given that the pH is < 7.5, then this suggests that only Cl_2 and HClO would be generated and appear to be the predominant species in the degradation of BAC-C12 [15].

Similarly, the average pH decreased from 5.98 to 2.59 during degradation of S2NS. This again suggests the acidification thus confirming protons are being produced. This indicates that active chlorine species are produced and available for pollutant degradation. Likewise to BAC-C12 the pH was < 7.5 thus indicating that only Cl_2 and HClO are the active chlorine species responsible for S2NS degradation [15].

It is beneficial that both degradation experiments produce hypochlorous acid over hypochlorite ion as it has a strong disinfection ability [15]. Low pH is also beneficial for S2NS (anionic surfactant) degradation as the positive charged holes are dominant species compared to $\bullet\text{OH}$. Thus, driving more negative charged surfactants to the photoanode surface allowing for higher degradation.

5.2.5 The Feasibility of Surfactant Degradation Via Photoelectrocatalysis

The pH of the treated solution needs to be taken into consideration when determining the feasibility of utilising this technology. Releasing effluents which are too high or low in pH can cause damage to aquatic life, with a majority only surviving in a range of 6.5 - 9 [17]. The results in Table 5.7 shows that during the BAC-C12 degradation the pH decreased significantly, due to the production of H^+ . Due to the treated solution pH being 2.60 then a post-treatment would be required to help neutralise the solution. Similarly, the pH of the S2NS treated solution was 2.59 which would be too acidic to release into the environment thus requiring neutralisation. The drawback of adding a further post treatment would be that it increases the cost of photoelectrocatalysis.

5.3 Conclusion

It is imperative to identify a technology that can eliminate surfactants from wastewater as it is causing bacteria to build a resistance to disinfectants whilst being toxic to aquatic life. The issue with current wastewater treatment technologies is that whilst they can remove the majority of surfactants, they are unable to completely eliminate them. This results in surfactants ending up in the environment. Therefore, the feasibility of PEC techniques to remove surfactants from industrial wastewater was investigated.

It was established that the PEC system with $2\text{WO}_3/1\text{BiVO}_4$ photoanode was able to completely remove BAC-C12 (cationic) and S2NS (anionic) at low concentrations ($50 \mu\text{g/mL}$). It was established that the PEC system favoured the anionic more than the cationic surfactant. This is possibly due to the photoanode's surface being enriched with positively charged h^+ , thus encouraging the negative heads to the active sites. The experimental results prove that PEC has the potential to be utilised as a polishing step in wastewater treatment to degrade both cationic and anionic surfactants. However, further research would be required to verify if it can effectively degrade other anionic and cationic surfactants. The challenge of utilising this technology is that the treated solution has a low pH (less than 3) thus it would need a post-treatment step to help neutralise the solution before releasing into the environment.

It was determined that the species mainly responsible for the degradation of BAC-C12 were Cl_2 , HClO and $\bullet\text{OH}$. In relation to S2NS degradation it was the h^+ , Cl_2 , HClO , $\bullet\text{OH}$ and H_2O_2 which were mainly responsible. However, quantification experiments for these species would need to be conducted to ensure this is true.

5.4 Bibliography

1. James N Miller, J.C.M., *Statistics and Chemometrics for Analytical Chemistry*. Vol. Six. 2010, Essex: Pearson Education Limited.
2. Administration, U.S.D.o.H.a.H.S.F.a.D., *Bioanalytical Method Validation - Guidance for Industry*. 2018, The Food and Drug Administration (FDA): <https://www.fda.gov/regulatory-information/search-fda-guidance-documents/bioanalytical-method-validation-guidance-industry>.
3. Zhang, Y., et al., *Photoelectrocatalytic degradation of recalcitrant organic pollutants using TiO₂ film electrodes: An overview*. Chemosphere, 2012. **88**(2): p. 145-154.
4. Montenegro-Ayo, R., et al., *Scaling up Photoelectrocatalytic Reactors: A TiO₂ Nanotube-Coated Disc Compound Reactor Effectively Degrades Acetaminophen*. Water, 2019. **11**(12): p. 2522.
5. Hora, P.I. and W.A. Arnold, *Photochemical fate of quaternary ammonium compounds in river water*. Environmental Science: Processes & Impacts, 2020. **22**(6): p. 1368-1381.
6. Kuźmiński, K., A.W. Morawski, and M. Janus, *Adsorption and Photocatalytic Degradation of Anionic and Cationic Surfactants on Nitrogen-Modified TiO₂*. Journal of Surfactants and Detergents, 2018. **21**(6): p. 909-921.
7. Yu, L., et al., *Photoelectrocatalytic performance of TiO₂ nanoparticles incorporated TiO₂ nanotube arrays*. Applied Catalysis B: Environmental, 2012. **113-114**: p. 318-325.
8. Garcia-Segura, S. and E. Brillas, *Applied photoelectrocatalysis on the degradation of organic pollutants in wastewaters*. Journal of Photochemistry and Photobiology C: Photochemistry Reviews, 2017. **31**: p. 1-35.
9. Yang, J., et al., *Effects of hydroxyl radicals and oxygen species on the 4-chlorophenol degradation by photoelectrocatalytic reactions with TiO₂-film electrodes*. Journal of Photochemistry and Photobiology A: Chemistry, 2009. **208**(1): p. 66-77.
10. Zhou, Y., G. Zhang, and J. Zou, *Photoelectrocatalytic generation of miscellaneous oxygen-based radicals towards cooperative degradation of multiple organic pollutants in water*. Journal of Water Reuse and Desalination, 2021.
11. Papagiannis, I., et al., *Photoelectrocatalytic production of hydrogen peroxide using a photo(catalytic) fuel cell*. Journal of Photochemistry and Photobiology A: Chemistry, 2020. **389**: p. 112210.
12. Chen, S. and Y. Liu, *Study on the photocatalytic degradation of glyphosate by TiO₂ photocatalyst*. Chemosphere, 2007. **67**(5): p. 1010-1017.
13. Sun, J., et al., *H₂O₂ assisted photoelectrocatalytic degradation of diclofenac sodium at g-C₃N₄/BiVO₄ photoanode under visible light irradiation*. Chemical Engineering Journal, 2018. **332**: p. 312-320.
14. Li, X., et al., *Synergetic activation of H₂O₂ by photo-generated electrons and cathodic Fenton reaction for enhanced self-driven photoelectrocatalytic degradation of organic pollutants*. Applied Catalysis B: Environmental, 2018. **235**: p. 1-8.
15. Zaroni, M.V.B., et al., *Photoelectrocatalytic Production of Active Chlorine on Nanocrystalline Titanium Dioxide Thin-Film Electrodes*. Environmental Science & Technology, 2004. **38**(11): p. 3203-3208.
16. Wu, X., et al., *Investigation on the Photoelectrocatalytic Activity of Well-Aligned TiO₂ Nanotube Arrays*. International Journal of Photoenergy, 2012. **2012**: p. 832516.

17. Fondriest Environmental, I. *pH of Water*. Fundamentals of Environmental Measurements 2013.

Chapter 6 : Hydrogen Production

6.1 Introduction

The aim of this chapter was to quantify the hydrogen gas produced via the developed PEC system and verify if it can simultaneously produce hydrogen gas while degrading pollutants. The work presented in this chapter was the result of utilising the PEC system with the developed $\text{WO}_3/\text{BiVO}_4$ photoanode to produce hydrogen gas in pure electrolyte, during ibuprofen degradation (with a lower and higher electrolyte concentration), during light and dark conditions and finally during surfactant degradation. This chapter is important as hydrogen is currently being produced via steam reforming which produces CO_2 and is not sustainable. Therefore, there is a drive for researchers to find an alternative method for producing hydrogen gas.

6.2 Results and Discussion

6.2.1 Hydrogen Production Without Pollutants

Several studies have reported on how PEC has successfully produced hydrogen from freshwater based electrolytes [1-6]. In this study, the system utilised was $2\text{WO}_3/1\text{BiVO}_4$ (working electrode), Ag/AgCl (reference electrode) and Pt wire (counter electrode) in 0.5 M of NaCl and 1.2 V (vs AgCl/AgCl) applied potential and 1 Sun of solar light. The reaction occurred in a two compartment PEC cell separated by a Nafion membrane. The Nafion membrane (proton exchange membrane) was utilised to ensure that the hydrogen ions (protons, H^+) were the only species that could travel into the cathodic compartment to react with the electrons on the Pt counter electrode. Thus, it improves the amount of hydrogen gas produced as no other species generated by the water splitting reaction could travel to the counter electrode. This has also been reported by other researchers such as Zhang et al who used a proton exchange membrane to help separate hydrogen and oxygen resulting in improved hydrogen production [3].

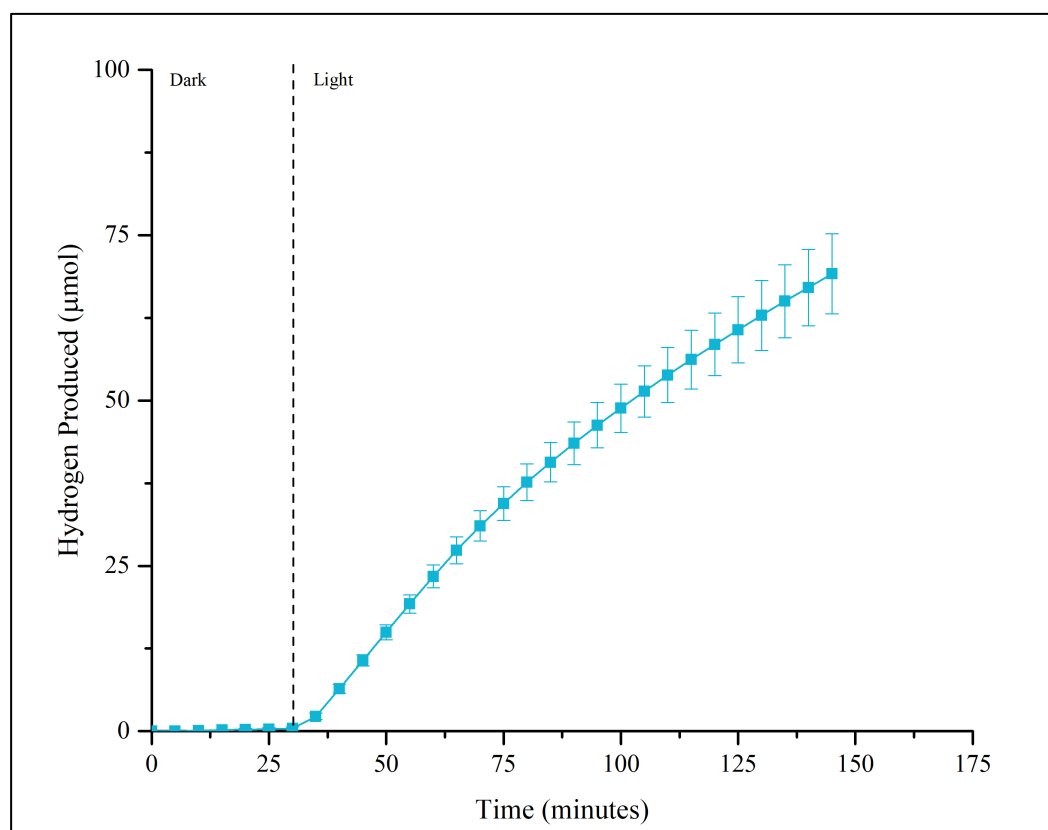


Figure 6.1 - Hydrogen production for the developed PEC system. Note that The PEC system utilised for hydrogen production used $2\text{WO}_3/\text{BiVO}_4$ (photoanode), Pt mesh (counter electrode), Ag/AgCl (reference electrode), 1.2 V applied potential, 0.5 M sodium chloride as the supporting electrolyte and 1 Sun of Solar Light irradiation (2 hours) after 30 minutes in the dark.

Figure 6.1 established that this PEC system was very successful in generating hydrogen as an average of $68.79 \mu\text{mol}/\text{cm}^2$ was produced during the 2 hours of light irradiation. This equates to $34.40 \mu\text{mol}/\text{cm}^2\text{hr}$, which is competitive when compared to the literature and demonstrates the effectiveness of this PEC system. Sfaelou et al reported the production of $120 \mu\text{mol}/\text{hr}$ of hydrogen when they utilised a larger active surface area ($3.5 \text{ cm} \times 5 \text{ cm}$) photoanode and higher applied potential of 1.6V (vs Ag/AgCl) [1]. This would mean Sfaelou et al only produced $6.86 \mu\text{mol}/\text{cm}^2\text{hr}$ which is only 10% the amount that this system this producing. This might be due to the highly mesoporous nature of $\text{WO}_3/\text{BiVO}_4$ photoanode architecture allowing effective mass transport of the electrolyte and lowering charge recombination.

Another researcher found that they were able to produce a significant amount of hydrogen ($130 \mu\text{mol}/\text{hr}$) when utilising utilised WO_3 as a photoanode with 0.5 M H_2SO_4 as the supporting electrolyte, 0.1 Wcm^{-2} light intensity (with UV filter) and 1.2 V applied potential [2]. However, their photoanode had an active area of 9 cm^2 which is much greater than this study's photoanode (1 cm^2 active surface) [2]. Having a high active area means that it has more photoactive material for photon absorption, thus a higher amount of electron excitation. It

would suggest that to increase hydrogen production for this system then increasing the photoanode's active area would be recommended.

6.2.2 Hydrogen Production During Ibuprofen Degradation

The optimised PEC system utilised in Chapter 4 was very effective in degrading ibuprofen due to its success in generating reactive species from long hole lifetimes caused by the heterojunction in the photoanode. During the production of reactive species via water oxidation, H^+ are generated as a by-product in the anodic compartment. These protons (H^+) can transfer to the cathodic compartment through the Nafion membrane and react with the electrons on the counter electrode thus generating hydrogen while other ions and reactive species remain in the anodic compartment to degrade ibuprofen. Therefore, it would be expected that there is high selectivity of hydrogen gas production at the cathode.

Figure 6.2 demonstrates that the PEC system was able to generate similar amounts of hydrogen gas in the presence and absence of ibuprofen in the electrolyte (anode compartment). The PEC system produced 62.76 μmol of hydrogen whilst simultaneously degrading ibuprofen in the water. This compares to 69.18 μmol in pure 0.5 M NaCl and implies that hydrogen production is not significantly affected by ibuprofen degradation. This is due to the Nafion membrane which successfully separates the ibuprofen degradation reactions (at the anode) from the hydrogen production (at the cathode). If the membrane was absent the secondary by-products from ibuprofen degradation would further reduce at the cathode surface, which would be a competitive reaction for hydrogen gas production. Therefore, a two-compartment PEC cell with a proton exchange membrane is recommended for high hydrogen yield.

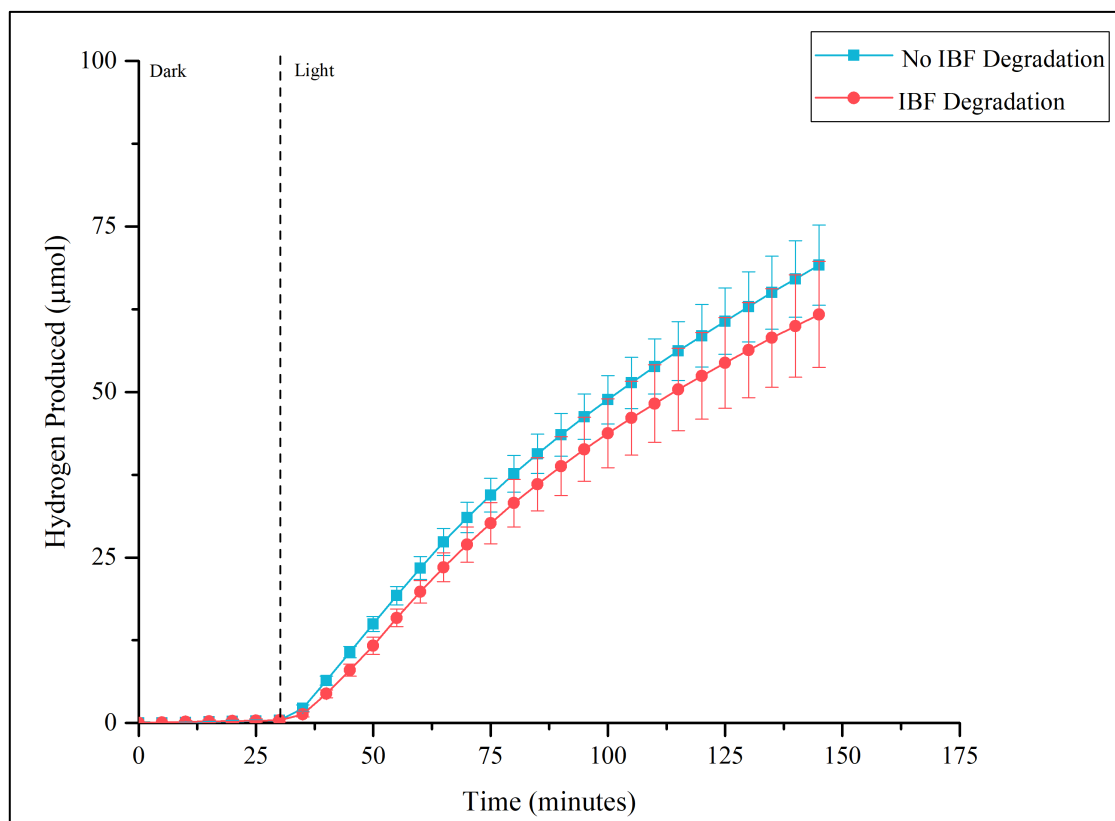


Figure 6.2 - Hydrogen production for the developed PEC system during ibuprofen degradation (red) and no ibuprofen degradation (blue). Note that The PEC system utilised for hydrogen production used $2\text{WO}_3/\text{1BiVO}_4$ (photoanode), Pt mesh (counter electrode), Ag/AgCl (reference electrode), 1.2 V applied potential, 0.5 M sodium chloride as the supporting electrolyte and 1 Sun of Solar Light irradiation (2 hours) after 30 minutes in the dark.

To determine the influence of light irradiation on hydrogen generation, the PEC hydrogen production during ibuprofen degradation was repeated under dark conditions. This will also help determine if $2\text{WO}_3/\text{1BiVO}_4$ is a dark catalyst which means that it is able to achieve electron excitation in dark conditions.

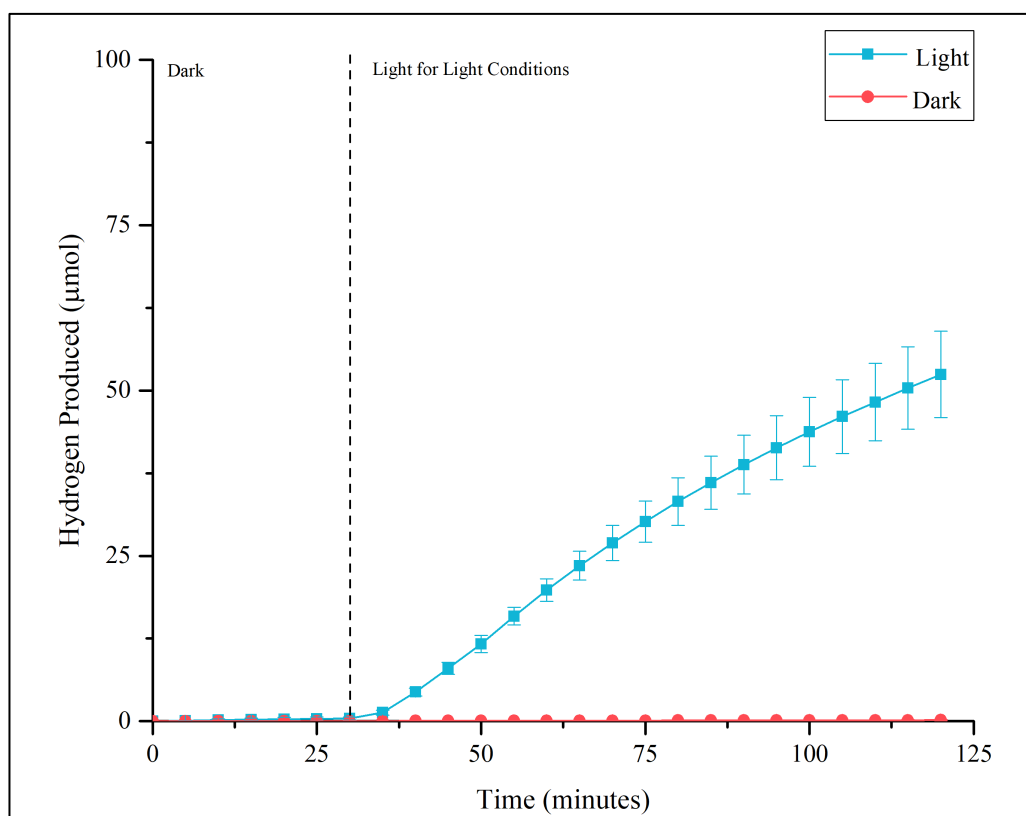


Figure 6.3 - Hydrogen production for the developed PEC system in complete dark conditions (blue) and during 1 Sun of Solar Light irradiation (2 hours) after 30 minutes in the dark (red). Note that The PEC system utilised for hydrogen production used $2\text{WO}_3/\text{1BiVO}_4$ (photoanode), Pt mesh (counter electrode), Ag/AgCl (reference electrode), 1.2 V applied potential and 0.5 M sodium chloride as the supporting electrolyte.

Figure 6.3 demonstrates hydrogen production during dark conditions is negligible compared to light irradiation. This confirms that the photoanode is not a dark catalyst as the hydrogen production is dependent on light irradiation thus it is purely a photoelectrocatalytic process [1]. As photon absorption excites the electrons from the VB to CB of the photoanode, the applied potential helps separate and drive these electrons to the FTO substrate then to the counter electrode for hydrogen production [2].

It has been identified that increasing the supporting electrolyte concentration can increase pollutant degradation due to the higher conductivity resulting in higher charge carrier separation [7]. This is due to extra photogenerated electrons being captured by the external electrical field thus a greater number travelling to the counter electrode [7]. Therefore, it is assumed that increasing the supporting electrolyte's concentration should increase hydrogen production. To ensure this assumption was true, the PEC hydrogen gas production was quantified in two different concentrations of NaCl electrolyte (0.5 and 1 M).

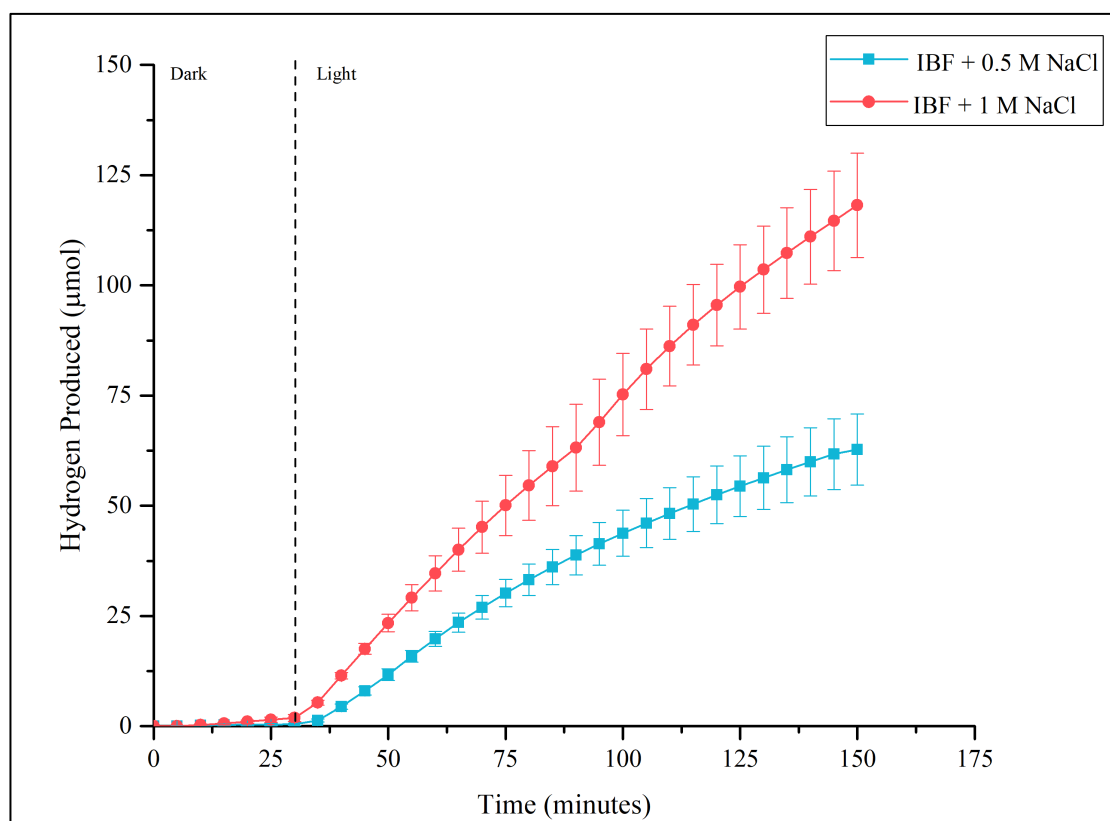


Figure 6.4 - Hydrogen production for the developed PEC system in ibuprofen degradation in 0.5 M NaCl (blue) and ibuprofen degradation in 1 M NaCl (red). Note that The PEC system utilised for hydrogen production used $2\text{WO}_3/\text{BiVO}_4$ (photoanode), Pt mesh (counter electrode), Ag/AgCl (reference electrode), 1.2 V applied potential and 1 Sun of Solar Light irradiation (2 hours) after 30 minutes in the dark.

As expected, the hydrogen production increased from 62.76 μmol to 118.17 μmol for 150-minute reaction. Doubling the NaCl concentration resulted in the hydrogen gas quantity to increase by nearly 2-fold. This demonstrates that the electrolyte's concentration is a critical parameter in promoting hydrogen production. Therefore, it is evident that a high supporting electrolyte concentration results in high hydrogen production.

6.2.3 Hydrogen Production During Surfactant Degradation

As hydrogen production was not affected by ibuprofen degradation (Figure 6.2) it was necessary to testify this was true for surfactant degradation. Therefore, hydrogen gas generation during surfactant degradation was analysed. It was hypothesised that the hydrogen production during surfactant degradation would be similar to ibuprofen degradation.

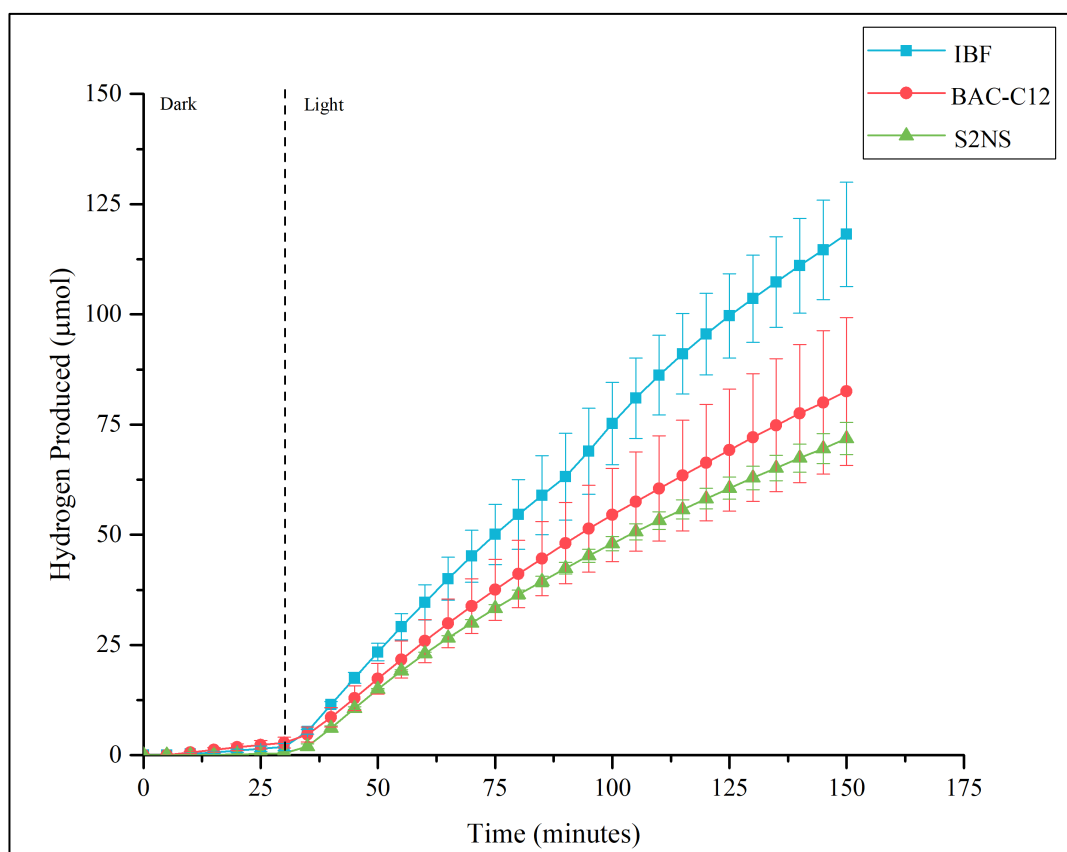


Figure 6.5 - Hydrogen production for the developed PEC system during S2NS degradation (blue), BAC-C12 degradation (red) and ibuprofen degradation. Note that The PEC system utilised for hydrogen production used $2\text{WO}_3/\text{BiVO}_4$ (photoanode), Pt mesh (counter electrode), Ag/AgCl (reference electrode), 1.2 V applied potential, 1 M sodium chloride as the supporting electrolyte and 1 Sun of Solar Light irradiation (2 hours) after 30 minutes in the dark.

Figure 6.5 demonstrated that hydrogen generated during PEC degradation of BAC-C12 and S2NS surfactant was significantly lower (82.51 μmol and 71.81 μmol , respectively) compared to ibuprofen. This implies that the production of hydrogen depends on the type of pollutant degraded and relates to the hole scavenging properties of the pollutant species. This was also identified by Zhao et al who established that the hydrogen generation was dependent on the removal efficiency [8]. The higher the removal efficiency, the higher the hydrogen production indicating that a higher amount of photogenerated holes react with the pollutant while the photogenerated electrons are transferred to the cathode for hydrogen production [8]. This means the pollutant acts as a sacrificial agent [8]. The recovery of hydrogen gas from pharmaceutical (ibuprofen) and surfactants (BAC-C12 and S2NS) pollutants are compared in Figure 6.5. It demonstrates that the ibuprofen pollutants degradation process allows more hydrogen gas recovery from cathode compartment than the surfactants-based pollutant degradation process. However, note that the pollutant concentration is not identical between ibuprofen (100 $\mu\text{g}/\text{mL}$) and surfactants (50 $\mu\text{g}/\text{mL}$). For instance, a higher concentration of ibuprofen offers excellent hole scavenging from photoanode to electrolyte thus resulting in

higher photoelectrons collection at the charge collector. However, too high a pollutant concentration restricts the degradation rate as it lowers the number of active sites to pollutant species. Therefore, increasing pollutant concentration is a trade-off between hydrogen production at the cathode and pollutant degradation performance at the anode.

6.2.4 Limitations of these Hydrogen Production Studies

6.2.4.1 Temperature Control

The cell set-up made it impossible to control the temperature as there was no cooling jacket or cooling tank available to go around the PEC cell. Therefore, while the reactions were conducted at room temperature, due to the constant light irradiation the temperature of the solution in the PEC cell would increase. It has been reported by J.J Velazquez et al that increasing the reaction temperature results in higher hydrogen production [9]. The reason hydrogen production is dependent on temperature can be explained by Arrhenius equation [2]. As the Arrhenius equation is [2]:

$$k = k^0 \exp\left(\frac{-E_a}{RT}\right) \quad (\text{Equation 6.1})$$

Where:

k = reaction rate

k^0 = pre-exponential factor

E_a = activation energy

R = universal gas constant

T – absolute temperature

Therefore, it is important to monitor the temperature and control the temperature during the experiment to help determine the actual hydrogen production at room temperature. The other experiment which should be considered for the future would be controlling the temperature of the reaction and altering the temperature to determine the best temperature for maximum hydrogen production.

6.2.4.2 Solar to Hydrogen Energy Conversion Efficiency

Another limitation with the set-up of the hydrogen study conducted in this thesis was the inability to calculate the solar to hydrogen conversion efficiency. This is due to the conventional equation (Eq 6.1) utilised for solar to hydrogen conversion efficiency being

unsuitable in this study as the PEC system utilises an applied potential to help improve hydrogen generation [10]. The equation utilised to calculate the solar to hydrogen conversion efficiency is [10]:

$$\eta_{STH} = \frac{\Delta G \times r_{H_2}}{P \times S} \quad (\text{Equation 6.2})$$

Where [10]:

ΔG = Gibbs free energy (237 kJ mol⁻¹)

r_{H_2} = Hydrogen production rate (mols/s)

P = Light intensity (mW/cm²)

S = Area of the illuminated photoanode (cm²)

As this PEC system utilises an applied potential then it is necessary to find an equation which allows the electrical energy to be subtracted from the redox potential of water splitting [10]. This would mean to calculate the energy efficiency of the PEC system then the applied bias photon-to-current efficiency (ABPE) could be used instead (please see equation 6.3) [10].

$$ABPE = \frac{J_{photo}(V_{redox} - V_{bias})}{P} \quad (\text{Equation 6.3})$$

Where [10]:

J_{photo} = Generated photocurrent density (mA/cm²)

V_{redox} = Redox potential for water splitting (1.23 V vs NHE)

V_{bias} = Potential difference between the working and counter electrode (V vs NHE)

P = Light intensity (mW/cm²)

However, this requires knowing the potential difference between the working and the counter electrode [10]. Since the only potential known is the potential between the working and reference electrode, this equation cannot be utilised either. Therefore, it is suggested that to calculate the solar to hydrogen conversion efficiency of this system it would be necessary to repeat the experiments without utilising an applied potential and then utilising an applied potential but with a 2-electrode set-up to identify the potential difference between the working and counter electrode.

6.3 Conclusion

It can therefore be concluded that the PEC system based on the mesoporous $2\text{WO}_3/\text{BiVO}_4$ photoanode developed in this study was extremely effective in producing hydrogen gas. As a result of utilising a low potential of 1.2 V (vs Ag/AgCl) and a supporting electrolyte concentration of 0.5 M was able to produce $34.40 \mu\text{mol}/\text{cm}^2\text{hr}$ of hydrogen. This quantity is highly competitive compared to the literature. The PEC system was also very effective in simultaneously degrading ibuprofen and producing hydrogen, as the hydrogen generation was not affected by ibuprofen degradation in the anodic compartment. The Nafion (proton exchange) membrane played a key role in achieving higher selectivity of H^+ reduction at the cathode as it obstructs the other by-products from pollutant degradation from reacting with the photoelectrons on the cathode. Therefore, it is suggested that if the PEC system is utilised to produce hydrogen and simultaneously degrade a pollutant then the process needs to be run in a two compartment PEC cell with a proton exchange membrane to prevent any undesired reactions interfering with hydrogen production.

It was assumed that the pollutant degradation rate would not affect hydrogen production. However, this is not the case as hydrogen production during the surfactant degradation was much reduced compared to ibuprofen degradation. The pollutants can act as sacrificial agents which means it scavenges the photogenerated holes so that more electrons can travel to the cathode. This helps to explain why the surfactant degradation resulted in a lower hydrogen production compared to ibuprofen degradation, as the surfactant concentration in the anodic compartment is much less than the ibuprofen. This means there are less holes being scavenged thus some electrons are being recombined. Therefore, the hydrogen production during pollutant degradation is affected by the types of pollutant and its concentration. However more research is required in this field of work.

It was recognised that hydrogen production is highly dependent on the supporting electrolyte concentration. Increasing the supporting electrolyte concentration from 0.5 M to 1 M resulted in an increase of approximately $59.09 \mu\text{mol}/\text{cm}^2\text{hr}$ of hydrogen produced. This is due to the excellent photocharge carrier separation at the photoanode/electrolyte interfaces due to the reduction in solution resistivity. Therefore, more electrons are transferred to the counter electrode for hydrogen production.

Overall, this chapter demonstrates how successful the PEC process is in green hydrogen generation. Thus, it has significant potential as an alternative to steam reforming due to its sustainability. The other considerable benefit relates to its ability to produce hydrogen whilst degrading pollutants. However, more research is required to determine the optimum working conditions for achieving high hydrogen production and pollutant degradation, whilst also doing the experiments with conditions that meet the requirements which allows the solar to hydrogen energy conversion efficiency to be calculated and to quantify the hydrogen produced for different temperatures by controlling the temperature of the PEC process.

6.4 Bibliography

1. Sfaelou, S., et al., *Mesoporous WO₃ photoanodes for hydrogen production by water splitting and PhotoFuelCell operation*. International Journal of Hydrogen Energy, 2016. **41**(14): p. 5902-5907.
2. Zhao, W., et al., *Hydrogen generation via photoelectrocatalytic water splitting using a tungsten trioxide catalyst under visible light irradiation*. International Journal of Hydrogen Energy, 2012. **37**(1): p. 908-915.
3. Zhang, Y., et al., *Enhancing hydrogen evolution by photoelectrocatalysis of water splitting over a CdS flowers-loaded TiO₂ nanotube array film on the Ti foil substrate*. Ceramics International, 2020. **46**(11, Part A): p. 17606-17613.
4. Wang, W., et al., *Photoelectrocatalytic hydrogen generation and simultaneous degradation of organic pollutant via CdSe/TiO₂ nanotube arrays*. Applied Surface Science, 2016. **362**: p. 490-497.
5. Wu, Z., et al., *Simultaneous photoelectrocatalytic aromatic organic pollutants oxidation for hydrogen production promotion with a self-biasing photoelectrochemical cell*. Electrochimica Acta, 2017. **254**: p. 140-147.
6. Guaraldo, T.T., et al., *Hydrogen production and simultaneous photoelectrocatalytic pollutant oxidation using a TiO₂/WO₃ nanostructured photoanode under visible light irradiation*. Journal of Electroanalytical Chemistry, 2016. **765**: p. 188-196.
7. Ding, Y., et al., *Photoelectrochemical activity of liquid phase deposited TiO₂ film for degradation of benzotriazole*. Journal of Hazardous Materials, 2010. **175**(1): p. 96-103.
8. Zhao, X., et al., *g-C₃N₄ photoanode for photoelectrocatalytic synergistic pollutant degradation and hydrogen evolution*. Applied Surface Science, 2019. **467-468**: p. 658-665.
9. Velázquez, J.J., et al., *Effect of reaction temperature and sacrificial agent on the photocatalytic H₂-production of Pt-TiO₂*. Journal of Alloys and Compounds, 2017. **721**: p. 405-410.
10. Jiang, C., et al., *Photoelectrochemical devices for solar water splitting – materials and challenges*. Chemical Society Reviews, 2017. **46**(15): p. 4645-4660.

Chapter 7 : Conclusion and Future Outlook

As the global population rises every day, the demand for clean water has gradually increased. The World Health Organisation (WHO) identified that at least 2 billion people who do not have clean drinking water which results in 829,000 deaths per year [1]. These deaths could have been prevented if better water sanitation had been available. However current water treatment processes are complex to use, require a large amount of space and are expensive. This results in many developing countries being unable to provide clean water.

Water UK has estimated that the average person uses nearly 142 litres per day and UK companies consume 64 million litres of water [2]. This demonstrates the vast amount of water consumed in the UK alone. One of the solutions for managing the water demand issue is to promote recycled water, instead of utilising fresh water for many applications. Therefore, it is vital that water cleaning technologies completely eradicate pollutants from water so that it can be used for drinking, agricultural, domestic and industrial use. Unfortunately, many reports have established that current water technologies are unable to completely eliminate pollutants from water.

The consequence of an ever-growing population is that the need for pharmaceutical drugs has increased in healthcare sectors as have the use of surfactants in disinfectant applications in the domestic sector. Due to recent research, the potential threats of pharmaceutical and surfactant waste in water are being recognised. This shows how important it is for water technology to remove these pollutants. However, current water technologies are not appropriately designed to remove some of these pollutants in lower concentrations ($\mu\text{g/mL}$). On the other hand, although a few of the current water technologies can achieve very high removals; they would require a high amount of energy and produce a significant amount of waste. As a result it is critical to explore different technologies that can remove low concentration organic pollutants from water. Therefore, this thesis set out to find an alternative technology that could completely eliminate these types of pollutants.

PEC is a promising route for pollutant degradation due to water oxidation and reduction reactions occurring by light driven catalytic reaction. The excitation of photoelectrons in the semiconductor (photoanode) creates holes which can either degrade pollutants directly or

produce reactive species which can degrade the pollutants. The photoelectrons from the conduction band of the semiconductor are transferred to the counter electrode and react with the hydrogen ions to produce hydrogen gas. PEC technology has demonstrated that it can completely degrade pollutants, without emitting CO₂ to the environment. For lab-scale demonstration, the instrumentation utilised for PEC is powered by grid electricity however it can be operated by renewable energy such as solar or wind.

This thesis had several aims to help evaluate if PEC could potentially replace the current secondary or tertiary water treatment process. These were:

- Design an effective heterostructure metal oxide photoanode
- Determine if PEC can completely remove a pharmaceutical compound from water without impacting on the environment.
- Verify if PEC can completely remove an anionic and cationic surfactant compound from water.
- Quantification of hydrogen gas production during PEC pollutant degradation processes.

7.1 Photoanode Development

Primarily, heterostructured WO₃/BiVO₄ photoanode was preferred for the PEC system in this thesis. The performance of the heterostructure WO₃/BiVO₄ photoanode was significantly higher than pristine WO₃ photoanode (2.75 mA/cm² compared to 0.8 mA/cm², respectively). This is due to the higher photon absorbance and the effective photogenerated charge carrier separation. The UV-Vis demonstrated that adding a layer of BiVO₄ to the WO₃ photoanode resulted in the wavelength absorption range increasing from 450 nm to 490 nm, thus higher photon absorption. This is due to BiVO₄ having a narrower bandgap, thus more photons are absorbed resulting in higher electron excitation. The heterojunction enables separation of the photogenerated charge carriers which as evidenced by the IMPS data which demonstrated that the electron transit time was much lower in WO₃/BiVO₄ photoanode compared to pristine WO₃ photoanode. This is due to the electrons not being captured into charge recombination reactions meaning they travel to the FTO substrate faster. Other techniques such as XRD and XPS confirmed that the method utilised for synthesising WO₃ and BiVO₄ produced monoclinic WO₃ and BiVO₄ crystalline structure. This was essential as it has been established that monoclinic WO₃ and BiVO₄ have the highest photocatalytic activity compared to other crystallinity forms.

The thickness effect of WO_3 and BiVO_4 in the $\text{WO}_3/\text{BiVO}_4$ heterostructured photoanode controlled the charge transfer and played a significant part in photocurrent generation. It was identified that 2 layers of WO_3 and 1 layer of BiVO_4 is the optimised thickness for achieving the best performance. Therefore, $2\text{WO}_3/1\text{BiVO}_4$ configuration was chosen as the benchmarking photoanode to test the pollutant degradation experiments. The operating parameters such as applied potential, light irradiation, electrolyte concentration and pollutant concentration also influenced the PEC performance. Based on the experimental conditions tested in Chapter 3, it was recognised the best operating parameters were utilising 1 M of sodium chloride (NaCl) with an applied potential of 1.2 V (vs Ag/AgCl) for $2\text{WO}_3/1\text{BiVO}_4$ photoanode.

7.2 Ibuprofen Degradation

The developed PEC system showed excellent ibuprofen degradation as it achieved an average degradation of 96.70%. This was achieved with $2\text{WO}_3/1\text{BiVO}_4$ photoanode (1 cm^2), Pt wire as the counter electrode, Ag/AgCl as the reference electrode, 1 M NaCl as the supporting electrolyte, an applied potential of 1.2 V (vs Ag/AgCl) with 1 Sun of solar light irradiation for 2 hours (after 30 minutes in the dark). It is often assumed that PEC will be environmentally friendly as it does not produce any solid waste or CO_2 and the energy for applied potential and light irradiation could be provided by renewable energy. However, it was found that ibuprofen degraded via PEC produced several by-products. One of the by-products was *4-isobutylacetophenone* and it is highly hazardous for aquatic life. This would indicate that *4-isobutylacetophenone* should be degraded before the treated solution is discharged into water. This is easily achievable by prolonging the PEC treatment duration to at least a few hours (typically 4 - 6 hrs) to degrade *4-Isobutylacetophenone* completely and then PEC can be adopted as a safe treatment route for wastewater treatment industries. Furthermore, after the PEC process the electrolyte pH is reduced from 6 to 2.75. However, this can be resolved simply with an additional post-treatment to help neutralise the pH level for safe discharge into water sources.

In literature, many reports assume that hydroxyl radicals ($\bullet\text{OH}$) are responsible for ibuprofen degradation. However, it was discovered that the $2\text{WO}_3/1\text{BiVO}_4$ photoanode could not produce sufficient $\bullet\text{OH}$ for quantification. This would imply that the ibuprofen degradation occurred mainly via h^+ on the photoanode surface and possibly active chlorine which was assumed to be produced and by the small amount of $\bullet\text{OH}$.

7.2.2 Future Work

- The LC-MS method was successful in identifying the m/z values of the by-products acknowledged in the LC-UV chromatogram. It enabled the optimisation of the fragmentation which breaks down these compounds into product ions and produces a peak with a corresponding m/z value which can be used to determine the chemical structure. However, the only fragmentation pattern that matched with literature was 4-isobutylacetophenone. The other by-products' fragmentation pattern did not match the by-products in the literature. Therefore, an LC-MS system with accurate mass function should be utilised to identify the other products.
- The 4-isobutylacetophenone is a potential toxic by-product identified after ibuprofen degradation. This by-product can be degraded in several ways (a) increasing the photoanode surface area to promote the number of active sites, thus resulting in higher pollutant degradation, (b) increase the light intensity or reaction duration period that would enhance the photocharge carrier, thus accelerating more reactive species generation, which is expected to degrade 4-Isobutylacetophenone completely.
- The quantification of free radical generation from $2\text{WO}_3/1\text{BiVO}_4$ photoanode was evaluated by only one technique. Therefore, it is suggested that other quantification experiments are required to quantify the very small amount of $\bullet\text{OH}$ which was implied by the generation of 4-isobutylacetophenone from ibuprofen degradation.
- It would be essential to look for an active chlorine quantification technique to ensure that active chlorine is being produced.

7.3 Surfactant Degradation

The PEC cell with $2\text{WO}_3/1\text{BiVO}_4$ photoanode (1 cm^2), Pt wire as the counter electrode, Ag/AgCl as the reference electrode, 1 M NaCl as the supporting electrolyte, completely removed ($50\text{ }\mu\text{g/mL}$) BAC-C12 (cationic surfactant) within 2 hours of simulated solar light irradiation under 1.2 V vs Ag/AgCl applied potential. However, when the concentration of BAC-C12 was higher ($100\text{ }\mu\text{g/mL}$) the degradation rate was significantly decreased to 52.91%. This is due to the increased competition for the active sites and reactive species. Therefore, the PEC system is successful in removing cationic surfactants at low concentration. In relation to S2NS ($50\text{ }\mu\text{g/mL}$) complete degradation was achieved after 1 hour of solar light irradiation

when utilising the same PEC system. This established that the PEC system achieved higher degradation rates for anionic surfactants than cationic surfactants. This was due to the positively charged photoanodes (results from h^+ enriched surface) attracting the negatively charged anionic surfactants more than the cationic surfactants. It was established that the species responsible for S2NS was most probably the positively charged holes. While for BAC-C12 it could be the active chlorine or hydroxyl radicals. Whilst active chlorine is very good for degrading pollutants it causes a reduction in pH due to the production of protons. Therefore, after treatment the pH of the solution decreased significant < 3 for each pollutant. This demonstrates that while PEC is very successful at completely removing a cationic and anionic surfactant, a post treatment time would be required to ensure that the pH can be neutralised preventing any harm to aquatic life when released.

7.3.2 Future Work

- The COVID lockdown and unexpected significant accidental fire at lab premises disrupted this research for almost seven months. This resulted in being unable to carry out different types of photoanode fabrication, wide material characterisation, gas quantification, and analytical work. The instrument unavailability and the crisis of supporting chemicals availability in the market (supply chain issue) affected the experimental work. For instance, degradation of S2NS, identified a few by-products formed during the PEC process. Unfortunately, there was insufficient time to identify these by-products due to the circumstances and issues mentioned above. Hence, future work should be focused on identifying these by-products. In relation to the degradation of BAC-C12 (50 $\mu\text{g/mL}$), no by-products were formed according to the LC-UV. However, ideally this could be further ensured with LC-MS to identify if any by-products are formed or not. It helps to confirm if the PEC process is environmentally friendly and eliminate any by-products that could be more harmful to aquatic life.
- COD is a parameter widely utilised in the water industry to quantify the organic compounds in the solution. The vials utilised for analysing the quality of electrolytes before and after the PEC process, were too low of a range to measure the COD as the surfactant treated solutions had a COD value of > 300 mg/L. Therefore, COD measurements should be repeated however utilising vials that allow the higher COD range to be quantified.

- Similar to ibuprofen degradation it would be essential to look at appropriate •OH and active chlorine quantification techniques to determine how the amount produced during surfactant degradation.

7.4 Hydrogen production

The PEC system with $2\text{WO}_3/1\text{BiVO}_4$ photoanode (1 cm^2), Pt wire as the counter electrode, Ag/AgCl as the reference electrode, 0.5 M NaCl as the supporting electrolyte, an applied potential of 1.2 V with a 1 Sun of solar light irradiation for 2 hours (after 30 minutes in the dark) produced $68.79\text{ }\mu\text{mol}/\text{cm}^2$ of hydrogen gas. Thus, demonstrating that this system was extremely successful in producing clean hydrogen gas, as compared to other studies which only achieved slightly higher hydrogen production with much higher photoanode surface areas.

The PEC system also demonstrated that it could produce high amounts of hydrogen gas whilst degrading pollutants. It was established that the degradation of ibuprofen did not affect the production of hydrogen. The Nafion membrane separating the two compartments was very effective in preventing the ibuprofen degradation from moving into the cathodic compartment while effectively transferring the hydrogen ions into the cathodic cell to react with the electrons. It was also established that increasing the concentration of NaCl increased hydrogen production by approximately $55.41\text{ }\mu\text{mol}$. It implies that increasing the supporting electrolyte could increase hydrogen production as it enhances ion transfer by reducing the resistance in the solution. It was assumed that pollutant degradation did not affect the hydrogen production, as ibuprofen degradation did not alter the amount of hydrogen gas produced. However, changing the pollutant type i.e to surfactants resulted in less hydrogen production compared to ibuprofen degradation. Therefore, the assumption was wrong, and the quantity of hydrogen gas generation did depend on the type of pollutant degradation reaction in the anodic compartment. However, of significance this thesis successfully demonstrated the feasibility of recovering hydrogen gas during PEC wastewater treatment.

7.4.2 Future Work

- It was recognised that pollutants act as electron sacrificial agents, which help to promote the charge separation at photoanode/electrolyte interfaces. However, the effect of surfactants concentration on hydrogen generation couldn't be investigated. Further studies on different surfactant concentrations will shed more light on the

interrelationship between photoanode catalytic activity and surfactant molecules degradation.

- It would also be recommended ~~to~~ that the hydrogen experiments be repeated utilising a two-electrode set up to identify the actual potential difference between the working and counter electrode in order to determine the ABPE. In addition, conducting it without an applied bias to determine the STH of the developed $2\text{WO}_3/\text{BiVO}_4$ photoanode.
- It is also important that for future hydrogen experiments it is necessary to control and monitor the temperature of the experiment to establish the hydrogen generation for that set temperature. It will also be recommended to do the hydrogen experiments at different temperatures to determine the best temperature for hydrogen production via PEC.

7.5 Bibliography

1. Organization, W.H. *Drinking-water*. 2019.
2. UK, W. *Vast Majority of Brits Have No Idea How Much Water They Use Each Day*. News 2020.

Appendix 1.1

Figure S1 shows the photography images of WO_3 paste synthesis at different stages (grinding, mixing, evaporation).

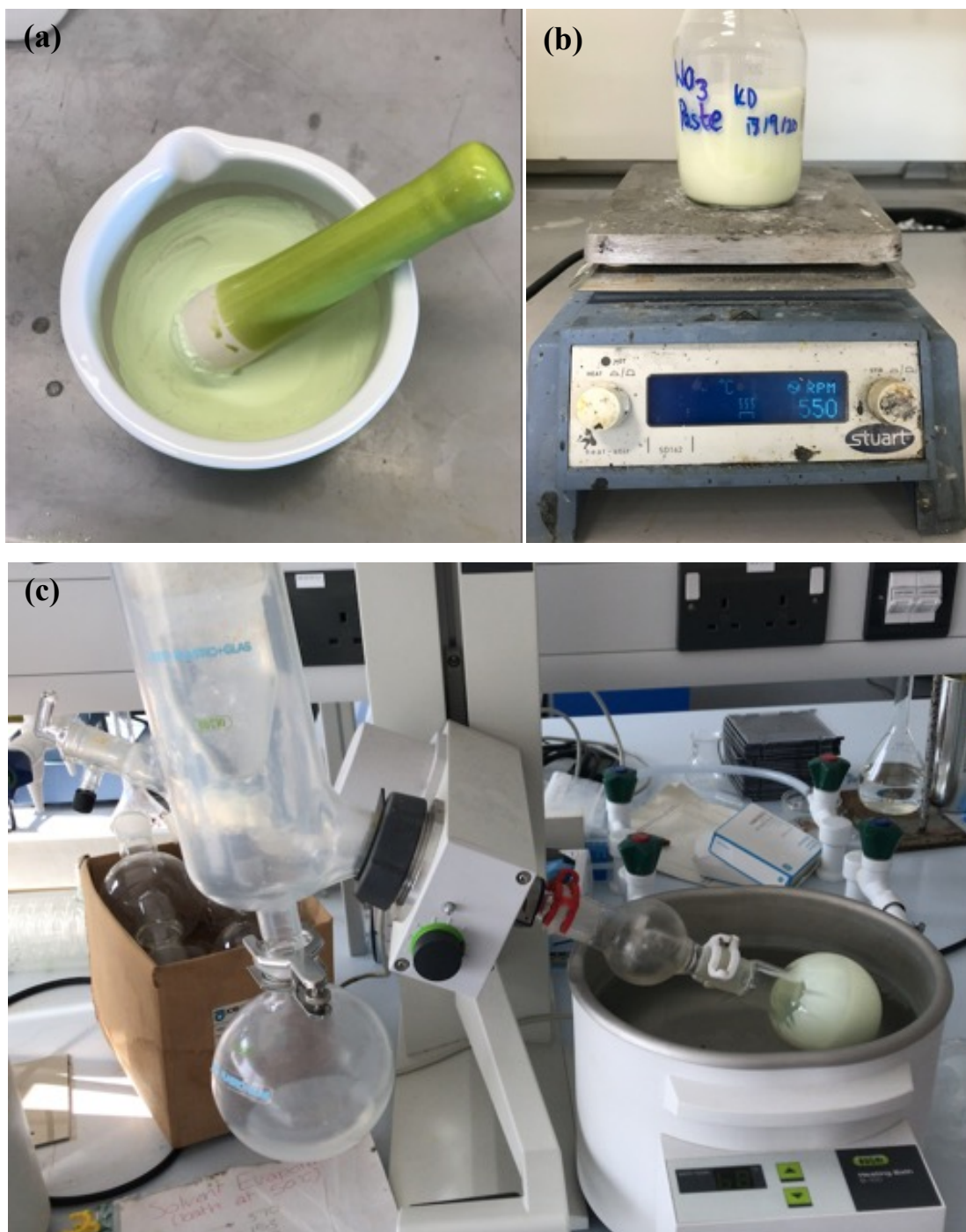


Figure S1 - Photography images of the WO_3 paste synthesis (a) pre-synthesised WO_3 powder grinding with mortar, (b) WO_3 paste mixing and (c) Vacuum evaporation of WO_3 paste.

Once the homogenous WO_3 paste was achieved, it spread as thin film on the conducting substrate by doctor blade technique. Finally, it was annealed at $450\text{ }^\circ\text{C}$ for 3 hours under an air atmosphere. Please refer Figure S2.

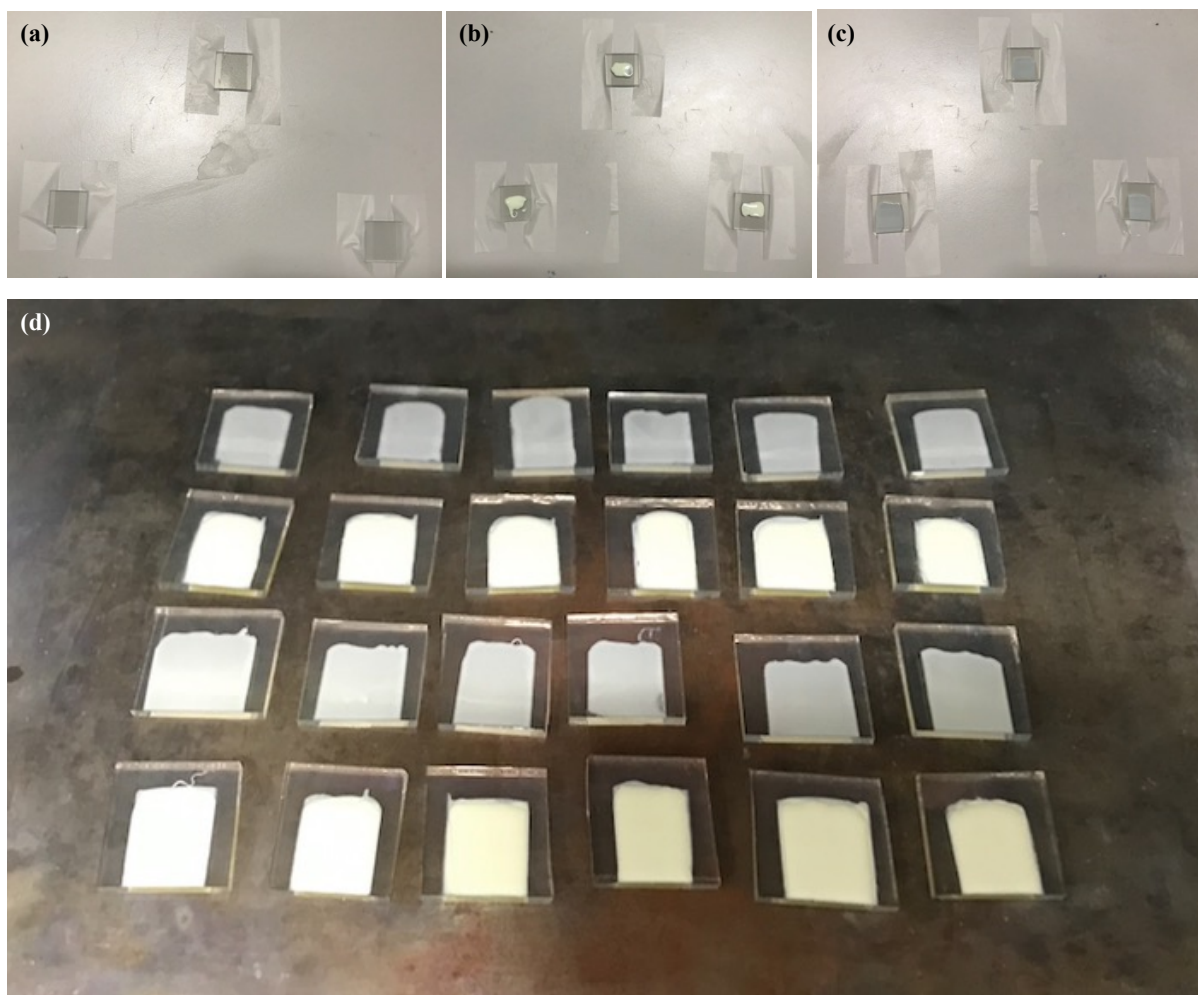


Figure S2 -The photography images of (a) scotch tape fixed on the edges of FTO conducting substrate, (b) WO_3 paste spread on the FTO, (c) doctor blade derived WO_3 coating and (d) WO_3 films annealed on the hot plate.

Figure S3 shows the photography images of the application of BiVO_4 on top of WO_3 by utilising a spin coater.

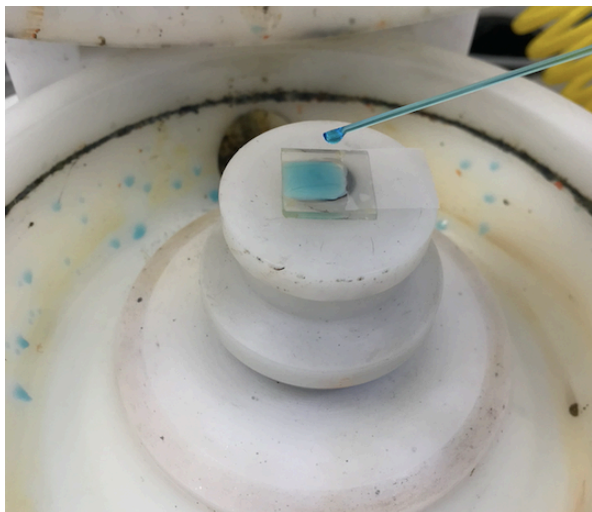


Figure S3 – A photography image showing the BiVO_4 application on top of WO_3 via spin coating.

Once the BiVO_4 was spin coated onto the WO_3 layer then it was annealed at $500\text{ }^\circ\text{C}$ for 1 hour under an air atmosphere.



Figure S4 - A photography image showing the BiVO_4 film being annealed via the hot plate.

Appendix 2.1

The chromatograms produced during the method development for the detection of the ibuprofen are displayed below.

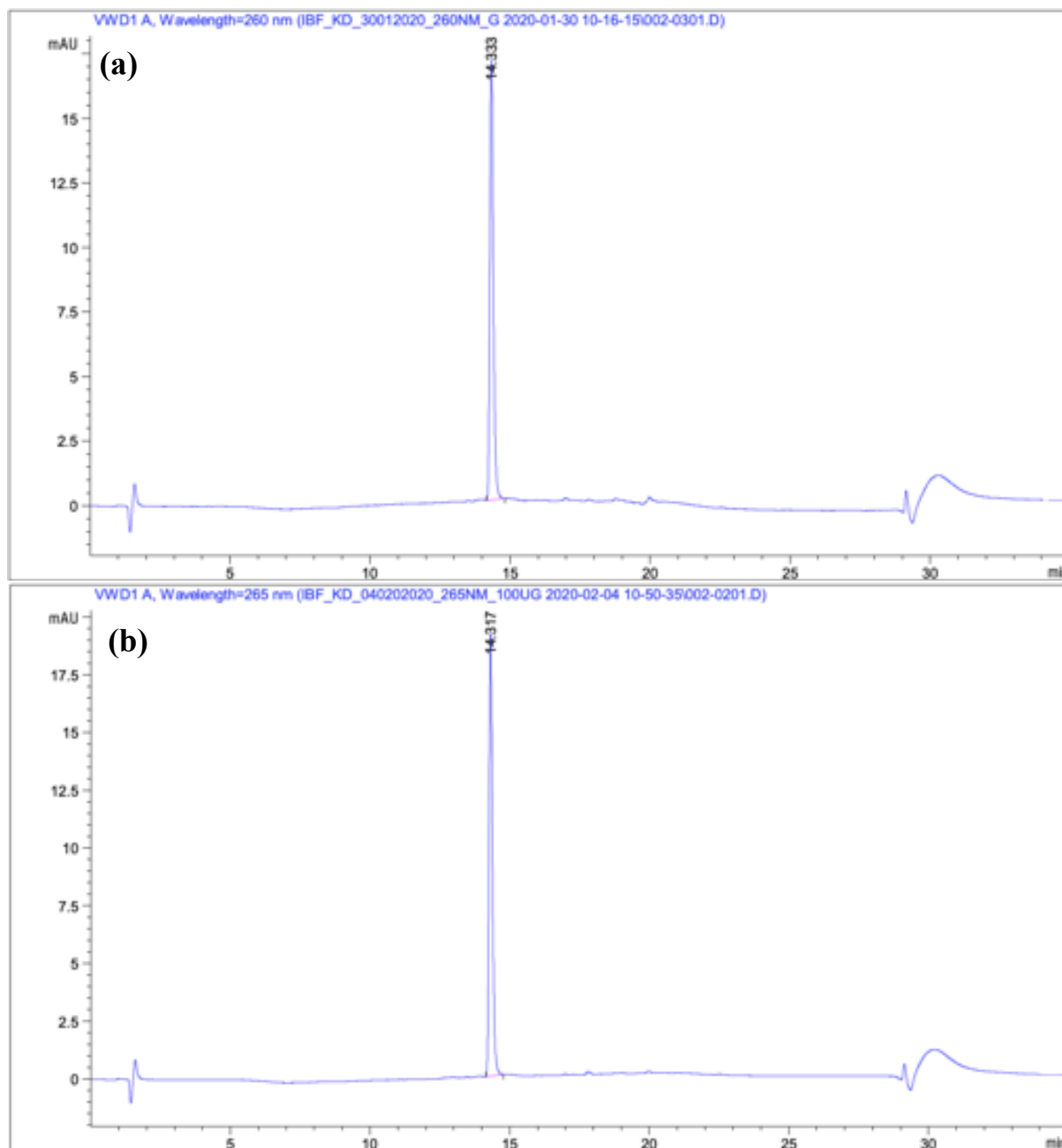


Figure S5 - The chromatogram produced for the ibuprofen standard using (a) 1st method and (b) 2nd method.

Appendix 2.2

The chromatograms produced for the blank samples after each set of the multiple injections of the same high concentration standard of ibuprofen are shown below. They demonstrate that there was no carry over of ibuprofen into the next injection.

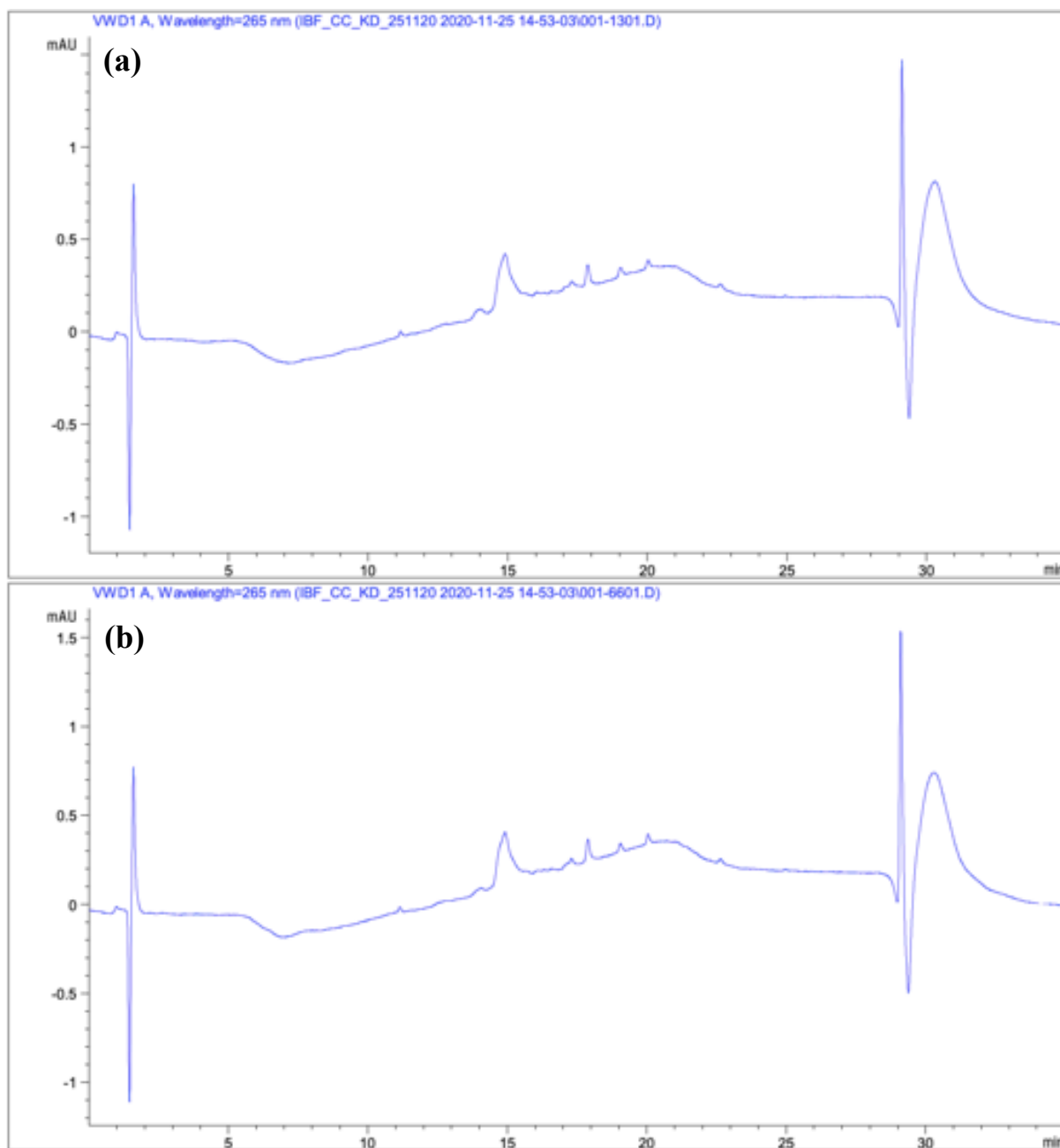


Figure S6 - The blank chromatogram after ibuprofen reproducibility test on (a) day 1 and (b) day 2.

Appendix 2.3

The tables below are displaying the peak areas obtained from the LC-UV analysis of the reproducibility standard for ibuprofen (200 ug/mL) for day 1 and 2. Included in the tables are the calculated mean peak areas, the standard deviation, and the CV%.

Table S1 - The calculated parameters from the LC-UV data obtained from the reproducibility test for ibuprofen for day 1.

Sample Name	Peak Area	Mean Peak Area	Standard Deviation Peak Area	CV%
Reprod 1 200ug	267.71414	268.516428	0.47312218	0.1761986
Reprod 2 200ug	268.15631			
Reprod 3 200ug	267.77435			
Reprod 4 200ug	268.68027			
Reprod 5 200ug	268.59882			
Reprod 6 200ug	268.68866			
Reprod 7 200ug	268.82819			
Reprod 8 200ug	269.11694			
Reprod 9 200ug	268.75394			
Reprod 10 200ug	268.85266			

Table S2 - The calculated parameters from the LC-UV data obtained from the reproducibility test for ibuprofen for day 2.

Sample Name	Peak Area	Mean Peak Area	Standard Deviation Peak Area	CV%
Reprod 11 200ug	269.08429	268.582005	2.39861447	0.89306596
Reprod 12 200ug	269.24536			
Reprod 13 200ug	269.39948			
Reprod 14 200ug	269.5954			
Reprod 15 200ug	262.68356			
Reprod 16 200ug	269.84879			
Reprod 17 200ug	269.67584			
Reprod 18 200ug	269.12332			

The coefficient of variation (CV %) was utilised to help calculate the spread of the variables.

While the F-test was utilised to determine the difference between the two sets of data.

Katherine Davies

Coefficient of Variation (%):

$$CV(\%) = \frac{0.47312218}{268.516428} \times 100 = 0.176\% \text{ (to 3 d.p)}$$

F-test:

$$F - test = \frac{2.39861447^2}{0.47312218^2} = 3.891 \text{ (to 3 d.p)}$$

Appendix 2.4

In continuation with injection repeatability tests, the retention time repeatability was assessed. The table S3 and S4 contained the retention time (RT) for the solvent front, the retention time of ibuprofen, adjusted RT, mean RT, mean adjusted RT, standard deviation RT, standard deviation adjusted RT, CV% RT and CV% adjusted RT.

Table S3 - A table displaying the results from the reproducibility test for ibuprofen for day 1.

Sample Name	Solvent Front RT	Sample RT	Adjusted RT	Mean RT	Mean Adjusted RT	Standard Deviation RT	Standard Deviation Adjusted RT	%CV RT	%CV Adjusted RT
Reprod 1 200ug	1.6	14.355	12.755	14.3607	12.7582	0.02420767	0.02440765	0.16856885	0.1913095
Reprod 2 200ug	1.612	14.367	12.755						
Reprod 3 200ug	1.608	14.37	12.762						
Reprod 4 200ug	1.613	14.362	12.749						
Reprod 5 200ug	1.604	14.37	12.766						
Reprod 6 200ug	1.595	14.368	12.773						
Reprod 7 200ug	1.598	14.375	12.777						
Reprod 8 200ug	1.596	14.376	12.78						
Reprod 9 200ug	1.6	14.37	12.77						
Reprod 10 200ug	1.599	14.294	12.695						

Table S 4 - A table displaying the results from the reproducibility test for ibuprofen for day 2.

Sample Name	Solvent Front RT	Sample RT	Adjusted RT	Mean RT	Mean Adjusted RT	Standard Deviation RT	Standard Deviation Adjusted RT	%CV RT	%CV Adjusted RT
Reprod_11_200ug	1.595	14.369	12.774						
Reprod_12_200ug	1.594	14.372	12.778						
Reprod_13_200ug	1.597	14.361	12.764						
Reprod_14_200ug	1.598	14.361	12.763						
Reprod_15_200ug	1.597	14.357	12.76						
Reprod_16_200ug	1.598	14.366	12.768						
Reprod_17_200ug	1.597	14.373	12.776						
Reprod_18_200ug	1.598	14.374	12.776	14.366625	12.769875	0.00639056	0.00697828	0.044482	0.05464644

Similarly to the assessment of injection repeatability then the CV% and F-test values were calculated.

Coefficient of Variation (%):

$$CV (\%) = \frac{0.02420767}{14.3607} \times 100 = 0.16856885$$

$$CV(\%) \text{ of adjusted } RT = \frac{0.02440765}{12.7582} \times 100 = 0.1913095$$

F-test:

$$F - \text{test value} = \frac{0.00639056^2}{0.02420767^2} = 0.06960292$$

$$F - \text{test value of adjusted } RT = \frac{0.00697828^2}{0.02440765^2} = 0.081741991$$

Appendix 2.5

The peak areas and retention times obtained for the calibration standards from the HPLC-UV are displayed below.

Table S 5 - A table displaying the peak areas and actual concentrations obtained for the calibration standards.

Standard Name	Theoretical Concentration (µg/mL)	RT	Peak Area	Actual Concentration (µg/mL)
CC_1_10ug	10	14.383	12.93861	10.94014395
CC_2_10ug	10	14.382	12.9715	10.96524461
CC_3_10ug	10	14.37	12.98393	10.97473081
CC_1_30ug	30	14.371	40.65097	32.08938264
CC_2_30ug	30	14.374	40.7473	32.1628988
CC_3_30ug	30	14.363	40.92071	32.29524009
CC_1_50ug	50	14.367	64.79462	50.51508932
CC_2_50ug	50	14.359	64.20158	50.06249905
CC_3_50ug	50	14.371	64.40314	50.21632357
CC_1_70ug	70	14.38	88.63298	68.70780786
CC_2_70ug	70	14.381	89.04926	69.02550022
CC_3_70ug	70	14.371	89.28939	69.20876021
CC_1_100ug	100	14.37	131.05826	101.0855041
CC_2_100ug	100	14.371	130.49724	100.6573505
CC_3_100ug	100	14.368	131.25491	101.2355814
CC_1_130ug	130	14.364	156.58589	120.5674226
CC_2_130ug	130	14.359	156.68605	120.6438617
CC_3_130ug	130	14.372	157.6382	121.3705139
CC_1_160ug	160	14.367	210.35226	161.6002972
CC_2_160ug	160	14.364	210.80669	161.9471045
CC_3_160ug	160	14.371	211.45508	162.4419362
CC_1_200ug	200	14.373	265.06848	203.3580687
CC_2_200ug	200	14.361	265.20624	203.463203
CC_3_200ug	200	14.364	266.51962	204.4655351

Using the calibration standards with the regression tool then the quality control (QC) standards' actual concentrations were calculated along with their accuracy and precision.

Table S 6 - A table displaying the data collected and calculated for the QC standards (including the accuracy and precision).

Standard Name	Theoretical Concentration (µg/mL)	RT (minutes)	Peak Area	Calculated Concentration (µg/mL)	Accuracy	Mean Concentration (µg/mL)	St Dev	%Accuracy	%Precision
QC Low 1	20	14.369	27.43311	22.0019099	10.0095495	21.9433839	0.99493697	9.71691965	4.53410912
QC Low 2	20	14.371	29.32953	23.44920054	17.2460027				
QC Low 3	20	14.375	26.46588	21.26374909	6.31874545				
QC Low 4	20	14.374	27.62367	22.14733956	10.7366978				
QC Low 5	20	14.37	25.92992	20.85472056	4.27360279				
QC Mid 1	80	14.372	105.11835	81.28894584	1.61118231	81.10952	0.47923548	1.38690003	0.59084986
QC Mid 2	80	14.381	104.68623	80.95916487	1.19895609				
QC Mid 3	80	14.345	103.87717	80.34171464	0.4271433				
QC Mid 4	80	14.375	105.33163	81.45171472	1.8146434				
QC Mid 5	80	14.375	105.40284	81.50606005	1.88257506				
QC High 1	180	14.374	238.15131	182.8156951	1.56427505	183.860859	1.18546241	2.14492183	0.64476062
QC High 2	180	14.375	240.67422	184.741104	2.63394668				
QC High 3	180	14.377	238.05292	182.7406068	1.52255933				
QC High 4	180	14.364	239.16428	183.5887633	1.99375738				
QC High 5	180	14.366	241.56134	185.4181273	3.01007072				

Appendix 2.6

To assess the best filter for filtering the ibuprofen samples then it is necessary to calculate the difference between the concentration of the non-filtered standard and the filtered standard of each type of filter. To do this the table below was utilised which displayed the peak area and the real ibuprofen concentration for each non-filtered and filtered samples.

Table S 7 - The peak areas obtained from the LC-UV analysis and the calculated concentrations of the samples.

Sample Name	Peak Area	Calculated Concentration (µg/mL)
CC 1 10ug 0.5NaCl	13.18066	11.03779478
CC 1 30ug 0.5NaCl	38.62626	28.29094812
CC 1 50ug 0.5NaCl	67.32655	47.75091386
CC 1 70ug 0.5NaCl	95.85243	67.09262252
CC 1 100ug 0.5NaCl	139.83345	96.91354568
IBF 10ug PVDF	12.70589	10.71588138
IBF 30ug PVDF	39.2567	28.71841212
IBF 50ug PVDF	65.14901	46.27445304
IBF 70ug PVDF	95.21174	66.6582086
IBF 100ug PVDF	135.46565	93.95199935
IBF 10ug Hydrophilic PTFE	12.01404	10.24677889
IBF 30ug Hydrophilic PTFE	35.89063	26.43607954
IBF 50ug Hydrophilic PTFE	62.42825	44.42966693
IBF 70ug Hydrophilic PTFE	89.95284	63.09246018
IBF 100ug Hydrophilic PTFE	133.11107	92.3554982
CC 1 10ug RC	12.89781	9.3888414
CC 1 30ug RC	48.103	33.43995643
CC 1 50ug RC	74.9318	51.76857659
CC 1 70ug RC	104.90856	72.24778727
CC 1 100ug RC	149.00359	102.3721706
CC 1 10ug Hydrophobic PTFE	14.52186	10.49834296
CC 1 30ug Hydrophobic PTFE	45.03838	31.34630126
CC 1 50ug Hydrophobic PTFE	76.33397	52.72649649
CC 1 70ug Hydrophobic PTFE	107.52239	74.03347643
CC 1 100ug Hydrophobic PTFE	146.44902	100.6269661

To assess the loss of ibuprofen caused by the filter then it was necessary to obtain the peak areas for the non-filtered and filtered standards and calculate the ibuprofen concentrations in these standards. Once this was calculated then the percentage yield and loss % for the filters were calculated and displayed in the tables below.

Table S 8 - Table displaying the peak area and calculated concentrations obtained for the non-filtered and filtered ibuprofen standards.

Sample Name	Peak Area	Calculated Concentration (µg/mL)
0.5M NaCl Non Filtered IBF 1	145.60211	107.5480447
0.5M NaCl Non Filtered IBF 2	145.14532	107.2130777
0.5M NaCl Non Filtered IBF 3	145.17413	107.2342042
0.5M NaCl Filtered IBF 1	140.00871	103.4463687
0.5M NaCl Filtered IBF 2	139.69817	103.2186478
0.5M NaCl Filtered IBF 3	140.54034	103.8362164
1M NaCl Non Filtered IBF 1	142.65088	105.3838889
1M NaCl Non Filtered IBF 2	143.02007	105.6546183
1M NaCl Non Filtered IBF 3	142.50787	105.2790187
1M NaCl Filtered IBF 1	135.55165	100.1779782
1M NaCl Filtered IBF 2	135.20471	99.92356485
1M NaCl Filtered IBF 3	134.81253	99.63597676

$$\text{Recovery (\%)} = \frac{103.4463687}{107.5480447} \times 100 = 96.18619199$$

Table S 9 - A table displaying the calculated percentage yields and loss (%).

Sample Name	Recovery (%)	Average Recovery (%)
0.5M NaCl IBF 1	96.18619199	96.4305818
0.5M NaCl IBF 2	96.27430723	
0.5M NaCl IBF 3	96.83124631	
1M NaCl IBF 1	95.06005068	94.7585467
1M NaCl IBF 2	94.57567165	
1M NaCl IBF 3	94.63991777	

Appendix 2.7

The chromatograms below were utilised to help determine the degradation % of ibuprofen during the PEC process in the dark and light. They showed that during the dark conditions the ibuprofen degradation did not produce any by-products which would suggest that the ibuprofen is not being degraded by are being absorbed onto the photoanode surface.

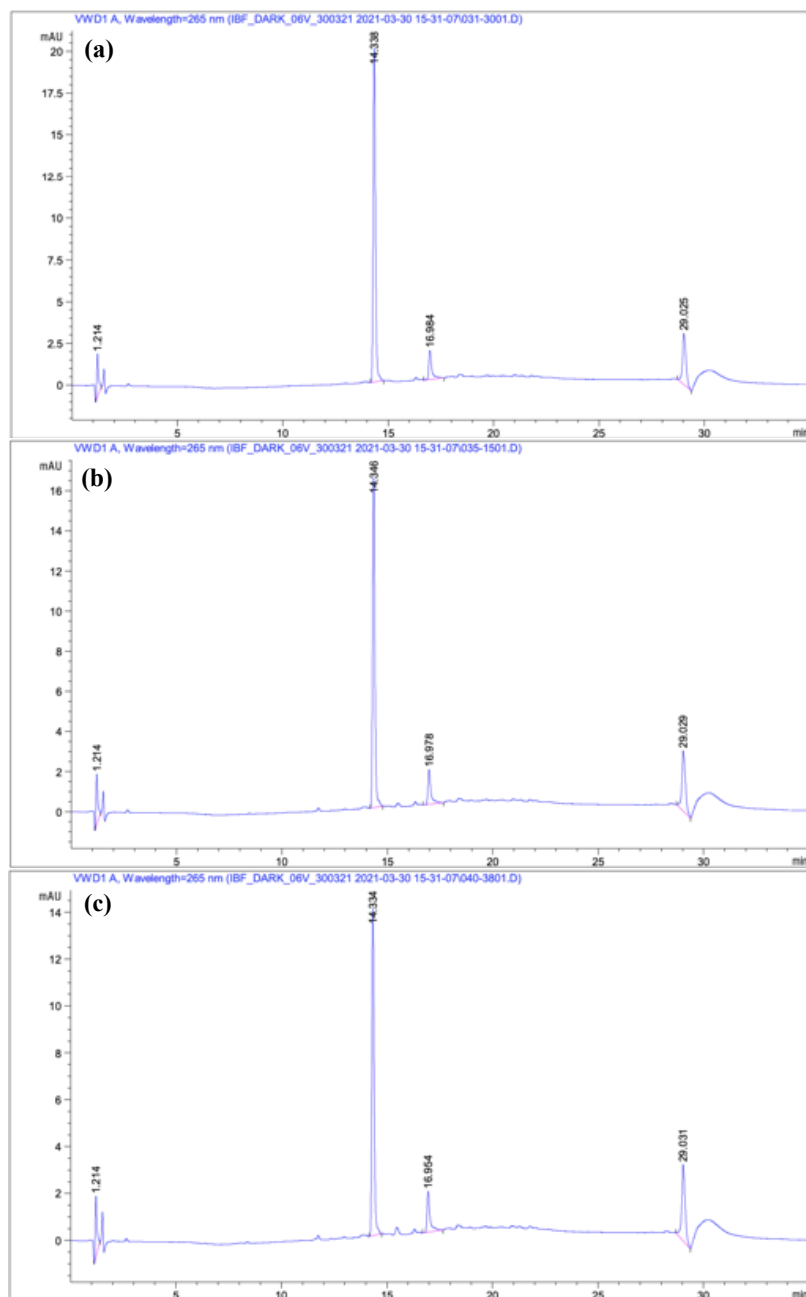


Figure S7 - Chromatogram obtained the dark ibuprofen degradation experiment at (a) 0 minutes, (b) 30 minutes, and (c) at 120 minutes.

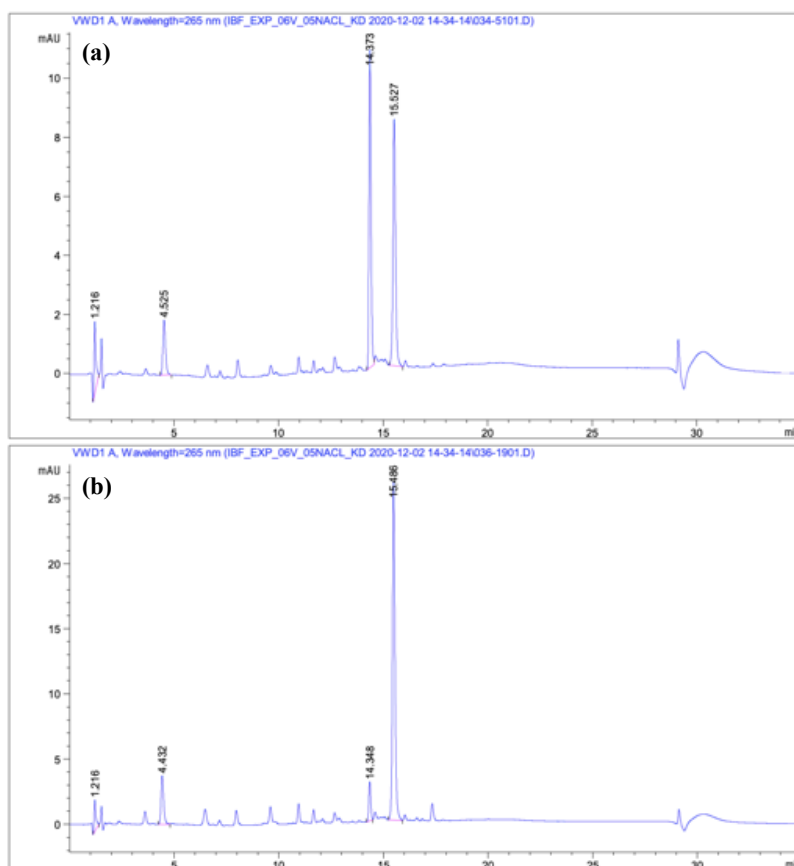


Figure S8 - Chromatogram obtained from the ibuprofen degradation under light irradiation (a) at 30 minutes and (b) at 120 minutes.

Appendix 2.8

The data obtained from the LC-UV for all the samples collected from the ibuprofen degradation experiments were converted to concentrations. Once these concentrations were calculated then the C_c/C_i value (current concentration divided by initial concentration) and ibuprofen degradation percentages were calculated. Using the Grubb's test then any outliers could be determined and eliminated from the average ibuprofen degradation values.

Table S10 - A table displaying the degradation (%) calculated for the degradation of ibuprofen when utilising 1 M NaCl.

Time (minutes)	Calculated Concentrations			Degradation (%)					
	Run 1	Run 2	Run 3	Run 1	Run 2	Run 3	Average	St Dev	Error
0	49.48845939	96.16832177	91.9573027	1	1	1	0	0	0
10	63.83623158	88.60198746	84.0469722	1.28992158	0.92132197	0.91397822	8.23499041	0.51928111	0.3671872
20	64.90534197	86.6222737	80.1270961	1.3115248	0.90073604	0.87135109	11.3956432	2.07782988	1.4692476
30	71.18826264	83.25397617	77.8868278	1.43848209	0.86571102	0.84698904	14.3649968	1.32384391	0.93609901
40	75.99357551	80.751633	74.7659153	1.53558176	0.83969057	0.81305033	17.3629549	1.88374947	1.33201203
50	77.34250913	79.09675905	73.2618564	1.5628393	0.82248247	0.79669427	19.0411628	1.82350111	1.28941
60	75.29437498	78.36268671	71.6143542	1.5214532	0.81484927	0.77877833	20.3186203	2.55060087	1.80354717
90	73.4287999	73.81867851	67.804804	1.48375603	0.7675987	0.73735094	24.7525179	2.13883912	1.51238764
120	69.94072994	70.95359633	64.5896995	1.41327353	0.73780633	0.70238793	27.9902871	2.50445895	1.77091991

Table S11 - A table displaying the Grubb's Test values calculated utilising in Table S10.

Time (minutes)	Grubb's Test		
	Run 1	Run 2	Run 3
0	0	0	0
10	-1.1545321	0.56018457	0.5943475
20	-1.1526407	0.51661686	0.63602387
30	-1.1542529	0.54928497	0.60496795
40	-1.15409	0.54453154	0.6095585
50	-1.1541933	0.54746056	0.60673278
60	-1.1536291	0.53374573	0.61988338
90	-1.1539604	0.54118204	0.61277839
120	-1.1535717	0.53257885	0.62099284

Table S12 - A table displaying the degradation (%) calculated for the degradation of ibuprofen when utilising 0.6V applied potential.

Time (minutes)	Calculated Concentrations			Degradation (%)					
	Run 1	Run 2	Run 3	Run 1	Run 2	Run 3	Average	St Dev	Error
0	98.0959548	97.7898256	92.676905	0	0	0	0	0	0
30	86.7464982	85.3959328	80.1705048	11.5697499	12.6740106	13.4946244	12.5794616	0.96591412	0.55767078
60	77.0711457	73.8352938	61.3137624	21.4329013	24.4959347	33.841379	26.5900716	6.46387169	3.73191806
90	67.8952562	64.284361	48.3125953	30.786895	34.2627307	47.8698655	37.6398304	9.02832053	5.21250329
120	60.3162845	49.6214811	33.3313299	38.5129747	49.2570103	64.0349126	50.6016325	12.8139898	7.39816047
150	53.348605	41.1057662	26.6270487	45.6158971	57.9651912	71.2689491	58.2833458	12.829485	7.40710664

Table S13 - A table displaying the Grubb's Test values calculated utilising the data in Table S12.

Time (minutes)	Grubb's Test		
	Run 1	Run 2	Run 3
0	0	0	0
30	-0.721954	-0.4703126	-0.2833093
60	-0.752842	-0.5908703	-0.0966878
90	-0.9915822	-0.6780724	0.54924979
120	-1.2244763	-0.4026579	0.72771365
150	-1.1848878	-0.3895704	0.4672163

Table S14 - A table displaying the degradation (%) calculated for the degradation of ibuprofen when utilising 0.9V applied potential.

Time (minutes)	Calculated Concentrations			Degradation (%)					
	Run 1	Run 2	Run 3	Run 1	Run 2	Run 3	Average	St Dev	Error
0	100.351189	83.5854532	91.9433503	0	0	0	0	0	0
30	84.0252682	79.9576138	72.886806	16.2687865	4.34027608	20.7263975	13.7784867	8.47215667	4.89140193
60	61.1965084	54.7208944	62.0667551	39.0176548	34.5329931	32.4945687	35.3484055	3.33711493	1.9266842
90	46.5276947	41.7256982	53.3375562	53.6351335	50.0801915	41.9886745	48.5679998	5.96867189	3.44601432
120	38.2488098	26.5621933	43.5118969	61.8850456	68.2215119	52.6753194	60.9272923	7.81722418	4.51327648
150	31.1173504	19.0137206	36.1860514	68.9915478	77.2523569	60.6431011	68.9623353	8.30466641	4.79470139

Table S15 - A table displaying the Grubb's Test values calculated utilising the data in Table S14.

Time (minutes)	Grubb's Test		
	Run 1	Run 2	Run 3
0	0	0	0
30	-0.3103394	-1.0117392	-0.0482306
60	-0.1730846	-0.5558913	-0.7298894
90	1.06087396	0.33213121	-1.3265834
120	0.17803672	1.16920469	-1.2625747
150	0.17600481	1.31996608	-0.9800925

Table S16 - A table displaying the degradation (%) calculated for the degradation of ibuprofen when utilising 1.2V applied potential.

Time (minutes)	Calculated Concentrations				Degradation (%)						
	Run 1	Run 2	Run 3	Run 4	Run 1	Run 2	Run 3	Run 4	Average	St Dev	Error
0	98.2049389	102.800632	94.998327	91.3190169	0	0	0	0	0	0	0
30	83.6705456	82.1435584	76.890654	75.5358442	14.8000635	20.0943057	19.0610441	17.2835553	17.8097421	2.318047	1.1590235
60	51.4199798	60.1563799	61.3801431	64.1924636	47.6401285	41.4824803	35.3881853	29.7052621	38.554014	7.73425872	3.86712936
90	29.161067	39.2456129	48.0463784	53.0959924	70.3059059	61.8235683	49.4239742	41.8565878	55.8525091	12.6723597	6.33617985
120	15.5352992	25.5327755	34.9414455	37.0420473	84.1807353	75.1628224	63.2188834	59.4366556	70.4997742	11.3183727	5.65918633
150	0	17.7985121	22.6130385	29.1800921	100	82.6863787	76.1963824	68.0459853	81.7321866	13.5717933	6.78589667

Table S17 - A table displaying the Grubb's Test values calculated utilising the data in Table S16.

Time (minutes)	Grubb's Test			
	Run 1	Run 2	Run 3	Run 4
0	0	0	0	0
30	-1.2983683	0.98555532	0.53980871	-0.2269958
60	1.17478802	0.37863567	-0.4093254	-1.1440983
90	1.14054503	0.47118764	-0.5072879	-1.1044448
120	1.20873924	0.41198928	-0.6432807	-0.9774478
150	1.34601323	0.070307	-0.4078904	-1.0084298

Table S18 - A table displaying the degradation (%) calculated for the degradation of ibuprofen when utilising 1.5V applied potential.

Time (minutes)	Calculated Concentrations			Degradation (%)					
	Run 1	Run 2	Run 3	Run 1	Run 2	Run 3	Average	St Dev	Error
0	95.7878423	95.0298865	93.6203218	0	0	0	0	0	0
30	79.8443599	79.248068	75.1336297	16.6445783	16.607216	19.7464522	17.6660821	1.80175013	1.04024092
60	62.0169075	59.8812142	63.4273896	35.2559719	36.9869665	32.2504042	34.8311142	2.39669223	1.3837309
90	47.5357657	34.4853684	50.1318056	50.3739049	63.7110285	46.4520046	53.5123127	9.04741288	5.22352626
120	35.2285996	16.9209324	37.4102059	63.2222641	82.1940939	60.040507	68.4856217	11.9780028	6.91550317
150	26.6785628	0	28.2809256	72.1482787	100	69.7918944	80.6467244	16.8017884	9.70051707

Table S19 - A table displaying the Grubb's Test values calculated utilising the data in Table S18.

Time (minutes)	Grubb's Test		
	Run 1	Run 2	Run 3
0	0	0	0
30	-0.5669509	-0.5876876	1.15463847
60	0.17726836	0.89951153	-1.0767799
90	-0.3468846	1.12725218	-0.7803676
120	-0.4394186	1.14447061	-0.705052
150	-0.505806	1.15185807	-0.6460521

Table S20 - A table displaying the degradation (%) calculated for the degradation of ibuprofen when utilising 1 M NaCl supporting electrolyte.

Time (minutes)	Calculated Concentrations			Degradation (%)					
	Run 1	Run 2	Run 3	Run 1	Run 2	Run 3	Average	St Dev	Error
0	92.7813459	92.7941387	91.9326078	0	0	0	0	0	0
30	74.5133085	73.5375817	75.6418694	19.6893429	20.7519109	17.7203049	19.3871863	1.53822387	0.88809397
60	55.0673173	55.1171898	53.1195796	40.6482879	40.6027249	42.2190006	41.1566711	0.9202863	0.53132754
90	31.3223356	31.9748668	27.5130532	66.2406971	65.5421481	70.0725848	67.2851433	2.43913204	1.40823354
120	18.444297	18.3173282	13.2224955	80.1206839	80.260253	85.6171865	81.9993745	3.13389418	1.80935465
150	9.19893258	0	0	90.0853642	100	100	96.6951214	5.72421767	3.30487861

Table S21 - A table displaying the Grubb's Test values calculated utilising the data in Table S20.

Time (minutes)	Grubb's Test		
	Run 1	Run 2	Run 3
0	0	0	0
30	0.19643218	0.88720808	-1.0836403
60	-0.5524186	-0.6019281	1.15434668
90	-0.4282041	-0.7145965	1.14280056
120	-0.5994748	-0.5549394	1.15441422
150	-1.1547005	0.57735027	0.57735027

Appendix 2.9

During the hydroxyl radical quantification, it was assumed that no umbelliferone was present as the PL spectrum below demonstrates the curve expected when umbelliferone is present in the solution. This was very different from the PL spectra obtained during the hydroxyl radical quantification experiment (Figure 4.15).

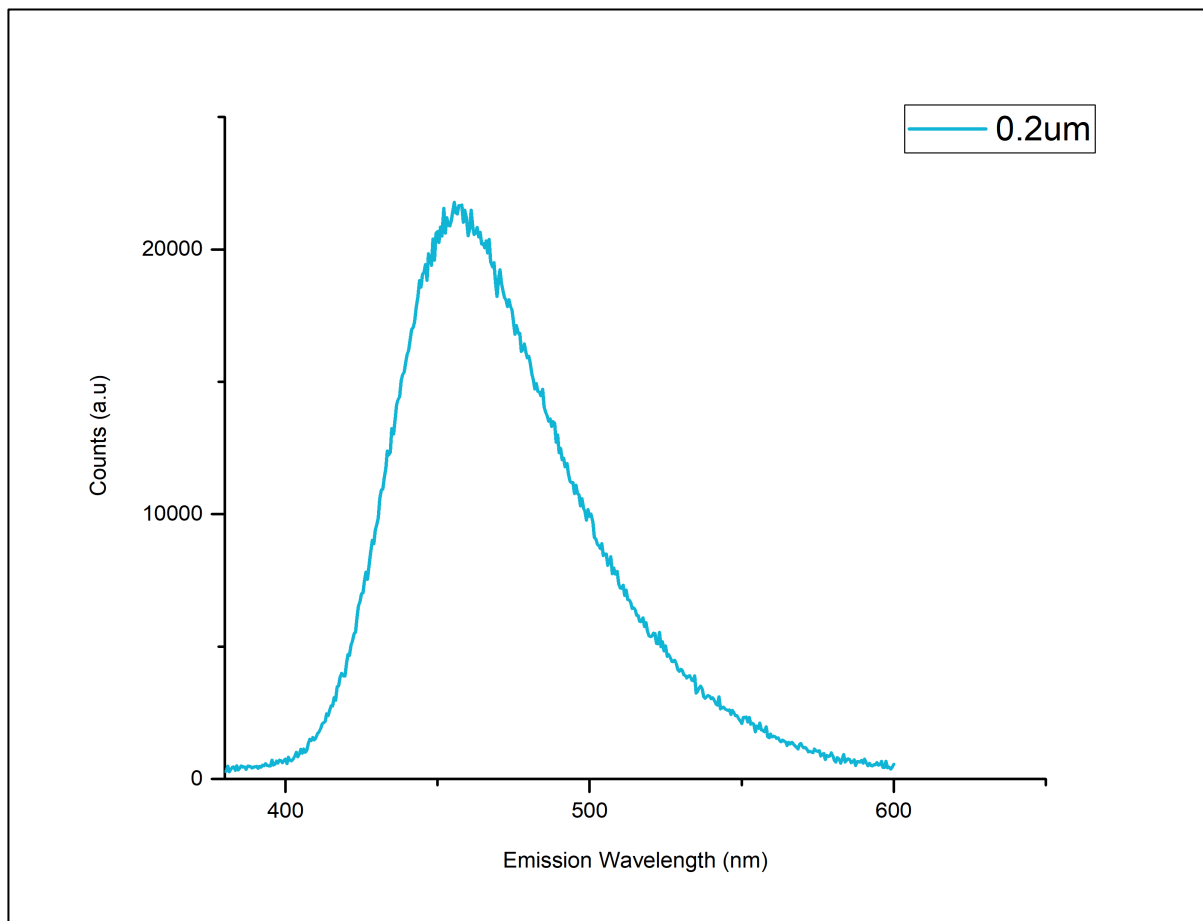


Figure S9 - The PL spectrum for a umbelliferone standard with a concentration of 0.2 μ M.

For the quantification of H₂O₂ then quantifix stripes were utilised and can be seen in the image below of how it works.



Figure S10 - Photograph of Quantifix stripes, the stripes after immersed in the electrolyte referred with colour code which infers the range of hydrogen peroxide quantity in mg/L.

While the table below displays all the H₂O₂ values obtained during the BAC-C12 and S2NS degradation experiments.

Table S22 - A table displays all the amounts of H₂O₂ produced during the degradation of ibuprofen.

Time	H ₂ O ₂ produced during ibuprofen Degradation (mg/L)			
	Run 1	Run 2	Run 3	Average
0	0	0	0	0
30	0	0	0	0
60	3	1	1	1.67
90	3	1	1	1.67
120	3	1	3	2.33
150	3	1	3	2.33

The table below shows all the pH values obtained for the ibuprofen solutions before and after treatment.

Table S 23 - A table displaying all the amount of H₂O₂ produced during the degradation of ibuprofen.

Time	pH during ibuprofen Degradation (mg/L)			
	Run 1	Run 2	Run 3	Average
Before	4.05	4.05	4.06	4.05
After	2.61	2.62	2.71	2.65

Appendix 2.10

The figures below are spectra taken from the LC-MS work conducted for the identification of the ibuprofen degradation by-products.

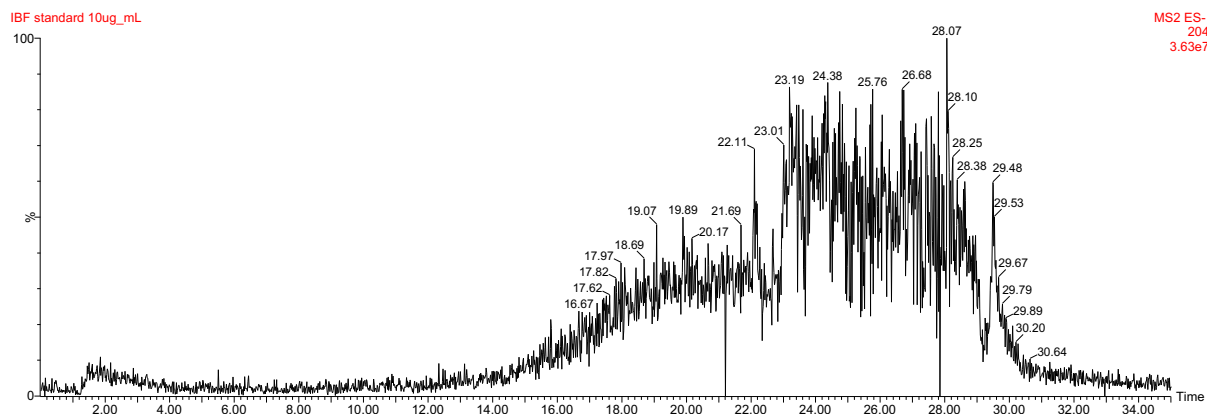


Figure S11 - Full mass scan of an ibuprofen standard utilising the electrospray in negative mode.

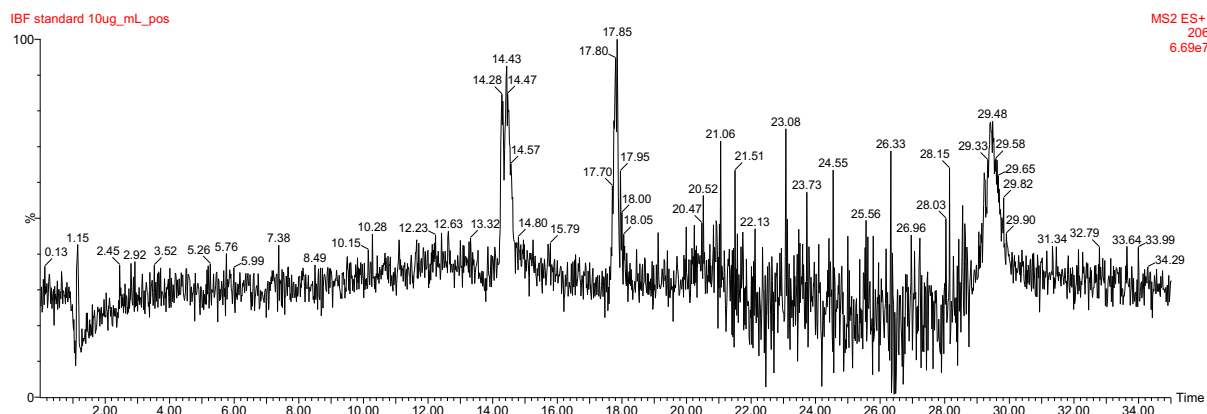


Figure S12 - Full mass scan of an ibuprofen standard utilising the electrospray in positive mode.

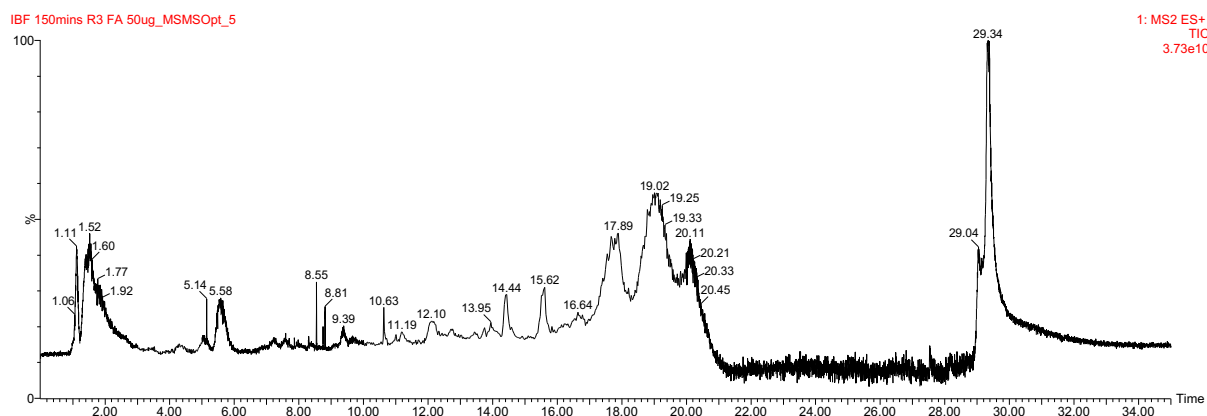


Figure S13 - Full mass scan of the sample taken at the end of the ibuprofen degradation experiments using the optimised LC-MS method.

Appendix 2.11

The figures below are the spectra obtained during the fragmentation step of the LC-MS analysis of the samples collected at the end of the ibuprofen degradation experiments.

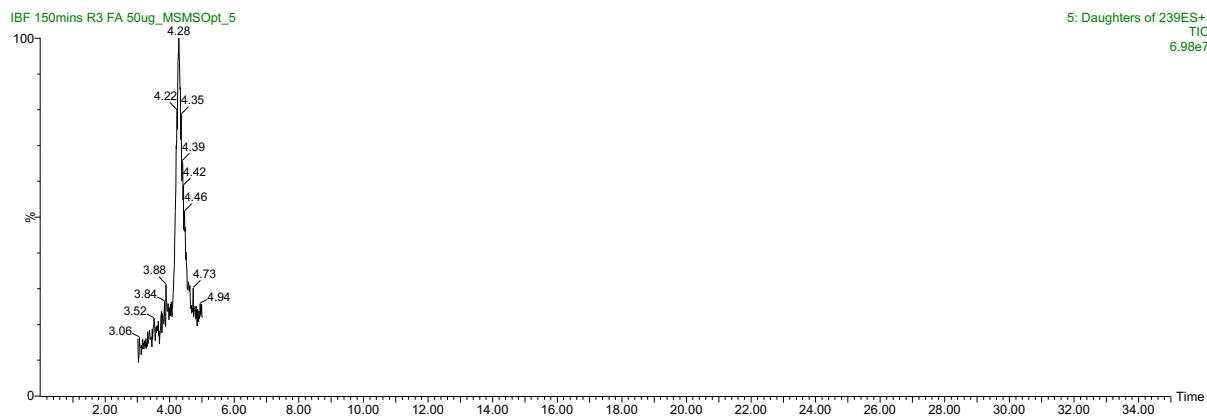


Figure S14 - The product scan of compound 239 in the sample.

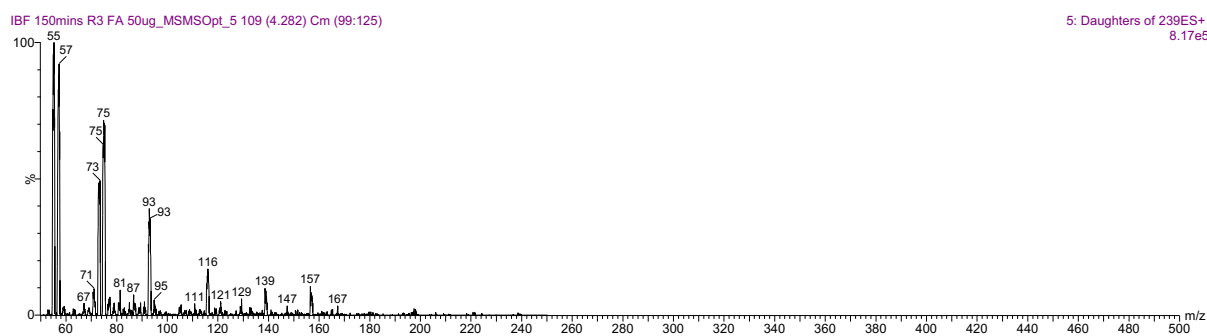


Figure S15 - The product ions obtained from the fragmentation of compound 239.

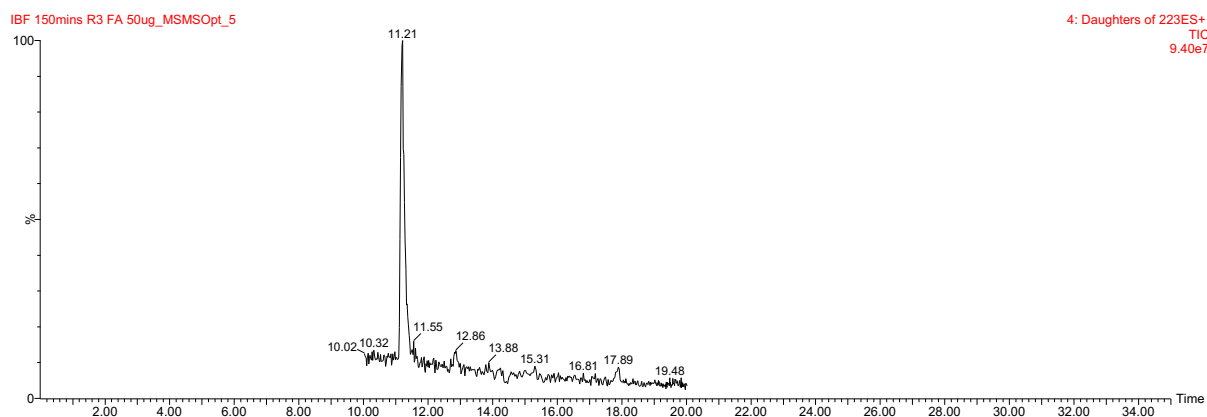


Figure S16 - The product scan of compound 223 in the sample.

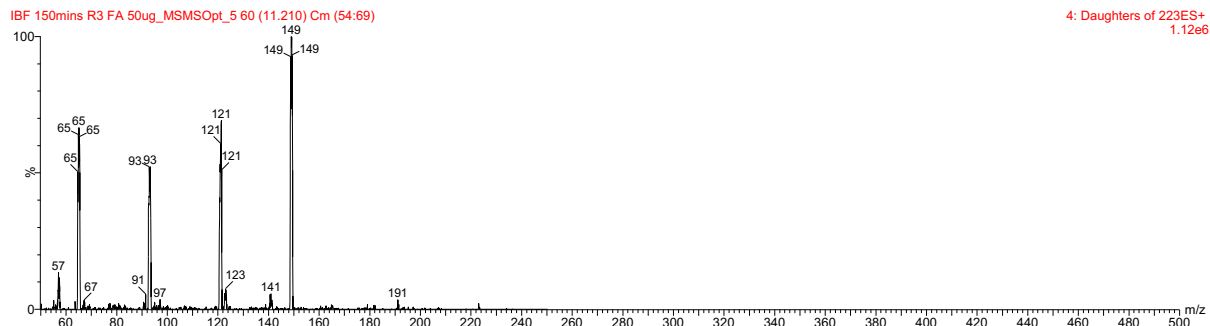


Figure S17 - The product ions obtained from the fragmentation of compound 223.



Figure S18 - The product scan of compound 221 in the sample.

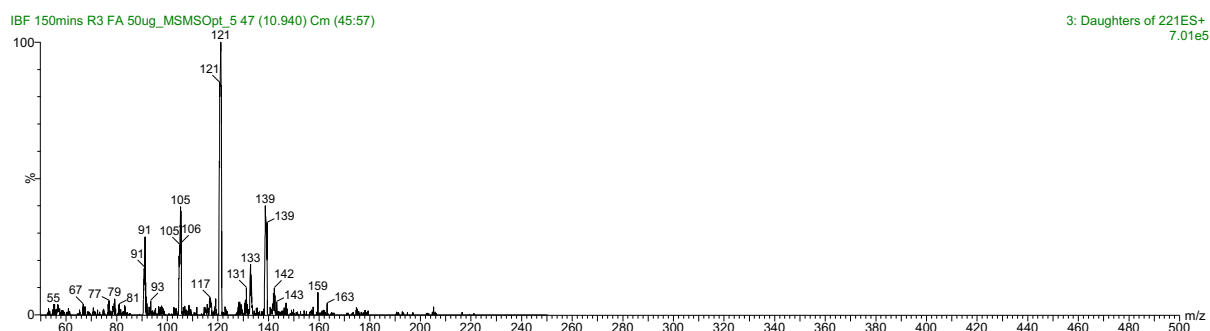


Figure S19 - The product ions obtained from the fragmentation of compound 221.

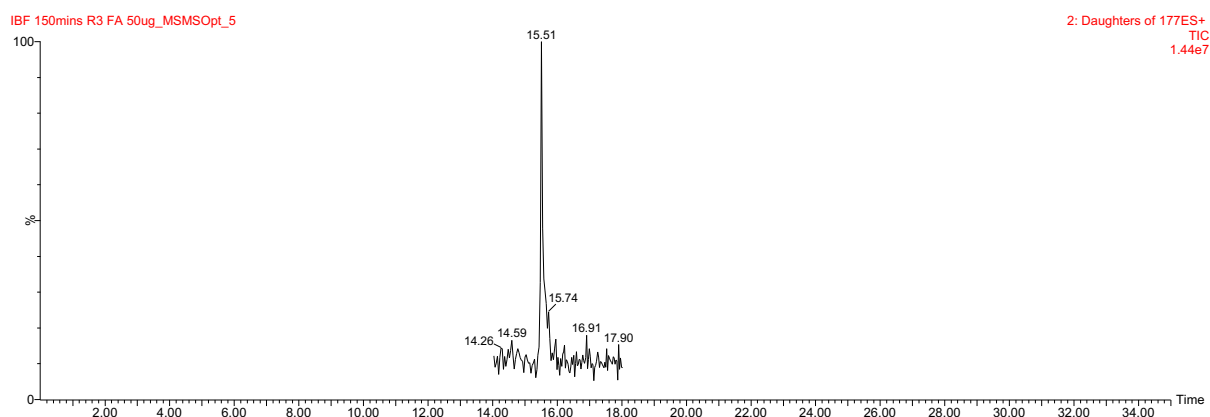


Figure S20 - The product scan of compound 177 in the sample.

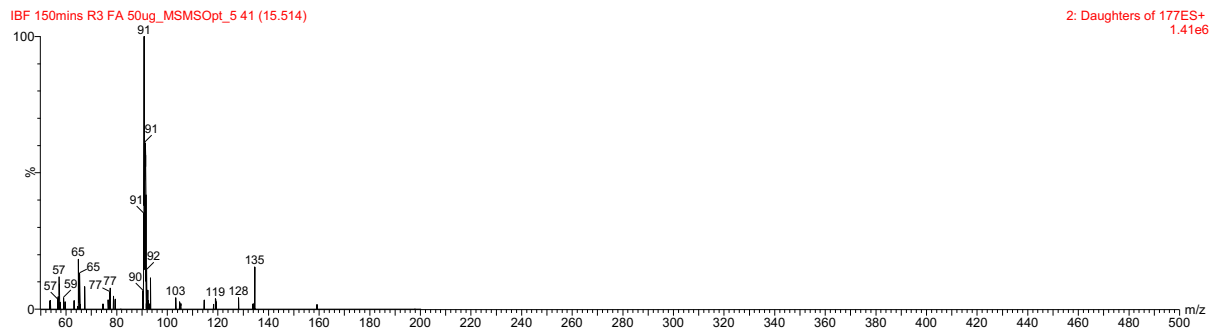


Figure S21 - The product ions obtained from the fragmentation of compound 177.

Appendix 3.1

The chromatograms below were obtained for the blank standards analysed by the LC-UV after the multiple injections of the high concentration standard of BAC-C12 and S2NS.

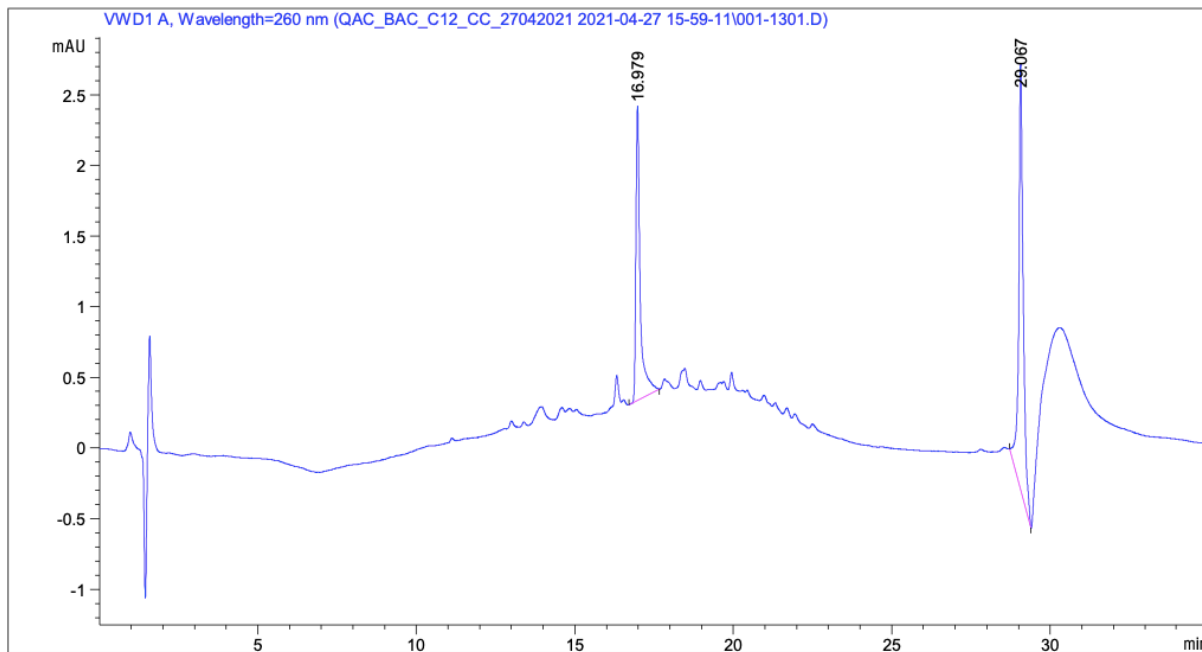


Figure S22 - The chromatogram of the blank sample after the reproducibility tests of BAC-C12 of day 1.

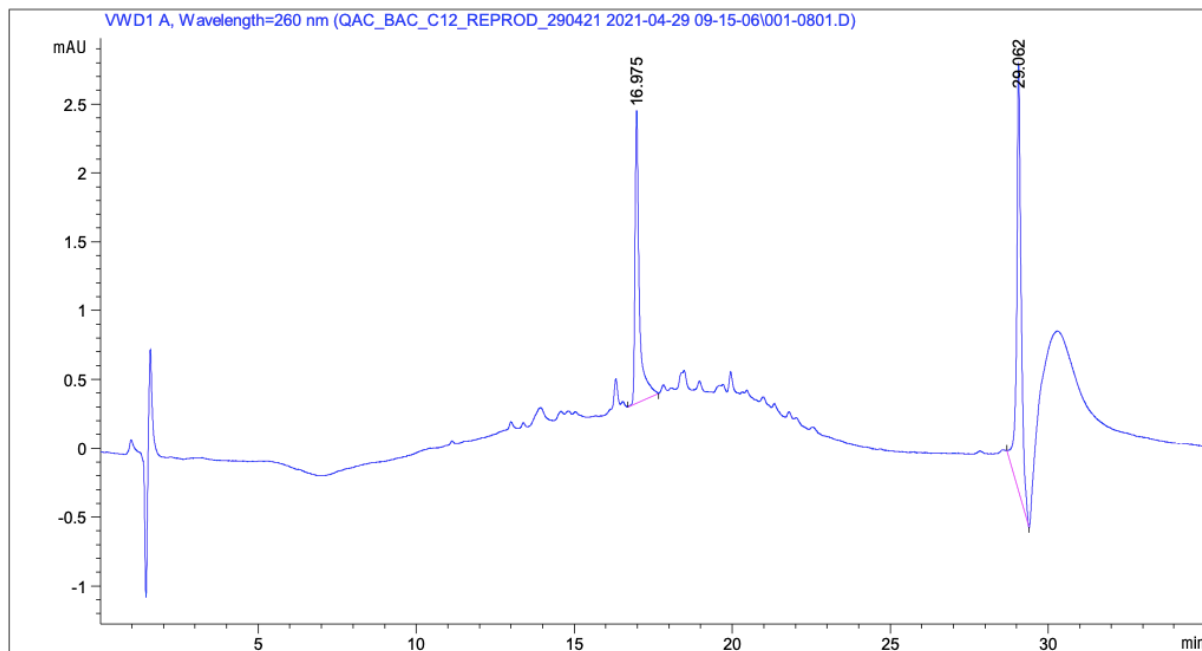


Figure S23 - The chromatogram of the blank sample after the reproducibility tests of BAC-C12 of day 2.

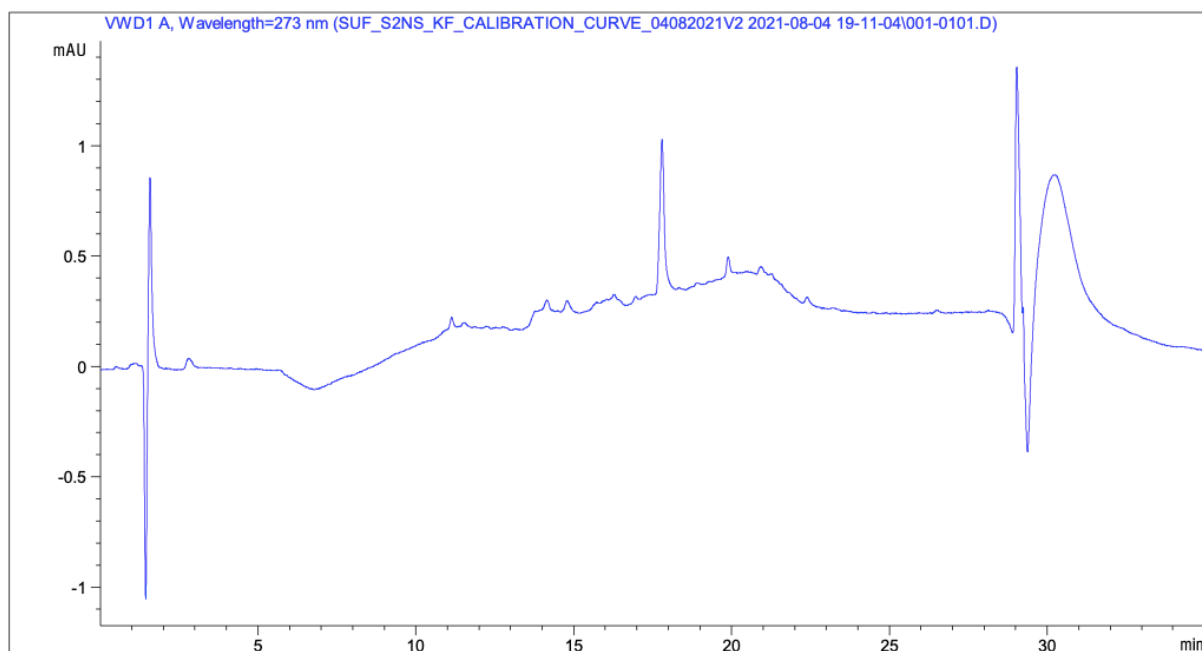


Figure S24 - The chromatogram of the blank sample after the reproducibility tests of S2NS of day 1.

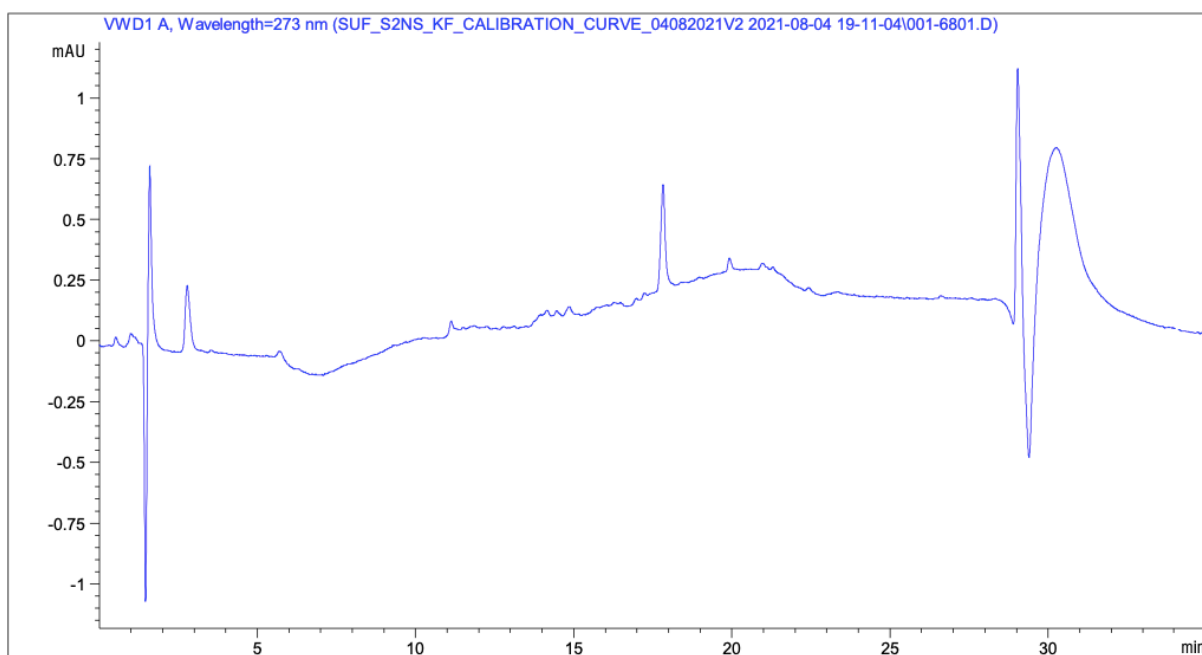


Figure S25 - The chromatogram of the blank sample after the reproducibility tests of S2NS of day 2.

Appendix 3.3

The tables below are displaying the peak areas obtained from the LC-UV analysis of the reproducibility standard for BAC-C12 (200 µg/mL) and S2NS (100 µg/mL) for day 1 and 2. Included in the tables are the calculated mean peak areas, the standard deviation, and the CV%.

Table S24 - A table displaying the results from the reproducibility test for BAC-C12 for day 1.

Sample Name	Peak Area	Mean Peak Area	Standard Deviation Peak Area	CV%
Reprod_1_200ug	217.65294	218.10788	0.50434034	0.23123435
Reprod_2_200ug	218.13051			
Reprod_3_200ug	217.82297			
Reprod_4_200ug	217.81638			
Reprod_5_200ug	217.20992			
Reprod_6_200ug	218.46243			
Reprod_7_200ug	218.36565			
Reprod_8_200ug	218.93985			
Reprod_9_200ug	218.58202			
Reprod_10_200ug	218.09613			

Table S25 - A table displaying the results from the reproducibility test for BAC-C12 for day 2.

Sample Name	Peak Area	Mean Peak Area	Standard Deviation Peak Area	CV%
Reprod_11_200ug	219.65466	218.780745	0.56785492	0.25955434
Reprod_12_200ug	219.27426			
Reprod_13_200ug	218.76264			
Reprod_14_200ug	218.68179			
Reprod_15_200ug	218.62801			
Reprod_16_200ug	218.64725			
Reprod_17_200ug	217.69292			
Reprod_18_200ug	218.90443			

Similar to the ibuprofen injection repeatability, the coefficient of variation (CV %) was utilised to help calculate the spread of the variables. While the F-test was utilised to determine the difference between the two sets of data.

Coefficient of Variation (%):

$$CV(\%) = \frac{0.50434034}{218.10788} \times 100 = 0.23\% \text{ (to 2 d.p)}$$

F-test:

$$F - test = \frac{0.56785492^2}{0.50434034^2} = 1.27 \text{ (to 2 d.p)}$$

Table S26 - A table displaying the results from the reproducibility test for S2NS for day 1.

Sample Name	Peak Area	Mean Peak Area	Standard Deviation Peak Area	CV%
Reprod 100ug 1	2378.47363	2370.92688	5.26138738	0.22191268
Reprod 100ug 2	2373.63892			
Reprod 100ug 3	2366.6521			
Reprod 100ug 4	2374.94971			
Reprod 100ug 5	2367.44824			
Reprod 100ug 6	2362.70435			
Reprod 100ug 7	2365.68921			
Reprod 100ug 8	2371.70581			
Reprod 100ug 9	2377.44531			
Reprod 100ug 10	2370.56152			

Table S27 - A table displaying the results from the reproducibility test for S2NS for day 2.

Sample Name	Peak Area	Mean Peak Area	Standard Deviation Peak Area	CV%
Reprod 100ug 11	2554.06519	2411.55948	58.8989032	2.44235748
Reprod 100ug 12	2419.14233			
Reprod 100ug 13	2388.57056			
Reprod 100ug 14	2394.01733			
Reprod 100ug 15	2379.30566			
Reprod 100ug 16	2381.66162			
Reprod 100ug 17	2384.38354			
Reprod 100ug 18	2391.32959			

Katherine Davies

Coefficient of Variation (%):

$$CV(\%) = \frac{5.26138738}{2370.92688} \times 100 = 0.22\% \text{ (to 2 d.p.)}$$

F-test:

$$F - test = \frac{58.8989032^2}{5.26138738^2} = 125.32 \text{ (to 2 d.p.)}$$

Appendix 3.4

The retention time repeatability was also assessed and the data was recorded in the tables below. Each table contained the retention time (RT) for the solvent front, the retention time of BAC-C12 or S2NS, adjusted RT, mean RT, mean adjusted RT, standard deviation RT, standard deviation adjusted RT, CV% RT and CV% adjusted RT.

Table S28 - A table displaying the results from the reproducibility test for BAC-C12 for day 1.

Sample Name	Solvent Front RT	Sample RT	Adjusted RT	Mean RT	Mean Adjusted RT	Standard Deviation RT	Standard Deviation Adjusted RT	%CV RT	%CV Adjusted RT
Reprod_1_200ug	1.579	13.119	11.54						
Reprod_2_200ug	1.586	13.111	11.525						
Reprod_3_200ug	1.582	13.101	11.519						
Reprod_4_200ug	1.582	13.103	11.521						
Reprod_5_200ug	1.582	13.101	11.519						
Reprod_6_200ug	1.585	13.097	11.512						
Reprod_7_200ug	1.586	13.084	11.498						
Reprod_8_200ug	1.585	13.084	11.499						
Reprod_9_200ug	1.583	13.098	11.515						
Reprod_10_200ug	1.584	13.098	11.514	13.0996	11.5162	0.0106479	0.01217283	0.08128416	0.10570179

Table S29 - A table displaying the results from the reproducibility test for BAC-C12 for day 2.

Sample Name	Solvent Front RT	Sample RT	Adjusted RT	Mean RT	Mean Adjusted RT	Standard Deviation RT	Standard Deviation Adjusted RT	%CV RT	%CV Adjusted RT
Reprod_11_200ug	1.595	13.06	11.465						
Reprod_12_200ug	1.596	13.052	11.456						
Reprod_13_200ug	1.586	13.066	11.48						
Reprod_14_200ug	1.585	13.072	11.487						
Reprod_15_200ug	1.588	13.076	11.488						
Reprod_16_200ug	1.587	13.076	11.489						
Reprod_17_200ug	1.583	13.086	11.503						
Reprod_18_200ug	1.584	13.085	11.501	13.071625	11.483625	0.01180723	0.0163002	0.09032719	0.14194296

Coefficient of Variation (%):

$$CV(\%) = \frac{0.0106479}{13.0996} \times 100 = 0.08\% \text{ (to 2 d.p)}$$

$$\text{Adjusted RT CV}(\%) = \frac{0.01217283}{11.5162} \times 100 = 0.11\% \text{ (to 2 d.p)}$$

F-test:

$$F - test = \frac{0.01180723^2}{0.0106479^2} = 0.81 \text{ (to 2 d.p)}$$

$$\text{Adjusted RT } F - test = \frac{0.0163002^2}{0.01217283^2} = 0.81 \text{ (to 2 d.p)}$$

Table S30 - A table displaying the results from the reproducibility test for S2NS for day 1.

Sample Name	Solvent Front RT	Sample RT	Adjusted RT	Mean RT	Mean Adjusted RT	Standard Deviation RT	Standard Deviation Adjusted RT	%CV RT	%CV Adjusted RT
Reprod_100ug_1	0	2.541	2.541	2.546	2.546	0.01379211	0.01379211	0.5417167	0.5417167
Reprod_100ug_2	0	2.548	2.548						
Reprod_100ug_3	0	2.534	2.534						
Reprod_100ug_4	0	2.562	2.562						
Reprod_100ug_5	0	2.577	2.577						
Reprod_100ug_6	0	2.538	2.538						
Reprod_100ug_7	0	2.536	2.536						
Reprod_100ug_8	0	2.549	2.549						
Reprod_100ug_9	0	2.536	2.536						
Reprod_100ug_10	0	2.539	2.539						

Table S31 - A table displaying the results from the reproducibility test for S2NS for day 2.

Sample Name	Solvent Front RT	Sample RT	Adjusted RT	Mean RT	Mean Adjusted RT	Standard Deviation RT	Standard Deviation Adjusted RT	%CV RT	%CV Adjusted RT
Reprod_100ug_11	0	2.517	2.517	2.533625	2.533625	0.05128057	0.05128057	2.02399983	2.02399983
Reprod_100ug_12	0	2.573	2.573						
Reprod_100ug_13	0	2.553	2.553						
Reprod_100ug_14	0	2.557	2.557						
Reprod_100ug_15	0	2.554	2.554						
Reprod_100ug_16	0	2.564	2.564						
Reprod_100ug_17	0	2.537	2.537						
Reprod_100ug_18	0	2.414	2.414						

Coefficient of Variation (%):

$$CV(\%) = \frac{0.01379211}{2.546} \times 100 = 0.54\% \text{ (to 2 d.p)}$$

F-test:

$$F - test = \frac{0.05128057^2}{0.01379211^2} = 13.82 \text{ (to 2 d.p)}$$

Appendix 3.5

The peak areas and retention times obtained for the calibration standards for BAC-C12 and S2NS are displayed below with the calculated concentrations.

Table S32 - A table displaying the peak areas and actual concentrations obtained for the BAC-C12 calibration standards.

Standard Name	Theoretical Concentration (µg/mL)	RT	Peak Area	Calculated Concentration (µg/mL)
CC_1_10ug	10	13.754	11.70619	10.53389846
CC_2_10ug	10	13.738	11.2481	10.11010736
CC_3_10ug	10	13.72	11.60795	10.44301406
CC_1_30ug	30	13.583	33.17486	30.39512966
CC_2_30ug	30	13.582	32.96526	30.20122319
CC_3_30ug	30	13.573	33.61972	30.80668135
CC_1_50ug	50	13.494	56.22143	51.71611764
CC_2_50ug	50	13.49	56.25807	51.75001427
CC_3_50ug	50	13.463	56.52287	51.99498772
CC_1_70ug	70	13.419	75.13461	69.21319784
CC_2_70ug	70	13.413	75.30601	69.37176449
CC_3_70ug	70	13.384	75.31934	69.38409642
CC_1_100ug	100	13.324	106.77576	98.4852578
CC_2_100ug	100	13.324	106.54575	98.2724695
CC_3_100ug	100	13.314	106.99535	98.68840628
CC_1_130ug	130	13.242	137.92792	127.3049403
CC_2_130ug	130	13.242	137.71107	127.1043266
CC_3_130ug	130	13.223	137.96506	127.3392994
CC_1_160ug	160	13.178	173.13635	159.8771848
CC_2_160ug	160	13.142	173.11691	159.8592003
CC_3_160ug	160	13.153	174.4402	161.0834107
CC_1_200ug	200	13.116	218.53975	201.8810641
CC_2_200ug	200	13.115	217.9735	201.3572113
CC_3_200ug	200	13.062	219.56224	202.8269965

Table S33 - A table displaying the data collected and calculated for the BAC-C12 QC standards (including the accuracy and precision)

Standard Name	Theoretical Concentration (µg/mL)	RT	Peak Area	Calculated Concentration (µg/mL)	Accuracy	Mean Concentration	St Dev	Accuracy %	Precision %
QC Low 1	20	13.651	22.2771	20.3133253	1.56662648	20.8754801	0.5330979	4.37740071	2.55370367
QC Low 2	20	13.642	23.82866	21.74871426	8.74357128				
QC Low 3	20	13.654	22.7855	20.78365951	3.91829753				
QC Low 4	20	13.628	22.8889	20.87931757	4.39658783				
QC Low 5	20	13.637	22.6436	20.65238409	3.26192043				
QC Mid 1	80	13.356	86.1977	79.44795333	-0.6900583	79.9566766	0.81010255	-0.0541543	1.01317687
QC Mid 2	80	13.37	88.04369	81.15572723	1.44465904				
QC Mid 3	80	13.378	87.27119	80.44106716	0.55133395				
QC Mid 4	80	13.387	86.1606	79.41363115	-0.7329611				
QC Mid 5	80	13.383	86.0648	79.32500405	-0.8437449				
QC High 1	180	13.12	196.85699	181.8217726	1.0120959	180.141765	4.71105131	0.07875859	2.61519104
QC High 2	180	13.136	185.95311	171.7343065	-4.592052				
QC High 3	180	13.123	197.37794	182.3037172	1.27984287				
QC High 4	180	13.12	197.82578	182.7180257	1.51001429				
QC High 5	180	13.114	197.19125	182.1310053	1.18389185				

Table S34 - A table displaying the peak areas and actual concentrations obtained for the S2NS calibration standards.

Standard Name	Theoretical Concentration (µg/mL)	RT	Peak Area	Calculated Concentration (µg/mL)
CC 1 1ug	1	2.814	39.22562	1.669058194
CC 2 1ug	1	2.773	38.77045	1.649827999
CC 3 1ug	1	2.808	39.08579	1.663150603
CC 1 2ug	2	2.791	47.97499	2.038704894
CC 2 2ug	2	2.777	46.38802	1.971657984
CC 3 2ug	2	2.774	46.74127	1.986582224
CC 1 5ug	5	2.784	117.53805	4.977631424
CC 2 5ug	5	2.734	116.92992	4.951938918
CC 3 5ug	5	2.81	117.35737	4.969997987
CC 1 10ug	10	2.771	240.0502	10.15357118
CC 2 10ug	10	2.804	237.57355	10.04893673
CC 3 10ug	10	2.78	240.44299	10.17016592
CC 1 20ug	20	2.687	472.13666	19.95884793
CC 2 20ug	20	2.713	467.60733	19.76749108
CC 3 20ug	20	2.733	481.22787	20.34293681
CC 1 40ug	40	2.679	930.75647	39.33479152
CC 2 40ug	40	2.656	918.74347	38.82726174
CC 3 40ug	40	2.694	941.45502	39.78678792
CC 1 60ug	60	2.632	1400.24048	59.16972995
CC 2 60ug	60	2.646	1386.20764	58.57686521
CC 3 60ug	60	2.649	1412.63892	59.69354395
CC 1 100ug	100	2.505	2383.46777	100.7094892
CC 2 100ug	100	2.411	2353.39648	99.43902598

CC 3 100ug	100	2.573	2417.37476	102.1420046
------------	-----	-------	------------	-------------

Table S35 - A table displaying the data collected and calculated for the S2NS QC standards (including the accuracy and precision).

Standard Name	Theoretical Concentration (µg/mL)	RT	Peak Area	Calculated Concentration (µg/mL)	Accuracy	Mean Concentration	St Dev	Accuracy %	Precision %
QC Low 1	1.5	2,782	45.08815	1.916740584	27.7827056	1.86135625	0.20402367	24.0904169	10.9610221
QC Low 2	1.5	2.731	42.17295	1.793578109	19.5718739				
QC Low 3	1.5	2.792	42.02041	1.787133541	19.1422361				
QC Low 4	1.5	2.787	51.27543	2.178143135	45.2095423				
QC Low 5	1.5	2.815	38.3292	1.631185902	8.74572679				
QC Mid 1	15	2.731	366.70914	15.50470609	3.3647073	15.4791432	0.05924633	3.19428804	0.38274944
QC Mid 2	15	2.757	367.78326	15.55008592	3.66723949				
QC Mid 3	15	2.77	364.73294	15.42121485	2.80809898				
QC Mid 4	15	2.747	364.55585	15.41373308	2.75822055				
QC Mid 5	15	2.725	366.7392	15.50597608	3.37317387				
QC High 1	80	2.558	1909.46338	80.68357208	0.8544651	80.9559988	0.78650111	1.19499855	0.97151677
QC High 2	80	2.569	1947.9021	82.30754569	2.88443212				
QC High 3	80	2.612	1904.16321	80.45964849	0.57456061				
QC High 4	80	2.567	1902.37732	80.38419753	0.48024691				
QC High 5	80	2.589	1915.65198	80.9450304	1.181288				

Appendix 3.6

For the quantification of H_2O_2 then quantifix stripes were utilised and can be seen in the image below of how it works.



Figure S26 - Photograph of Quantifix stripes, the stripes after immersed in the electrolyte referred with colour code which infers the range of hydrogen peroxide quantity in mg/L.

While the table below displays all the H_2O_2 values obtained during the BAC-C12 and S2NS degradation experiments.

Table S 36 - A table displaying all the amount of H_2O_2 produced during the degradation of BAC-C12 and S2NS.

Time	H_2O_2 produced during BAC-C12 Degradation (mg/L)				H_2O_2 produced during S2NS Degradation (mg/L)			
	Run 1	Run 2	Run 3	Average	Run 1	Run 2	Run 3	Average
0	0	0	0	0	0	0	0	0
30	0	0	0	0	0	0	0	0
60	3	3	1	2.33	0	0	0	0
90	10	3	3	5.33	0	0	0	0
120	10	3	3	5.33	3	3	3	3
150	10	3	3	5.33	10	10	3	7.67

The table below shows all the pH values obtained for the BAC-C12 and S2NS solutions before and after treatment.

Table S37 - A table displaying all the amount of H₂O₂ produced during the degradation of BAC-C12 and S2NS.

Time	pH produced during BAC-C12 Degradation (mg/L)				pH produced during S2NS Degradation (mg/L)			
	Run 1	Run 2	Run 3	Average	Run 1	Run 2	Run 3	Average
Before	5.92	5.69	5.78	5.80	6.04	6.01	5.88	5.98
After	2.48	2.62	2.69	2.60	2.64	2.56	2.58	2.59